Synthesis of Super-Heavy Elements: Role of Uncertainty Analysis in Theoretical Modeling

Hongliang Lu

UNIVERSITÉ CAEN NORMANDIE

laboratoire commun CEA/DSM spiral2 CNRS/IN2P3

Normandie Université

Université de Caen Normandie

U.F.R. de Sciences

École Doctorale SIMEM

Thèse de doctorat

présentée et soutenue le : *18/11/2015*

par

Monsieur Hongliang LÜ

pour obtenir le

Doctorat de l'Université de Caen Normandie

Spécialité : Constituants élémentaires et physique théorique

Synthèse des noyaux super-lourds : Rôle de l'analyse d'incertitude dans la modélisation

MEMBRES du JURY :

M. D. ACKERMANN	Akademische Direktor, GSI, Darmstadt, Allemagne	(Rapporteur)
M. G. ROYER	Professeur, Université de Nantes, Nantes	(Rapporteur)
Mme F. GULMINELLI	Professeur, Normandie Université, Caen	(Présidente du jury)
Mme B. JURADO	Chargée de recherche, GENBG, Gradignan	(Examinatrice)
M. A. CHBIHI	Directeur de recherche, GANIL, Caen	(Directeur de thèse)
M. D. BOILLEY	Maître de conférence, Normandie Université, Caen	(Encadrant)

GANIL T 2015 03

If a man will begin with certainties, he
shall end in doubts; but if he will be content
to begin with doubts he shall end in certainties.
— Francis Bacon

To my parents and all my family . . .

Acknowledgements

How time flies! Three years have passed in the blink of an eye ... Standing at this turning point, so many pieces of memories come to mind. There are many people to whom I owe a debt of thinks for making my Ph.D. experience so fruitful.

First of all, I would like to express my sincere gratitude to the director of GANIL, Florent Staley, for giving me the opportunity to carry out my research project in theoretical nuclear physics at the GANIL laboratory. Then, I would like to thank Dr. Dieter Ackermann and Prof. Guy Royer for having accepted to be the referees of this thesis. I am also grateful to the other committee members, Prof. Francesca Gulminelli and Dr. Beatriz Jurado. Finally, let me express my deepest and sincere gratitude to my supervisors, Dr. Abdelouahad Chbihi and Dr. David Boilley, for their enlightening guidances and having faith in me. I would like to specially thank David, to whom I owe a special debt for all his support and help over the past years and for giving me the confidence as well as the independence that are indispensable for doing scientific research. When I was stuck somewhere in my work, he was always able to set me on the right track with his exceptional insight and depth of knowledge.

Many thanks to our collaborators, without whom, this Ph.D. work would never have been achieved. First, I would like to extend my heartfelt gratitude to the amiable Prof. Yasuhisa Abe, whose reputation as an excellent physicist precedes him and with whom I had many fruitful discussions. I would also like to thank him for the invitation to Japan, which allowed me to get involved in a long-lasting scientific collaboration. Then, I am very grateful to Prof. Caiwan Shen for his support and help when I stayed at Huzhou University, and for teaching me how to use his code for studying heavy-ion fusion. I was really impressed by his warm welcome, his kindness as well as his patience. In addition, I am deeply indebted to Dr. Anthony Marchix for his attention and the numerous discussions about the development of a computer code which served as the basis for my Ph.D. work. Without his help, this thesis would never have achieved its current form. Finally, I will never forget Dr. Yoann Lallouet and would like to thank him for his help at the beginning of my research project.

And now, my sincere gratitude and appreciation go to all my colleagues working at the GANIL laboratory. It is quite hard to enumerate all of them in a few lines ! Thanks to Pieter Van Isacker and Marek Płoszajczak, whose culture and erudition never cease to impress me. I would also like to thank them for kindly inviting me to attend the Talent Course, which

turned out to be an unforgettable experience during my Ph.D. thesis. Thanks to François de Olivera for sharing his knowledge and enthusiasm for astrophysics and also giving me helpful advice for my post-doc. I am deeply grateful to Beyhan Bastin and Julien Piot for inviting me to get involved in an experimental project at the beginning of my thesis. I am also grateful to the present leader of the physics group, Fanny Farget, for her attention and appreciation on my Ph.D. work. I would also like to express my deep sorrow over the passing away of Mr. Jean-Francois Libin, who was passionate about Chinese culture, and my heartfelt thanks for the invitation to visit his precious collections, the snuff bottles, and to lunch at his house. May his soul rest in peace. Finally, I would like to express my deepest gratitude to all the permanent stuff of the GANIL, Gilles de France, Christelle Stodel, Virginie Lefebvre, Sabrina Lecerf-Rossard, Christine Lemaître, Nicolas Ménard, Michel Lion ... for helping or supporting me in different ways during the past three years. I thought I was lucky to have chance to work in such a homelike environment.

Over the past three years, I also had chance to meet many Ph.D. students or post-docs, with whom I shared lots of great moments. Thanks to Igor, Guillaume, Olivier, Yannen, Paola, Mark, Danilo, Carme, Haïfa, Jose, Marija, Alexis, Kévin, Florent, Pierre, Mathieu, Quentin, Dennis, Nicolas, Bortholmé, Guoxiang, Kosuke, Kazuyuki, Yongjia, Chenchen, Hai, Min, Yunghee ... Thanks to my first office mate, Igor, for the nice moments we shared together during the first year. Thanks to Marija for reading part of the manuscript and her useful comments. Special thanks to my current office mates, Pierre and Kosuke, for their friendship. And also to Mathieu, it will always be my great pleasure to be your tour guide if you still plan to travel to China someday. Sincere thanks to Kévin and Guillaume for their help in solving some physics or numerical problems. I am also grateful to Kazuyuki for kindly guiding me on my trip to Tokyo. I will never forget Yongjia, Chenchen and Hai, for their kindly help when I stayed in Shenzhen and Huzhou, and I miss lots of moments of fun we shared together during the two months. Finally, best wishes to Bartholomé for the rest of his Ph.D. work.

I would like express my gratitude to Prof. Olivier Juillet for accepting me to spend some time teaching at the University of Caen. I am also grateful to Jean-Christophe Poully, Michaël Fromager,Alain Mery and Julie Douady for their help in preparing the practical works. Thanks to Prof. François Mauger, for whom I have a lot of admiration and also for many helpful discussions concerning numerical methods.

Before the end of this acknowledgements section, a special gratitude and love goes to my parents for their eternal support and great encouragement over the past years, especially during the tough times in my research. I would also like to extend my deepest gratitude to all my family and friends.

Hongliang LÜ
GANIL
September 2015

Contents

I Introduction en français

Depuis la découverte de la radioactivité par Henri Becquerel [1], beaucoup d'efforts théoriques et expérimentaux ont été faits dans le but d'approfondir notre compréhension de l'interaction nucléaire et de la structure des noyaux atomiques. En parallèle, de nombreuses applications de la physique nucléaire, telles que la production d'énergie par fission et la médecine nucléaire, ont déjà profondément modifié notre vie quotidienne. Mais en dépit de son succès remarquable jusqu'à maintenant, il reste encore de nombreuses questions ouvertes dans la recherche fondamentale en physique nucléaire, telles que

- Où se trouvent les "drip-lines" de neutrons et de protons ?
- Quelle est l'origine astrophysique des éléments lourds ?
- Quelle est la nature des étoiles à neutrons ainsi que la matière nucléaire dense ?
- ...

La présente thèse a pour objet d'aborder l'une de ces questions intéressantes. En d'autres termes, combien d'éléments peuvent exister dans notre univers ou comment pouvons-nous atteindre la frontière supérieure de la carte des noyaux ?

Il est bien connu que le noyau d'un atome est composé de protons et de neutrons. L'uranium est l'élément le plus lourd, présent sur Terre à l'état naturel, avec 92 protons. Au-delà de ce nombre de protons, les noyaux deviennent de moins en moins stables et ne peuvent exister que pendant des temps qui peuvent devenir très courts. Ce fait provient essentiellement de la compétition entre deux facteurs déterminants, la force nucléaire attractive qui lie protons et neutrons ensemble à l'intérieur d'un noyau atomique et la force coulombienne entre les protons, de sorte que les noyaux lourds deviennent assez instables contre la fission.

Cependant, d'après le modèle en couches, un "îlot de stabilité" a été prédit pour des noyaux constitués d'un nombre de protons bien supérieur à ceux des actinides. Ce sont des éléments dits "super-lourds" (ou transactinides, comportant plus de 103 protons). Dans ce sens, puisque la barrière de fission devient pratiquement nulle aux alentours de $Z = 103$ [2], les éléments super-lourds ne peuvent exister que grâce aux effets de couches qui dépendent

fortement des détails de la structure nucléaire des noyaux.

Les noyaux super-lourds sont d'un intérêt particulier à la fois pour la physique nucléaire et la chimie. Leur existence fournit directement des repères pour tester les prédictions théoriques des différents modèles. Avec la production de nouveaux éléments. les frontières du tableau périodique et de la carte des noyaux sont ainsi étendues. En outre, la caractérisation chimique des éléments super-lourds est également un sujet extrêmement fascinant. L'une des questions très importantes est de comprendre les effets relativistes sur leurs propriétés chimiques.

Les noyaux super-lourds peuvent être formés par la fusion entre deux noyaux plus légers. Il est à mentionner que, au niveau expérimental, le choix de la combinaison projectile-cible serait essentiel pour favoriser la production des noyaux super-lourds et ainsi maximiser les sections efficaces qui sont extrêmement faibles en général, typiquement de l'ordre du picobarn. Pour réaliser ces expériences, deux types de réactions, par fusions froide et chaude, ont été utilisés avec un grand succès pour synthétiser des noyaux avec une charge Z allant de 104 à 118. Leurs principales caractéristiques et avantages (et inconvénients) ainsi que certains résultats assez récents seront présentés et discutés dans un chapitre ultérieur.

Les noyaux super-lourds doivent être formés avec des ions lourds. D'un point de vue théorique, la réaction de fusion-évaporation, utilisée pour former des noyaux lourds, peut généralement être décomposée en deux phases consécutives :

- **La phase de fusion**, au cours de laquelle la collision entre deux noyaux conduit à la formation d'un noyau composé dans un état excité.
- **La phase de déexcitation**, durant laquelle le noyau composé se refroidit par l'évaporation des particules légères et de photons γ, qui entre en compétition avec la fission nucléaire.

En revanche, bien qu'il y ait un accord général sur le mécanisme de la réaction, des ambiguïtés théoriques persistent au niveau théorique. Les calculs théoriques pour la probabilité de fusion peuvent souvent différer d'au plus deuxou trois ordres de grandeur [3, 4], ce qui signifie que la capacité prédictive de la théorie de la fusion reste encore assez mauvaise. En conséquence, il est urgent de trouver de nouvelles façons pour évaluer et contraindre les différents modèles afin d'établir une théorie de la fusion plus fiable, qui sera particulièrement utile pour guider les expériences à venir.

Dans le contexte actuel, certains aspects de la théorie de la fusion des noyaux lourds restent à clarifier. L'analyse de l'incertitude associée à la modélisation de la réaction nucléaire peut être une méthode pour évaluer les modèles. Dans notre cas, il existe trois sources d'incertitude principales : les paramètres d'entrée, les modèles et les données expérimentales utilisées pour contraindre certains paramètres. L'objectif principal de cette thèse est d'appliquer des méthodes statistiques à la quantification des différents sources d'incertitude et de regarder de plus près leur impact sur les résultats finaux. Dans le chapitre 6, après avoir examiné certaines questions centrales en rapport avec la synthèse des éléments super-lourds, nous allons proposer une stratégie pour évaluer les modèles de fusion en étudiant un problème

inverse, c'est-à-dire, contraindre la probabilité de fusion avec l'analyse d'incertitude. Suivant cette stratégie, dans le chapitre 7, nous allons utiliser des approches canoniques [5, 6] et des résultats originaux seront présentés et discutés. Ensuite, les chapitres 8 et 9 seront consacrés à l'introduction de certaines méthodes statistiques avancées, telles que l'inférence bayésienne et la théorie de la régression linéaire pour aborder la réaction de fusion-évaporation à basses énergies. Nous avons adapté ces approches et ainsi fait de premières tentatives pour essayer de contraindre le paramètre le plus important, c'est-à-dire la barrière de fission, et aussi étudier les corrélations entre des grandeurs physiques, telles que l'énergie de séparation d'un neutron et la barrière de fission, ainsi que leur impact sur la probabilité de survie.

Avant d'entrer dans la discussion principale sur l'analyse d'incertitude, dans les deux premiers chapitres, nous allons commencer par rappeler les théories nucléaires qui sont couramment utilisées pour modéliser les deux étapes de réaction mentionnées ci-dessus.

II Conclusions et perspectives

En résumé, une premières tentative a été faite dans le but d'appliquer l'analyse d'incertitude à l'étude de la production des noyaux super-lourds. Comme mentionné au début de la thèse, la théorie de la fusion pour des systèmes lourds, qui est essentielle pour la synthèse des noyaux super-lourds, n'a pas encore été bien établie. Bien qu'il y ait un accord général sur le mécanisme de la réaction, de grands écarts entre les prédictions théoriques basées sur les différents modèles persistent toujours. La question centrale que nous avons posée est, comment évaluer les modèles afin d'établir une théorie de la réaction fiable pour guider de futures expériences ?

Il convient de rappeler que, d'un point de vue conventionel, le processus de fusion pour des systèmes lourds peut être divisé en deux étapes consécutives, c'est-à-dire, la phase de capture correspondant au passage de la barrière coulombienne et la phase de formation correspondant à surmonter une barrière interne (existant seulement pour les systèmes lourds). En ce qui concerne la phase de capture, les données expérimentales sont généralement disponibles dans la littérature, alors que ce n'est pas le cas pour la phase de formation en raison du processus de quasi-fission qui est extrêmement difficile à discriminer du celui de fusion-fission. Certains modèles couramment utilisés pour estimer les sections efficaces de capture ont été brièvement présentés dans la première partie du chapitre 4. Des exemples de calcul ont été montrés et confrontés aux données disponibles, essentiellement à des énergies sous ou à proximité de la barrière coulombienne. Cette étude qualitative nous a permis d'évaluer de façon approximative l'incertitude associée aux modèles de capture. Compte tenu de la simplicité des modèles de capture utilisés, le pouvoir prédictif est plutôt limité. À cet effet, une revue plus exhaustive des modèles de capture disponibles et une comparaison systématique avec les données mesurées devrait être effectuée.

Dans un deuxième temps, afin de mieux comprendre la phase de formation, qui est spécifique à la production des noyaux super-lourds, nous avons présenté un travail récent sur le mécanisme de la fusion entravée à l'aide d'une équation de Langevin bidimensionnelle. Il a été bien établi que le couplage entre le col et la distance radiale a un rôle crucial à jouer dans la description de l'étape de formation pendant le processus de fusion. Il convient de noter que ce modèle est encore un peu trop simple et le travail de suivi est actuellement en cours dans

le but de clarifier l'influence des autres variables, telles que le paramètre d'asymétrie, sur la probabilité de fusion. En plus des ambiguïtés théoriques, puisque les données expérimentales sur la probabilité de fusion ne sont pas disponibles ou sont peu fiables, le principal défi consiste à trouver des moyens pour évaluer et contraindre la description théorique de cette étape intermédiaire pour la production des noyaux super-lourds.

Par rapport à la phase de fusion, la déexcitation des noyaux excités est mieux connue. Dans le chapitre 5, nous avons donné une description complète des ingrédients physiques pour la modélisation de la phase de déexcitation. Certains calculs typiques ont été illustrés et comparés aux données disponibles (sans entrave à la fusion). Puisque l'incertitude sur les paramètres demeure assez importante,il est nécessaire d'examiner son influence sur les résultats de simulation. Dans cette mesure, bien que la phase de désexcitation soit bien décrite, certains paramètres clés, tels que la barrière de fission, ne peuvent pas être déterminés avec précision.

Ensuite, nous avons proposé une stratégie prometteuse pour évaluer les modèles de la fusion à l'aide de la quantification de l'incertitude associée à la phase de désexcitation et à la probabilité empirique de formation. Certaines méthodes avancées, qui sont notamment basées sur des méthodes de Monte-Carlo, ont été présentées en détail. En inspectant les incertitudes dues à la fois aux paramètres et aux modèles, il a été clairement démontré que la barrière de fission a une influence significative sur les résultats des calculs. En conséquence, la question la plus complexe à laquelle nous sommes confrontés ici est comment prendre en compte et contraindre simultanément la fission barrière et le processus de formation ? Est-il possible de faire cela séparément ? Sinon, comment pouvons-nous améliorer le pouvoir prédictif des modèles de la fusion ? Toutes ces questions devraient être résolues afin d'établir une théorie de la fusion satisfaisante et fiable.

Comment faire pour déterminer de façon rigoureuse l'incertitude associée à la barrière de fission ? Sur la base des conclusions tirées de l'analyse d'incertitude de la phase de formation, nous avons proposé de considérer l'inférence bayésienne pour un problème inverse, c'est-à-dire, comment extraire des informations utiles sur la barrière de fission à partir des données mesurées ? Des résultats intéressants ont été obtenus et discutés sous l'hypothèse que la compétition n'a lieu qu'entre l'évaporation d'un neutron et la fission nucléaire. Comme les données expérimentales ne sont généralement pas disponibles à l'heure actuelle, dans un premier temps nous nous sommes limités à des données inventées et avons essayé d'appliquer l'inférence bayésienne à l'étude des systèmes de réaction sans entrave à la fusion. Il a été clairement démontré que l'incertitude sur la barrière de fission extraite semble être assez sensible au nombre et à la précision de données. L'impact des paramètres de nuisance sur l'incertitude de la barrière de fission a été également étudié. La friction ne peut pas être contrainte par l'observable choisie et induit une grande incertitude sur la barrière de fission. De plus, la corrélation entre pseudo-données a été aussi abordée et pourrait avoir un impact significatif sur les résultats finaux. Puisque ce type de calcul est généralement assez long, des efforts supplémentaires au niveau numérique seront nécessaires afin de construire un cadre

plus général permettant de manipuler la distribution de probabilité postérieure de la barrière de fission, en utilisant des techniques avancées, telles que la méthode de Monte-Carlo par chaînes de Markov, dans le but d'améliorer la vitesse de calcul numérique.

Pour contraindre la phase de formation (déterminée par la barrière interne) et la barrière de fission, il faut utiliser le même cadre. Ici, nous avons choisi le modèle de la goutte liquide. Dans ce sens, ces deux étapes doivent être corrélées l'une avec l'autre. Ainsi, nous avons reévalué la formule de masse simple à l'aide de la théorie de la régression linéaire afin de déterminer les incertitudes sur les paramètres du modèle ainsi que la corrélation entre des quantités physiques, telles que l'énergie de séparation d'un neutron et la barrière de fission. D'après les résultats obtenus, il a été clairement montré que la corrélation entre ces quantités physiques pourrait être considérablement forte dans certains cas. De plus, l'impact de leurs covariances sur la probabilité de survie était abordée par le biais de l'analyse d'incertitude avec un modèle simplifié. Selon les résultats préliminaires, il a été montré que l'impact des corrélations sur les résultats finaux serait important et mérite plus de considérations à l'avenir. Il convient également de noter que les incertitudes associées aux corrections de couches n'ont pas été pris en compte, mais elles pourraient être considérablement grandes, en particulier dans la région des noyaux super-lourds. Cette approche pourrait également être généralisée à l'étude relative au processus de formation car la barrière interne est aussi basée sur le modèle de la goutte liquide. Une étude plus approfondie est donc nécessaires pour tenir compte de la corrélation entre les corrections de couches et les barrières de fusion. En conséquence, l'analyse d'incertitude aura un rôle crucial à jouer dans la modélisation et doit être encore développée et adaptée à la théorie de la réaction consacrée à la synthèse des noyaux super-lourds. Dans ce sens, la présente thèse a ouvert de nouvelles voies et il y a encore beaucoup de travail à faire à l'avenir.

Dans une perspective générale, nous aurions aussi besoin d'avoir plus de données expérimentales dans le but de mieux contraindre les modèles de la fusion. Quelles sont les observables pertinentes ? Est-il possible de concevoir de telles expériences avec la technologie de nouvelle génération ? La présente thèse ne va pas jusqu'à la fin, mais il est espéré que la stratégie proposée ici peut être davantage exploitée afin de décrire correctement le mécanisme de la réaction avec de nouvelles données expérimentales.

III General introduction

Since the discovery of radioactivity by Becquerel in 1896 [1], nuclear physics has flourished over the past hundred years. Many fascinating breakthroughs have been made in our understanding of the nuclear interaction and the structure of atomic nuclei. Along with the development of theory, nuclear physics has also wide applications in numerous fields, such as power generation and nuclear medicine, which deeply impact our daily lives. But despite its remarkable success so far, there still remain many open questions on both experimental and theoretical levels, such as

- Where are the proton and neutron drip lines situated?
- Where does the nuclear chart end?
- What is the astrophysical origin of the heavy elements?
- What is the nature of neutron stars as well as dense nuclear matter?
- ...

The topic of the present Ph.D. thesis mainly addresses one of these interesting questions, that is to say, how many elements might exist or how to reach the upper end of the nuclide chart?

Early nuclear theory proposed that the atomic nucleus could be thought of as a charged liquid drop, which is now known as the liquid-drop model [7, 8]. On the basis of this model, nuclear fission of heavy nuclei, first discovered by Hahn and Straßmann [9, 10], was correctly explained [11] and limits the number of chemical elements or the number of nucleons (protons and neutrons) inside atomic nuclei. This is mainly due to the fact that, according to Ref. [2], the liquid-drop fission barrier would vanish at around $Z = 103$ so that nothing would prevent the nucleus from splitting. Such an estimate mainly arises from the competition between two important parameters, namely the attractive nuclear force that binds protons and neutrons together inside an atomic nucleus and thus creates a surface tension, and the repulsive Coulomb force between protons, so that heavier nuclei become quite unstable against fission.

Nevertheless, the liquid-drop model has some fundamental limitations. For instance, it is not able to interpret the appearance of the so-called magic numbers as well as the extra stability

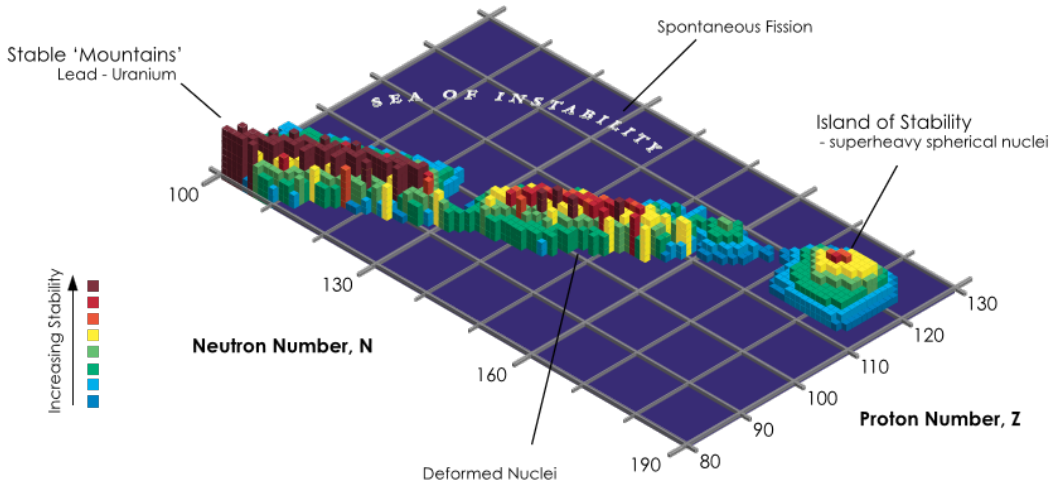

Figure III.1 – “Island of stability", which stands for a set of as-yet undiscovered isotopes of trans-actinides having long half-lives, is indicated in the upper right-hand corner of the nuclear chart. Figure is taken from the Wikipedia website.

associated with these special numbers of nucleons. Like the electron shell structure of atoms, it is commonly known that nuclei at the conventional magic numbers (2, 8, 20, 28, 50, 82 for both neutrons and protons, and 126 for neutrons) have an increased binding energy compared to the average trend. This phenomenon was later successfully explained by the well-known nuclear shell model [12–14]. By means of the shell model, an extrapolation into unknown regions was undertaken and thus led to the possibility of producing super-heavy elements (SHE, also called trans-actinides, with atomic numbers greater than $Z = 103$), which do not exist on Earth. In this sense, the existence of super-heavy nuclei is exclusively determined by quantum (shell correction) effects and strongly dependent on the details of the nuclear structure.

SHE are subjects of special interest to both nuclear physics and chemistry. The existence and properties of super-heavy nuclei provide perfect benchmarks for theoretical predictions of the nuclear shell model. With the production of new SHE, the boundaries of the periodic table and nuclide chart are thus extended. Furthermore, chemical characterization of SHE is also an extremely fascinating subject. A very important and interesting question is to clarify chemical properties of these elements, such as ionic charge and radius, complex formation and so on, and to elucidate the influence of relativistic effects on their chemical properties.

Since the late 1960s, extensive experimental and theoretical efforts have been made to synthesize new SHE. Over the last several decades, a number of new exotic nuclei far from the valley of stability have been accessible in almost any region of the nuclide chart thanks to the development of cutting-edge technology, namely large heavy-ion facilities. The only exception is the northeast part of the chart where the predicted “island of stability” might

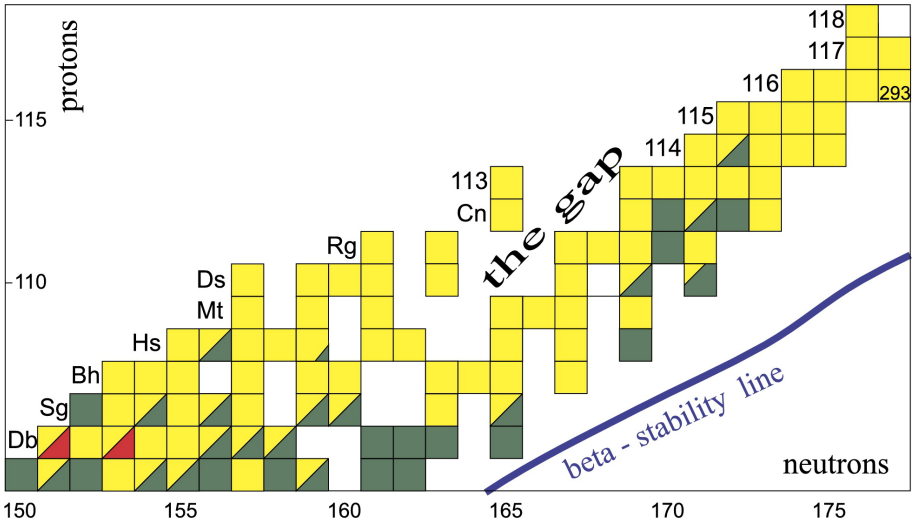

Figure III.2 – Upper end of the nuclear chart. Two groups of isotopes of SHE synthesized using cold-fusion reactions (from $Z = 104$ to $Z = 113$) and hot-fusion reactions (from $Z = 112$ to $Z = 118$) are shown together with the gap separating them. Figure is taken from Ref. [18].

be located, as shown in Fig. III.1. However, its precise position still remains a mystery to us. Based upon some recent advances in macroscopic and microscopic theories, the next possible magic number of neutrons for spherical nuclei is likely to be 184, but some possible magic proton numbers have been predicted to be 114 [15], 120 and 126 [16, 17]. Hence, one of the biggest challenges for theorists is to figure out this incoherence between different types of theories on the prediction of this "magic zone". Anyhow, this can be considered to a direct test for probing the validity of different nuclear models under extreme conditions.

In the European Union, the synthesis and study of SHE has a long glorious history, dating back to the early 1970s (formation of the GSI Helmholtz Center for Heavy Ion Research in Darmstadt). It still remains an active research area and continues to be supported at both national and European levels. For instance, at the GANIL laboratory in Caen, a very promising project, called SPIRAL2 [19], is currently under construction and the first experiments will be performed in the coming years. It should be noted that the research of SHE has become a priority within the new project. Several experiments have been proposed, for instance, the investigation of the nuclear structure of ^{254}No with S^3 (Superconducting Separator Spectrometer) has already been scheduled within the SPIRAL2 project [20]. In a worldwide context, several similar heavy-ion facilities are currently in service (e.g., HIRFL Lanzhou, Riken Tokyo, FLNR Dubna, LBNL Berkeley, etc.), it is reasonably believed that, by means of all these powerful set-ups, new breakthroughs are expected to be made in a near future, and thus boost the research of SHE. An exciting new era for nuclear physics is coming towards us.

From an experimental point of view, they can only be artificially synthesized by bombarding the heaviest targets available nowadays with intense heavy-ion beams (heavy-ion fusion reaction). Such a process could eventually lead to the formation of a super-heavy nucleus after

surviving nuclear fission. To perform such kind of experiment, one practically needs three pieces of special equipment:

- **An accelerator**, which aims to generate intense heavy-ion beams used to bombard the heavy targets.
- **A separator device**, which is employed to separate the events of interest from everything else produced during the reaction.
- **A detection system**, which is able to observe and record all events that take place during the experiment. This is crucial because the newly-formed heavy nucleus cannot be directly seen, but needs to be identified mainly from α decays.

The choice of the projectile-target combination would be essential for the magnitude of production cross-sections which are extremely low, typically of the order of picobarn. To realize such experiments, two crucial types of fusion reactions, namely cold and hot fusions, have been successfully employed to synthesize SHE with atomic number from 104 to 118 (cf. Fig. III.2). More concretely, the former corresponds to the fusions of ^{208}Pb, ^{209}Bi with massive projectiles (heavier than calcium), where the excitation energy of the newly-formed heavy nucleus ranges from 10 to 20 MeV, leading to the evaporation of one or two neutrons, whereas the latter corresponds to the collision of a lighter projectile with some actinide targets, where the resulting excitation energy is basically a bit higher, say around 30 – 60 MeV, leading to the evaporation of more than two or three neutrons. Their main characteristics and advantages (and disadvantages) as well as some recent achievements will be presented and discussed in a later chapter.

It should be mentioned that SHE can only be formed in massive colliding systems. Hence, the nuclear reaction theory for heavy systems would be crucially important for the synthesis of SHE. From a theoretical viewpoint, the synthesis of SHE can be realized with the help of the so-called fusion-evaporation reaction, which is divided into two separate phases:

- **Fusion phase**, during which a nucleus-nucleus collision leads to the formation of an excited heavy nucleus.
- **De-excitation phase**, where the newly-formed heavy nucleus has to be chilled by evaporation of light particles, nuclear fission or γ-ray emission.

However, although we have reached a general agreement on the reaction mechanism, crucial discrepancies still persist in quantitative predictions made by different theoretical models. For instance, as clearly shown in Refs. [3, 4], theoretical predictions for the fusion probability can differ by at least two orders of magnitude, which means that the predictive capability of the reaction theory remains quite poor. Hence, it would be urgent to find new ways to assess the fusion models so as to establish a reliable and accurate reaction theory that would be particularly helpful for guiding future experiments on the synthesis of SHE.

Since some aspects of the nuclear reaction theory remain ambiguous, it is necessary to clarify the uncertainty in reaction modeling. Basically, there exist three main sources of

uncertainty in our case: input parameters, models (approximations) and experimental data used to infer some parameters. The main aim of the present Ph.D. thesis is to employ some advanced statistical methods to quantify the different uncertainty sources and look more closely at their impact on the calculated results. In Chapter 6, after examining some central issues related to the synthesis of SHE, we propose a general framework for assessing the fusion models by dealing with an inverse problem, that is to say, constraining the fusion probability with uncertainty analysis of the de-excitation phase. Following this strategy, in Chapter 7, we will employ the canonical approaches presented in Refs. [5, 6] to constrain the fusion probability for cold-fusion reactions and some crucial results will be reported. After that, Chapter 8 and Chapter 9 will be devoted to the application of some advanced statistical methods, such as Bayesian inference and linear regression theory to studying the fusion-evaporation reaction at low energies. It should be noted that this is the first time that we have adapted these approaches and made our first attempts in this field to constrain the most crucial parameter, namely the fission barrier, and investigate the correlations between some physical quantities, such as the neutron-separation energy and fission barrier, as well as their impact on the survival probability.

Before getting into the main discussion on uncertainty analysis, in the following two chapters, we shall start by recalling some state-of-the-art nuclear theories that are commonly employed to model the two reaction stages mentioned above.

IV Heavy-ion fusion

> Learn from yesterday, live for today, hope for tomorrow. The important thing is not to stop questioning.
>
> Albert Einstein

The fusion of two heavy ions, forming a heavier nucleus, is a topic of wide interest to many active areas of nuclear physics. It is particularly essential for fundamental research because it might give access to exotic nuclei that do not exist on Earth. From a theoretical point of view, the heavy-ion fusion can be generally decomposed into two successive stages:

- **Capture step**, corresponding to the passage over the Coulomb (or Bass [31]) barrier, after which two colliding nuclei stick together.
- **Formation step**, leading to the creation of a composite system, where the incident particle combines with the target nucleus and the total energy is shared among all the nucleons contained in such a system. This is the so-called compound nucleus (CN). Here, it should be mentioned that the formation step was introduced to explain the so-called "fusion hindrance" phenomenon that only occurs in heavy reaction systems (with a charge product of the projectile-target combination $Z_p Z_t \gtrsim 1600 - 1800$ [29]). Regarding lighter systems, the colliding nuclei automatically fuse after crossing the Coulomb barrier.

As an illustration, Fig. IV.1 shows the conventional view of the fusion process including the above two steps. A stable nucleus is finally formed after cooling down by emission of light particles and γ-rays.

In this chapter, we plan to investigate these two steps in a separate manner, including a discussion of recent theoretical progress as well as some further prospects. Then, a combined reaction model is presented in detail and applied to the study of the reaction ^{129}Xe+^{nat}Sn that was well measured with the INDRA detector at the GANIL laboratory [32].

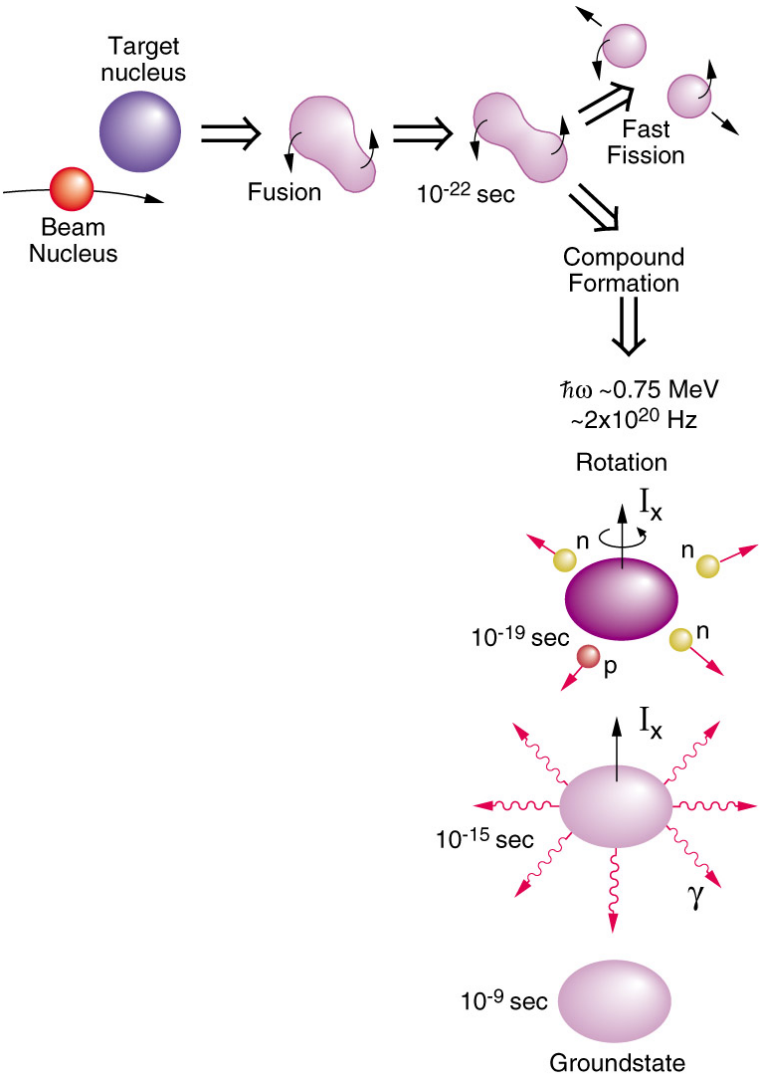

Figure IV.1 – Illustration of the reaction mechanism for the fusion process leading to the formation of super-heavy nuclei. For heavy colling systems, fast fission or quasi-fission [21–29] comes into play after overcoming the Coulomb barrier. After the fusion process, a new heavier nucleus is formed in an excited state. Figure is taken from the website [30].

IV.1 Capture Step

Thanks to the development of new experimental techniques over the past few decades, capture excitation functions can now be measured precisely over a wide energy range, especially at sub-barrier energies [33–36]. With such high-precision measurements, some renewed interest in sub-barrier fusion has been generated. For instance, they have enabled a detailed study of channel-coupling effects on the capture reaction by means of the so-called barrier-distribution method. Extensive experimental as well as theoretical studies have revealed that such reactions are strongly influenced by the coupling of the relative motion of the colliding

nuclei to several nuclear collective states [37, 38]. This can be essential when discussing the so-called cold-fusion reaction, where the single-neutron evaporation channel usually lies within the sub- or near-barrier energy region.

The aim of this section is to investigate the capture step using different theoretical approaches so as to clarify their limitations. The section is organized as follows. First, we briefly review three commonly used models for estimating capture cross-sections. Then, some theoretical calculations are performed and the results are carefully confronted with the selected experimental data (mainly for heavy systems). The uncertainty related to the capture model is also roughly estimated.

IV.1.1 Coupled-channels description

According to the standard quantum mechanics, the fusion of two colliding nuclei by crossing the Coulomb barrier can be described by the radial wave function that obeys the following Schrödinger equation:

$$\left(-\frac{\hbar^2}{2\mu}\frac{\mathrm{d}^2}{\mathrm{d}r^2}+\frac{l(l+1)\hbar^2}{2\mu r^2}+V(r)-E_{\mathrm{cm}}\right)\phi_l(r)=0, \tag{IV.1}$$

where μ refers to the reduced mass of the system and $V(r)$ is the total potential energy, which is composed of the nuclear part $V_N(r)$ and the Coulomb part $V_C(r)$, namely $V(r)=V_N(r)+V_C(r)$. When the projectile and target nuclei are both assumed to be spherical, they are respectively given by

$$V_C(r)=\frac{Z_pZ_te^2}{r} \tag{IV.2}$$

and

$$V_N(r)=-\frac{V_0}{1+\exp[(r-R_0)/a]}, \tag{IV.3}$$

where a phenomenological Woods-Saxon potential has been introduced to describe the nuclear interaction. To solve Eq. (IV.1), we adopt the following boundary conditions:

$$\phi_l(r)=\sqrt{\frac{k}{k_l(r)}}T_l\exp\left[i\int_r^{r_{\mathrm{abs}}}k_l(r')\mathrm{d}r'\right],\ \text{for } r\le r_{\mathrm{abs}}, \tag{IV.4}$$

$$\sim\frac{i}{2}\left[H_l^{(-)}(kr)-S_lH_l^{(+)}(kr)\right],\ \text{for } r\to+\infty. \tag{IV.5}$$

Here, r_{abs} denotes the absorption radius that is considered to be inside the potential pocket. k and $k_l(r)$ represent the wave numbers, which can be explicitly written as follows:

$$k=\sqrt{\frac{2\mu E_{\mathrm{cm}}}{\hbar^2}}, \tag{IV.6}$$

$$k_l(r)=\sqrt{\frac{2\mu}{\hbar^2}\left(E_{\mathrm{cm}}-V(r)-\frac{l(l+1)\hbar^2}{2\mu r^2}\right)}. \tag{IV.7}$$

Eq. (IV.4) is the so-called incoming wave boundary condition (IWBC) which is often used in the study of heavy-ion fusions (e.g., the CCFULL code [39]). It is clearly understood that the IWBC corresponds to the case where a strong absorption appears within the inner region of the potential, so that the incoming flux never returns back. As mentioned in Ref. [37], in the case of heavy-ion collisions, calculated results would not be sensitive to the value of $r_{\rm abs}$, which is often taken to be the minimum position of the potential pocket.

Using the IWBC, it would not be difficult to obtain the following formula for estimating capture cross-sections:

$$\sigma_{\rm cap}\,(E_{\rm cm}) = \frac{\pi}{k^2}\sum_{l\geq 0}(2l+1)P^l_{\rm cap}(E_{\rm cm}), \tag{IV.8}$$

where $P^l_{\rm cap}(E_{\rm cm})$ is nothing else but the capture probability of the l-th partial wave, which is simply given as follows:

$$P^l_{\rm cap}(E_{\rm cm}) = |T_l|^2\,. \tag{IV.9}$$

Here, T_l is usually referred to as the transmission coefficient, whose value is closely related to the nuclear potential introduced in the one-dimensional capture model. It will thus be necessary to say a bit more about the phenomenological nuclear potential.

Three potential parameters appearing in Eq. (IV.3), namely R_0, V_0 and a. were commonly determined with the help of a least-squares fit to the data of heavy-ion elastic scattering (cf. Ref. [40]). A phenomenological potential thus constructed, sometimes called the Akyüz-Winther (AW) potential, has been quite successful in reproducing experimental angular distributions of elastic and inelastic scattering for many reaction systems. In this section, we adopt the following parameterization for the AW potential [41]:

$$\begin{aligned}
a^{-1} &= 1.17\left[1+0.53\left(A_p^{-1/3}+A_t^{-1/3}\right)\right]\ {\rm fm}^{-1},\\
R_0 &= R_p + R_t \text{ with } R_i = (1.2A_i^{1/3} - 0.09)\ {\rm fm},\\
\overline{R} &= R_p R_t/\left(R_p+R_t\right)]\ {\rm fm},\\
V_0 &= 16\pi\gamma\overline{R}a{\rm MeV},\\
\gamma &= 0.95\left[1-1.8\left(\frac{N_p-Z_p}{A_p}\right)\left(\frac{N_t-Z_t}{A_t}\right)\right]\ {\rm MeV/fm}^2,
\end{aligned} \tag{IV.10}$$

where γ refers to the average surface energy of two colliding nuclei. Here, the typical value of the surface diffuseness parameter, namely a, is typically around 0.63 fm. However, recent experimental data for heavy-ion sub-barrier capture reactions suggest that a much larger value of the diffuseness parameter, ranging from around 0.75 to 1.5 fm, might be required for fitting to the measured data [36, 42]. The reason for this huge conflict of the parameter values extracted from both heavy-ion scattering data and fusion analyses is not yet fully understood. One possible reason could be that heavy-ion scattering only occurs near the nuclear surface, whereas other effects can also come into play inside the nucleus. In practice, it would be necessary to somehow tune values of the potential parameters so as to give reasonable and consistent results with respect to experimental data. In this sense, theoretical predictability of

the capture model seems to be rather limited by the potential parameterization.

Let us now take the intrinsic states of projectile and target nuclei into consideration. In this case, the simple one-dimensional model (cf. Eq. (IV.1)) can be improved using the so-called coupled-channels (CC) approach. To illustrate this method, one might consider a collision between two nuclei with the coupling of relative motion to a nuclear intrinsic state, denoted by ξ. The resulting Hamiltonian for this reaction system can be expressed in the following form:

$$H(\mathbf{r},\xi) = -\frac{\hbar^2}{2\mu}\Delta + V(r) + H_0(\xi) + V_{\text{coup}}(\mathbf{r},\xi), \tag{IV.11}$$

where $H_0(\xi)$ and $V_{\text{coup}}(\mathbf{r},\xi)$ correspond to the intrinsic and coupling Hamiltonians, respectively. Then, on the basis of such this composite Hamiltonian, it would be easy to derive a system of coupled differential equations for the radial wave function, namely

$$\left[-\frac{\hbar^2}{2\mu}\frac{\mathrm{d}^2}{\mathrm{d}r^2} + \frac{J(J+1)\hbar^2}{2\mu r^2} + V(r) - E_{\text{cm}}\right]\phi_n^J(r) = -\sum_{n'}\left[\epsilon_n\delta_{nn'} + V_{nn'}(r)\right]\phi_{n'}^J(r), \tag{IV.12}$$

where n represents a certain quantum state and J the total angular momentum that is equal to the sum of relative orbital angular momentum and spin of intrinsic motion. Here, ϵ_n refers to the energy eigenvalue of the intrinsic Hamiltonian H_0 (satisfying $H_0\phi_n = \epsilon_n\phi_n$) and $V_{nn'} = \langle n|V_{\text{coup}}|n'\rangle$ denotes the coupling matrix elements estimated by means of V_{coup}. It should be mentioned that, in writing Eq. (IV.12), we have employed the so-called no-Coriolis or iso-centrifugal approximation [39], which states that the angular momentum of the relative motion in each channel can be replaced by the total angular momentum of the compound system. This results from the assumption that variation of the relative orbital angular momentum between the colliding nuclei due to the excitation of intrinsic states might be negligible. Together with the IWBC, one gets the following formula for estimating the capture probability:

$$P_{\text{cap}}^J(E_{\text{cm}}) = \sum_n \left|T_{nn_i}^J\right|^2, \tag{IV.13}$$

where n_i refers to quantum state for the entrance channel. It is obvious that the capture cross-section can be calculated as follows:

$$\sigma_{\text{cap}}(E_{\text{cm}}) = \frac{\pi}{k^2}\sum_{J\geq 0}(2J+1)P_{\text{cap}}^J(E_{\text{cm}}), \tag{IV.14}$$

except that the capture probability is now affected by intrinsic states. Eq. (IV.13) is the main outcome of the CC approach.

A pedagogical example

To illustrate the impact of channel couplings on the capture probability, we would like to introduce a toy model which is similar to that proposed in Refs. [43, 44]. Let us consider a coupling potential V_{coup} which can be factored into a product of the relative part, say $F(r)$,

and the intrinsic part, say $G(\xi)$. The coupling matrix elements are thus given by

$$V_{nn'}(r) = F(r)\langle n|G(\xi)|n'\rangle. \tag{IV.15}$$

In the special case where only two levels are taken into account, one can rewrite Eq. (IV.12) in matrix form as

$$\left[-\frac{\hbar^2}{2\mu}\frac{\mathrm{d}^2}{\mathrm{d}r^2} + V_J(r) - E_{\mathrm{cm}}\right]\begin{pmatrix}\phi_0^J(r)\\ \phi_1^J(r)\end{pmatrix} = -\begin{pmatrix}0 & F\\ F & G\end{pmatrix}\begin{pmatrix}\phi_0^J(r)\\ \phi_1^J(r)\end{pmatrix}, \tag{IV.16}$$

where the matrix elements are assumed to be constant. Here, $V_J(r)$ denotes $J(J+1)\hbar^2/2\mu r^2 + V(r)$. The eigenvalues of coupling matrix are simply given by $\lambda_\pm = (G \pm \sqrt{G^2+4F^2})/2$. By diagonalizing the coupling matrix, Eq. (IV.16) can be transformed into the following linear form:

$$\begin{pmatrix}-\frac{\hbar^2}{2\mu}\frac{\mathrm{d}^2}{\mathrm{d}r^2} + V_J(r) + \lambda_+ - E_{\mathrm{cm}} & 0\\ 0 & -\frac{\hbar^2}{2\mu}\frac{\mathrm{d}^2}{\mathrm{d}r^2} + V_J(r) + \lambda_- - E_{\mathrm{cm}}\end{pmatrix}\begin{pmatrix}U_{00}\phi_0^J(r) + U_{01}\phi_1^J(r)\\ U_{10}\phi_0^J(r) + U_{11}\phi_1^J(r)\end{pmatrix} = 0, \tag{IV.17}$$

where $U_{nn'}$ represent elements of the transformation matrix that is used to diagonalize the coupling matrix. Accordingly, it is clearly shown that the effect of channel couplings consists in replacing the original barrier by two eigenbarriers $V_J(r) + \lambda_\pm$. Thus, the capture probability becomes

$$P_{\mathrm{cap}}^J(E_{\mathrm{cm}}) = w_+ P_{\mathrm{cap}}^J(E_{\mathrm{cm}} - \lambda_+) + w_- P_{\mathrm{cap}}^J(E_{\mathrm{cm}} - \lambda_-), \tag{IV.18}$$

where $w_\pm$ correspond to the weight coefficients and should be normalized to unity, namely $w_- + w_+ = 1$. In other words, with the presence of channel couplings, the capture probability naturally splits into two independent components resulting from two different effective fusion barriers, respectively.

The above conclusion can be readily generalized to the case where more intrinsic states come into play and thus more effective fusion barriers shall be generated. The general conclusion is that, for a given total angular momentum J and a given energy E_{cm}, the capture probability should be expressed as a sum of all coupling contributions, namely

$$P_{\mathrm{cap}}^J(E_{\mathrm{cm}}) = \sum_i w_i P_{\mathrm{cap}}^J(E_{\mathrm{cm}} - \lambda_i), \tag{IV.19}$$

where $\sum w_i = 1$ and $P_{\mathrm{cap}}^J(E_{\mathrm{cm}} - \lambda_i)$ is the capture probability corresponding to an effective barrier shifted by λ_i, which is nothing else but a generalization of Eq. (IV.18). One simple interpretation for this expression is that fusion occurs through certain eigenchannels or transition states labeled by i. More concretely, each eigenstate i has an excitation energy, say λ_i, and the effective barrier height corresponding to that channel is given by $V_B + \lambda_i$, where V_B denotes the barrier height coming from V_J. The weight coefficient w_i represents the probability of arriving at the barrier of transition state i. It should be mentioned that, Eq. (IV.19) contains crucial information that allows us to explore the inner structure of the

nucleus. By measuring the shape of fusion excitation function or the corresponding barrier distribution [45], it would be possible to investigate intrinsic states of the nucleus by means of the CC approach.

Until now, we have briefly outlined some basic features of the CC method. This has been completely incorporated into the CCFULL code [39]. Using this computer code, coupled differential equations are numerically solved, provided that matrix elements of the coupling Hamiltonian can be explicitly estimated. In the following study, the CCFULL code will be employed to estimate capture cross-sections. It should be noted that, for heavy colliding systems, since the number of intrinsic states rapidly goes up with incident energy, the CC calculation becomes increasingly complicated and some additional ambiguities would arise. In such cases, approximate methods can be very useful. In the following subsections, two commonly used alternatives to the CC approach will be presented.

IV.1.2 Empirical barrier-distribution method

A powerful method based on the barrier distribution to calculate the capture cross-section was first proposed in Ref. [46]. It was assumed that the fusion excitation function at a given energy E can be written as follows:

$$\sigma_{\rm cap} = \int_0^\infty \sigma_{\rm cap}(E_{\rm cm}, B) D(B) {\rm d}B, \tag{IV.20}$$

where $D(B)$ refers to a normalized weight function for the interaction barrier B, which can be directly determined from measured data [45]. A theoretical justification of Eq. (IV.20) can be derived from a CC treatment under certain approximations (cf. the previous subsection). When neglecting internal excitation energies or intrinsic states, the weight coefficient can be reasonably approximated by a Gaussian function [47, 48],

$$D(B) = \frac{1}{\sqrt{2\pi}w} \exp\left[-\frac{(B-B_0)^2}{2w^2}\right], \tag{IV.21}$$

with the mean value B_0 and width of the distribution w.

Moreover, it is commonly known that the classical capture cross-section corresponding to a certain barrier B can be simply given as follows: $\sigma_{\rm fus}(E_{\rm cm}, B) = \pi R^2(1 - B/E_{\rm cm})$. Hence, within this framework, the capture cross-section is obtained via the following folding procedure:

$$\begin{aligned} \sigma_{\rm cap}(E_{\rm cm}) &= \int_0^{E_{\rm cm}} \sigma_{\rm cap}(E_{\rm cm}, B) D(B) {\rm d}B \\ &= \sqrt{\frac{\pi}{2}} \frac{R^2 w}{E_{\rm cm}} \left\{\sqrt{\pi} X \left[1 + {\rm erf}(X)\right] + \exp\left(-X^2\right)\right\} \end{aligned} \tag{IV.22}$$

where

$$X = \frac{E_{\rm cm} - B_0}{w\sqrt{2}}, \tag{IV.23}$$

and erf(x) is the Gaussian error function. Here, the parameters B_0 and w, as well as the radius parameter R, were determined from the analysis of capture excitation functions for about 50 reaction systems. Thus, the mean barrier height B_0 is parameterized as a cubic polynomial, namely

$$B_0 = 0.853\,315z + 0.001\,169\,5z^2 - 0.000\,001\,544z^3 \text{ MeV}, \tag{IV.24}$$

where $z = Z_t Z_p/(A_t^{1/3} + A_p^{1/3})$. The parameter R is taken to be $R = 1.16(A_t^{1/3} + A_p^{1/3})$ fm. The width parameter w is given by

$$w = CB_0\sqrt{\delta_t^2 + \delta_p^2 + \delta_0}, \tag{IV.25}$$

where $\delta_i = R_i^2\beta_i^2/4\pi$ with the radii R_t and R_p defined as $1.15A_i^{1/3}$ and their quadrupole deformation parameters β_2 taken from Ref. [15]. Finally, the parameters C and δ_0 are estimated to be $C = 0.042\,1$ fm^{-1} and $\delta_0 = 0.531$ fm [49].

In the following study, the empirical barrier-distribution (EBD) method will be employed to estimate capture cross-sections. It might be noted that this approach is somewhat similar to the CC method, that is to say, accounting for the coupling between collective states. The effective barrier thus follows a Gaussian distribution. However, we should be aware that the closed-form formula, Eq. (IV.22), has been obtained by folding a Gaussian distribution with the classical formula for estimating capture cross-sections. In practice, due to the large uncertainty remaining in the parameterization of w (up to about 1 MeV), we should be cautious when making theoretical predictions, especially at sub-barrier energies.

Finally, to include the angular momentum in this approach, a step function for the penetration probability is proposed, namely

$$P_{\text{cap}}^J(E_{\text{cm}}, B) = \theta\left[E_{\text{cm}} - B - \frac{\hbar^2 J(J+1)}{2\mu R^2}\right]. \tag{IV.26}$$

Using the same folding procedure, together with $B_0/(\sqrt{2}w) \gg 1$, one obtains the following approximate expression for the partial-wave capture possibility:

$$\begin{aligned} P_{\text{cap}}^J(E_{\text{cm}}) &= \int_0^{E_{\text{cm}}} P_{\text{cap}}^J(E_{\text{cm}}, B)D(B)\mathrm{d}B = \frac{1}{2}\,\text{erf}\left[\frac{E_{\text{cm}} - B - \frac{\hbar^2 J(J+1)}{2\mu R^2}}{\sqrt{2}w}\right] + \frac{1}{\sqrt{\pi}}\int_0^{\frac{B_0}{\sqrt{2}w}} \exp(-u^2)\mathrm{d}u \\ &\simeq \frac{1}{2}\left\{1 + \text{erf}\left[\frac{E_{\text{cm}} - B - \frac{\hbar^2 J(J+1)}{2\mu R^2}}{\sqrt{2}w}\right]\right\}. \end{aligned} \tag{IV.27}$$

IV.1.3 Semi-classical method: one-dimensional model

As can be seen above, the CC approach would be capable of providing a complete description of the capture process, as the collective properties of colliding nuclei are taken into

consideration. However, due to the complexity of this approach, namely solving a number of coupled differential equations, it would always be helpful to have an easy-to-use formula in hand for practical calculations.

On the basis of a semi-classical framework, in the case of two spherical colliding nuclei, the partial-wave penetration probability can be evaluated using the Wentzel-Kramers-Brillouin (WKB) approximation, namely

$$P^J_{\rm cap}(E_{\rm cm}) = \exp\left[-2\int_{r_{\rm in}}^{r_{\rm out}} {\rm d}x' \sqrt{\frac{2\mu}{\hbar^2}\left(V_J(x') - E_{\rm cm}\right)}\right] = \exp(-2\Omega), \tag{IV.28}$$

where $r_{\rm in}$ and $r_{\rm out}$ respectively denote the inner and outer classical turning points that satisfy the following relationship: $V_l(r_{\rm in}) = V_l(r_{\rm out}) = E$. In Ref. [50], Kemble proposed a more general solution:

$$P_{\rm cap}(E_{\rm cm}, J) = \frac{1}{1+\exp(2\Omega)}, \tag{IV.29}$$

which would be valid at both sub- and above-barrier energies. The potential V_J is given as follows:

$$V_J(r) = V_N(r) + V_C(r) + V^J_{\rm cent}(r), \tag{IV.30}$$

with

$$V_C(r) = \frac{Z_p Z_t e^2}{r} \text{ and } V^J_{\rm cent}(r) = \frac{J(J+1)\hbar^2}{2\mu r^2}. \tag{IV.31}$$

Regarding the nuclear part $V_N(r)$, the well-known proximity potential [51] is often employed. In general, it can be written as $V_N(r) = 4\pi\gamma b\overline{R}\Phi(\xi)$. The latest best-fit values of the parameters involved in the above formula can be found in Ref. [52], where a Fermi function was applied to the density distributions of spherical nuclei within the droplet model (leptodermous approximation). Nevertheless, it should be noted that, according to the results from studies based upon the CC method, such a simple one-dimensional WKB approach would not be suitable for describing the capture process at sub-barrier energies, as the coupling between low-lying collective (rotational or vibrational) states in colliding nuclei [37] is not taken into account. Some numerical tests were carefully conducted and have clearly shown that, together with the potential parameterization proposed in Ref. [52], the estimated capture cross-sections are found to be in nice agreement with experimental results at energies well above the Coulomb barrier, whereas a significant underestimation has been observed at sub-barrier energies. To improve calculations, we decided to keep using the same parameterization as that employed in the HIVAP code [53, 54], namely

$$\begin{aligned}
\overline{R} &= R_p R_t/(R_p+R_t), \text{ with } R_i = 1.126A_i^{1/3},\\
\Delta &= \xi - 2.54, \text{ with } \xi = \left(r - R_p - R_t\right)/b,\\
\phi(\xi) &= \begin{cases} 0.5\Delta^2 - 0.085\,2\Delta^3, \text{ if } \xi \le 1.2511,\\ -3.437\exp(-\xi/0.75), \text{ otherwise,}\end{cases}
\end{aligned} \tag{IV.32}$$

where the diffuseness parameter b has been set equal to 0.79 fm. The factor $4\pi\gamma$ equals 59 MeV,

Table IV.1 – Parameter values of the Akyüz-Winther potential used in the CCFULL code [39] for coupled-channel calculations.

Reaction	V_0 [MeV]	r_0 [fm]	a [fm]
^{16}O+^{154}Sm	62.533	1.177	0.76
^{16}O+^{208}Pb	64.971	1.179	0.76
^{16}O+^{238}U	66.033	1.179	0.76
^{48}Ca+^{208}Pb	82.169	1.181	0.76
^{50}Ti+^{208}Pb	84.587	1.181	0.76
^{48}Ca+^{238}U	85.403	1.181	0.76

which is considerably larger than the typical values estimated from most proximity-potential models. As a result, a stronger nuclear attraction can be generated so as to favor the capture process at sub-barrier energies. This potential will be marked as "ProxHIVAP". Anyhow, as will be shown later, more attention should still be drawn to deformed colliding nuclei where a strong coupling between rotational states and the ground state intervenes at low incident energies.

In the literature, other approximations are also available, for instance, the famous Wong formula [55] obtained be means of the Hill-Wheeler ansatz (inverted-parabolic approximation at the top of the barrier) and its recent generalization [56]. Here, we will not get into more details on these models.

IV.1.4 Uncertainty estimation for capture models

By means of the three methods previously introduced, we would like to perform some theoretical calculations for as set of selected reaction systems. The calculated results will be discussed with the purpose of providing a rough estimate of the uncertainty related to the capture model. To this end, we mainly focus on the heavy fusing systems leading to the formation of heavy and super-heavy compound nuclei.

Regarding the CC approach, we shall employ the CCFULL code [39]. As previously mentioned, several physical parameters are required for doing such calculations. For instance, the input values include the nucleus-nucleus potential, the coupling strengths of collective states and their excitation energies and so forth. In addition, some choices have to be made through various assumptions and approximations required for solving the coupled differential equations. It should be mentioned that, apart from the low-lying collective excitations, there exist many other modes of excitation in nuclei. However, non-collective excitations appear to be weakly coupled to the ground state and thus they would not significantly affect the capture process, even though the number of non-collective modes could be large in general.

The Akyüz-Winther potential is usually adopted for performing CC calculations. Here, values of the potential parameters for each selected reaction system are listed in Tab. IV.1

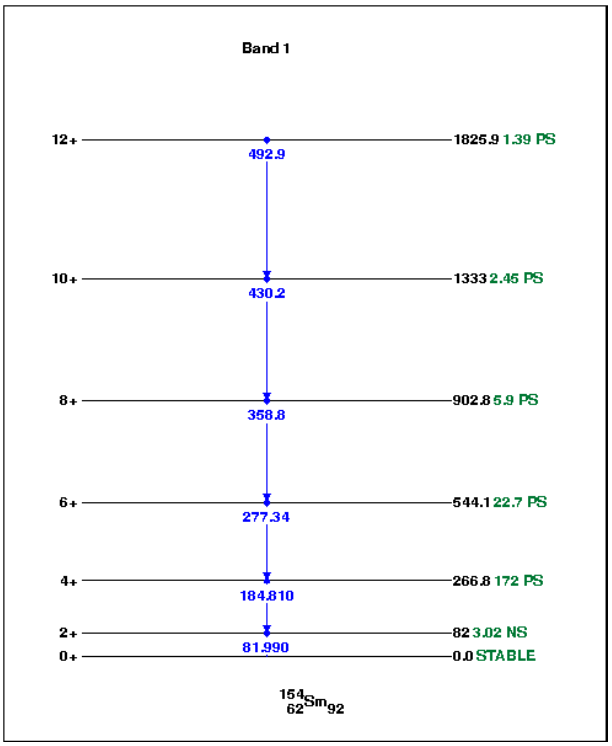

Figure IV.2 – Experimental level scheme of ^{154}Sm (in units of keV). The blue arrows indicate the γ-transition energies. The experimental data are taken from Ref. [58].

(namely those calculated from Eqs. (IV.10). However, some ambiguities still persist in the determination of parameter values for the AW potential, especially in the surface-diffuseness parameter a. Hence, the predictive capability of the CC approach can be quite limited. Here, a is kept fixed at 0.76 fm for all the CC calculations presented in this section. As regards the other two approximate methods, namely the EBD approach and the WKB approximation with an empirical proximity potential, their parameter values are set equal to the default ones.

In the following calculations, to distinguish different energy regions, the Bass barrier will be estimated as follows [57]:

$$\frac{Z_t Z_p e^2}{R_{\rm int}} - \frac{b_0 R_t R_p}{(R_t + R_p)}, \tag{IV.33}$$

where the interaction distance $R_{\rm int}$ is defined as $R_t + R_p + 3.2$ fm and $R_i = 1.12A_i^{1/3} - 0.94A_i^{-1/3}$ ($i = t, p$). The parameter b_0 is taken to be 1.0 MeV/fm.

Capture reaction: ^{16}O+^{154}Sm

First of all, let us start by looking at this well measured capture reaction to show how the coupling of collective motions gets involved in the heavy-ion capture process.

The low-lying excited modes in even-even nuclei are essentially due to collective motions,

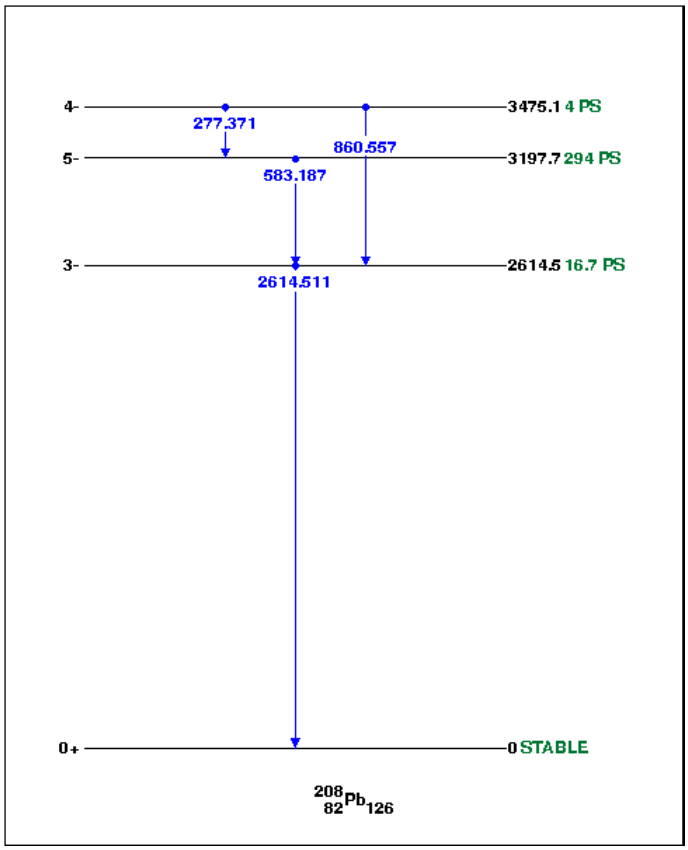

Figure IV.3 – Same as Fig. IV.2 but for the nucleus of ^{208}Pb.

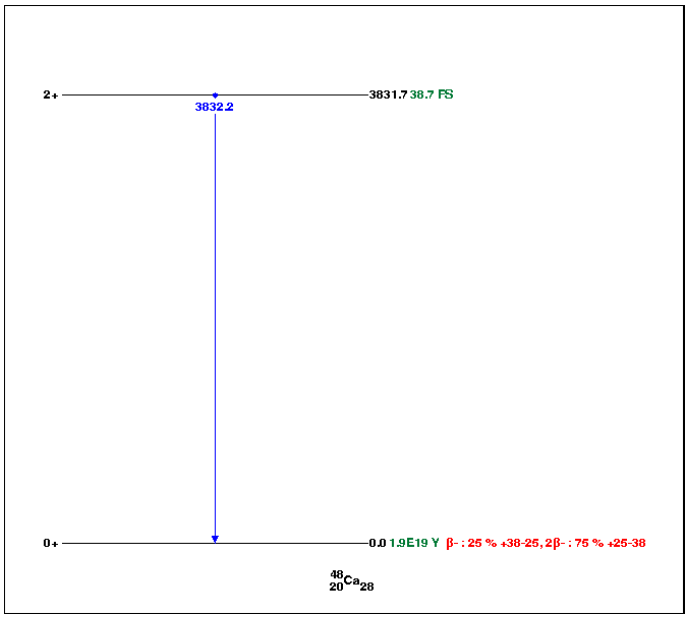

Figure IV.4 – Same as Fig. IV.2 but for the nucleus of ^{48}Ca.

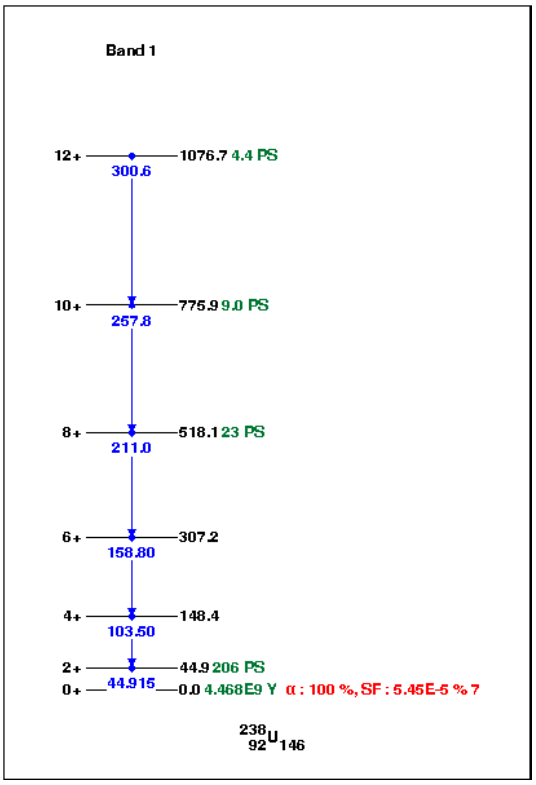

Figure IV.5 – Same as Fig. IV.2 but for the nucleus of ^{238}U.

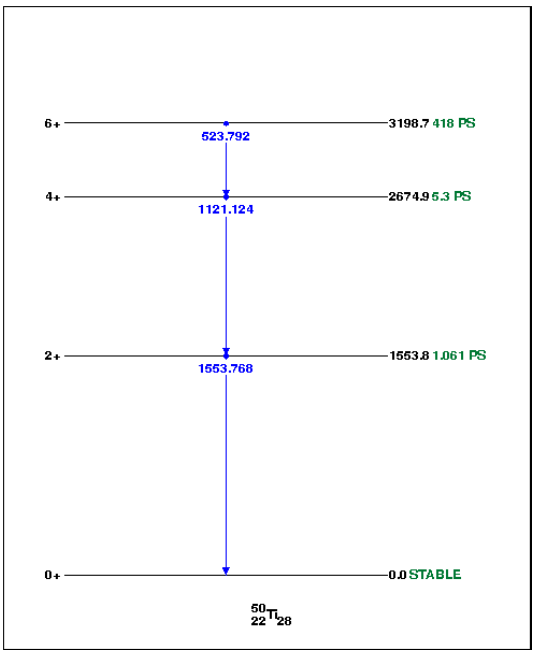

Figure IV.6 – Same as Fig. IV.2 but for the nucleus of ^{50}Ti.

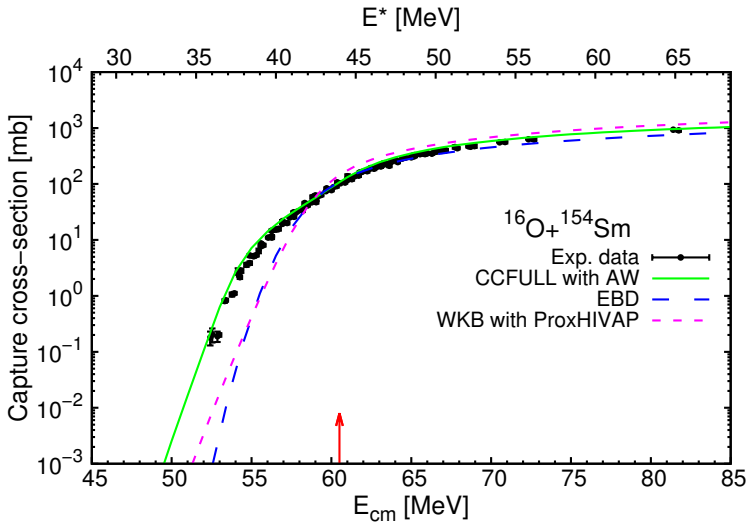

Figure IV.7 – Comparison of different theoretical calculations for the capture reaction ^{16}O+^{154}Sm. The solid circles represent the experimental data taken from Ref. [59]. The solid line is the CC calculation taking into account the first six low-lying rotational states of ^{154}Sm. The dashed line stands for the EBD approach. The short-dashed line is the WKB approximation with an empirical proximity potential. The upper axis indicates the excitation energy of CN. The Bass barrier is indicated by the red arrow.

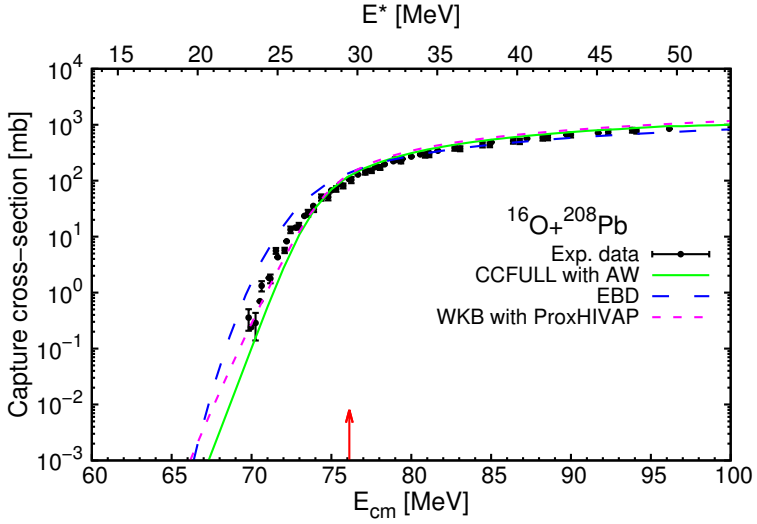

Figure IV.8 – Comparison of different theoretical calculations for the capture reaction ^{16}O+^{208}Pb. The solid circles represent the experimental data taken from Ref. [36, 60, 61]. The solid line is the CC calculation taking into account the low-lying vibrational states (3^-_1, 5^-_1) of ^{208}Pb. The dashed line corresponds to the EBD approach. The short-dashed line is the WKB approximation with an empirical proximity potential. The upper axis indicates the excitation energy of CN. The Bass barrier is indicated by the red arrow.

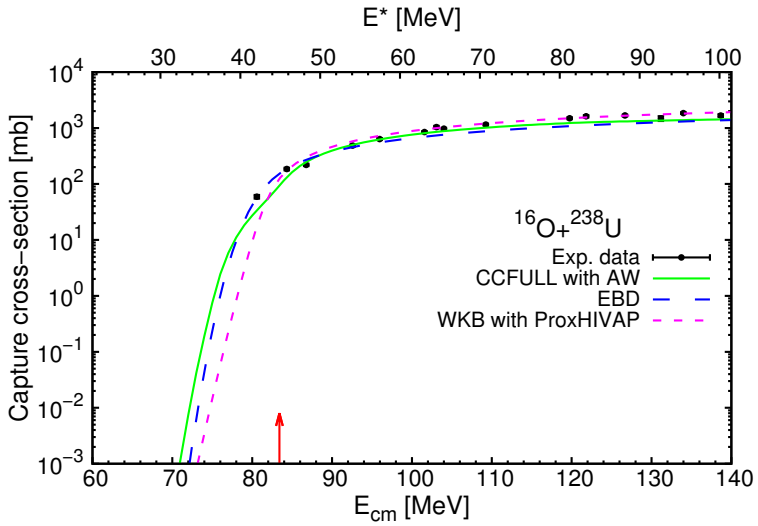

Figure IV.9 – Comparison of different theoretical calculations for the capture reaction ^{16}O+^{238}U. The solid circles represent the experimental data taken from Ref. [62–66]. The solid line is the CC calculation taking into account the first six low-lying rotational states of ^{238}U. The dashed line stands for the EBD approach. The short-dashed line is the WKB approximation with an empirical proximity potential. The upper axis indicates the excitation energy of CN. The Bass barrier is indicated by the red arrow.

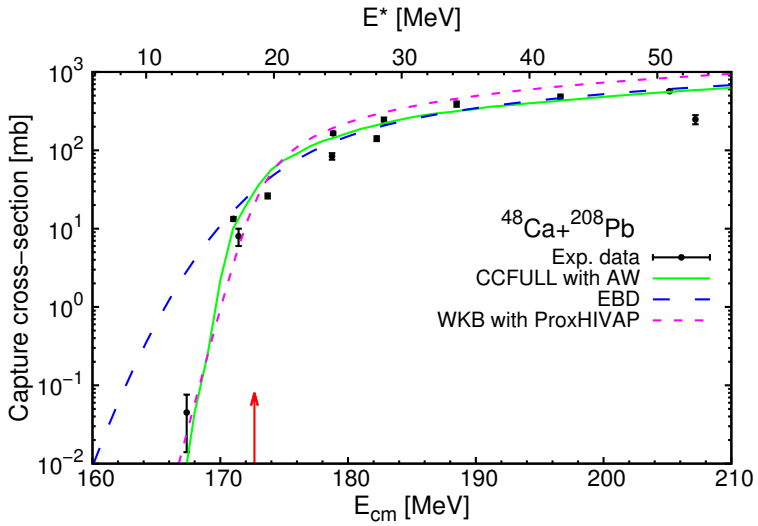

Figure IV.10 – Comparison of different theoretical calculations for the capture reaction ^{48}Ca+^{208}Pb. The solid circles represent the experimental data taken from Ref. [67–69]. The solid line is the CC calculation taking into account the coupling of two single-phonon states in ^{208}Pb together as well as the single-phonon state in ^{48}Ca. The dashed line stands for the EBD approach. The short-dashed line is the WKB approximation with an empirical proximity potential. The upper axis indicates the excitation energy of CN. The Bass barrier is indicated by the red arrow.

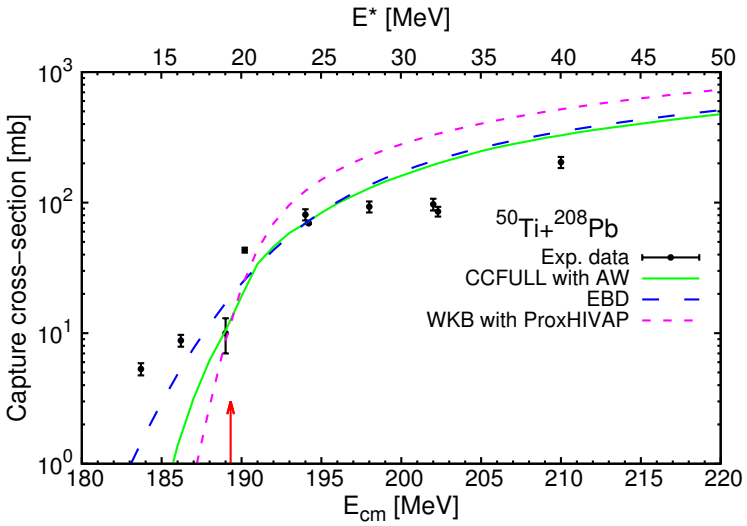

Figure IV.11 – Comparison of different theoretical calculations for the capture reaction ^{50}Ti+^{208}Pb. The solid circles represent the experimental data taken from Ref. [35]. The solid line is the CC calculation taking into account the coupling of two single-phonon states of ^{208}Pb as well as the single-phonon state in ^{50}Ti. The dashed line stands for the EBD approach. The short-dashed line is the WKB approximation with an empirical proximity potential. The upper axis indicates the excitation energy of CN. The Bass barrier is indicated by the red arrow.

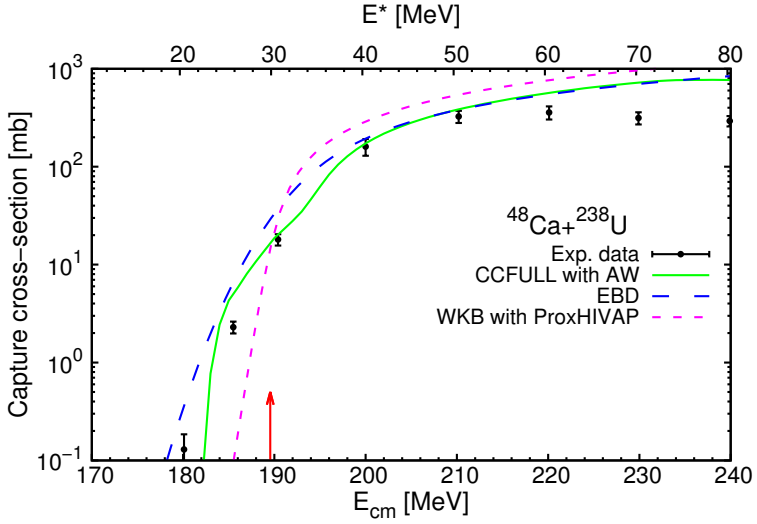

Figure IV.12 – Comparison of different theoretical calculations for the capture reaction ^{48}Ca+^{238}U. The solid circles represent the experimental data taken from Ref. [35]. The solid line is the CC calculation taking into account the first six low-lying rotational states of ^{238}U as well as the single-phonon state in ^{48}Ca. The dashed line stands for the EBD approach. The short-dashed line is the WKB approximation with an empirical proximity potential. The upper axis indicates the excitation energy of CN. The Bass barrier is indicated by the red arrow.

which are strongly coupled to the ground state and could have strong isospin dependences. To illustrate this, the experimental level scheme of ^{154}Sm is displayed in Fig. IV.2, where all these states are members of the first rotational band of the ground state. It is thus clear that ^{154}Sm is a well-deformed nucleus with a developed ground-state rotational band. To perform a CC calculation, the first six excited states $(2^+, 4^+, 6^+, 8^+, 10^+, 12^+)$ have been taken into account. The first rotational excitation energy $E(2^+)$ is equal to 0.082 MeV. Moreover, as already investigated in Ref. [70], it appears that only low-lying collective sates (with excitation energies less than around $1 \sim 2$ MeV) could significantly affect the fusion process. Hence, it would be reasonable to neglect the vibrational motions of ^{16}O (about 6.1 MeV for the first octupole vibrational state). The ground-state deformation parameters used in the CCFULL code are taken from the theoretical mass table [15].

In Fig. IV.7, the calculated capture cross-sections and the measured values are reported within a center-of-mass energy range from 45 MeV to 85 MeV. It can be readily seen that a significant enhancement of the experimental capture excitation function at sub-barrier energies with respect to the calculated results based upon two approximate models. Using the CC method, the experimental data can be perfectly reproduced at low energies. This result thus confirms that the coupling of collective motions can strongly affect the capture phase at sub-barrier energies. Regarding the EBD approach, it seems to have a similar trend compared to the CC method, but somehow falls more rapidly at sub-barrier energies. This might result from the fact that the parametrization of the width parameter is not accurate enough in most cases. Regarding the WKB approximation with an empirical proximity potential, the result appears quite close to that obtained with the EBD approach. It should be recalled that the values of the parameters involved in the proximity potential were specially adjusted to reproduce experimental data [54].

Capture reaction: ^{16}O+^{208}Pb

In this reaction, the projectile remains the same as the previous one, whereas the target nucleus has been replaced by the ^{208}Pb nucleus.

It is commonly known that, because of the double shell closures, ^{208}Pb is highly stable and has a spherical ground-state configuration with a few low-lying vibrational states. Fig. IV.3 shows the experimental level scheme of ^{208}Pb, from which it is clear that the dominant channels are single phonon states. Accordingly, the CC calculation has been performed considering a coupling to both the 3_1^- and 5_1^- single-phonon states in ^{208}Pb, together with their excitation energies $E(3_1^-) = 2.614\,5$ MeV and $E(5_1^-) = 3.197\,7$ MeV, respectively. As regards the deformation parameters used in the code, namely β_λ, they are evaluated be means of the following relationship:

$$\beta_\lambda = \frac{4\pi}{3ZR_0^\lambda}\left[\frac{B(E\lambda)\uparrow}{e^2}\right]^{1/2}, \tag{IV.34}$$

where R_0 is the sharp nuclear radius and the experimental transition strengths $B(E\lambda)\uparrow$ are

taken from Refs. [36, 71, 72].

Fig. IV.8 shows that the CC method succeeds in reproducing the measured capture excitation function. The calculated results based upon the other two methods are also displayed in Fig. IV.8. They are all compared with the experimental data over a wide center-of-mass energy range from 60 MeV to 100 MeV. A slight enhancement is clearly presented at deep sub-barrier energies and the result based upon the WKB approximation seems quite close to the measured capture excitation function. Overall, all these results are found to be in good agreement with experimental data. This might be because the coupling of vibrational states to the ground state appears a bit weaker than that between the rotational ones.

Capture reaction: ^{16}O+^{238}U

It is commonly known that the target nucleus ^{238}U is a typical well-deformed nucleus. The experimental low-lying states of ^{238}U are displayed in Fig. IV.5, which clearly shows that ^{238}U possesses a well developed ground-state rotational band as that of ^{154}Sm. Therefore, the first rotational band including six excited states ($2^+, 4^+, 6^+, 8^+, 10^+, 12^+$) have been considered. The first excitation energy $E(2^+)$ is taken to be 0.044 9 MeV. As previously explained, it would not be necessary to take into account the vibrational states of ^{16}O. In addition, the ground-state deformation parameters are taken from the theoretical mass table [15].

In Fig. IV.9, the estimated capture cross-sections and the measured values are reported within a center-of-mass energy range from 60 MeV to 140 MeV. It is clearly shown that the CC approach and the EBD method are both able to reproduce the measured data at sub-barrier energies, whereas the WKB method considerably underestimates the experimental data when the incident energy becomes lower than the Coulomb barrier. This result again confirms that the coupling of collective motions to the ground state can strongly affect the capture process at sub-barrier energies.

Capture reaction: ^{48}Ca+^{208}Pb

Regarding this reaction, the projectile nucleus, ^{48}Ca, is a well-known doubly magic nucleus like ^{208}Pb. The experimental level scheme of ^{48}Ca is shown in Fig. IV.4, which tells us that the first vibrational state of ^{48}Ca has an excitation energy equal to 3.831 7 MeV, which appears comparable to that of the target nucleus. As previously mentioned, the first two low-lying vibrational states of ^{208}Pb are respectively 3_1^- and 5_1^-, with their excitation energies $E(3_1^-)$ = 2.614 5 MeV and $E(5_1^-)$ = 3.197 7 MeV, respectively. Accordingly, the first vibrational state in the projectile nucleus should be considered for performing CC calculations. Moreover, a double-phonon coupling has been considered in the present calculation so as to include higher-order corrections with the aim of reproducing the measured values.

Fig. IV.10 displays the calculated capture cross-sections over the energy range from 160 MeV to 210 MeV. It is clearly demonstrated that the CC method successfully reproduces the

data points at sub-barrier energies, whereas the EBD approach with the default parameter values fails this time to reproduce the measured values. This might be again due to the large uncertainty associated with the width parameter. It should be noted that the WKB approximation with an empirical proximity potential, however, reasonably reproduces the measured data at sub-barrier energies, but slightly overestimates experimental values at above-barrier energies.

Capture reaction: ^{50}Ti+^{208}Pb

This example is of particular interest, because the reaction ^{50}Ti+^{208}Pb has successfully produced the super-heavy element rutherfordium via the cold-fusion reaction. To carry out the CC calculation, we recall that the ^{208}Pb nucleus has two low-lying vibrational states which are considered to be dominant in the collective excitation. Regarding the projectile, ^{50}Ti, as shown in Fig. IV.6, it appears quite similar to the ^{48}Ca but has a much lower vibrational state 2^+, whose excitation energy is taken to be 1.554 MeV. Thus, the main effect would result from the coupling of the vibrational states of the projectile and target nuclei. Furthermore, a double-phonon coupling has been considered in the present calculation so as to take into account higher-order corrections. The ground-state deformation parameters are taken from the theoretical mass table [15].

In Fig. IV.11, the calculated capture cross-sections are compared with the measured values within an energy range from 180 MeV to 220 MeV. It is clearly seen that, at sub-barrier energies, the theoretical results do not converge to each other and the experimental data seem to have some ambiguities on the magnitude. Anyhow, the uncertainty related to the theoretical calculation could reach one order of magnitude over the energy range for the single-neutron evaporation (at excitation energies around 15 MeV).

Capture reaction: ^{48}Ca+^{238}U

As a last example, it would be mentioned that the reaction ^{48}Ca+^{238}U is also of particular interest, since it has been employed to produce the super-heavy element copernicium by means of the hot-fusion reaction. As previously discussed, the main contribution to the CC calculation would come from the coupling between rotational states of ^{238}U. For the sake of prudence, the double-phonon state in ^{48}Ca has also been kept in calculations. The ground-state deformation parameters used in the CCFULL code are taken from the theoretical mass table [15].

In Fig. IV.12, the calculated capture cross-sections are compared with the measured values within an energy range from 170 MeV to 240 MeV. It should be noted that, at relatively high energies, the measured data start to gradually go down, as other exit channels come into play. Put differently, the fusion becomes incomplete. Regarding the approximate methods, it is clearly displayed that the EBD method can reproduce relatively well the experimental

data at sub-barrier energies, whereas the WKB approximation appears to underestimate the measurements at sub-barrier energies. However, over the energy range for multi-neutron evaporation (at excitation energies above 30 MeV), the discrepancy might reach about 50%, which appears less important than cold-fusion reactions.

IV.1.5 Summary

Until now, we have carefully reviewed the CC method and its two commonly used alternatives, namely the EBD approach and the WKB approximation with an empirical proximity potential. It should be mentioned that, in the literature, the CC method has been well tested with a number of measurements, but mainly for relatively light reaction systems. In our case, we mostly focus on heavy colliding systems leading to the formation of heavy and super-heavy nuclei. The predictive power of capture models has shown to be somewhat poor, especially at sub-barrier energies due to uncertainties in potential parameters.

In general, the capture models seem able to reproduce the measured data with a precision of about 50%, or even poorer, up to more than one order of magnitude at low energies. It should be noted that this is especially the case for cold-fusion reactions where the incident energy is commonly near or slightly lower than the Coulomb barrier. However, when comparing calculated results with the available experimental data for the formation of very heavy or super-heavy nuclei via hot-fusion reactions, the agreement should be better, since all the theoretical estimates appear to converge in the above-barrier energy region and are found to be in good agreement with the measured data. This is the main conclusion that can be drawn from the present study, which is crucial for the remaining part of the this thesis concerning uncertainty analysis. It should be emphasized that special attention always needs to be given, especially when estimating capture cross-sections for cold-fusion reactions.

IV.2 Formation step

So far, we have examined the impact of collective motion on the capture step, which simply corresponds to the passage of the Coulomb barrier. After that, the colliding nuclei automatically fuse together to form an excited heavy nucleus in the case of light systems. However, regarding heavy colliding systems, it is experimentally known that, in addition to the passage over the Coulomb barrier, there is an additional step before reaching the CN configuration. This phenomenon, known as fusion hindrance, only occurs in heavy systems.

Fig. IV.13 clearly demonstrates the appearance of the fusion hindrance phenomenon when the charge product of projectile-target combination exceeds around 1600. In this case, overcoming the Coulomb barrier would not be enough for determining the total fusion probability, but an extra energy above the barrier would be required for the composite system to fuse [75]. This can be understood by looking into the potential energy surface. More concretely, after surmounting the Coulomb barrier, the colliding nuclei stick with each other

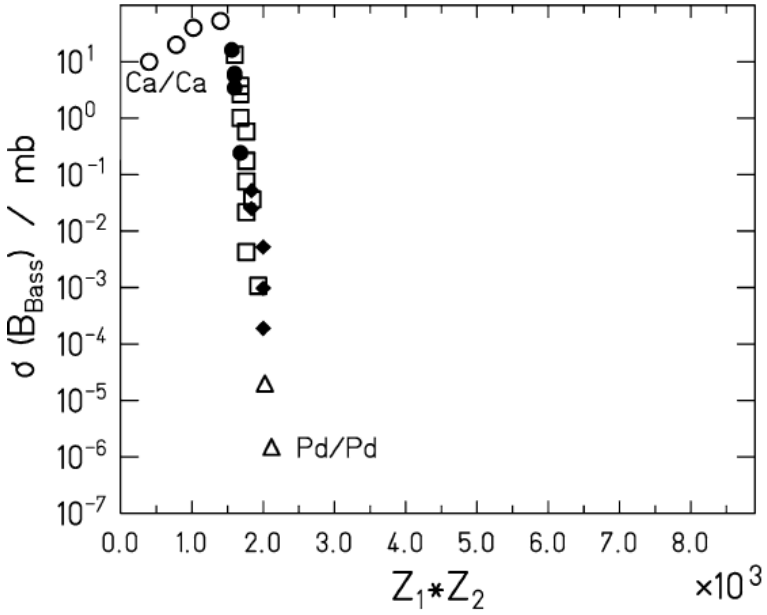

Figure IV.13 – Experimental evidence of the fusion hindrance. The solid and open symbols represent the measured total evaporation cross-sections for symmetric or nearly-symmetric fusing systems at energies around the Bass barrier. A dramatic decrease starts at a charge product of the projectile-target combination of around 1600 – 1800. Figure is taken from Ref. [73].

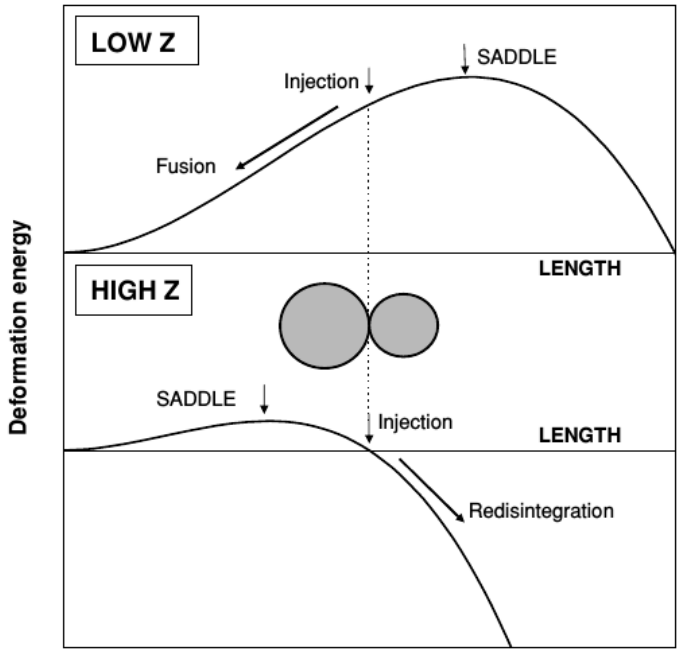

Figure IV.14 – Illustration of a hindrance to fusion for massive reaction systems in elongation space. For reactions between lighter nuclei, the contact position is considered to be located inside the liquid-drop potential pocket. Beyond a critical size of the reaction system, the contact point moves outside the saddle-point configuration so that an inner barrier appears. Figure is taken from Ref. [48]

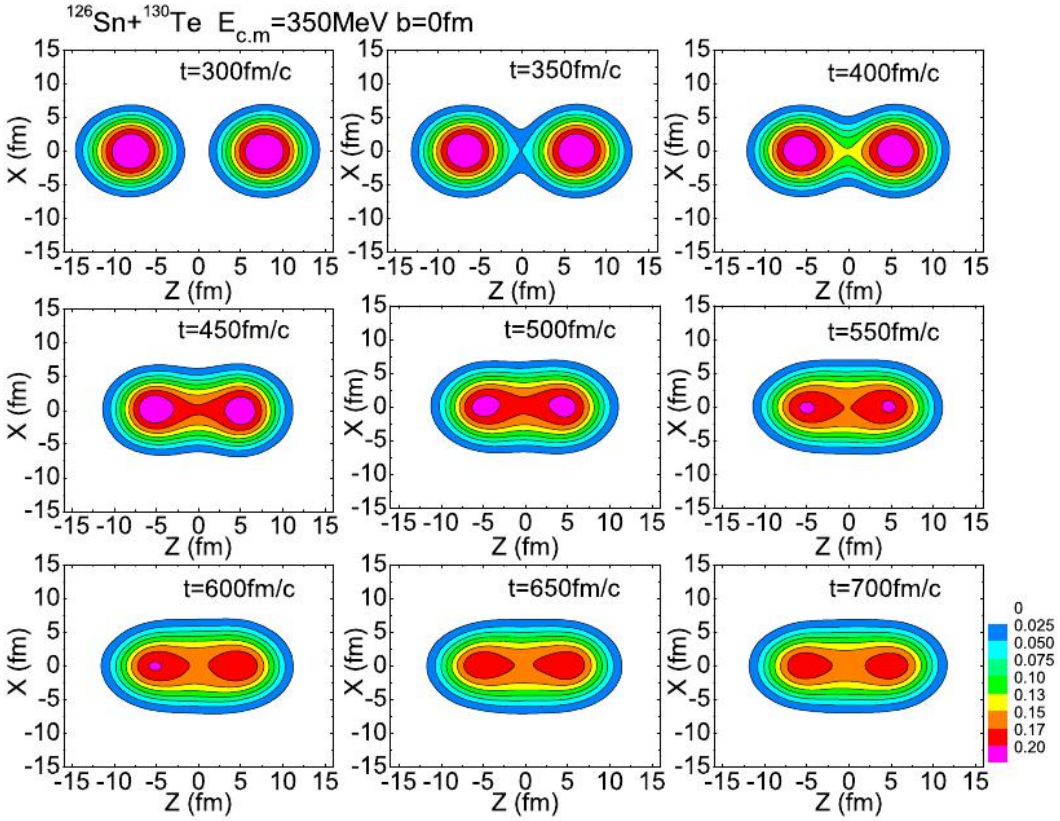

Figure IV.15 – Illustration of the neck evolution based upon the quantum molecular dynamics. The neck parameter characterizes the size of the connecting part between the two nuclei. Figure is taken from Ref. [74].

to form a pear-shaped configuration. However, the contact point is supposed to be located outside the conditional saddle point, or put differently, the ridgeline associated with the potential surface. To reach the CN state, the composite system has to pass over a second inner barrier, which is mainly due to the Coulomb repulsion, as clearly shown in Fig. IV.14). In such a situation, it has been demonstrated that the initial radial kinetic energy should be completely dissipated [76] so that the composite system is assumed to be well heated up and thus can be described using statistical mechanics. Accordingly, the shape evolution toward the CN state can be regarded as a Brownian motion coupled with the heat bath at constant temperature, and thus can be described within the framework of a multi-dimensional Langevin equations [77, 78],

$$\begin{aligned}
\frac{\mathrm{d}q_i}{\mathrm{d}t} &= (m^{-1})_{ij}p_j, \\
\frac{\mathrm{d}p_i}{\mathrm{d}t} &= -\frac{\partial U}{\partial q_i} - \frac{1}{2}\frac{\partial}{\partial q_i}(m^{-1})_{jk}p_j p_k - \gamma_{ij}(m^{-1})_{jk}p_k + g_{ij}F_j(t), \\
g_{ik}g_{jk} &= D_{ij},
\end{aligned} \tag{IV.35}$$

where q_i and p_i denote the generalized coordinates and the corresponding conjugate momenta, respectively, and $D_{ij} = \gamma_{ij} T$ due to the fluctuation-dissipation theorem [79]. Here, the summation is taken over all repeated suffixes. γ and m are the friction and inertia tensors, respectively. Furthermore, F_i refers to a Gaussian random force without considering the memory effect.

Within the framework of the two-center liquid-drop model [80, 81], one needs to introduce three generalized coordinates: the asymmetry α, the relative radial distance r and the neck parameter ε. The first one is defined as $\alpha = (A_t - A_p)/(A_t + A_p)$, where A_t and A_p stand for the mass numbers of the target and projectile nuclei, respectively. The second one is defined as $r = R/R_0$, where R denotes the distance between two centers of the colliding nuclei, and R_0 the radius of a spherical compound nucleus. The neck parameter ε is related to the cleft between two sticking nuclei. $\varepsilon = 1$ represents two connecting hard spheres (di-nucleus), whereas $\varepsilon = 0$ correspond to the absence of this cleft, which describes a super-deformed mono-nucleus. Hence, the neck parameter can be used to describe the shape evolution from di-nucleus to mono-nucleus (cf. Fig. IV.15).

It should be mentioned that, besides the Langevin approach, another commonly used method to describe the evolution of a pear-shaped di-nucleus is the so-called di-nuclear systems (DNS) model [82–86]. This model is essentially based upon the fact that a compound system is formed by a series of nucleon transfers between two colliding nuclei. The dynamics of DNS can be thus regarded as a combined diffusion in both the asymmetry and radial coordinates, whereas the neck parameter is considered to be frozen. The potential barrier appearing in the former could explain a hindrance for the fusion process. This conclusion on the inner barrier is actually commonly accepted as discussed in most of theoretical studies. However, certain ambiguities still exist, such as

- How to exactly estimate the inner barrier height?
- What is the key variable dominant for fusion dynamics?
- What is the dissipation strength?
- ...

In this section, we only concentrate on the Langevin model. For the sake of clarity, first, we recall some basic results of a one-dimensional model. Then, we mainly attempt to deal with the evolution of the neck parameter in order to clarify its impact on the formation step. Finally, we shall employ a combined two-step model to investigate a near-symmetric reaction system ^{129}Xe+^{nat}Sn.

IV.2.1 Radial evolution

Let us briefly recapitulate some essential results obtained from a one-dimensional Langevin model for describing a diffusion process along the radial degree of freedom. In this subsection, it is simply denoted by q and the corresponding conjugate momentum by p together with

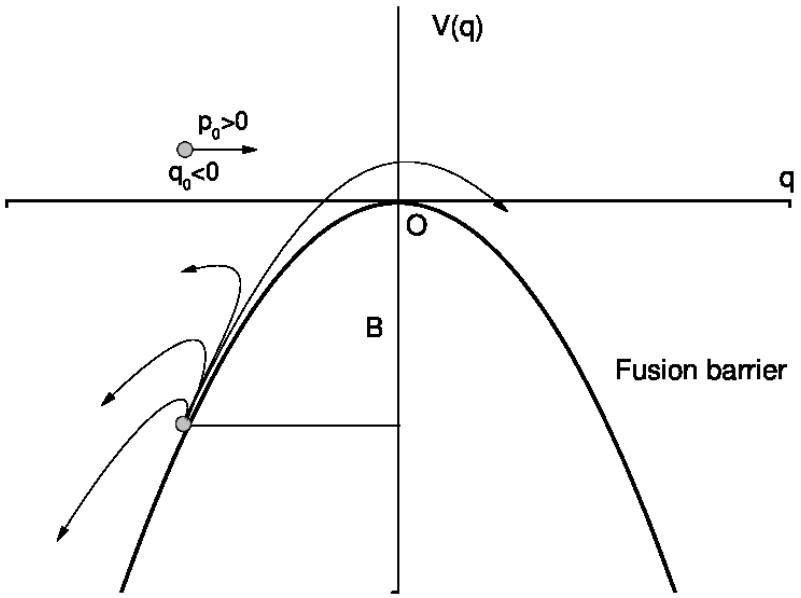

Figure IV.16 – Inverted parabolic potential $-1/2m\omega^2 q^2$ characterized by its curvature $\hbar\omega$. The particle struggles to overcome the top of the barrier under a fluctuating driving force. Here the inner-barrier height is indicated by B.

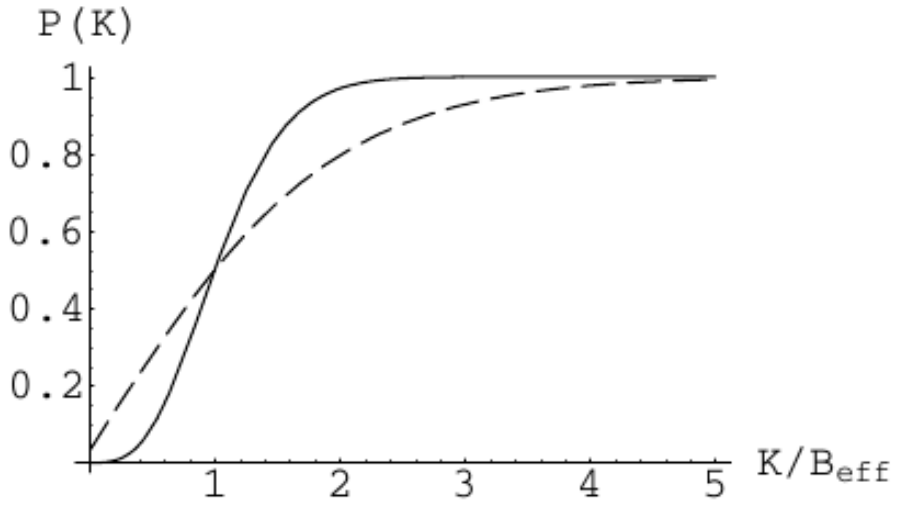

Figure IV.17 – Formation probability as a function of the ratio of K to B_{eff} (cf. Eq. (IV.39)) for $B/T = 10$ (solid curve) and $B/T = 2$ (dashed curve). Here $\eta' = 3$. Figure taken from Ref. [87].

their initial values q_0 and p_0. By means of the inverted-parabola approximation (cf. Fig. IV.16) and under the assumption that transport coefficients are considered to be constant around the inner saddle point, the problem can be exactly solved and an analytic explanation concerning the origin of fusion hindrance is thus provided.

In the one-dimensional case, the multi-dimensional Langevin equation Eq. (IV.35) is reduced to the following form:

$$\frac{\mathrm{d}^2 q(t)}{\mathrm{d}t^2} = -\frac{\gamma}{m}\frac{\mathrm{d}q(t)}{\mathrm{d}t} + \omega^2 q(t) + \rho(t) \tag{IV.36}$$

where m and ω denote the inertia mass and the potential curvature at the saddle point, respectively. The reduced friction parameter $\beta = \gamma/m$ is defined with the friction coefficient γ and $\rho(t)$ denotes a white Gaussian noise, which is assumed to obey the fluctuation-dissipation theorem, namely

$$\left\langle \rho(t)\rho(t') \right\rangle = 2T\beta/m\delta(t-t'). \tag{IV.37}$$

The probability of passing over the inner barrier, namely the formation probability, is simply given as follows:

$$\begin{aligned} P(t|q_0,p_0) &= \int_0^{+\infty} \mathrm{d}q P(q,t|q_0,p_0) = \int_0^{+\infty} \frac{\mathrm{d}q}{\sqrt{2\pi}}\frac{1}{\sigma_q(t)} \exp\left[-\frac{(q-\left\langle q(t)\right\rangle)^2}{2\sigma_q^2(t)}\right] \\ &= \frac{1}{2}\mathrm{erfc}\left[-\frac{\left\langle q(t)\right\rangle}{\sqrt{2}\sigma_q(t)}\right], \end{aligned} \tag{IV.38}$$

where the average trajectory $\left\langle q(t)\right\rangle$ and the variance $\sigma_q(t)$ can be estimated in a analytical manner [78, 87]. As a long-time limit, the probability of passing over the barrier tends to a finite value, namely

$$P_{\mathrm{form}} = \lim_{t\to\infty} P(t|q_0,p_0) = \frac{1}{2}\,\mathrm{erfc}\left[\sqrt{\frac{\eta'+\sqrt{\eta'^2+1}}{2\eta'}}\left(\sqrt{\frac{B}{T}} - \frac{1}{\eta'+\sqrt{\eta'^2+1}}\sqrt{\frac{K}{T}}\right)\right], \tag{IV.39}$$

where $B = m\omega^2 q_0^2/2$ stands for the saddle point height measured from the starting point q_0 with a initial kinetic energy $K = p_0^2/(2m)$. The critical kinetic energy $K_c = (\eta'+\sqrt{\eta'^2+1})^2 B$ with $\eta' = \beta/(2\omega)$, which allows half of the particles to pass over the inner barrier (cf. Fig. IV.17), is usually referred to as an effective barrier B_{eff} that takes into account the effect of viscosity. Since the effective barrier B_{eff} is greater than B, the formation probability would be dramatically reduced and the whole process is thus largely hindered. In the over-damped case, that is to say, when the friction coefficient becomes considerably strong ($\eta' \gg 1$), Eq. (IV.39) can be further simplified into

$$P_{\mathrm{form}} = \frac{1}{2}\,\mathrm{erfc}\left(\sqrt{\frac{B}{T}}\right), \tag{IV.40}$$

which has been successfully applied to the synthesis of super-heavy nuclei formed via the so-called cold-fusion reaction [48]. Additionally, in deriving Eq. (IV.38), the initial position and

momentum have been assumed to be sharply distributed. This can be readily generalized by considering a Gaussian dispersion of the initial values, namely

$$W(q_0, p_0, t_0) = \frac{1}{\sqrt{2\pi}\sigma_{q_0}} \frac{1}{\sqrt{2\pi}\sigma_{p_0}} \exp\left[-\frac{(q_0-\overline{q}_0)^2}{2\sigma_{q_0}^2}\right] \exp\left[-\frac{(p_0-\overline{p}_0)^2}{2\sigma_{p_0}^2}\right], \tag{IV.41}$$

where $\overline{q}_0$ and $\overline{p}_0$ refer to the initial values of position and momentum, respectively, and the variance $\sigma_{p_0}^2 = \mu T_0$. Inserting Eq. (IV.41) into Eq. (IV.38) and integrating over all possible q_0 and p_0, one obtains a new formula for the formation probability,

$$P(t|\overline{q}_0, \overline{p}_0) = \frac{1}{2}\mathrm{erfc}\left[-\frac{\langle \overline{q}(t)\rangle}{\sqrt{2}\sigma'_q(t)}\right], \tag{IV.42}$$

with the new variance

$$\sigma_q^{'2} = \sigma_q^2 + \sigma_{q_0}^2 R^2(t) + mT_0 S^2(t), \tag{IV.43}$$

where the functions $R(t)$ and $S(t)$ are given in Ref. [87]. Hence, owing to the dispersion of initial conditions, the variance becomes larger compared to the old one.

Some crucial characteristics of the radial fusion have been discussed in Ref. [87]. For instance, owing to a strong energy dissipation, the formation probability is governed by the diffusion process and the time scale of the radial evolution appears quite long. (Typically, it is of the order of several $\hbar$/MeV.) This result is important for the following discussion. Moreover, there are some interesting questions, such as

- How to exactly estimate the barrier height B and the associated uncertainty?
- What is the magnitude of the reduced friction parameter β?
- How many more degrees of freedom do we need to describe the fusion process?
- ...

For instance, the dissipation effect, which is characterized by the reduced friction parameter, would have a crucial role to play in estimating the effective barrier, knowing that, for $\beta = 2.0$ zs^{-1} and $\hbar\omega = 1.0$ MeV, $B_{\mathrm{eff}} \backsimeq 3.5B$, and for $\beta = 5.0$ zs^{-1} and $\hbar\omega = 1.0$ MeV, $B_{\mathrm{eff}} \backsimeq 11.0B$.

In the following part of this section, we shall address one of these interesting questions, that is to say, what is the role of other variables in describing the formation step?

IV.2.2 Neck formation

Supposing that the neck parameter is weakly coupled to other degrees of freedom, it would be possible to investigate its time evolution by means of a simplified one-dimensional Langevin equation.

Fig. IV.18 shows that the liquid-drop energy for symmetric colliding systems turns out to be an approximate linear function of the neck parameter. For the sake of simplicity, one

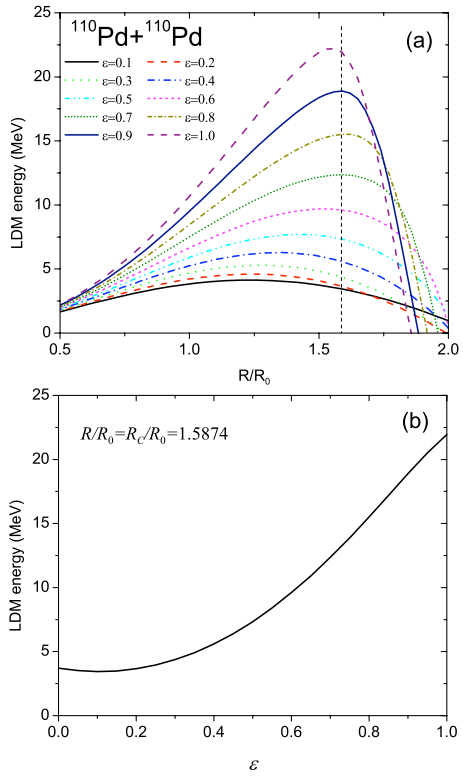

Figure IV.18 – Top: Evolution of the liquid-drop potential energy with the radial parameter $r = R/R_0$ for different neck values. Bottom: Liquid-drop energy as a function of the neck parameter at the contact point (indicated by the vertical dashed line).

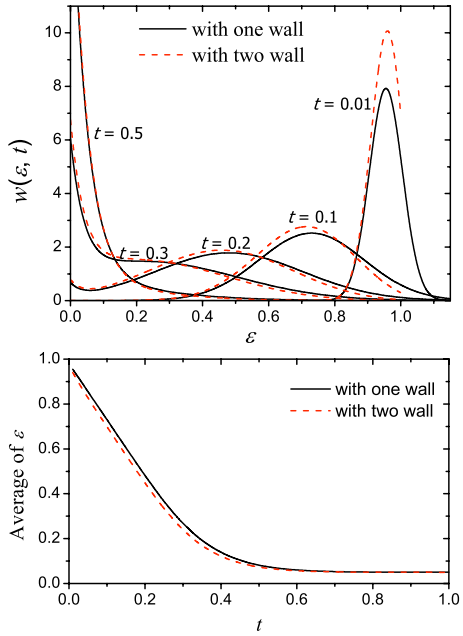

Figure IV.19 – Top: Time evolution of the neck parameter. Bottom: Average value of the neck parameter as a function of time. The solid line corresponds to the case with one reflective wall at $\varepsilon = 0$ and the dashed one to the case with two reflective walls at $\varepsilon = 0, 1$. Here, $\varepsilon_0 = 0.95$, $C = 2.5$ MeV/$\hbar$ and $D = 0.125$ MeV/$\hbar$.

can assume that $V(\varepsilon) \simeq f\varepsilon$, which has the advantage that one can readily obtain an analytical solution for studying the time evolution of the neck parameter.

The simplified Langevin equation for describing the time evolution of the neck parameter is given as follows:

$$\dot{\varepsilon}(t) = -C + \sqrt{2D} \cdot \xi(t), \tag{IV.44}$$

Where $C = f/\gamma$ and $D = T/\gamma$. Based on the two-center liquid-drop model, typical values of C would range from 1.1 to 2.7 MeV/$\hbar$. It should be noted that we have neglected the inertia term because the formation process is considered to be dominated by a strong dissipation. Here, ξ denotes a random force satisfying the fluctuation-dissipation theorem, namely $\langle \xi(t)\xi(t') \rangle = 2D\delta(t-t')$. Physically, the value of ε must be comprised in the interval $[0,1]$ (two walls).

Eq. (IV.44) can be analytically solved [88, 89]. With only one wall at $\varepsilon = 0$, the average value of ε is given by

$$\begin{aligned} \langle \varepsilon(t) \rangle = \varepsilon_0 - Ct + \frac{1}{2}\left(\frac{D}{C} - \varepsilon_0 + Ct\right) \mathrm{erfc}\left(\frac{\varepsilon_0 - Ct}{\sqrt{4Dt}}\right) \\ - \frac{D}{2C} \exp\left(\frac{C\varepsilon_0}{D}\right) \mathrm{erfc}\left(\frac{\varepsilon_0 + Ct}{\sqrt{4Dt}}\right) + \sqrt{\frac{Dt}{\pi}} \exp\left[-\frac{(\varepsilon_0 - Ct)^2}{4Dt}\right] \end{aligned}. \tag{IV.45}$$

With two walls at $\varepsilon = 0, 1$, it becomes

$$\begin{aligned} \langle \varepsilon(t) \rangle = \frac{D}{C} + \frac{1}{1 - \exp[C/D]} + 32\pi^2 D^4 \exp\left[\frac{D}{2C}\varepsilon_0 - \frac{C^2 t}{4D}\right] \\ \times \sum_{k=1}^{\infty} \left\{ \exp\left(-k^2\pi^2 Dt\right) \frac{k^2}{(C^2 + 4D^2k^2\pi^2)^2} \left[\cos(k\pi\varepsilon_0) - \frac{C}{2D}\frac{1}{k\pi}\sin(k\pi\varepsilon_0)\right] \right. \\ \left. \left[(-1)^k \exp\left(-\frac{C}{2D}\right) - 1\right] \right\}. \end{aligned} \tag{IV.46}$$

Fig. IV.19 shows the neck distribution and its average value as a function of time for the two cases. It is clearly demonstrated that the two solutions do not differ so much.

The time scale of the fusion process along the relative distance was mentioned in the previous subsection. For a diffusive process corresponding to the actual situation, the typical time to overcome the inner barrier is about one order of magnitude longer than the neck evolution. This is actually due to the presence of a strong driving force acting on the neck degree of freedom, whereas the radial coordinate is mainly governed by thermal diffusion. Thus, we can, as a first approximation, considering that the neck parameter is completely thermalized during the second stage of the fusion process.

IV.2.3 A simple two-dimensional model

The other collective degrees of freedom are connected through the liquid-drop potential and friction tensor. To combine r and ε, let us consider the following two-dimensional

Langevin equation:

$$\gamma \begin{pmatrix} \dot{\varepsilon} \\ \dot{r} \end{pmatrix} = - \begin{pmatrix} \partial V/\partial \varepsilon \\ \partial V/\partial r \end{pmatrix} + \begin{pmatrix} \rho_1(t) \\ \rho_2(t) \end{pmatrix} \tag{IV.47}$$

$$\text{or } \begin{pmatrix} \dot{\varepsilon} \\ \dot{r} \end{pmatrix} = -\gamma^{-1} \begin{pmatrix} \partial V/\partial \varepsilon \\ \partial V/\partial r \end{pmatrix} + \begin{pmatrix} \zeta_1(t) \\ \zeta_2(t) \end{pmatrix}, \tag{IV.48}$$

Where $\rho(t)$ and $\xi(t)$ should verify the following relationships:

$$\left\langle \rho_i(t)\rho_j(t') \right\rangle = 2T\gamma_{ij}\delta(t-t') \text{ with } \left\langle \rho_i(t) \right\rangle = 0, \tag{IV.49}$$

$$\left\langle \zeta_i(t)\zeta_j(t') \right\rangle = 2T[\gamma^{-1}]_{ij}\delta(t-t') \text{ with } \langle \zeta_i(t) \rangle = 0, \tag{IV.50}$$

where γ^{-1} corresponds to the inverse of the friction matrix γ and T denotes the nuclear temperature. Here, the inertia terms have been neglected because of a strong dissipation or the initial kinetic energy has been completely dissipated [76].

To solve the two-dimensional Langevin equation, the method of transformation matrix is more efficient [78]. Without imposing the reflective boundary conditions, the analytical solution can be obtained in the case of a simple combined parabolic potential for the radial and neck variables, namely

$$V(\varepsilon, r) = V_s + \frac{1}{2}g\varepsilon^2 - \frac{1}{2}h(r-r_s)^2, \tag{IV.51}$$

where r_s denotes the conditional saddle point, g and h are constants. It should be noted that this potential landscape is somewhat crude, but allows us to analytically solve Eq. (IV.48) [89].

The two-dimensional model thus constructed is nothing else but a toy model to understand the influence of coupling between the neck and radial variables on the formation step. However, it still allows us to conduct some qualitative studies in order to clarify the role of the neck variable in the fusion process.

Adiabatic approximation

As previously pointed out, the neck parameter evolves much faster than the radial one. This fact would allow us to make an adiabatic approximation so as to decrease the number of degrees of freedom. In other words, can we thus reduce the study to the radial coordinate only?

For the sake of simplicity, we assume here that around the saddle, the friction tensor is independent of r and ε. As previously shown, the potential map is composed of a U shape for the neck variable and a barrier shape for the radial one. Then, the fast neck dynamics can be approximately studied as follow:

$$\dot{\varepsilon} = -[\gamma^{-1}]_{\varepsilon\varepsilon}\frac{\partial V}{\partial \varepsilon} - [\gamma^{-1}]_{r\varepsilon}\frac{\partial V}{\partial r}\,|_{r=r_0} + \zeta_1(t). \tag{IV.52}$$

Due to the fact that the slope of the driving potential for the neck parameter can be much steeper compared to that of the radial one, it can be reasonably assumed that $|\partial V/\partial\varepsilon|_{\varepsilon=\varepsilon_0} \gg |\partial V/\partial r|_{r=r_0}$. Thus, the time evolution of the neck parameter is governed by

$$\dot{\varepsilon} = -[\gamma^{-1}]_{\varepsilon\varepsilon}\frac{\partial V}{\partial \varepsilon} + \zeta_1(t). \tag{IV.53}$$

We have shown that it is quickly thermalized and tends to a long-time limit ε_∞ determined by the Botzmann distribution.

To study the time evolution of r, we consider the following equation:

$$\gamma_{r\varepsilon}\dot{\varepsilon} + \gamma_{rr}\dot{r} = -\frac{\partial V}{\partial r} + \rho_2(t). \tag{IV.54}$$

After the thermalization of the neck parameter, we only have to deal with the radial time evolution. This can be done by dividing it into two time scales. First, during the quick evolution of the neck parameter, the average value can be approximated by

$$\gamma_{r\varepsilon}\langle\dot{\varepsilon}\rangle + \gamma_{rr}\langle\dot{r}\rangle \simeq 0, \tag{IV.55}$$

which gives rise to $\Delta\langle r\rangle \simeq -(\gamma_{r\varepsilon}/\gamma_{rr})\Delta\langle\varepsilon\rangle$. Note that, here, we have also neglected the term $\partial V/\partial r$ because during this transient regime $\partial V/\partial\varepsilon$ is dominating. The initial variance of the relative distance is also related to the final variance of the neck variable corresponding to the Boltzmann distribution, namely

$$\sigma_{r_0}^2 = \frac{\gamma_{\varepsilon r}^2}{\gamma_{rr}^2}\sigma_{\varepsilon_\infty}^2. \tag{IV.56}$$

Second, once the neck parameter is frozen, that is to say, $\dot{\varepsilon} \simeq 0$, one has

$$\gamma_{rr}\dot{r} \simeq -\frac{\partial V}{\partial r} + \rho_2(t), \tag{IV.57}$$

which is a simple one-dimensional Langevin equation for the relative distance only, with the initial condition for the variance.

For an inverted parabolic potential, it is not difficult to get the following solutions for the average trajectory and the corresponding variance:

$$\langle r(t) - r_s\rangle = \left[(\overline{r_0} - r_s) + \overbrace{\frac{\gamma_{\varepsilon r}}{\gamma_{rr}}(\varepsilon_0 - \varepsilon_\infty)}^{\text{initial shift}}\right]\exp\left(\frac{ht}{\gamma_{rr}}\right), \tag{IV.58}$$

$$\sigma_r'^2(t) = \frac{T}{h}\left[\exp\left(\frac{2ht}{\gamma_{rr}}\right) - 1\right] + \sigma_{r_0}^2\exp\left(\frac{2ht}{\gamma_{rr}}\right), \tag{IV.59}$$

where σ_{r_0} is given by Eq. (IV.56) and ε_∞ represents the asymptotic value of the neck parameter evaluated using the Boltzmann distribution (cf. the next sub-subsection). To derive

Eq. (IV.59), according to Ref. [87], we have made a similar assumption, under which the initial condition follows a normal distribution, namely $W(r_0,t)=\frac{1}{\sqrt{2\pi\sigma_{r_0}^2}}\exp\left[-\frac{(r_0-\overline{r_0})^2}{2\sigma_{r_0}^2}\right]$. Hence, the time-dependent formation probability is given as follows:

$$\begin{aligned}P(t)&=\int_{-\infty}^{r_s}\int_{-\infty}^{+\infty}W(r_0,t)P(r,t)\mathrm{d}r\mathrm{d}r_0\\&=\int_{-\infty}^{r_s}\int_{-\infty}^{+\infty}\frac{1}{\sqrt{2\pi\sigma_{r_0}^2}}\frac{1}{\sqrt{2\pi\sigma_r^2}}\exp\left[-\frac{(r_0-\overline{r_0})^2}{2\sigma_{r_0}^2}\right]\exp\left[-\frac{(r-\langle r\rangle)^2}{2\sigma_r^2}\right]\mathrm{d}r\mathrm{d}r_0\\&=\frac{1}{2}\mathrm{erfc}\left[\frac{\langle r(t)-r_s\rangle}{\sqrt{2\sigma_r'^2(t)}}\right],\end{aligned}\tag{IV.60}$$

from which one obtains the time evolution of the variance $\sigma_r'^2(t)$ that takes into account the dispersion of initial conditions.

The average trajectories and the formation probabilities of the uncoupled case and the approximate or exact coupled case are shown in Fig. IV.20. It clearly shows that the dynamical coupling has a crucial role to play in the formation step. With the help of this toy model, the initial radial shift is estimated to be of the order of few fm, which is large enough to have a significant impact on the fusion hindrance. Moreover, it can be seen that the initial shift of the relative distance should be always positive and thus enlarges the height of the inner barrier by fusing nuclei. Fig. IV.20 also demonstrates that the approximate solutions are in nice agreement with the exact ones. Therefore, the adiabatic approximation has been well justified. It is also clearly shown that the fusion probability has been remarkably reduced by orders of magnitude because of the initial radial shift and thus the fusion becomes much more hindered compared to light reaction systems.

The results obtained from the present study appear quite consistent with the conclusion on the injection point given in Ref. [48]. Actually, the initial shift has been phenomenologically introduced in Ref. [48] so as to reproduce the experimental data. Hence, we provided a theoretical justification of it, which could be another possible contribution to the fusion hindrance.

Asymptotic value of the neck variable and its variance

Up to now, the reflective boundary conditions have not been taken into consideration when solving the two-dimensional Langevin equation. Using the adiabatic approximation, we have deduced a radial initial shift that might remarkably enlarge the size of the inner barrier. As can be seen from Eq. (IV.58), this shift is closely related to the difference between initial and asymptotic values of the neck parameter. Hence, it is meaningful to inquire into the influence of neck confinement, namely $\varepsilon\in[0,1]$, on the asymptotic value of the neck parameter.

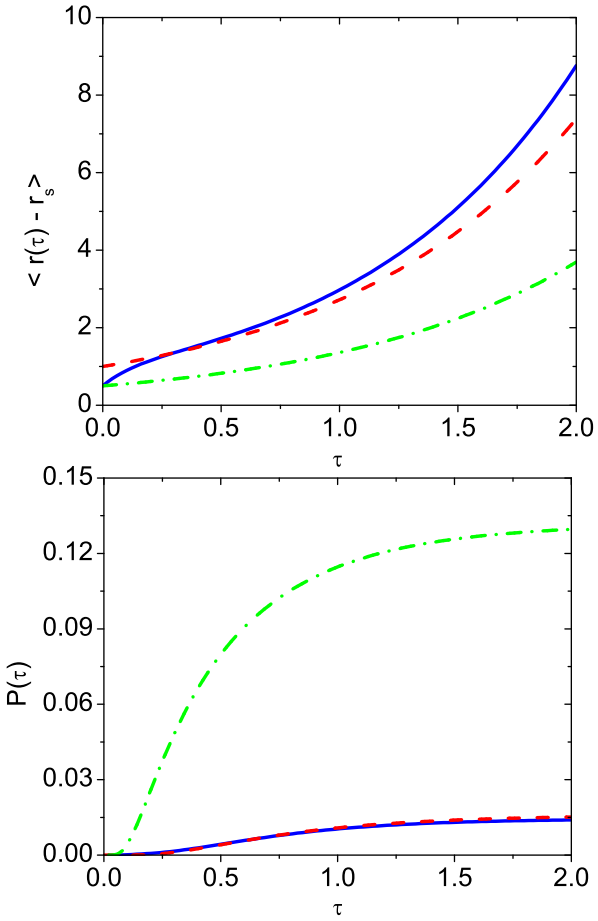

Figure IV.20 – Average trajectory (top) and fusion probability (bottom) as a function of time for a simple parabolic potential. The solid blue line represents the exact solution. The green dotted-dashed one is the uncoupled one ($\gamma_{r\epsilon} = 0$). The dashed red curve corresponds to the approximate solution. Here, $\gamma_{\epsilon\epsilon}/\gamma_{rr} = 0.6$, $\gamma_{r\epsilon}/\gamma_{rr} = 0.5$, $g/h = 3$ and $T/h = 0.2$. The time unit is γ_{rr}/h and T is the temperature. r_s and γ denote the location of the conditional saddle point and the friction tensor, respectively.

Once the equilibrium has been achieved, the neck parameter obeys the Boltzmann distribution and thus its limit can be evaluated as follows:

$$\varepsilon_\infty = \frac{\int \varepsilon \exp\left[-\frac{V(\varepsilon,r)}{T}\right] \mathrm{d}\varepsilon}{\int \exp\left[-\frac{V(\varepsilon,r)}{T}\right] \mathrm{d}\varepsilon}. \tag{IV.61}$$

Without the neck confinement, namely $\varepsilon \in [-\infty, +\infty]$, the asymptotic value of the neck is given as follows:

$$\varepsilon_\infty = \frac{\int_{-\infty}^{\infty} \varepsilon \exp\left[-\frac{V_s + \frac{1}{2}g\varepsilon^2 - \frac{1}{2}h(r-r_s)^2}{T}\right] \mathrm{d}\varepsilon}{\int_{-\infty}^{\infty} \exp\left[-\frac{V_s + \frac{1}{2}g\varepsilon^2 - \frac{1}{2}h(r-r_s)^2}{T}\right] \mathrm{d}\varepsilon} = 0.0. \tag{IV.62}$$

As a comparison, when the neck parameter is comprised in $[0,1]$, its asymptotic value can be evaluated in a similar manner, namely

$$\varepsilon_\infty = \frac{\int_0^1 \varepsilon \exp\left[-\frac{V_s+\frac{1}{2}g\varepsilon^2-\frac{1}{2}h(r-r_s)^2}{T}\right]\mathrm{d}\varepsilon}{\int_0^1 \exp\left[-\frac{V_s+\frac{1}{2}g\varepsilon^2-\frac{1}{2}h(r-r_s)^2}{T}\right]\mathrm{d}\varepsilon} \simeq 0.2, \tag{IV.63}$$

where $g/T = 15$, $g/h = 3$ and $\varepsilon_0 = 0.95$. It can be seen that the difference between ε_0 and ε_∞ does not change so much. Hence, the radial shift would remain small in both cases. Of course, the above calculation would be dependent on the potential landscape, but in general, the asymptotic value of the neck parameter is considered to be quite small, say around 0.1.

As regards the variance associated with neck parameter $\sigma^2_{\varepsilon_\infty}$, it is similarly defined as

$$\sigma^2_{\varepsilon_\infty} = \frac{\int(\varepsilon-\varepsilon_\infty)^2 \exp\left[-\frac{V(\varepsilon,r)}{T}\right]\mathrm{d}\varepsilon}{\int \exp\left[-\frac{V(\varepsilon,r)}{T}\right]\mathrm{d}\varepsilon}. \tag{IV.64}$$

To clarify the impact of the neck confinement on $\sigma^2_{\varepsilon_\infty}$, for a parabolic potential, one has

$$\sigma^2_{\varepsilon_\infty} = \frac{\int_0^1(\varepsilon-\varepsilon_\infty)^2 \exp\left[-\frac{V_s+\frac{1}{2}g\varepsilon^2-\frac{1}{2}h(r-r_s)^2}{T}\right]\mathrm{d}\varepsilon}{\int_0^1 \exp\left[-\frac{V_s+\frac{1}{2}g\varepsilon^2-\frac{1}{2}h(r-r_s)^2}{T}\right]\mathrm{d}\varepsilon} \simeq 0.024\,2. \tag{IV.65}$$

Here, the neck parameter has been considered to be comprised in the interval $[0,1]$. Without the neck confinement, it becomes

$$\sigma^2_{\varepsilon_\infty} = \frac{\int_{-\infty}^{\infty}(\varepsilon-\varepsilon_\infty)^2 \exp\left[-\frac{V_s+\frac{1}{2}g\varepsilon^2-\frac{1}{2}h(r-r_s)^2}{T}\right]\mathrm{d}\varepsilon}{\int_{-\infty}^{\infty} \exp\left[-\frac{V_s+\frac{1}{2}g\varepsilon^2-\frac{1}{2}h(r-r_s)^2}{T}\right]\mathrm{d}\varepsilon} \simeq 0.066\,7, \tag{IV.66}$$

Hence, the variance does not differ so much in both cases.

IV.2.4 Approximation limits

Finally, it would be worth discussing the relative error of the adiabatic approximation in the case of a simple combined parabolic potential, which can be defined as

$$e = \lim_{t\to+\infty} \frac{P_{\text{approx}}(t) - P_{\text{exact}}(t)}{P_{\text{exact}}(t)}, \tag{IV.67}$$

where P_{exact} and P_{approx} refer to the exact fusion probability and the approximate one based upon the adiabatic approach, respectively. Here we do not take the absolute value. This definition allows us to look more closely into the limitations related to the one-dimensional

model.

The comparison results are systematically displayed in Fig. IV.21. For each selected value of g/h, it can be remarked that the relative error increases with $r_0 - r_s$. In the present study, the ratio g/h has always been fixed at 3 and the initial relative distance without dimension has been chosen as $\overline{r_0} - r_s = 0.5$. In this case, the relative error is estimated to be $e \simeq 9\%$. However, this model does not seem to be so accurate for the real problem. For instance, in the case of the reaction ^{110}Pd+^{110}Pd, we have $g/h \simeq 1$, $\overline{r_0} - r_s \simeq 0.4$ and the relative error appears quite small, as can be seen in Fig. IV.21. However, it should be noted that, for a heavier reaction, say ^{132}Cs+^{132}Cs, one has $g/h \simeq 2.5$, $r_0 - r_s \simeq 1.0$ and the relative error might become large. (Note that the friction tensor is also dependent on the reaction system.).

So far, we have presented a simplified fusion model based upon the two-dimensional Langevin equation with a combined parabolic potential. It has been revealed that, due to a large driving force for the neck parameter, the initial value of the radial distance is shifted so that the fusion reaction becomes more hindered. It should be mentioned that the potential landscape employed here appears quite crude and would only be valid in the vicinity of the conditional saddle point. What if we have a more realistic potential landscape? Can we still get an initial shift of the relative distance? To answer these questions, since the analytical solution is not available anymore, numerical estimation should be required. Recently, according to some follow-up work done by other groups, using the numerical simulation with a more complicated potential landscape, the initial radial shift has also been confirmed [90–92].

IV.3 Two-step model

IV.3.1 Brief review

In the previous two sections, we have separately investigated the capture step and the formation step. At the present time, it is not possible to establish a unified consistent reaction theory, which can be applied to the whole fusion process. Put differently, one has to always decompose the fusion of heavy systems into two separate parts. In this section, we shall briefly introduce a combined fusion model based upon this strategy. It is the so-called two-step model [76, 93].

The total fusion cross-section is usually given as follows:

$$\sigma_{\rm fus} = \frac{\pi}{k^2} \sum_J (2J+1) P^J_{\rm fus}(E_{\rm cm}), \tag{IV.68}$$

where $P_{\rm fus}$ refers to the fusion probability for massive systems, which is much smaller compared to light colliding systems. As previously mentioned, the reason is mainly due to the fusion hindrance phenomenon that occurs during the collision, which is experimentally well known and qualitatively interpreted, but still has some serious ambiguities in theoretical predictions. Concerning light colliding systems, the fusion probability simply corresponds to

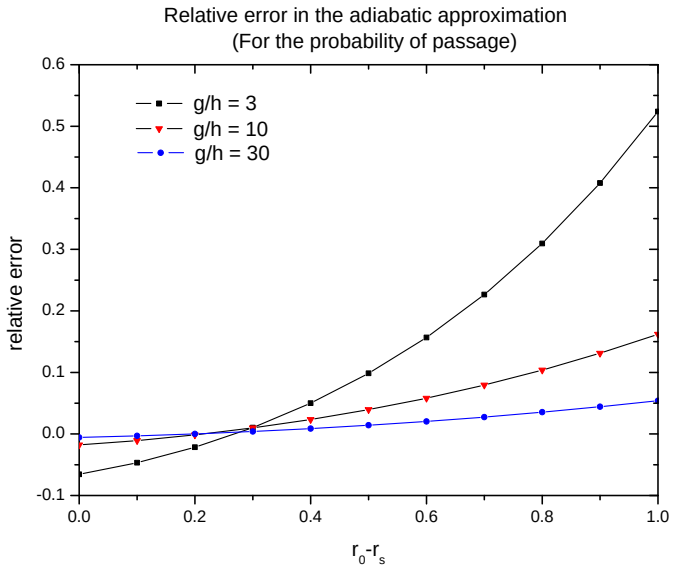

Figure IV.21 – Relative error of the adiabatic approximation. Here we have checked it for three different values of g/h. It is clearly shown that, for the same initial positions, the accuracy of the adiabatic approach becomes much better with increasing g/h, which is equivalent to a more rapid thermalization of the neck parameter.

the capture one, whereas this is not the case for very massive systems. Thus, it is reasonably proposed that the total fusion probability can transform into a product of two factors, namely

$$P^J_{\rm fus}(E_{\rm cm}) = P^J_{\rm cap}(E_{\rm cm}) \cdot P^J_{\rm form}(E_{\rm cm}). \tag{IV.69}$$

This ansatz has been widely employed to study the synthesis of SHE.

To describe the capture step, as previously discussed, either the EBD approach or WKB approximation is adopted for the calculation of the capture probability. As regards the formation step, the evolution of the di-nuclear system from the contact point into the compound configuration can be described by means of the multi-dimensional Langevin equation with a complicated liquid-drop potential. Here, two degrees of freedom are currently being used in our code, namely the relative distance between two centers r and mass asymmetry α [76, 93]. Their initial values are defined as

$$r_0 = (A_p^{1/3} + A_t^{1/3})/(A_p + A_t)^{1/3} \tag{IV.70}$$

and

$$\alpha_0 = (A_t - A_p)/(A_t + A_p), \tag{IV.71}$$

respectively. Regarding the neck parameter, based upon the above discussions, it is assumed to be frozen due to the rapid thermalization at the beginning of the formation step. In the two-

step model, it has been fixed at 0.1 by default. Thus, within the multi-dimensional Langevin equation, namely Eq. (IV.35), q_1 and q_2 correspond to r and α, respectively, whereas p_1, p_2 are nothing else but their conjugate momenta. The LD potential energy is calculated using the two-center liquid-drop model [80, 81] and the unified potential model for fusion and fission [94], together with the rotational energy of the compound system estimated with the rigid body moment of inertia. The angular-momentum-dependent nuclear temperature, T^J, is defined as

$$T^J = \sqrt{(E_{\text{c.m.}} + Q - \Delta E_{\text{sh}} - E^J_{\text{rot}})/a}, \tag{IV.72}$$

which is defined in the case of compound ground state for each total angular momentum. The shell-correction energy ΔE_{sh} and nuclear mass are taken from Ref. [15]. The level-density parameter a is taken to be approximately $(A_p + A_t)/10$, which is reasonable for massive nuclei [95].

To evaluate the formation probability P^J_{form}, the code initiates N trajectories for the same initial radial momentum p_0 and then counts the number of trajectories contributing to the formation of the compound nucleus, denoted by N', and the probability is thus given by

$$F^J(p_0, T^J) = N'/N. \tag{IV.73}$$

Since the radial momentum at the contact point is assumed to obey a Gaussian distribution centered at $\overline{p}^J_0$ due to a heating-up process by the dissipation-fluctuation theorem, namely

$$g^J(p_0, \overline{p}^J_0, T^J) = \frac{1}{\sqrt{2\pi\mu T^J}} e^{-(p_0-\overline{p}^J_0)^2/(2\mu T^J)}, \tag{IV.74}$$

then finally the formation probability is given by

$$P^J_{\text{form}}(E_{\text{cm}}) = \int F^J(p_0, T^J) g^J(p_0, \overline{p}^J_0, T^J) \mathrm{d}p_0, \tag{IV.75}$$

where $\overline{p}^J_0$ refers to the mean value of initial momentum p_0. According to the results obtained from the surface friction model [96], it has been kept fixed at zero, which is mainly due to a strong energy dissipation in the capture channel [76, 97], or put differently, the radial motion is completely damped and reaches the thermal equilibrium when two colliding nuclei stick together.

It should be noted that, due to the quasi-fission phenomenon occurring in heavy systems, the measured fusion cross-sections are usually not reliable so that a systematic comparison with theoretical calculations would not be possible.

IV.3.2 Application to the fusion reaction: ^{129}Xe+^{nat}Sn

In this subsection, we employ the two-step model to investigate only one fusing system, namely ^{129}Xe+^{nat}Sn, which was measured at GANIL.

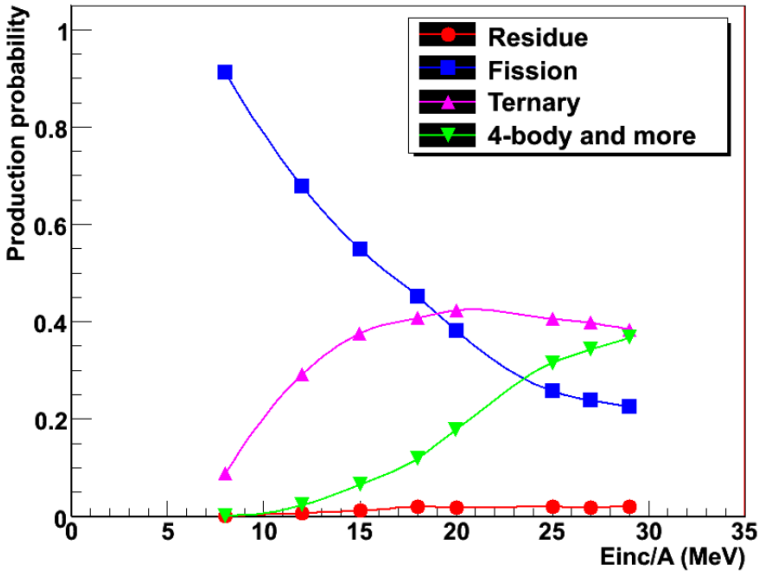

Figure IV.22 – Production rate of the four exit channels as a function of the incident energy for the central collisions of ^{129}Xe+^{nat}Sn. Figure is taken from Ref. [32].

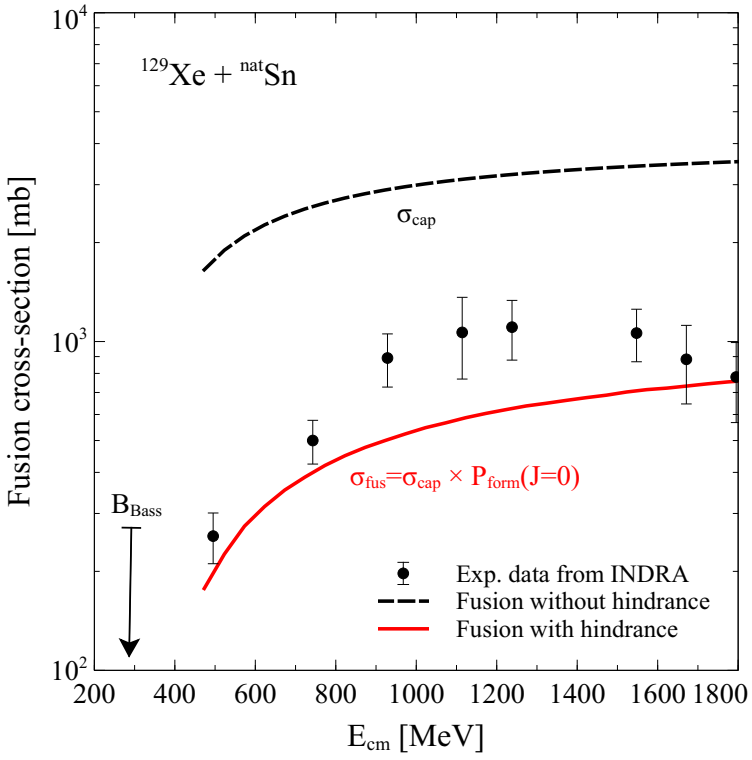

Figure IV.23 – Comparison of the calculated fusion excitation function with the measured data (solid black circles). The experimental data are taken from Ref. [32]. The approximate Bass barrier is indicated by the vertical dashed line.

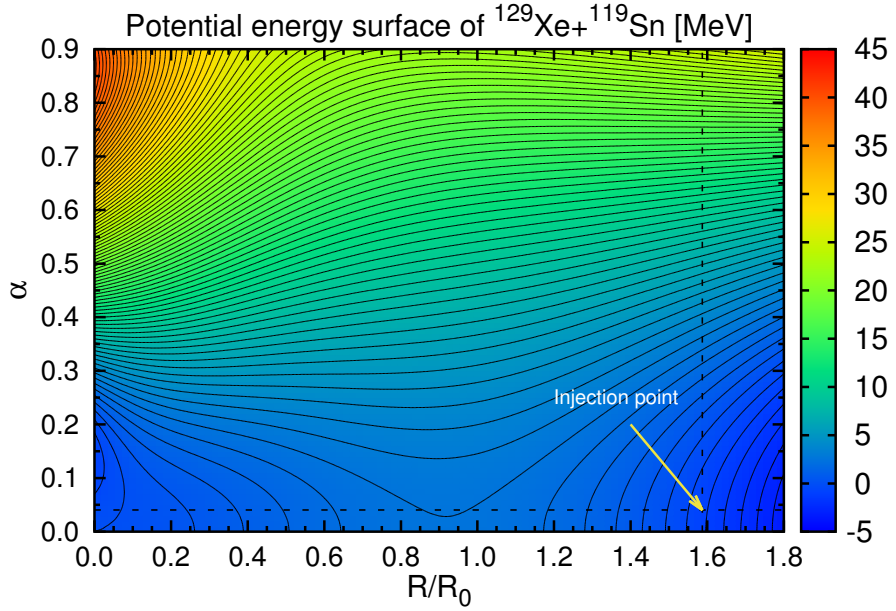

Figure IV.24 – Potential energy surface (in MeV) of the reaction system ^{129}Xe+^{119}Sn. The horizontal axis indicates the relative distance and the vertical one denotes the asymmetry parameter. The injection point is estimated to be located at $r_0 \sim 1.58$ and $\alpha_0 \sim 0.04$. The reaction system should overcome the inner barrier to reach the fusion region through a random process. The neck parameter is assumed to be thermalized at $\varepsilon \simeq 0.1$.

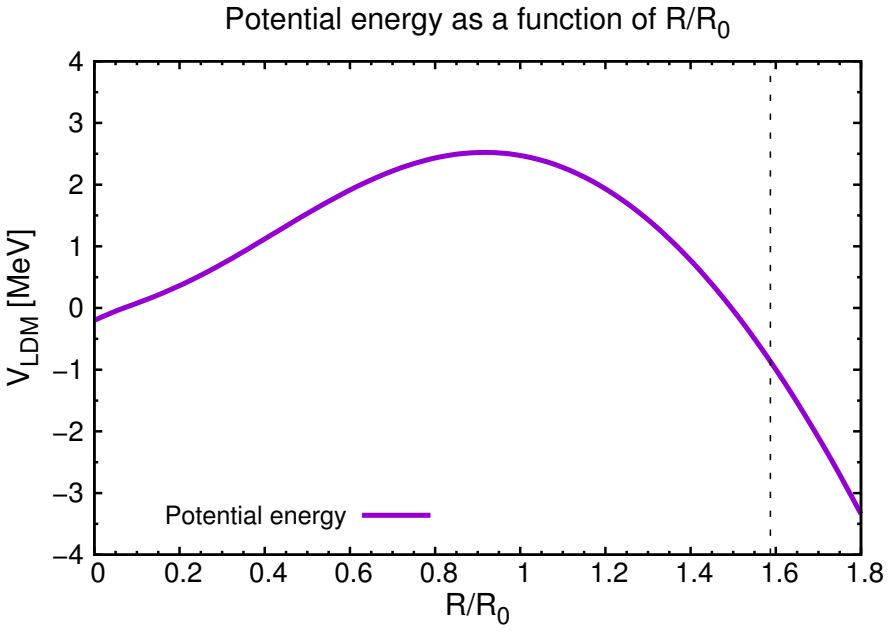

Figure IV.25 – Illustration of the conditional saddle point for the same reaction. The contact point is indicated by the vertical dashed line. The inner barrier height is estimated to be around 3.5 MeV.

The reaction ^{129}Xe+^{nat}Sn ($Z_pZ_t = 2700$) was performed at incident beam energies from 8 to 29 MeV/A_p, by using the 4π INDRA (Identification de Noyaux et Détection avec Résolutions Accrues) multi-detector [98] at the GANIL laboratory. This detector, which is composed of 336 detection cells arranged in 17 rings centered on the beam axis, covers about 90% of the solid angle and is able to identify the charge of fragments from hydrogen to uranium with low thresholds.

Central collisions have been measured using a kinematic global variable applied to the heaviest fragment in the event. Accordingly, the preliminary fusion cross-sections have been well measured and are reported in Fig. IV.23. It clearly shows a maximum value of the excitation function at $E_{\rm lab}/A_p = 18-20$ MeV (or about $E_{\rm cm} = 1200$ MeV), which still remains an open question. To understand the experimental data, the relative yield of the four measured exit channels in the energy range $E_{\rm lab}/A_p = 8-29$ MeV is shown in Fig. IV.22. It is demonstrated that more than 90% of yield goes into fission at the lowest energy and it decreases monotonically to 20% at the highest energy. By contrast, the 3-fragment exit channel increases, saturates, and eventually decreases at high energies. The 4-fragment exit channel appears at $E_{\rm lab}/A_p = 12$ MeV and increases at highest energy, indicating that the multi-fragmentation decay mode becomes dominant. The crossing of the fission and 3-fragment exit channels is located between $E_{\rm lab}/A_p = 18$ and 20 MeV, exactly at the maximum cross-section. One can speculate that the attractive nuclear potential overcomes the repulsive centrifugal one at this energy. For more experimental details, the reader is referred to Ref. [32]. This arises some interesting questions, such as

- Did the fusion really occur and thus lead to the formation of compound nuclei?
- Is it possible to have an explanation for the measured cross-sections on the basis of a fusion model?

To answer these questions, we attempt to employ the two-step model to study this reaction.

Fig. IV.24 shows the potential energy map of the reaction ^{129}Xe+^{119}Sn, calculated using the two-center liquid-drop model [80, 81] and the unified potential model for fusion and fission [94]. The contact point is estimated to be located at $r_0 \sim 1.58$ and $\alpha_0 \sim 0.04$. As can be seen in Fig. IV.24, the " injection point" is located outside the ridgeline of the potential. To reach the region where the fusion takes place (left-bottom part of the map), the binary system needs to pass over the inner conditional point through a random process. Fig. IV.25 clearly displays the conditional point that the di-nuclear system has to overcome. The barrier height is thus strongly dependent on the position of the "injection point" after passing over the Coulomb barrier. According to the previous section, the rapid decoupling between the neck variable and the radial degree of freedom causes an initial shift and thus leads to an enlargement of the inner barrier seen by the fusing system. Accordingly, this nearly symmetric reaction system is considerably hindered.

The calculated fusion excitation function based on the two-step model is displayed in Fig. IV.23. The solid black circles represent the preliminary experimental fusion cross-sections

in central collisions. The black dashed curve stands for the capture cross-section estimated using the EBD approach, which clearly overestimate the measured cross-section. After taking the formation probability into consideration, the theoretical prediction (with $J \simeq 0$) agrees rather well with the measured data, especially at energies close to the barrier (the first two data points). As discussed above, this corresponds to the energy region where the fission (of compound nuclei) is dominant. Therefore, with the help of the two-step model, this would be a direct evidence for the formation of compound nuclei. Regarding the high energy part (starting from around $E_{\rm lab}/A_p = 15$), the concept of CN might lose its validity, which can be indicated by the emergence of other possible exit-channels could also come into play, such as the multi-fragmentation process. In any case, the fusion model is not appropriate anymore here.

IV.4 Summary and conclusions

First, for the purpose of roughly estimating the uncertainty in the capture model, a detailed comparison of the estimated capture cross-sections based upon three different approaches has been made for the reactions ^{16}O+^{154}Sm, ^{16}O+^{208}Pb, ^{16}O+^{238}U, ^{48}Ca+^{208}Pb, ^{50}Ti+^{208}Pb and ^{48}Ca+^{238}U. The importance of considering the coupling between some low-lying collective states has been accentuated. It has been clearly shown that the EBD approach and the WKB approximation with an empirical proximity potential can be regarded as two adequate alternatives to the CC method, especially at near- and above-barrier energies. This is the main reason why, in the KEWPIE2 code (cf. the next chapter), we keep employing these two approximate methods for the reproduction of experimental capture cross-sections. Nevertheless, it should be borne in mind that the EBD formula was derived from a classical framework, and therefore its validity region remains limited at near-barrier or over-barrier energies. Moreover, the large uncertainty in the width of barrier distribution will be another delicate issue that has to be more closely considered. In any case, at energies above the Coulomb barrier, the quantum approach and the semi-classical approximation should logically tend to be equivalent. Finally, more accurate potential parameterizations for the study of heavy-ion fusions will be required in the hope of improving the predictive capability.

Regarding the formation step, the importance of the neck evolution has been clearly stressed. First, by solving a one-dimensional Langevin equation, it has been well proven that the neck evolution is far quicker than the radial one. After that, we proposed a simple theoretical model based upon a two-dimensional Langevin equation. Since the “denecking” process is very rapid, it enables us to decouple the neck variable from the radial one by means of the adiabatic approximation, which gives rise to an initial radial shift. Accordingly, the size of the inner barrier is considerably enlarged. This provides a possible explanation to the amplitude of the fusion hindrance occurring in the formation process. However, it should be emphasized that the present model is somewhat too crude, for instance, the potential landscape was simply approximated by a combined parabolic barrier and the neck confinement ($\epsilon \in [0,1]$) was not taken into account. The magnitude of the initial shift should be estimated more

precisely for experimental predictions. On the other hand, the influence of the asymmetry variable should also be considered within the same framework in order to provide a complete description, not only for symmetric reactions, but also for the asymmetric ones which are commonly employed to synthesize new SHE. To this extent, neglecting the asymmetry variable could have a great impact on the formation step. Can we perform a similar treatment using the adiabatic approximation? Further consideration will be needed and some follow-up work of this research is currently underway.

V Statistical decay of excited nuclei

> The purpose of models is not to fit the data but to sharpen the questions.
>
> Samuel Karlin

This chapter is devoted to describing the statistical de-excitation of excited heavy nuclei. For this purpose, we have developed a new cascade code, called KEWPIE2 [99], which serves as a basic tool for uncertainty analysis. The main contents of this chapter are actually based upon a recent paper submitted to Computer Physics Communications [100].

V.1 Brief introduction

The de-excitation of excited heavy nuclei is usually accompanied by a competition between light-particle evaporation or γ-ray emission and nuclear fission. To simulate such a process, there are actually many computer codes available on the market, such as HIVAP [53] and PACE4 [101]. All of them are based upon various theoretical assumptions and models. In the region of SHE, since the survival probability is extremely low, it would be helpful to have a computer code which is able to efficiently handle the rare events occurring during the reaction. This is the main reason why we have developed a new cascade code that avoids Monte-Carlo methods so as to have a great computational efficiency when dealing with extremely low probability events. The numerical scheme is essentially based upon the Bateman equations, which allows us to compute both statistical and dynamical observables, such as the survival probability of a decaying nucleus and fission time distribution. In this chapter, we mainly concentrate on the statistical part of the code.

The first version of KEWPIE [102] was released in 2004. KEWPIE2 is an upgraded version of the KEWPIE code, which was completely rewritten in C++ language [99]. Accordingly, owing to the object-oriented features of C++, further developments would become much easier. The code has been continually developed since that time and was employed to provide theoretical

calculations for many applications [20, 103–105]. In the current version, the basic algorithm has been upgraded and the main physical content has been greatly improved by adding some recent theoretical models. As a consequence, some parameter values that appeared incorrect have been corrected and thus become more consistent with recent advances in nuclear physics research.

Here, we mainly focus upon the fusion-evaporation reaction which is of special interest within many areas of nuclear physics. For instance, it is commonly used to synthesize exotic nuclei far from the valley of stability and thus to explore the boundaries of the nuclide chart. To illustrate it, we might consider the following process: the collision of a projectile, a, with a target nucleus, A, forms a intermediate state, C, called compound nucleus, which subsequently evaporates a light particle b, thus transforming itself into a residual nucleus B. The whole process can be illustrated as follows:

$$a + A \longrightarrow C^* \longrightarrow B + b,$$

where the compound system is denoted by C and the asterisk indicates an excited state that is characterized by nuclear temperature T. In general, such a reaction can be divided into two stages: the collision of two nuclei leading to the formation of a CN and its subsequent decay by light-particle evaporation in competition with nuclear fission and γ-ray emission. According to the so-called Bohr independence hypothesis [106], these two reaction steps are considered to be independent of each other. Accordingly, the production or evaporation-residue (ER) cross-section can thus be expressed as

$$\sigma_{\mathrm{ER}}(E_{\mathrm{cm}}) = \sum_{J_C \geq 0} \sigma_{\mathrm{fus}}(E_{\mathrm{cm}}, J_C) P_{\mathrm{sur}}(E_C^*, J_C), \tag{V.1}$$

with

$$\sigma_{\mathrm{fus}}(E_{\mathrm{cm}}, J_C) = \frac{\pi}{k^2}(2J_C + 1) P_{\mathrm{fus}}(E_{\mathrm{cm}}, J_C), \tag{V.2}$$

where J_C is the total angular momentum of the compound system and k the wave number of relative motion between the projectile and target nuclei. In writing Eqs. (V.1) and (V.2), we have employed the No-Coriolis or Iso-centrifugal approximation [39], which states that the entrance-channel orbital angular momentum of the binary system can be replaced by the total angular momentum or the spin of the compound system. The relationship between the incident energy in the centre-of-mass frame E_{cm} and the total excitation energy of the compound nucleus E_C^* is simply given by $E_C^* = E_{\mathrm{cm}} + Q$, where the Q-value is evaluated from the most recent experimental ground-state masses [107, 108]. If the measured values are not available, the theoretical mass table [15] shall be employed.

It should be mentioned that the KEWPIE2 code mainly handles the final stage of the fusion-evaporation reaction. The physical processes included in the code remain basically the same compared to the previous version. As a whole, they are divided into two main categories, namely light-particle evaporation and fission. To treat the former, the code has accommo-

dated two standard approaches, namely the Weisskopf-Ewing [109, 110] and Hauser-Feshbach models [111]. It should be noted that the latter takes into account the spins of the mother and daughter nuclei, whereas the former can be somewhat regarded as a classical limit that neglects the intrinsic quantum states of the compound system. Owing to its simplicity, the Weisskopf-Ewing evaporation model has been commonly employed in analytical calculations [3, 48, 49] devoted to studying the synthesis of super-heavy nuclei. Nevertheless, as emphasized in Refs. [112–121], the Hauser-Feshbach formalism appears more suitable and would thus be recommended for heavy-ion reaction calculations in spite of its computational inefficiency. As regards the fission process, the decay rate can be estimated within the framework of the Bohr-Wheeler statistical theory [2]. According to Kramers [122], nuclear fission can be described by a diffusion process above the potential barrier along the deformation coordinate. Since this pioneering work, it has been well established that the dynamical effect of nuclear fission can be modeled using the Klein-Kramers equation or its equivalent Langevin equation [123–127]. Accordingly, the whole process is not only dependent on the potential-energy landscape of the compound system but also on the friction parameter characterizing the nuclear viscosity. As a result, the fission rate has to take a finite time to reach its stationary value. This transient effect has been included in the code by introducing a user-defined time delay, which would be necessary when computing some dynamical observables related to the fission rate. Furthermore, the ground-state and saddle-point deformations have also been taken into consideration in our model. Such effects on the nuclear structure would be essential as pointed out in Ref. [128]. Apart from the evaporation and fission processes, some recent developments [129, 130] in the study of γ-ray emission have been considered as well.

In addition to the de-excitation process, KEWPIE2 contains a calculation of the fusion probability using either the WKB approximation with an empirical proximity potential [52, 53, 131, 132] or the EBD method [47, 48], as presented in the previous chapter. In light-ion induced reactions, the fusion probability exactly corresponds to the one for surmounting the Coulomb barrier, that is, to the capture probability.

The aim of this chapter is to provide a complete description of the physical ingredients involved in the code for describing the de-excitation of excited nuclei. First, we start by recalling the numerical framework for describing a decay process and some of its simple implementations. Then, the various nuclear models currently being used are presented in detail. After that, several calculational examples are shown and the computational results are carefully compared with the available experimental data, and in the meantime, we perform a sensibility analysis for both input parameters and reaction models. Finally, some conclusions are drawn and future prospects are discussed as well in the end.

V.2 Numerical framework for compound-nucleus decay

This section briefly presents the conceptual framework for modeling physical processes so as to illustrate how the code works. For the sake of completeness, we first recall some basic

ideas and definitions. A detailed description of the numerical scheme is then provided.

V.2.1 Single chain

Population as a function of time

Let us consider a single cascade-decay chain starting from an excited compound nucleus, assuming that the competition only occurs between the neutron evaporation and nuclear fission. The general equations describing the time evolution of such a disintegration chain read

$$\begin{aligned}
\frac{\mathrm{d}P_0}{\mathrm{d}t} &= -\Gamma^0_{\mathrm{tot}} P_0 \quad \text{with} \quad P_0(0) = 1, \\
\frac{\mathrm{d}P_1}{\mathrm{d}t} &= \Gamma^0_n P_0 - \Gamma^1_{\mathrm{tot}} P_1 \quad \text{with} \quad P_2(0) = 0, \\
&\vdots \\
\frac{\mathrm{d}P_s}{\mathrm{d}t} &= \Gamma^{s-1}_n P_{s-1} - \Gamma^s_{\mathrm{tot}} P_s \quad \text{with} \quad P_s(0) = 0,
\end{aligned} \tag{V.3}$$

where Γ^s_{tot} is the total decay width for the nucleus labeled with s and Γ^s_n the particle-evaporation width. The total decay width is then $\Gamma^s_{\mathrm{tot}} = \Gamma^s_n + \Gamma^s_f$, where Γ^s_f corresponds to the fission-decay width. Here, $P_s(t)$ denotes the population of the nucleus having emitted s neutrons at time t. If the decay widths are time-independent, it is very easy to analytically solve these coupled-differential equations by means of the Laplace transform. According to [133], the corresponding solutions are summarized as follows:

$$\begin{aligned}
P_0(t) &= e^{-\Gamma^0_{\mathrm{tot}} t}, \\
P_1(t) &= \frac{\Gamma^0_n}{\Gamma^1_{\mathrm{tot}} - \Gamma^0_{\mathrm{tot}}} (e^{-\Gamma^0_{\mathrm{tot}} t} - e^{-\Gamma^1_{\mathrm{tot}} t}), \\
&\vdots \\
P_{s_{\max}}(t) &= \prod_{k=0}^{s_{\max}-1} \Gamma^k_n \sum_{i=0}^{s_{\max}} \frac{e^{-\Gamma^i_{\mathrm{tot}} t}}{\prod_{j \neq i} (\Gamma^j_{\mathrm{tot}} - \Gamma^i_{\mathrm{tot}})},
\end{aligned} \tag{V.4}$$

where it has been assumed that the Γ's are all different from each other and are not equal to zero. $s_{\max}$ represents the maximum number of neutrons ejected from the compound nucleus. Once all populations have been obtained, it would not be difficult to compute some measured observables.

As a typical example, Fig. V.1 shows the time evolution of the populations calculated with the Bateman equations. Here, the excitation energy of the initial nucleus was set equal to 70 MeV. Here, the sharp decrease of the total population is mainly caused by nuclear fission. It should also be noted that the time scale spans several orders of magnitudes, before the total population stabilizes.

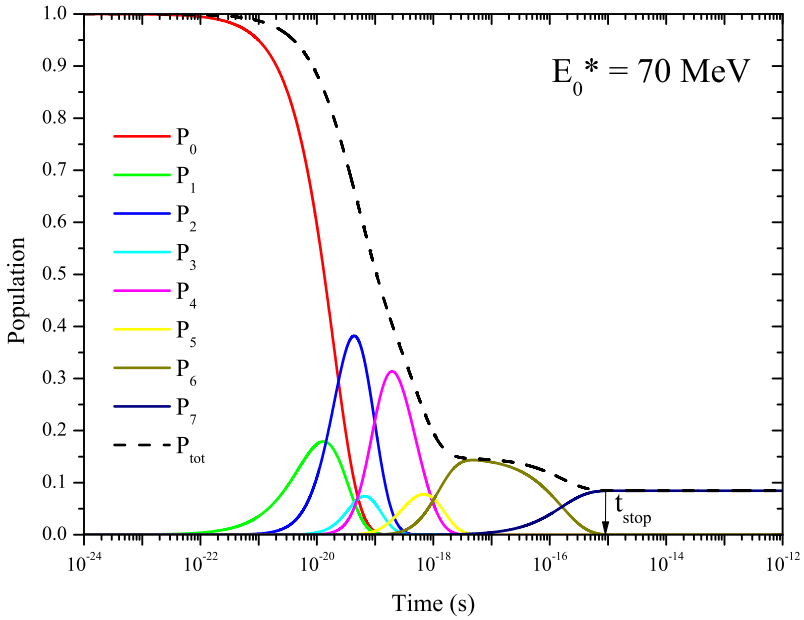

Figure V.1 – Example of the time evolution of the population of each isotope for a single decay chain where only the competition between the neutron evaporation and nuclear fission is taken into consideration.

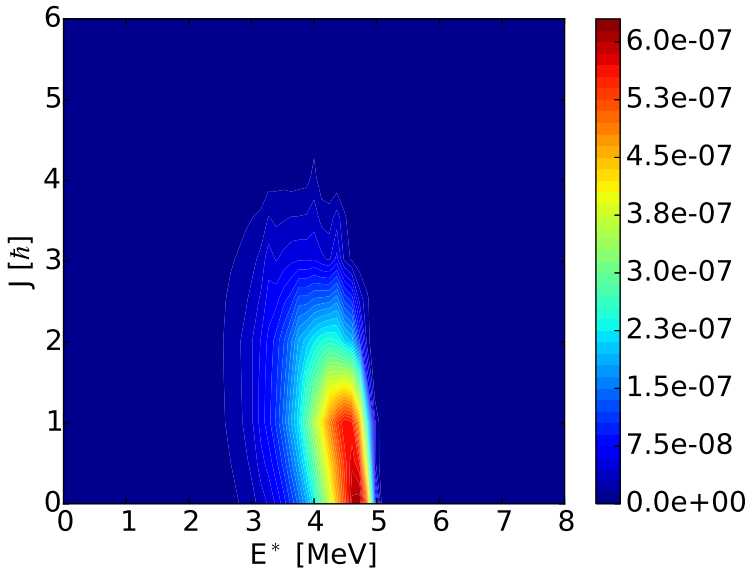

Figure V.2 – Example of a two-dimensional spectrum of the daughter nucleus (^{255}No) obtained using the spectral discretization method. The horizontal axis denotes the excitation energy and the vertical axis the nuclear spin. Here, the color bar represents the population distribution (in arbitrary units).

Experimental observables

Here, we would like to provide some typical examples that were already given in Refs. [134, 135]. The probability for the compound nucleus to emit exactly s neutrons prior to fission is given as follows:

$$\begin{aligned} p_s &= \int_0^{+\infty} \mathrm{d}t \Gamma_f^s P_s(t) \\ &= \frac{\Gamma_f^s}{\Gamma_{\mathrm{tot}}^s} \prod_{i=0}^{s-1} \frac{\Gamma_n^i}{\Gamma_{\mathrm{tot}}^i}. \end{aligned} \tag{V.5}$$

At the end of the cascade-decay chain, it turns into

$$p_{s_{\max}} = \prod_{i=0}^{s_{\max}} \frac{\Gamma_n^i}{\Gamma_{\mathrm{tot}}^i}. \tag{V.6}$$

These results have commonly been implemented in various statistical codes. The average neutron multiplicity thus reads

$$\langle \nu \rangle = \sum_{i=0}^{s_{\max}-1} s p_s. \tag{V.7}$$

Other observables related to p_s can also be defined in a similar manner.

Finally, we are also able to calculate the average fission time which can be evaluated within the same framework. To compute this quantity, the population of each isotope at any time must be available. It is thus given by

$$\begin{aligned} \tau_f &= -\frac{1}{P_{\mathrm{tot}}(0) - P_{\mathrm{tot}}(+\infty)} \int_0^{+\infty} t \frac{\mathrm{d}P_{\mathrm{tot}}}{\mathrm{d}t} \mathrm{d}t, \\ &= \frac{1}{P_{\mathrm{tot}}(0) - P_{\mathrm{tot}}(+\infty)} \sum_{s=0}^{s_{\max}} \int_0^{+\infty} t \Gamma_f^s P_s(t) \, \mathrm{d}t, \end{aligned} \tag{V.8}$$

where $P_{\mathrm{tot}}(0)$ and $P_{\mathrm{tot}}(+\infty)$ represent the total populations at initial time and its long-time limit, respectively. It should be mentioned that the KEWPIE2 code can be employed to estimate not only the statistical but also dynamical observables, such as the survival probability and fission time distribution. the former corresponds to the long-time limit whereas the latter requires a full resolution of the Bateman equations.

V.2.2 Multi-channel scheme

At high excitation energies, charged particles can be emitted as well. In the KEWPIE2 code, we only consider two kinds of charged particles, namely protons and α particles.

The populations are labeled as $P_{i,j}$ with i being the number of evaporated neutrons and j that of protons. To keep a triangular form (namely an initial nucleus starting at the top, with the residual nuclei that are placed at each level according to their neutrons and proton

numbers), the populations are ordered following the number of evaporated nucleons, starting with neutrons. Similar time-dependent differential equations including the evaporation of charged particles can thus be written down without any difficulty. The first ones are given by

$$
\begin{aligned}
\frac{\mathrm{d}P_{0,0}}{\mathrm{d}t} &= -\Gamma^{0,0}_{\mathrm{tot}} P_{0,0} \quad \text{with} \quad P_{0,0}(0) = 1, \\
\frac{\mathrm{d}P_{1,0}}{\mathrm{d}t} &= \Gamma^{0,0}_{n} P_{0,0} - \Gamma^{1,0}_{\mathrm{tot}} P_{1,0} \quad \text{with} \quad P_{1,0}(0) = 0, \\
\frac{\mathrm{d}P_{0,1}}{\mathrm{d}t} &= \Gamma^{0,0}_{p} P_{0,0} - \Gamma^{0,1}_{\mathrm{tot}} P_{0,1} \quad \text{with} \quad P_{0,1}(0) = 0, \\
\frac{\mathrm{d}P_{2,0}}{\mathrm{d}t} &= \Gamma^{1,0}_{n} P_{1,0} - \Gamma^{2,0}_{\mathrm{tot}} P_{2,0} \quad \text{with} \quad P_{2,0}(0) = 0, \\
\frac{\mathrm{d}P_{1,1}}{\mathrm{d}t} &= \Gamma^{0,1}_{n} P_{0,1} + \Gamma^{1,0}_{p} P_{1,0} - \Gamma^{1,1}_{\mathrm{tot}} P_{1,1} \quad \text{with} \quad P_{1,1}(0) = 0, \\
\frac{\mathrm{d}P_{0,2}}{\mathrm{d}t} &= \Gamma^{0,1}_{p} P_{0,1} - \Gamma^{0,2}_{\mathrm{tot}} P_{0,2} \quad \text{with} \quad P_{0,2}(0) = 0, \\
&\vdots \\
\frac{\mathrm{d}P_{2,2}}{\mathrm{d}t} &= \Gamma^{2,1}_{p} P_{2,1} + \Gamma^{1,2}_{n} P_{1,2} + \Gamma^{0,0}_{\alpha} P_{0,0} - \Gamma^{2,2}_{\mathrm{tot}} P_{2,2} \quad \text{with} \quad P_{2,2}(0) = 0, \\
&\vdots
\end{aligned}
\tag{V.9}
$$

Here $\Gamma^{i,j}_{\mathrm{tot}}$ refers to the total decay width of the residual nucleus after evaporating i neutrons and j protons. Other Γ's are respectively the particle-evaporation and fission-decay widths according to their subscripts.

The population of each decaying nucleus corresponds to the sum of the single chains over all possible paths. For instance, considering the neutron and proton evaporations, we have $(i+j)!/(i!j!)$ possible paths from the initial nucleus $(0,0)$ to (i,j). Using the same Laplace transform technique, one ends up with a general formula that is of course the sum of the single-chain terms over all possible paths. Indeed, the linearity of the Bateman equations enables tracing of interconnected chains by manually accumulating results from separate calculations of single decay chains. This general property would also be valid for the calculated observables. It is then possible to collect similar terms together at each step, but this can surely make formulas much more complicated. As mentioned in Ref. [102], the complexity of calculations is eventually due to the multi-channel scheme, but not to the dynamics that can be exactly implemented. In the KEWPIE2 code, the statistical observables are directly computed with the help of a specially-designed algorithm without solving the time-dependent equations.

V.2.3 Numerical scheme

The numerical implementation is briefly discussed in this subsection. For the sake of simplicity, we only focus upon the scheme for a single cascade-decay chain. It can be then ex-

tended to a multi-channel cascade decay in a similar way. One of the most essential features of the KEWPIE2 code is that the energy spectra of produced nuclei and their angular-momentum distributions (when the Hauser-Feshbach formalism is chosen) are completely calculated and processed. In our case, Monte-Carlo methods might not be suitable, since we are mainly interested in a tiny fraction of events leading to the formation of heavy or super-heavy nuclei.

Discretization of the population spectrum

Supposing that one has a mother nucleus labeled with n. Its population spectrum $S_n(E_n^*, J_n)$, which is a function of the excitation energy E_n^* and angular momentum J_n, can be discretized into N and M bins, respectively. The normalization condition results in

$$\begin{aligned} P_n &= \sum_{J_n} \int_0^{+\infty} S_n(E_n^*, J_n)\, \mathrm{d}E_n^* \\ &= \sum_{j'}^{N} \sum_{k'}^{M} S_n(j', k'). \end{aligned} \tag{V.10}$$

Regarding the daughter nucleus, the spectral bin (j,k) corresponding to the excitation energy E_{n+1}^* and angular momentum J_{n+1} is thus fed by

$$\delta S_{n+1}(j,k) = \sum_{J_n} \int_0^{+\infty} \mathrm{d}E_n^*\, S_n(E_n^*, J_n) \frac{\gamma(E_n^* \rightarrow E_{n+1}^*, J_n)}{\Gamma_{\mathrm{tot}}^n}, \tag{V.11}$$

where the total decay width Γ_{tot}^n has already been integrated over the whole range of excitation energies. The function $\gamma(E_n^* \rightarrow E_{n+1}^*, J_n)$ is proportional to $\rho(E_{n+1}^*)/\rho(E_n^*)$ with ρ being the state density. It is closely related to the partial-decay width $\Gamma_\nu(E_n^*, J_n)$ (cf. Sections V.3 and V.4) by

$$\Gamma_\nu(E_n^*, J_n) = \int_{V_c}^{E_n^* - S_\nu} \mathrm{d}\epsilon_\nu\, \gamma(E_n^* \rightarrow E_{n+1}^*, J_n), \tag{V.12}$$

where ϵ_ν is the kinetic energy of the emitted particle labeled by ν and S_ν the corresponding particle-separation energy. V_c denotes the Coulomb barrier between the daughter nucleus and the emitted particle. The spectrum of the daughter nucleus S_{n+1} is thus increased by δS_{n+1} and should again be normalized to its population, namely

$$P_{n+1} = \sum_{j'}^{N} \sum_{k'}^{M} S_{n+1}(j', k'). \tag{V.13}$$

Fig. V.2 illustrates a typical two-dimensional spectrum of the daughter nucleus. At the beginning of this decay chain, the spectrum of a mother nucleus has been normalized and is then depleted through the nuclear disintegration towards its daughter nucleus, whose population spectrum is again served as an input for the next step of the cascade, and so forth. In practice, the spectrum of each residual nucleus can be computed by means of the spectral discretization method, which consists in dividing the whole spectrum into a number of energy

bins of 0.1 MeV, which can be adjusted by the user, as well as a number of angular moment bins, which is limited by the maximum spin of the compound nucleus.

Time resolution

The method described above can be improved to take into account the time evolution. In this case, at a time t_i, the normalization condition (cf. Eq. (V.10)) becomes

$$P_n(t_i) = \sum_j^N \sum_k^M S_n(t_i, j, k). \tag{V.14}$$

During a time interval of δt_i, because of the disintegration of the mother nuclei, the population of its daughter P_{n+1} continuously rises. At a given excitation energy E_n^*, this feeding term is simply expressed as $P_n(t_i)N_n^i$ with

$$N_n^i = \frac{\Gamma_\nu}{\Gamma_{\rm tot}^n}\left[1 - \exp(-\Gamma_{\rm tot}^n \delta t_i)\right]. \tag{V.15}$$

At the same time, this population exponentially declines, namely $P_{n+1}(t_i + \delta t_i) = P_{n+1}(t_i)D_{n+1}^i$ with $D_{n+1}^i = e^{-\Gamma_{\rm tot}^{n+1}\delta t_i}$. Finally, the iterative equation for the population P_{n+1} reads

$$P_{n+1}(t_i + \delta t_i) = P_{n+1}(t_i)D_{n+1}^i + P_n(t_i)N_n^i. \tag{V.16}$$

When the population spectrum is taken into account, the time dependence is obtained by means of Eq. (V.11), which gives

$$\begin{aligned}\delta S_{n+1}(t_i + \delta t_i, j', k') = &\sum_{J_n} \int_0^{+\infty} {\rm d}E_n^*\, S_n(t_i, E_n^*, J_n) \\ &\times \frac{\gamma(E_n^* \to E_{n+1}^*, J_n)}{\Gamma_{\rm tot}^n} \\ &\times \left[1 - \exp(-\Gamma_{\rm tot}^n \delta t_i)\right].\end{aligned} \tag{V.17}$$

In principle, the approach described above can be readily generalized to the multi-channel situation, but the representation would get much more complicated. Anyhow, this issue can be handled within the same framework. One can calculate the number of nuclei undergoing fission at each step by looking at the quantity $P_n(t_i)F_n^i$ with $F_n^i = \Gamma_f^n/\Gamma_{\rm tot}^n(1 - e^{-\Gamma_{\rm tot}^n \delta t_i})$ for each nucleus n at time t_i. The average fission time or other dynamical observables can be similarly deduced with a discretized version of Eq. (V.8). On the basis of this approach, one would be able to solve more sophisticated dynamics including γ-ray emission or a transient time during which the fission rate is considerably reduced.

It should be mentioned that the calculation of dynamical variables is often quite time-consuming, owing to the fact that the dynamical decay is a relatively slow process that usually spans several orders of magnitude on the time scale. To solve this issue, we have introduced

an increasing time step, namely $\delta t_{i+1} = \theta \delta t_i$. The parameter θ is employed to enlarge the time step along the cascade, and thus the whole process evolves at very different time scales. The optimum value for the parameter θ was tested and has been set equal to 1.1 by default, which might lead to a relative error of about 10% (result tested for single neutron evaporation). The initial value δt_0 was fixed at 0.01 $\hbar$/MeV.

The calculational examples on the dynamical observables, such as the fission-time distribution and average fission time are shown in Refs. [99, 100]. It should be stressed that, in the present study, only the statistical part will be employed to estimate the survival probability.

V.3 Light-particle evaporation and γ-ray emission

V.3.1 Detailed balance

From this section, we shall focus on the physical ingredients involved in the KEWPIE2 code. The capture step has been discussed in the previous chapter, so we start with the last step, namely the disintegration of excited nuclei.

Let us now consider a de-excitation process that can be illustrated as follows:

$$C^* \longrightarrow \underbrace{B + b}_{\beta'},$$

where β' denotes a specified exit channel and the whole process is assumed to take place within a finite region characterized by a certain volume $\mathcal{V}$. The total kinetic energy of the exit channel in the centre-of-mass frame is simply given by $\epsilon_{\beta'} = \mu_{\beta'} v_b^2/2$, where v_b represents the velocity of b relative to B. The reduced mass of the binary system is denoted by $\mu_{\beta'}$, namely $\mu_{\beta'} = m_b m_B/(m_b + m_B)$.

According to the reciprocity theorem [109], the decay rate $R_{C^* \to B+b}$ is related to its time-reversed decay rate $R_{b+B \to C^*}$ by

$$R_{C^* \to B+b} = R_{b+B \to C^*} \frac{\rho_{\beta'}(E_{\beta'})}{\rho_C(E_C^*)}, \tag{V.18}$$

where $E_{\beta'}$ represents the total energy of the binary system in the centre-of-mass frame, which is simply given by $E_{\beta'} = \epsilon_{\beta'} + E_B^* = E_C^* - S_b$ with S_b being the separation energy of the emitted particle. $\rho_{\beta'}(E_{\beta'})$ corresponds to the total state density of the binary system obtained by convolution. Thus, one gets the following expression for the decay width:

$$\frac{\Gamma_b}{\hbar} = \frac{\rho_{\beta'}(E_{\beta'})}{\rho_C(E_C^*)} R_{b+B \to C^*} = \frac{\rho_{\beta'}(E_{\beta'})}{\rho_C(E_C^*)} \frac{v_b}{\mathcal{V}} \sigma_{\text{inv}}^b, \tag{V.19}$$

where σ_{inv}^b denotes the time-reversed cross-section. Here, the spin degeneracy of the emitted particle $2s_b + 1$ has been considered in the combined state density $\rho_{\beta'}(E_{\beta'})$.

V.3.2 Weisskopf-Ewing model

With Eq. (V.19), one obtains the following well-known formula [109, 110, 136]:

$$\Gamma_b(E_C^*) = \frac{(2s_b+1)\mu_{\beta'}}{\pi^2\hbar^2}\int_{V_c}^{\epsilon_b^{\max}} \frac{\sigma_{\rm inv}^b(\epsilon_{\beta'})\rho_B(E_B^*)}{\rho_C(E_C^*)}\epsilon_{\beta'}{\rm d}\epsilon_{\beta'}, \tag{V.20}$$

where V_c denotes the Coulomb barrier, which is equal to zero for neutrons, and s_b refers to the spin of the emitted particle. The upper limit for the integral $\epsilon_{\beta'}^{\max}$ is taken to be $E_C^* - S_b$. In the case of neutrons, the cross section for the time-reversed reaction is given by [137]

$$\sigma_{\rm inv}^b(\epsilon_{\beta'}) = g_0(1+\frac{g_1}{\epsilon_{\beta'}})\pi\tilde{R}^2, \tag{V.21}$$

where $g_0 = 0.76 + 1.93A_B^{-1/3}$, $g_0 g_1 = 1.66A_B^{-2/3} - 0.05$ and $\tilde{R} = 1.7A_B^{1/3}$ fm. For charged particles, one has [138]

$$\sigma_{\rm inv}^b(\epsilon_{\beta'}) = (1-\frac{V_c}{\epsilon_{\beta'}})\pi\tilde{R}^2, \tag{V.22}$$

with $\tilde{R} = r_0A_B^{1/3} + R_b$, $r_0 = 1.42$ fm and $V_c = Z_bZ_Be^2/(r_eA_B^{1/3} + R_b)$. For protons, $R_b = 1.44$ fm and $r_e = 1.81$ fm. For α particles, $R_b = 2.53$ fm and $r_e = 2.452 - 0.408\log_{10}(Z_bZ_B)$ fm. Here A_B and Z_B correspond to the mass and charge of the daughter nucleus B, respectively.

V.3.3 Hauser-Feshbach formalism

So far, we have ignored the spin degree of freedom. To incorporate it, one needs to rewrite the reciprocity theorem (cf. Eq. (V.19)) in the following form:

$$\frac{\Gamma_b}{\hbar} = \frac{(2s_B+1)\,\rho_{B+b}(E_{\beta'},s_B)}{(2J_C+1)\,\rho_C(E_C^*,J_C)}\frac{v_b}{V}\sigma_{\rm inv}^b. \tag{V.23}$$

Moreover, within the Hauser-Feshbach formalism [111], $\sigma_{\rm inv}^b$ can be evaluated as follows:

$$\sigma_{\rm inv}^b = \frac{\pi}{k^2}\frac{2J_C+1}{(2s_b+1)(2s_B+1)}\sum_{s_{\beta'}=|s_B-s_b|}^{s_B+s_b}\sum_{l_{\beta'}=|J_C-s_{\beta'}|}^{J_C+s_{\beta'}} T_{l_{\beta'}}(\epsilon_b), \tag{V.24}$$

where the channel spin is denoted by $\overrightarrow{s_{\beta'}} = \overrightarrow{s_B} + \overrightarrow{s_b}$ and the total orbital angular momentum in the centre-of-mass frame by $\overrightarrow{l_{\beta'}}$. Substituting Eq. (V.24) into Eq. (V.23) and integrating over all possible kinetic energies, a generalized expression is obtained for the partial decay width, which reads

$$\begin{aligned}\Gamma_b(E_C^*,J_C;s_B) = \int_0^{\epsilon_{\beta'}^{\max}} &\sum_{s_{\beta'}=|s_B-s_b|}^{s_B+s_b}\sum_{l_{\beta'}=|J_C-s_{\beta'}|}^{J_C+s_{\beta'}}\rho_B(E_B^*,s_B)\\ &\times\frac{T_{l_{\beta'}}(\epsilon_{\beta'}){\rm d}\epsilon_{\beta'}}{2\pi\rho_C(E_C^*,J_C)}.\end{aligned} \tag{V.25}$$

Finally, after summing over all possible values of the spin s_B, one obtains

$$\Gamma_b(E_C^*, J_C) = \int_0^{\epsilon_{\beta'}^{\max}} \sum_{s_B} \sum_{s_{\beta'}=|s_B-s_b|}^{s_B+s_b} \sum_{l_{\beta'}=|J_C-s_{\beta'}|}^{J_C+s_{\beta'}} \rho_B(E_B^*, s_B) \times \frac{T_{l_{\beta'}}(\epsilon_{\beta'})\mathrm{d}\epsilon_{\beta'}}{2\pi\rho_C(E_C^*, J_C)}. \tag{V.26}$$

In obtaining Eq. (V.26), one first couples the spin vectors $\overrightarrow{s_B}$ and $\overrightarrow{s_b}$ to form $\overrightarrow{s_{\beta'}}$, which is followed by coupling of $\overrightarrow{l_{\beta'}}$ and $\overrightarrow{s_{\beta'}}$ to generate the total angular momentum $\overrightarrow{J_C}$. This is just a matter of choice. In the KEWPIE2 code, we adopt another procedure that is, coupling of $\overrightarrow{s_b}$ and $\overrightarrow{l_{\beta'}}$ to form $\overrightarrow{j_b}$, and then combining with $\overrightarrow{s_B}$ to generate the spin vector of the compound nucleus $\overrightarrow{J_C}$. In that case, one obtains a similar formula for the particle-evaporation width,

$$\Gamma_b(E_C^*, J_C) = \int_0^{\epsilon_{\beta'}^{\max}} \sum_{l_{\beta'}=0}^{l_{\beta'}^{\max}} \sum_{j_b=|l_{\beta'}-s_b|}^{l_{\beta'}+s_b} \sum_{s_B=|J_C-j_b|}^{J_C+j_b} \rho_B(E_B^*, s_B) \times \frac{T_{l_{\beta'},j_b}(\epsilon_{\beta'})\mathrm{d}\epsilon_{\beta'}}{2\pi\rho_C(E_C^*, J_C)}. \tag{V.27}$$

Note that the summation over $l_{\beta'}$ terminates as long as the transmission coefficient vanishes, namely at the upper limit $l_{\beta'}^{\max}$. Such a scheme, which has been incorporated into the current version of the code, would be more suitable when the spin-orbit interaction is considered in the nuclear optical potential. In this case, as seen in Eq. (V.27), the transmission coefficient $T_{l_{\beta'},j_b}$ should be dependent on both $l_{\beta'}$ and j_b.

Optical potential

In the previous version of the code, the Becchetti-Greenless [139] and Wilmore-Hodgson [140] empirical optical-potential parameterizations were introduced for incident neutrons and protons, respectively. However, they were both developed during the 1960s and since then, there have been many important advances in our understanding of the nuclear optical potential. Furthermore, more accurate data for scattering cross-sections have become available and the computational ability to optimize models parameters has been largely improved. Based upon these considerations, a new optical parameterization proposed by Varner *et al.* [141] has been included in the current version of the code for both protons and neutrons. In this model, the local optical potential for nucleon-nucleus scattering is expressed as

$$\begin{aligned} V_{\mathrm{opt}}(r) = &-V_r f_{\mathrm{ws}}(r, R_0, a_0) - iW_v f_{\mathrm{ws}}(r, R_w, a_w) \\ &- iW_s(-4a_w)\frac{\mathrm{d}}{\mathrm{d}r} f_{\mathrm{ws}}(r, R_w, a_w) \\ &+ \frac{\lambda\!\!\!^{-2}_{\pi}\,\overrightarrow{\sigma}\cdot\overrightarrow{l_{\beta'}}}{r}(V_{\mathrm{so}} + iW_{\mathrm{so}})\frac{\mathrm{d}}{\mathrm{d}r} f_{\mathrm{ws}}(r, R_{\mathrm{so}}, a_{\mathrm{so}}), \end{aligned} \tag{V.28}$$

with $\lambda\!\!\!^{-2}_{\pi} = 2$ fm^2 and

$$f_{\rm ws}(r,R,a) = \frac{1}{1+\exp\left(\dfrac{r-R}{a}\right)}. \tag{V.29}$$

The Coulomb potential for the emission of protons is simply given by

$$V_c = \begin{cases} \dfrac{Z_B e^2}{r}, & \text{for } r \geq R_c, \\ \dfrac{Z_B e^2}{2R_c}\left(3 - \dfrac{r^2}{R_c^2}\right), & \text{for } 0 \leq r \leq R_c, \end{cases} \tag{V.30}$$

where R_c represents the Coulomb radius. As for the parameters involved within this parameterization, the reader is referred to [141]. In addition, another more recent optical potential [142], which is valid for both neutrons and protons with incident energies from 1 keV up to 200 MeV, has also been included in the code.

Then, let us take a look at α particles, whose optical potential is taken to be

$$\begin{aligned} V_{\rm opt}(r) = &- \left[(c_0 + c_1 \frac{Z_B}{A_B^{1/3}} + c_2 E_\alpha) f_{\rm ws}(r, r_v, a_v) \right] \\ &- i \left[(c_0' + c_1' A_B^{1/3} + c_2' E_\alpha) f_{\rm ws}(r, r_w, a_w) \right], \end{aligned} \tag{V.31}$$

and the diffuseness parameters are given by

$$\begin{aligned} a_v &= d_0 + d_1 A_B^{1/3}, \\ a_w &= d_0' + d_1' A_B^{1/3}. \end{aligned} \tag{V.32}$$

The best-fit values of these parameters, which were obtained by optimizing the χ^2 function for the scattering data at energies above 80 MeV, can be found in Ref. [143]. It should be noted that this parameterization has been extended to lower energies by Avrigeanu *et al.* [144].

Transmission coefficient

The usual procedure to calculate the transmission coefficient $T_{l_{\beta'}, j_b}(\epsilon_{\beta'})$ consists in solving numerically the Schrödinger equation, which reads

$$\left\{ \frac{{\rm d}^2}{{\rm d}r^2} - \frac{l_{\beta'}(l_{\beta'}+1)}{r^2} - \frac{2\mu_{\beta'}}{\hbar^2}[V_c(r) + V_{\rm opt}(r) - E_{\rm cm}] \right\} u(r) = 0, \tag{V.33}$$

from $r = 0$ to infinity by means of the modified Numerov method. The computation time is mainly dependent on the step-size Δr for the numerical integration and the maximal distance $R_{\rm max}$ that is much larger than the range of the nuclear interaction so as to match the solutions of Eq. (V.33) to the Coulomb functions. Their default values have been chosen to be 0.05 fm and 50 fm, respectively. Special attention should be drawn to the case of nucleons, both of which have a spin $s_b = 1/2$. Hence, for each $l_{\beta'}$, one has two eigenstates for j_b, namely

$l_{\beta'} - 1/2$ and $l_{\beta'} + 1/2$, as a result of the spin-orbit coupling. This has actually been considered in Eq. (V.28), where the coupling term $\vec{\sigma} \cdot \vec{l_{\beta'}}$ can be rewritten in terms of $\vec{j_b}$ and $\vec{l_{\beta'}}$ as follows:

$$\vec{\sigma} \cdot \vec{l_{\beta'}} = j_b(j_b+1) - l_{\beta'}(1+l_{\beta'}) - 3/4, \tag{V.34}$$

where $\vec{\sigma}$ denotes the Pauli matrix. By making use of this definition, the transmission coefficient $T_{l_{\beta'},j_b}$ appearing in Eq. (V.27) is automatically computed at each iteration.

Finally, as pointed out by Alexander *et al.* [145], the transmission coefficient obtained from the optical model would not be appropriate for treating the evaporation of light particles. Indeed, statistical-model calculations are only concerned with the evaporation of a particle from an excited nucleus or its time-reversed process, namely absorption, whereas usual optical-potential models also comprise other effects related to inelastic scattering, size resonances, etc. As a consequence, the transmission coefficient might not approach unity at energies well above the barrier (transparency effect). To ensure a full absorption within the potential well (elimination of other effects), as discussed in Ref. [145], one only needs to keep the real part of the optical potential and the incoming-wave boundary condition (IWBC) [146] is thus applied to estimating the transmission coefficient $T_{l_{\beta'},j_b}$. In our case, the IWBC would be crucial for both neutrons and protons, but appears slightly less important for α particles because they already experience strong absorption inside the Coulomb barrier.

Fig. V.3 shows a comparison between the transmission coefficients calculated within the optical and IWBC models. It is readily observed that, under the IWBC, the transmission coefficient gradually tends to unity. For more details on the implementation of the IWBC in the code, the reader is referred to Ref. [100]. Fig. V.4 illustrates a comparison of the WE and HF models for a typical calculation of production cross-sections. A good agreement has been demonstrated in the case where only neutrons are evaporated from the mother nucleus.

V.3.4 γ-ray emission

Apart from the evaporation of light particles, the residual nucleus can also emit γ rays. Basically, the γ-ray emission would be dominant when the excitation energy becomes lower than both the fission and particle-evaporation thresholds. In the case of very-heavy and super-heavy nuclei, since the fission barrier could be much smaller than the particle-evaporation threshold, the competition between γ-ray emission and fission would be essential at low excitation energies. Moreover, some recent studies [105, 147] showed that the distribution of spin and excitation energy of the residual nucleus, which results from the γ-ray emission, can be employed to explore fission barrier in heavy nuclei.

By analogy with the Hauser-Feshbach formalism, the γ-decay width is defined as

$$\Gamma_\gamma(E_C^*, J_C) = \int_0^{E_C^*} \sum_\lambda \sum_{s_B=|J_C-\lambda|}^{J_C+\lambda} \rho_B(E_C^* - \epsilon_\gamma, s_B) \times \frac{T_{X\lambda}(\epsilon_\gamma)\mathrm{d}\epsilon_\gamma}{2\pi\rho_C(E_C^*, J_C)}, \tag{V.35}$$

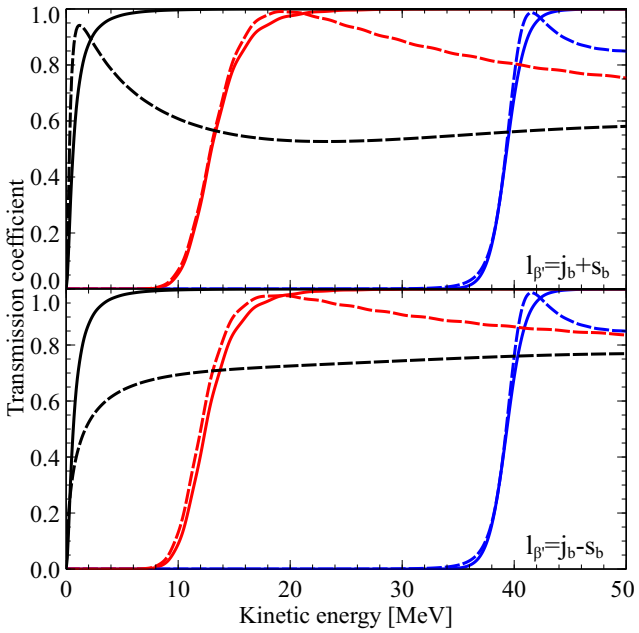

Figure V.3 – Comparison of the calculated transmission coefficients based upon the optical and IWBC models as a function of the kinetic energy of the emitted particle in the centre-of-mass frame. The solid and dashed curves (black for neutrons, red for protons and blue for α particles) correspond to the calculations performed with the IWBC and optical models, respectively. Here, the mother nucleus is ^{243}Cm and $j_b = 1$. Two spin-orbit components have been shown ($s_b = 1/2$ for neutrons and protons, $s_b = 0$ for α particles.).

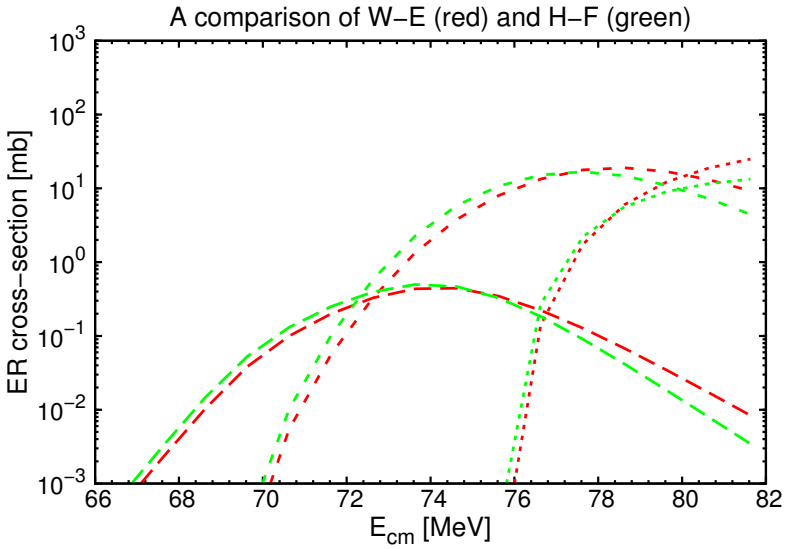

Figure V.4 – Comparison of the ER cross-sections for 2n-, 3n- and 4n-channels (from left to right) calculated with the help of two evaporation models. The red dashed curve is the result based upon the Weiskopf-Ewing model and the green one based upon the Hauser-Feshbach model.

where $T_{X\lambda}$ stands for the transmission coefficient for the γ decay of type X (electric or magnetic transition), which reads

$$T_{X\lambda}(\epsilon_\gamma) = 2\pi\epsilon_\gamma^{2\lambda+1} f_{X\lambda}(\epsilon_\gamma), \tag{V.36}$$

with λ being the multi-polarity and $f_{X\lambda}(\epsilon_\gamma)$ the radiative strength function.

Traditional methods of estimating radiative strength functions are usually based upon the Weisskopf single-particle model [148]. Nevertheless, the nuclear-structure effects are known to modify the Weisskopf estimates by introducing an enhancement factor up to two or three orders of magnitude. Fortunately, one can make great improvements on this issue with the help of the Brink-Axel hypothesis [149, 150], which states that, at energies around the resonance, the radiative strength function is assumed to have a Lorentzian-like line shape. Within this framework, the radiative strength function is generally expressed as

$$f_{X\lambda}^{\mathrm{SLO}}(\epsilon_\gamma) = \frac{26\times10^{-8}}{2\lambda+1} \times \sigma_r\Gamma_r\epsilon_\gamma^{3-2\lambda} \frac{\Gamma_r}{(\epsilon_\gamma^2 - E_r^2)^2 + \epsilon_\gamma^2\Gamma_r^2}, \tag{V.37}$$

where σ_r and E_r respectively correspond to the cross-section and energy of giant-dipole resonance, and the resonance width Γ_r is considered to be constant. The unit of the strength function is MeV^{-3}. Eq. (V.37) is usually called the Standard Lorentzian model (SLO) and has largely been employed for fitting to experimental data.

The γ-ray emission plays a crucial role in the fission-time calculations. Accordingly, some recent parameterizations based upon the SLO for calculating the radiative strength function have been taken into consideration in our model and will be briefly introduced in this subsection.

E1 strength function

It is well known that the γ-decay strength function is mainly governed by the giant dipole resonance. An improved version of the SLO, known as the Enhanced Generalized Lorentzian model (EGLO), was proposed in Ref. [151] for the calculation of the E1 strength function, namely

$$f_{E1}^{\mathrm{EGLO}}(\epsilon_\gamma) = 8.674\cdot10^{-8} \times \sigma_r\Gamma_r \times \left[\frac{\epsilon_\gamma\Gamma_K(\epsilon_\gamma, T_f)}{(\epsilon_\gamma^2 - E_r^2)^2 + \epsilon_\gamma^2\Gamma_K^2(\epsilon_\gamma, T_f)} + \frac{0.7\Gamma_K(\epsilon_\gamma, T_f)|_{\epsilon_\gamma=0}}{E_r^3} \right], \tag{V.38}$$

where the energy-dependent collisional width $\Gamma_K(\epsilon_\gamma, T_f)$ is given by

$$\Gamma_K(\epsilon_\gamma, T_f) = \chi(\epsilon_\gamma)\frac{\Gamma_r}{E_r^2}\left[\epsilon_\gamma^2 + (2\pi T_f)^2\right], \tag{V.39}$$

which is assumed to be proportional to an empirical function $\chi_\gamma(\epsilon_\gamma)$ that is defined as

$$\chi(\epsilon_\gamma) = \tau + (1-\tau)\frac{\epsilon_\gamma - \epsilon_0}{E_r - \epsilon_0}, \tag{V.40}$$

where the factor τ is dependent on the model employed to describe the nuclear state density, whereas ϵ_0 is kept fixed at 4.5 MeV. In our model, we adopt the following parameterization [152] for τ:

$$\tau = \begin{cases} 1, & A_C < 148, \\ 1 + 0.09(A_C - 148)^2 \exp\left[-0.18(A_C - 148)\right], & A_C \geq 148. \end{cases} \tag{V.41}$$

Recalling that A_C corresponds to the mass number of the compound nucleus. In the above formulas, T_f represents the nuclear temperature of the final state, which is closely related to the excitation energy of the residual nucleus. Within the back-shifted Fermi-gas model, it can be approximately estimated as follows:

$$T_f = \sqrt{\frac{E_C^* - \Delta_{\text{pair}} - \epsilon_\gamma}{a(E_C^* - \Delta_{\text{pair}})}}, \tag{V.42}$$

where Δ_{pair} denotes the paring energy and $a(E_C^* - \Delta_{\text{pair}})$ the energy-dependent level-density parameter (cf. Section V.5).

However, the EGLO expression for the γ-decay strength function contradicts some aspects of microscopic theoretical studies [153–155]. Particularly, it has been established that the shape of the γ-decay strength function is not consistent with the nuclear linear response theory for heated nuclei. This drawback was approximately avoided in some recent studies [129, 130], where a new closed-form formula that is referred to as the Modified Lorentzian model (MLO) was proposed, namely

$$f_{E1}^{\text{MLO}}(\epsilon_\gamma) = 8.674 \cdot 10^{-8} \sigma_r \Gamma_r \Lambda(\epsilon_\gamma, T_f) \frac{\epsilon_\gamma \Gamma(\epsilon_\gamma, T_f)}{(\epsilon_\gamma^2 - E_r^2)^2 + \epsilon_\gamma^2 \Gamma^2(\epsilon_\gamma, T_f)}, \tag{V.43}$$

where $\Lambda(\epsilon_\gamma, T_f)$ refers to the scaling factor that reflects the enhancement of the strength function in the warm nuclei, which is usually defined as

$$\Lambda(\epsilon_\gamma, T_f) = 1/[1 - \exp(-\epsilon_\gamma / T_f)]. \tag{V.44}$$

Regarding the width function $\Gamma(\epsilon_\gamma, T_f)$, different semi-empirical expressions have been introduced in the MLO approach (MLO1, MLO2, MLO3), but obviously they should be in close agreement. In the KEWPIE2 code, we adopt the simplified version of the MLO model, namely the SMLO, which would be preferable due to its simple numerical implementation. More concretely, the energy-dependent width $\Gamma(\epsilon_\gamma, T_f)$ within this model simply reads $\Gamma_r E_C^* / E_r$.

In Refs. [156, 157], a new parameterization for σ_r, E_r and Γ_r appearing in Eqs. (V.38) and (V.43) was proposed. It can be summarized as follows:

$$\begin{aligned} E_r &= a_1(1 + b_1 I_C^2) A_C^{-1/3} + a_2(1 + b_2 I_C^2) A_C^{-1/6} \text{ MeV}, \\ \Gamma_r &= a_3 E_r^\delta \text{ MeV}, \\ S_r &= \pi \sigma_r \Gamma_r / 2 = 60 a_4 N_C Z_C / A_C \text{ mb} \cdot \text{MeV}, \end{aligned} \tag{V.45}$$

where I_C corresponds to the relative neutron excess of the compound nucleus, namely $I_C = (A_C - 2Z_C)/A_C$. Note that this might only be valid for spherical nuclei. For axially deformed nuclei, the $E1$ strength function can be expressed as the sum of two components, namely $(E_{r,1}, \Gamma_{r,1}, \sigma_{r,1})$ and $(E_{r,2}, \Gamma_{r,2}, \sigma_{r,2})$, which result from the collective motion along and perpendicular to the axis of symmetry, respectively. In practice, one can employ the following parametrization [152, 158]:

$$\begin{aligned} E_{r,1} &= E_{r,2}/(0.911 a_0/b_0 + 0.089), \\ E_{r,2} &= E_r \left[1 - 1.51 \times 10^{-2} (a_0^2 - b_0^2)\right], \\ \Gamma_{r,1} &= 0.026 E_{r,1}^{1.91}, \ \Gamma_{r,2} = 0.026 E_{r,2}^{1.91}, \\ \sigma_{r,1} &= \sigma_r/3, \ \sigma_{r,2} = 2\sigma_r/3, \end{aligned} \tag{V.46}$$

where E_r, Γ_r, and σ_r can be evaluated from Eq. (V.45). Here a_0 and b_0 denote the relative semi-axes of a spheroid that are related to the quadrupole deformation parameter β_2 by $a_0 = (1+\alpha_2)/\lambda$ and $b_0 = (1-0.5\alpha_2)/\lambda$ with $\beta_2 = \sqrt{4\pi/5}\alpha_2$, respectively. λ is expressed in terms of α_2, namely $\lambda^3 = 1 + 3\alpha_2^2/5 + 2\alpha_2^3/35$. The quadrupole deformation parameter β_2 is given in Ref. [15].

In the KEWPIE2 code, both the EGLO and SMLO approaches have been taken into account. The parameter values are summarized as follows:

- For EGLO, one has $\delta = 1.91$, $a_1 = 27.469 \pm 0.009$, $a_2 = 22.063 \pm 0.004$, $a_3 = 0.026\,91 \pm 0.000\,04$ and $a_4 = 1.222\,4 \pm 0.001\,9$. b_1 and b_2 are both taken to be 0.0.
- For SMLO, one has $\delta = 1.0$, $a_1 = 28.69 \pm 0.01$, $a_2 = 21.731 \pm 0.004$, $a_3 = 0.330\,78 \pm 0.000\,47$ and $a_4 = 1.266\,9 \pm 0.002\,1$. b_1 and b_2 are both taken to be 0.0.

The comparison of the calculated $E1$ strength functions based upon the EGLO and SMLO models is shown in Fig. V.5. In this example, the SMLO model seems a bit closer to the measured data.

E2 and M1 strength functions

As regards other higher-order γ-ray emissions, such as the $E2$ and $M1$ transitions, we adopt the SLO form (cf. Eq. (V.37)), as recommended in Ref. [152]. The default parameter values are given by

$$E_r = 63 A_C^{-1/3}\ \text{MeV},\ \Gamma_r = 6.11 - 0.012 A_C\ \text{MeV},\ \sigma_r = 1.5 \times 10^{-4} \frac{Z_C^2 E_r^2}{A_C^{1/3} \Gamma_r}\ \text{mb} \tag{V.47}$$

for $E2$ emission and by

$$E_r = 41 A_C^{-1/3}\ \text{MeV},\ \Gamma_r = 4.0\ \text{MeV},\ \sigma_r = 1.0\ \text{mb} \tag{V.48}$$

for $M1$ emission, respectively.

It should be mentioned that higher-order emissions are generally much weaker than the giant-dipole one, which would be dominant in γ-decay width calculations. Typically, based upon the Weisskopf single-particle model, one has the following crude estimates of their orders of magnitude [120]:

$$\frac{f_{E(\lambda+1)}}{f_{E(\lambda)}} \simeq 3.7 \cdot 10^{-5} A_C^{2/3} \epsilon_\gamma^2 \left[\frac{3+\lambda}{5+\lambda}\right]^2 \tag{V.49}$$

and

$$\frac{f_{M(\lambda+1)}}{f_{E(\lambda+1)}} \simeq 0.307 A_C^{-2/3}. \tag{V.50}$$

V.4 Nuclear fission

Nuclear fission is the ruling decay channel of heavy and super-heavy nuclei. It basically competes with the emission of light particles and thus determines the survival probability of the residual nucleus. In the case of super-heavy nuclei, the fission-barrier height is usually lower than the particle-emission threshold. Compared with the evaporation process, nuclear fission is considered much more complicated to describe since large-amplitude collective deformations come into play.

In the KEWPIE2 code, the fission-decay width is estimated within the Bohr-Wheeler transition-state model [2]:

$$\Gamma_f^{\mathrm{BW}}(E_C^*, J_C) = \frac{1}{2\pi\rho_C^{\mathrm{gs}}(E_C^*, J_C)} \int_0^{E_{\mathrm{gs}}^* - B_f} \rho_C^{\mathrm{sd}}(E_{\mathrm{sd}}^*, J_C) \mathrm{d}\epsilon_f, \tag{V.51}$$

where the excitation energy at the saddle point E_{sd}^* is equal to $E_{\mathrm{C}}^* - B_f - \epsilon_f$. One could also introduce a penetration factor, namely $T_{\mathrm{fiss}}(\epsilon_f)$, which corresponds to the well-known Hill-Wheeler transmission coefficient [160]. It takes the following form:

$$T_{\mathrm{fiss}}(\epsilon_f) = \frac{1}{1 + \exp\left(-\dfrac{2\pi\epsilon_f}{\hbar\omega_{\mathrm{sd}}}\right)}, \tag{V.52}$$

where $\hbar\omega_{\mathrm{sd}}$ represents the potential curvature at the saddle point. The default value of $\hbar\omega_{\mathrm{sd}}$ has been fixed at 1.0 MeV, which can be adjusted by the user. By default, Eq. (V.51) is employed without the penetration factor.

From a dynamical point of view, the fission-decay width evaluated by Eq. (V.51) can be refined by introducing a correction factor [122], which reads

$$K = \sqrt{1 + \left(\frac{\beta}{2\omega_{\mathrm{sd}}}\right)^2} - \frac{\beta}{2\omega_{\mathrm{sd}}}, \tag{V.53}$$

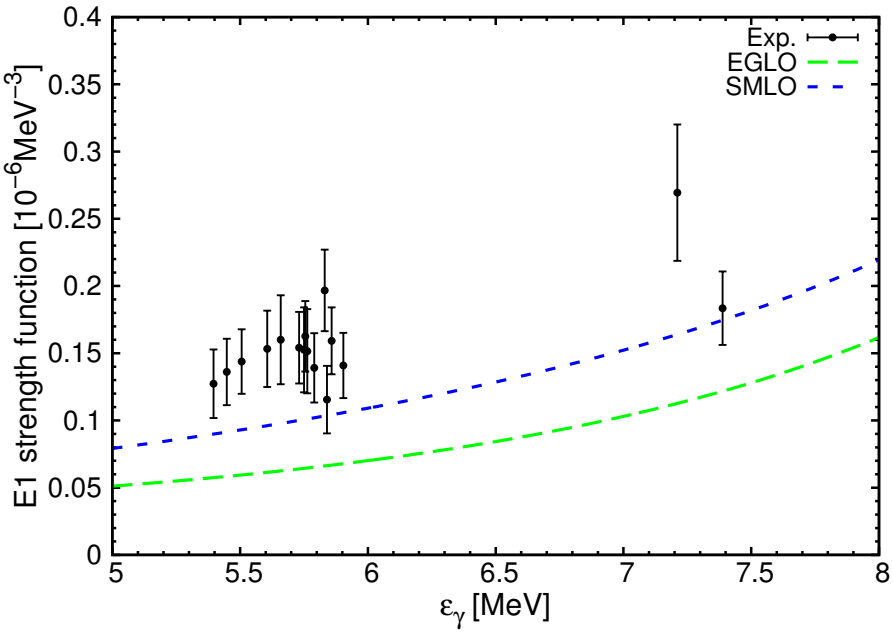

Figure V.5 – Comparison of the E1 radiative strength functions with the experimental measurements. The solid circles represent the measured data are taken from Ref. [159]. The blue dashed curve is the calculation based upon the SMLO model and the green one the calculation based upon the EGLO model.

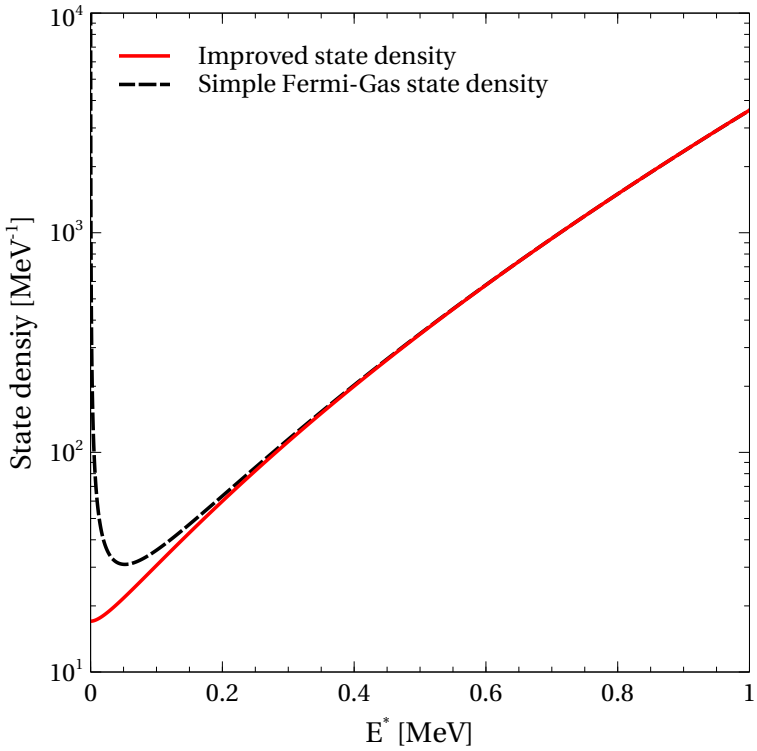

Figure V.6 – Comparison of Eq. (V.65) with the simple Fermi-Gas state-density formula (cf. Eq. (V.68)). The divergence at energies close to the origin has been well eliminated.

which takes into account the effect of viscosity on the fission process. Here β stands for the reduced friction parameter whose default value has been set to 5.0 zs^{-1}, which can be tuned by means of the input file. On the other hand, Strutinsky [161] first noticed that the difference in numbers of stationary collective states in the ground state and at the saddle point was erroneously ignored by Bohr and Wheeler. Hence, he suggested that the fission-decay width derived from the Bohr-Wheeler transition-state theory should be multiplied by

$$S = \frac{\hbar\omega_{\mathrm{gs}}}{T_{\mathrm{gs}}}, \tag{V.54}$$

where $\hbar\omega_{\mathrm{gs}}$ denotes the potential curvature in the ground state and is taken to be 1.0 MeV. T_{gs} stands for the nuclear temperature within the Fermi-gas model. Finally, the new combined fission-decay width is given by

$$\Gamma_f = K \cdot S \cdot \Gamma_f^{\mathrm{BW}}. \tag{V.55}$$

In the following study, the Kramers-Strutinsky factor will simply refer to the product $K \cdot S$.

V.4.1 Fission barrier

The fission-barrier height entering Eq. (V.51) can be approximated as

$$B_f = B_{\mathrm{LDM}} - \Delta E_{\mathrm{sh}}, \tag{V.56}$$

where B_{LDM} is the liquid-drop fission barrier and ΔE_{sh} the ground-state shell-correction energy. It is assumed here that ΔE_{sh} practically vanishes at saddle point as a consequence of the so-called topographical theorem [162].

Shell-correction energy

By default, the shell-correction energy is taken from the Möller-Nix table [15]. Additionally, a correction factor f is attached to it, namely

$$\Delta E_{\mathrm{sh}} = f \cdot \Delta E_{\mathrm{MN}}. \tag{V.57}$$

The introduction of this factor was motivated by the fact that large uncertainties still remain in the shell-correction energy, which is crucially important for describing the synthesis of super-heavy nuclei. Since the liquid-drop barrier gradually vanishes with atomic number, the shell-correction energy should be responsible for the extra stability of super-heavy nuclei. Hence, a small variation in this correction factor (or in the fission barrier) could lead to a significant change in final results (cf. Section V.6).

In the literature, there also exist other theoretical models based on either the microscopic or macroscopic approaches [163–167]. To examine different models, the code can directly

import a user-defined data file with the help of the option provided in the input file. Special care should be taken to guarantee the consistency between liquid-drop fission-barrier parameterizations and the corresponding shell-correction energies.

Thomas-Fermi model

Two parameterizations of $B_{\rm LDM}$ based upon the Möller-Nix table have been incorporated into the KEWPIE2 code. The first one, which has been developed within the framework of the Thomas-Fermi (TF) model [168], is simply written as

$$B_{\rm TF} = P \cdot F(X), \tag{V.58}$$

where the factor $P = A_C^{2/3}(1 - k_s I_C^2)$ is related to the nuclear surface energy, and the coefficient of isospin dependence k_s is defined as $1.9 + (Z_C - 80)/75$. The fission parameter X is given by

$$X = \frac{Z_C^2}{A_C\left(1 - k_s I_C^2\right)}. \tag{V.59}$$

As regards the function $F(X)$, the explicit expression was obtained by fitting the experimental liquid-drop barriers for about 120 nuclei covering the pre-actinide and actinide regions,

$$F(X) = \begin{cases} 0.595\,553 - 0.124\,136(X - X_1), & \text{for } 30 \le X \le X_1, \\ 1.997\,49 \cdot 10^{-4}(X_0 - X)^3, & \text{for } X_1 \le X \le X_0, \end{cases} \tag{V.60}$$

where X_0 and X_1 are taken to be 48.542 8 and 34.15, respectively.

As mentioned in Ref. [152], Eq. (V.58) would provide a fairly good description of the experimental fission barriers for pre-actinides. In the case of heavier nuclei, it could lead to an underestimation of measured values. In the KEWPIE2 code, the Thomas-Fermi model has been chosen to be the default option for estimating the liquid-drop fission barrier.

Empirical fission-barrier heights

The second formula was recently obtained within the Lublin-Strasbourg Drop (LSD) model [169]. Within this framework, the liquid-drop fission barrier can be well approximated by a Gaussian function, namely $B_{\rm LSD} = B_{\rm max} \exp\left[-\left(\frac{I_C - I_0}{\Delta I}\right)^2\right]$, with the following parameterizations for the parameters involved in the Gaussian function:

$$B_{\rm max} = a_0 + a_1 Z_C + a_2 Z_C^2 10^{-2} + a_3 Z_C^3 10^{-4}, \tag{V.61}$$

$$I_C = (A_C - 2Z_C)/A_C, \tag{V.62}$$

$$I_0 = a_4 + a_5 Z_C 10^{-4}, \tag{V.63}$$

$$\Delta I = a_6 + a_7 Z_C 10^{-2} + a_8 Z_C^2 10^{-4}. \tag{V.64}$$

As for the parameters involved in this parameterization, their best-fit values can be found in Ref. [169].

V.5 Nuclear level density

V.5.1 Intrinsic state-density formula

From the previous sections, it can be seen that the state density has a crucial role to play in describing the de-excitation of excited nuclei. In the code, an improved state-density formula, which was first proposed in Ref. [170], has been employed to estimate various decay widths. Compared to the simple Fermi-Gas model, the advantage of introducing this closed-form formula is that the divergence issue in the vicinity of the origin can be solved (cf. Fig. V.6). In this subsection, the state-density formula as well as some relevant quantities are briefly summarized.

The intrinsic state-density formula for a nucleus composed of two kinds of particles, namely protons and neutrons, is explicitly given by

$$\rho_{\rm int}(E^*) = \frac{\sqrt{\pi}}{12}\frac{\exp(\beta_0 E^* + a/\beta_0)}{\sqrt{\beta_0 E^{*3}}}\left(\frac{g_0^2}{4g_n g_p}\right)^{1/2}\frac{1-\exp(-a/\beta_0)}{\left[1-\frac{1}{2}E^*\beta_0\exp(-a/\beta_0)\right]^{1/2}}, \tag{V.65}$$

where g_n and g_p are respectively the neutron and proton single-particle state densities at the Fermi energy. For more details on the derivation of the above expression, the reader is referred to Appendix B. Here, $g_0 = g_n + g_p$ and typically, one has the following approximation: $g_n \simeq g_p$. In Eq. (V.65), a refers to the nuclear level-density parameter that will be discussed later. It should be noted that the implicit relationship between β_0 and E^* is expressed as

$$\left(\frac{a}{\beta_0}\right)^2 = \left(aE^*\right)\left[1-\exp\left(-\frac{a}{\beta_0}\right)\right]. \tag{V.66}$$

When the excitation energy tends to zero ($aE^* \ll 1$ or $a/\beta_0 \ll 1$), one simply has the limit $\beta_0 \to 1/E^*$, which leads to

$$\rho_{\rm int} \to \frac{1}{12}\sqrt{2\pi}ea\exp(aE^*), \tag{V.67}$$

where e is the base of the natural logarithm. At higher excitation energies ($aE^* \gg 1$ or $a/\beta_0 \gg 1$), one obtains the well-known textbook formula,

$$\rho_{\rm int} \to \frac{\sqrt{\pi}}{12}\frac{\exp(2\sqrt{aE^*})}{a^{1/4}E^{*5/4}}, \tag{V.68}$$

when $\beta_0 \to \sqrt{a/E^*} = 1/T$ with T being the nuclear temperature.

Eq. (V.65) is employed within the Weisskopf-Ewing evaporation model. Regarding the

Hauser-Feshbach formalism, the angular-momentum dependence of Eq. (V.65) should be considered. In this case, the level density with a fixed angular momentum is given by [171]

$$\rho_{\rm int}(E^*,J) = \frac{2J+1}{\sqrt{2\pi}\sigma_\perp^3}\exp\left[-\frac{(J+1/2)^2}{2\sigma_\perp^2}\right]\rho_{\rm int}(E^*). \tag{V.69}$$

where $\sigma_\perp^2$ is the spin cut-off parameter for axially deformed nuclei. It can be expressed as a function of the temperature T, namely

$$\sigma_\perp^2 = \frac{\Im_\perp T}{\hbar^2}, \tag{V.70}$$

where $\Im_\perp$ denotes the rigid-body moment of inertia perpendicular to the symmetry axis (cf. Subsection V.5.3). It should be noted that Eq. (V.69) would be considered to result from the following approximation: $\rho_{\rm int}(E^*,J) \propto \rho_{\rm int}(E^*-E_{\rm rot}) \sim \rho_{\rm int}(E^*)\exp(-E_{\rm rot}/T)$, which is based on that fact that, for any nucleus with the total excitation energy E^* and angular momentum J, only $E^*-E_{\rm rot}$ would be responsible for internal excitation. We would like to recall in this regard that the rotational energy $E_{\rm rot}$ is generally defined as $J(J+1)/(2\Im_\perp) \simeq (J+1/2)^2/(2\Im_\perp)$. Formal derivation can be made following the standard statistical approach [171].

V.5.2 Level-density parameter

Diffuse Thomas-Fermi model

The default level-density parameter has been taken from Ref. [172]. Within the extended Thomas-Fermi model, the level-density parameter for a given nucleus is written as

$$a = \frac{A}{14.61}\left(1+3.114\frac{\mathfrak{B}_s}{A^{1/3}}+5.626\frac{\mathfrak{B}_k}{A^{2/3}}\right)\left(1-\frac{I^2}{9}\right), \tag{V.71}$$

where I is the relative neutron excess and the surface term $\mathfrak{B}_s$ and the curvature term $\mathfrak{B}_k$ are respectively given by [173]

$$\begin{aligned}\mathfrak{B}_s &= 1+\frac{2}{5}\alpha_2^2-\frac{4}{105}\alpha_2^3-\frac{66}{175}\alpha_2^4,\\ \mathfrak{B}_k &= 1+\frac{2}{5}\alpha_2^2+\frac{16}{105}\alpha_2^3-\frac{82}{175}\alpha_2^4.\end{aligned} \tag{V.72}$$

Eq. (V.71) will be labeled by Tōke-Świątecki,

In the ground state, $\alpha_2 = \sqrt{5/4\pi}\beta_2$, where β_2 refers to the quadrupole deformation parameter for the ground state. At the saddle point, we adopt the following expression [173]:

$$\alpha_2 = \frac{7}{3}y-\frac{938}{765}y^2+9.499\,768y^3-8.050\,944y^4, \tag{V.73}$$

where $y = 1-x$. According to Ref. [174], the fissility parameter x can be parameterized as $x = \frac{Z^2}{49.22A(1-0.380I^2-20.489I^4)}$. Eq. (V.73) would only be valid for x close to unity. It should be

mentioned that, when the deformation parameter for the saddle point becomes smaller than that for the ground state, we simply add them together to redefine the quadrupole deformation of the saddle point. This ansatz can guarantee that the fission barrier shall always lie beyond the ground-state configuration.

Empirical model

A second level-density parameter included in the code is due to Reisdorf [53]. Using the leptodermous approximation within the Thomas-Fermi model, one obtains the following closed-form formula for the level-density parameter:

$$a = A\left(0.045\,43 r_0^3 + 0.135\,5 r_0^2 \frac{\mathfrak{B}_s}{A^{1/3}} + 0.142\,6 r_0 \frac{\mathfrak{B}_k}{A^{2/3}}\right), \tag{V.74}$$

where $\mathfrak{B}_s$ and $\mathfrak{B}_k$ are respectively the surface and curvature terms, as previously discussed. Here, r_0 has been determined to be 1.153 fm by fitting to the measured values [53].

Microscopic model

The last one was recently proposed by Nerlo-Pomorska *et al.* [175]. Finite-temperature macroscopic-microscopic calculations were performed with the Yukawa folded mean field for 134 spherical even-even nuclei and 6 deformed ones at temperatures $0 \leq T \leq 5$ MeV. The estimates for the level-density parameter obtained for different deformations are fitted by a liquid-drop type formula, which is expressed as follows:

$$a = 0.092A + 0.036A^{2/3}\mathfrak{B}_s + 0.275A^{1/3}\mathfrak{B}_k - 0.001\,46\frac{Z^2}{A^{1/3}}\mathfrak{B}_c, \tag{V.75}$$

where the new term $\mathfrak{B}_c$ is the Coulomb term for a deformed nucleus which is given as follows [173]:

$$\mathfrak{B}_c = 1 - \frac{1}{5}\alpha_2^2 - \frac{4}{105}\alpha_2^3 + \frac{51}{245}\alpha_2^4. \tag{V.76}$$

It would be worth mentioning that, based upon the microscopic model, Eq. (V.75) predicts a bit smaller values compared to those coming from the diffuse Thomas-Fermi approach.

V.5.3 Moment of inertia

Let us now consider an axially-symmetrical deformed nucleus, whose moment of inertia perpendicular to the symmetry axis is given as follows [176]:

$$\Im_\perp^{\mathrm{gs}} = \frac{2}{5} M_A R_A^2 \left(1 + \sqrt{\frac{5}{16\pi}}\beta_2 + \frac{45}{28\pi}\beta_2^2\right), \tag{V.77}$$

where M_A and R_A are the nuclear mass and the radius of the spherical shape, respectively.

At the saddle point, one only needs to replace the ground-state deformation parameter appearing in the above expression by the saddle-point one (cf. Eq. (V.73)) to obtain $\Im_{\perp}^{\rm sd}$.

It should be noted that, as shown in many experimental studies [177], the measured values of the inertia moment are usually lower than those estimated within the rigid-body model. This discrepancy has been corrected by multiplying $\Im_{\perp}^{\rm gs}$ and $\Im_{\perp}^{\rm sd}$ by a constant factor having a default value of 0.4. It can be adjusted by the user.

V.5.4 Ignatyuk's prescription

It has been realized for many years that the shell-correction effects on the level density parameter gradually drops with increasing excitation energy. To account for this damping phenomena, we adopt the so-called Ignatyuk's prescription [178], which assumes that the level-density parameter would be regarded as a function of the excitation energy. In the ground state, one has the following explicit expression:

$$a_{\rm gs}(E^*) = a\left[1+\left(1-e^{-E^*/E_d}\right)\frac{\Delta E_{\rm sh}}{E^*}\right], \tag{V.78}$$

where the default value of the damping energy E_d has been arbitrarily fixed at 19 MeV, which can be adjusted by the user.

V.5.5 Collective enhancement factor

Based upon the adiabatic formalism, where the internal and collective degrees of freedom are completely decoupled from each other, the intrinsic state density should be enhanced by a certain factor as a function of excitation energy E^*, namely $\rho(E^*,J) = \rho_{\rm int}(E^*,J)\kappa_{\rm coll}(E^*)$. The collective enhancement effect would quickly fall with increasing excitation energy. This can be interpreted in a way that, at higher energies, the fluctuations related to the nuclear deformation could become larger due to single-particle motions. As a consequence, the collective and internal degrees of freedom begin to interfere with each other. This would lead to an absorption of the collective states into the intrinsic ones. More concretely, one should have $\kappa_{\rm coll}(E^*) \to 1$ when E^* goes beyond a certain critical energy $E_{\rm cr}$.

In Ref. [128], Junghans *et al.* investigated the following parameterization for $\kappa_{\rm coll}(E^*)$:

$$\kappa_{\rm coll}(E^*) = \begin{cases} (\sigma_{\perp}^2-1)f(E^*)+1, & \text{for } \sigma_{\perp}^2 > 1, \\ 1, & \text{for } \sigma_{\perp}^2 \le 1, \end{cases} \tag{V.79}$$

in which the spin cut-off parameter $\sigma_{\perp}^2$ is given by

$$\sigma_{\perp}^2 = \begin{cases} \dfrac{\Im_{\perp}T}{\hbar^2}, & \text{when } |\beta_2| > 0.15 \text{ for rotations}, \\ S\Theta^2\dfrac{\Im_{\perp}T}{\hbar^2}, & \text{when } |\beta_2| \le 0.15 \text{ for vibrations}, \end{cases} \tag{V.80}$$

where β_2 is the quadrupole-deformation parameter and $\Theta = 0.022 + 0.003\Delta N + 0.005\Delta Z$ a dynamical deformation parameter that somehow accounts for the variation of vibrational energy levels as a function of the distance from the closed shell. The cut-off factor $f(E^*)$ is taken to be $1/\{1+\exp[(E^*-E_{\rm cr})/d_{\rm cr}]\}$ with $E_{\rm cr} = 40$ MeV and $d_{\rm cr} = 10$ MeV. S stands for a free parameter, whose optimum value was determined to be 25 [128]. Eq. (V.80) shows that the collective character of the nuclear motion can be described as a function of the quadrupole deformation parameter β_2 of the nuclear shape: the rotation dominates the collective motion of nuclei when $|\beta_2| > 0.15$ (deformed nuclei), whereas the vibration intervenes for $|\beta_2| \leq 0.15$. To some extent, it seems as if the rigid-body moment of inertia $\Im_\perp$ describing the rotational motion of deformed nuclei is gradually merged into the irrational-flow moment of inertia, namely $\Im_\perp^{\rm irr} = \Theta^2\Im_\perp$, which would be more appropriate for describing nuclear vibrations.

In Ref. [179], on the basis of Junghans *et al.*'s results, Zagrebaev *et al.* proposed an unified expression for the collective enhancement factor, which gives a smooth transition between $\Im_\perp^{\rm irr}$ and $\Im_\perp^{\rm rig}$. It is simply given by

$$\kappa_{\rm coll}(E^*) = \kappa_{\rm rot}(E^*)\varphi(\beta_2) + \kappa_{\rm vib}(E^*)[1-\varphi(\beta_2)], \tag{V.81}$$

with

$$\varphi(\beta_2) = \left[1+\exp\left(\frac{\beta_2^0 - |\beta_2|}{\Delta\beta_2}\right)\right]^{-1}, \tag{V.82}$$

where $\beta_2^0 = 0.15$ and $\Delta\beta_2 = 0.04$. This formula has been implemented in the current version of the code.

V.5.6 Pairing effect

The pairing effect can approximately be taken into account by replacing E^* by $E^* - \Delta_{\rm pair}$ in the above expressions. Following [180], it is simply given by

$$\Delta_{\rm pair} = \begin{cases} 0, & \text{if } Z \text{ and } N \text{ are both odd,} \\ 12/\sqrt{A}, & \text{if } A \text{ is odd,} \\ 24/\sqrt{A}, & \text{if } Z \text{ and } N \text{ are both even.} \end{cases} \tag{V.83}$$

As will be seen in the next section, this correction to the excitation energy would be necessary for the reproduction of experimental results.

V.6 Computational examples and sensibility analysis

In this section, some typical applications of the KEWPIE2 code to the study of de-excitation of heavy nuclei are shown. It is commonly known that the usefulness of any theoretical model is dependent on the accuracy and reliability of its outputs. However, since all models are not perfect, the exact input data are rarely, if ever available, which means that their theoretical

outcomes would always be uncertain to some extent. To figure out the impact of both model and parameter uncertainties on final results, a sensibility analysis is carried out for each reaction system. This would be especially helpful for guiding experiments.

Among all the input parameters comprised in the code, we are focusing on only three of them, namely reduced friction coefficient β, damping energy E_d and fission barrier B_f, which are determinant for theoretical calculations [99]. The first two parameters are considered free, whereas the third one is model-dependent. For the sake of clarity, their typical ranges of values are summarized as follows:

- The reduced friction parameter $\beta \sim 1.0 - 9.0$ zs^{-1} [127, 181].
- The damping energy $E_d \sim 13.0 - 25.0$ MeV [178, 182].
- The fission-barrier heights could differ by 1 or 2 MeV from each other [168, 169, 183].

As a starting point, we adopt the following default options for the present study: $\beta = 5.0$ zs^{-1}, $E_d = 19$ MeV and the fission barrier is estimated using the Thomas-Fermi model (cf. Eq. (V.58)). Furthermore, different corrections factors, such as the Kramers-Strutinsky factor and the collective enhancement factor, might also affect the calculated production cross-sections.

For comparison with experimental data, we mainly concentrate on the reaction systems where the fusion hindrance might not be present so as to avoid the remaining theoretical ambiguities on this phenomenon. To this extent, the fusion cross-section simply corresponds to the passage over the Coulomb barrier. The calculation of capture cross-sections has been discussed in the previous chapter. In addition, the Weisskopf-Ewing model is employed to estimate the particle-evaporation width and as previously shown, this approach can be regarded as a sufficient approximation of the Hauser-Feshbach formalism that is usually quite time-consuming. It should be also mentioned that the reaction systems selected in this section (lying within a wide energy range) would allow us to take a closer look at the effects of model uncertainties on the calculated results.

V.6.1 Reaction ^{208}Pb(^{16}O, xn)$^{224-x}$Th

First of all, we would like to investigate this well-measured fusion-evaporation reaction, where x equals 2, 3 and 4.

Regarding the evaporation process, 2n-, 3n- and 4n-channels have been investigated within the Weisskopf-Ewing model. Fig. V.7(a) compares the estimated ER excitation functions with the available experimental data. It is observed that the excitation function based upon the EBD method is largely enhanced at low energies compared to the WKB approximation. This is essentially due to the overestimation of the fusion cross-section at sub-barrier energies. As a whole, the experimental data can be reproduced rather well within the WKB approximation, especially for the 2n- and 3n-channels, whose peak positions or optimum energies are found to be in nice agreement with the measurements. This is because the neutron separation energies are calculated from the available experimental masses. Therefore, we shall adopt the WKB

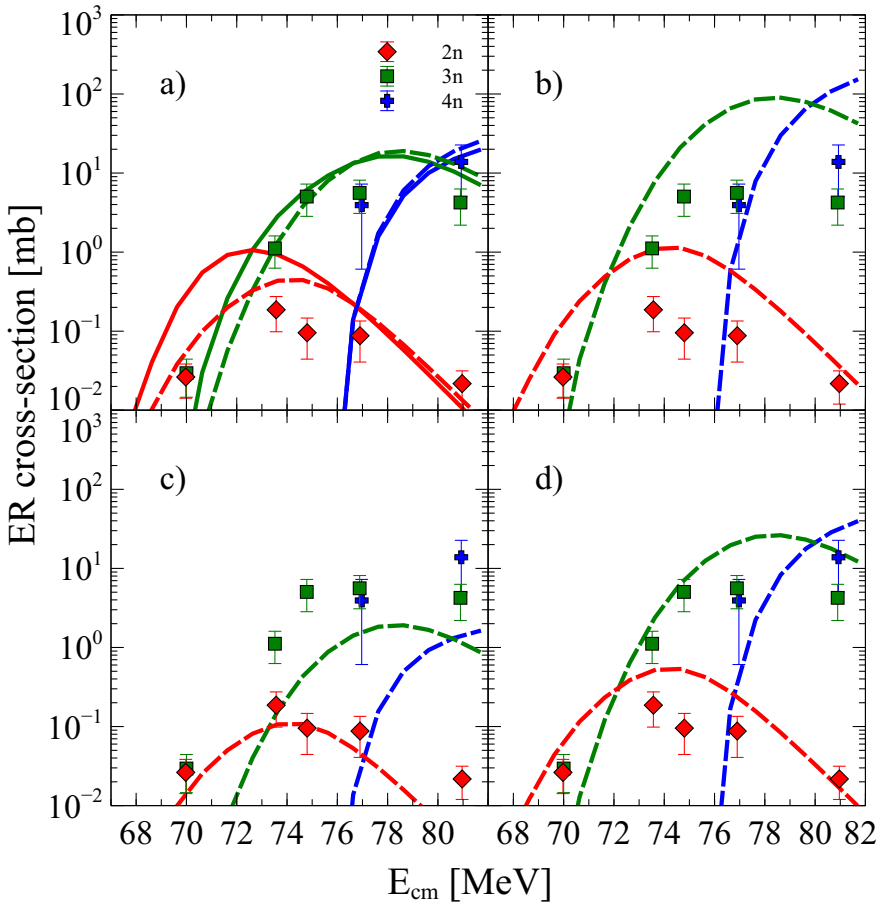

Figure V.7 – Comparison of the estimated ER excitation functions for the reaction ^{208}Pb(^{16}O, xn)$^{224-x}$Th. The solid symbols represent the experimental data taken from Ref. [184]. The calculated ER cross-sections of 2n-, 3n- and 4n-channels are respectively shown by the red, green and blue curves. The solid curves correspond to the calculations based upon the EBD method and dashed curves to those performed within the WKB approximation. Note that the WKB approximation has been chosen to calculate the capture cross-sections in Figs. V.7(b), (c) and (d). We compare the computational results obtained without considering the collective-enhancement factor (b), without considering the Kramers-Strutinsky correction factor (c) and without considering both of them (d).

approximation to estimate the ER excitation functions for the reaction ^{208}Pb(^{16}O, xn)$^{224-x}$Th.

Figs. V.7(b)-(d) illustrate the impact of modeling uncertainties on the ER excitation functions. Here, we mainly address two interesting factors, namely Kramers-Strutinsky correction factor and collective-enhancement factor. As previously mentioned, the former takes into account the influence of nuclear viscosity on the fission process and the latter would be responsible for the correction to the state density, which is due to the collective motions at low excitation energies. In the literature, some authors employed both of them [3, 179, 185], while others none of them [48]. The computational results obtained without considering

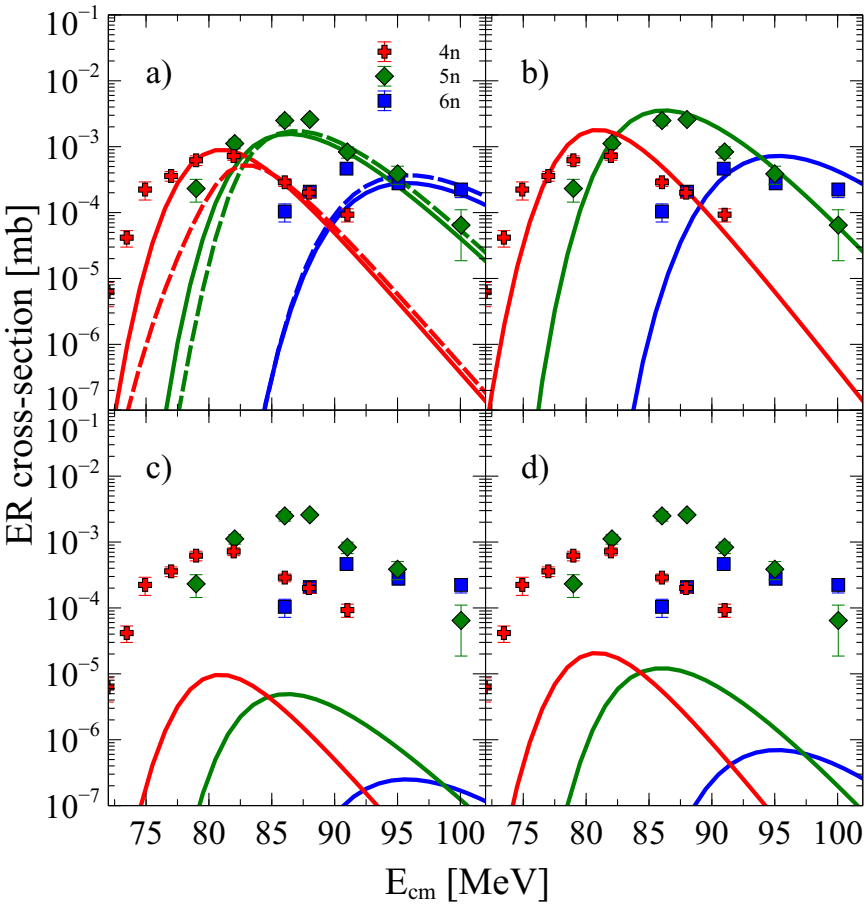

Figure V.8 – Same as Fig. V.7, but for the reaction ^{238}U(^{16}O, xn)$^{254-x}$Fm. The solid symbols stand for the experimental data taken from Ref. [34]. The calculated ER cross-sections of 4n-, 5n- and 6n-channels are respectively shown by the red, green and blue curves. Note that the EBD method has been chosen to calculate the capture cross-sections.

one or both of them have been clearly displayed in Figs. V.7(b)−(d). The default parameter values are kept for all these calculations. It is clearly shown that, without considering the collective-enhancement factor, the maximums of the estimated excitation functions seem to grow by a factor of about 7 – 10, whereas they drop by the same factor when taking into account the Kramers-Strutinsky correction factor. Even more interesting is the fact that, when both of them are removed, again the computational results gradually approach the measured data. This might explain why some simplified theoretical models without including both factors could also reproduce experimental data rather well.

V.6.2 Reaction ^{238}U(^{16}O, xn)$^{254-x}$Fm

The second calculational example aims to study the following fusion-evaporation reaction: ^{238}U(^{16}O, xn)$^{254-x}$Fm with x being 4, 5 and 6.

In Fig. V.8(a), the theoretical ER cross-sections estimated with both capture models are compared with the experimental data for the 4n-, 5n- and 6n-channels. A dramatic underestimation at sub-barrier energies has been confirmed in the case of the WKB approximation. However, using the EBD method, the calculated excitation functions are found to be in nice agreement with the measured data. Here the default parameter values are kept for the present calculations.

Figs. V.8(b)−(d) illustrates the same model sensitivity analysis for the present reaction. Fig. V.8(b) compares the theoretical calculations without accounting for the collective enhancement factor. The maximum values of the ER excitation functions appear to increase by a smaller factor compared to the previous reaction. This might be due to the fact that, as the excitation energy goes up, the collective effects would probably diminish in a gradual manner (cf. Section V.5). Fig. V.8(c) tells us that the estimated cross-sections are considerably reduced after taking out the Kramers-Strutinsky correction factor. The decrease in the maximum of the excitation function can even reach up to two or three orders of magnitude for 5- and 6n-channels. To explain this large discrepancy, we should be aware that the probability of evaporating s neutrons from a heavy nucleus would be roughly proportional to the product $\prod_{i=0}^{s-1}(\Gamma_n/\Gamma_f)_i$ (cf. Section V.2). Here, the Kramers-Strutinsky correction factor is estimated to be of the order of 0.2, so that the more neutrons evaporated, the more important its influence on the ratio of decay widths and thus on the neutron-evaporation probability. Moreover, the magnitude of this correction factor also becomes lower with increasing excitation energy. Finally, Fig. V.8(d) shows the result obtained without considering simultaneously these two factors. These factors would be crucially important for correctly modeling the competition between neutron emission and fission at high excitation energies. In this sense, the model uncertainty needs to be well considered when performing theoretical calculations [6].

V.6.3 Reaction ^{208}Pb(^{48}Ca, xn)$^{256-x}$No

As a third example, we try to investigate the reaction ^{208}Pb(^{48}Ca,xn) $^{256-x}$No with x being $1-3$, which is of special interest for experimentalists. For instance, a recent study concerning the measurement of the fission barrier in ^{254}No [188] has been performed by making use of this fusion-evaporation reaction. Furthermore, within the promising project SPIRAL2 at GANIL, the nuclear structure of ^{254}No will be investigated by means of the same reaction [20].

The estimated ER cross-sections for the 1n-, 2n- and 3n-channels are shown in Fig. V.9(a) and a comparison with the available experimental measurements has also been performed. In both cases, it is clearly shown that the calculated ER excitation functions are systematically higher compare to the measured data. To give a reasonable fit, we first adopt the WKB approximation for estimating the capture cross-section and employ the other fission-barrier model incorporated into the KEWPIE2 code, which was recently developed on the basis of the LSD model [169]. In Fig. V.9(b), it is readily seen that, after changing the fission-barrier parameterization, the estimated excitation functions are getting closer to the data points. For

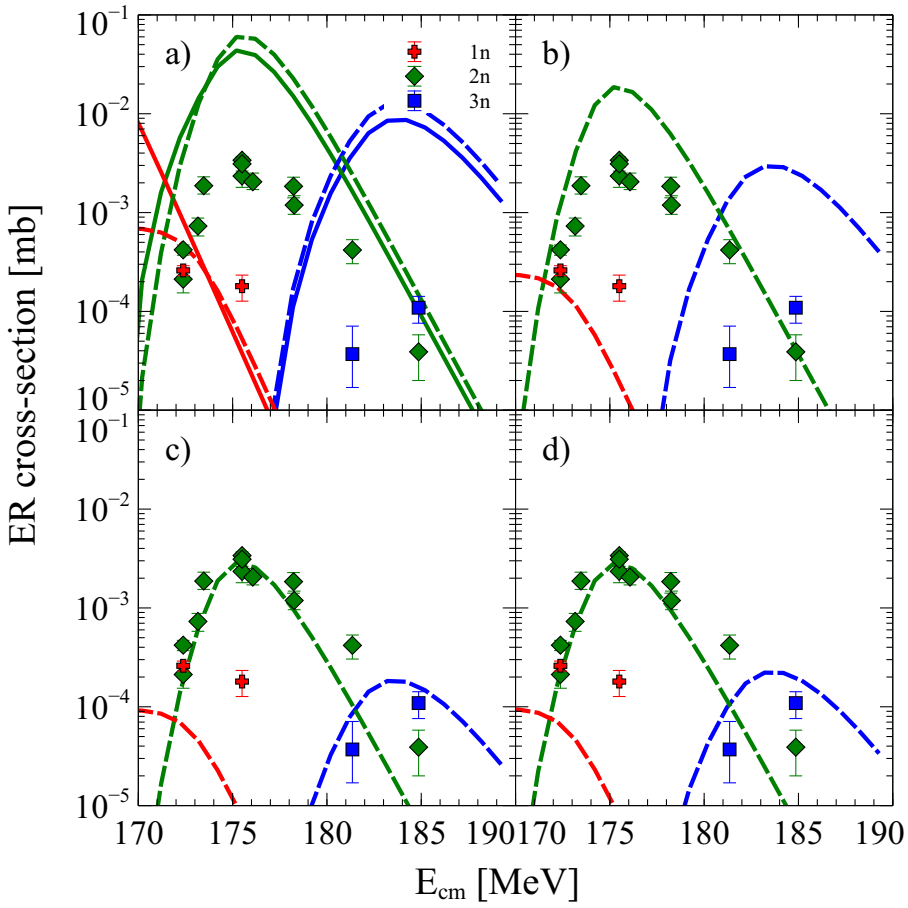

Figure V.9 – Comparison of the estimated ER excitation functions for the reaction ^{208}Pb(^{48}Ca, xn)$^{256-x}$No. The solid symbols stand for the experimental data taken from Refs. [186, 187]. The estimated ER cross-sections of 1n-, 2n- and 3n-channels are respectively shown by the red, green and blue curves. The solid curves correspond to the calculations based upon the EBD method and the dashed curves to those performed within the WKB approximation. Note that the WKB approximation has been chosen to estimate the capture cross-section in Figs. V.9(b), (c) and (d), where the estimated ER cross-sections are based upon the LSD fission-barrier model with the default parameter values (b), decreasing the value of β by about 80% (c), decreasing the value of E_d by about 30% (d).

the sake of clarity, the fission-barrier heights of the decaying isotopes are listed in Table V.1. Overall, the LSD fission-barrier heights appear a bit smaller than those based upon the TF model. Nevertheless, a considerable discrepancy still persists. Hence, based upon the LSD fission-barrier model, we separately tune the reduced friction coefficient and the damping energy. The calculated results have been illustrated in Figs. V.9(c) and V.9(d). More concretely, with respect to their default values, we modify only one parameter at each time. To reproduce the measured data, the reduced friction parameter β should be decreased by about 80% (down to 1.0 zs^{-1}) and E_d decreased by about 30% (down to 13 MeV). As can be seen from this example, we can tune parameter values within a reasonable range and choose pertinent

Table V.1 – The liquid-drop fission-barrier heights of the nobelium isotopes estimated within the TF and LSD models. Here the shell-correction energies are taken from [15].

Z	A	B_{TF} [MeV]	B_{LSD} [MeV]	ΔE_{sh} [MeV]
102	253	0.38	0.10	-4.49
102	254	0.40	0.10	-4.65
102	255	0.41	0.11	-4.44
102	256	0.42	0.11	-4.19

models to reproduce data, in spite of the fact that the measured values appear far lower with respect to theoretical calculations with default options. Furthermore, it should be also mentioned that the fusion hindrance might occur in this reaction system, that is to say, the fusion cross-section could be reduced by introducing the formation probability P_{form}, which is, however, not considered in the present calculation because of the remaining ambiguities.

V.7 Summary and conclusions

In summary, we have provided an introduction to the theoretical models included in the KEWPIE2 code for modeling the statistical de-excitation of excited heavy nuclei. As mentioned at the beginning of this chapter, the KEWPIE2 code will serve as a basic tool for the remaining part of this thesis mainly devoted to uncertainty analysis of fusion-evaporation reactions leading the synthesis of SHE.

According to the sensibility analysis performed at the end of this chapter, it has been clearly established that uncertainties coming from both parameters and models would play a crucial role for theoretical predictions and therefore should be investigated in a more formal manner. For instance, it appears that the final result is crucially sensitive to the uncertainty associated with fission-barrier heights, which could give rise to a remarkable change (up to orders of magnitude) in theoretical predictions [99, 100]. To have a more accurate description of the fusion-evaporation reaction, it would be necessary to perform a complete uncertainty analysis so as to look more closely at the propagation of different types of uncertainties in numerical modeling and thus to constrain input parameter values. For this purpose, some recent work on uncertainty quantification will be presented in the following chapters.

VI Problematics in the synthesis of SHE

> Essentially, all models are wrong, but some are useful.
>
> George E. P. Box

What have we done and learned from the previous chapters? On the one hand, the capture cross-sections for a set of selected reaction systems have been estimated on the basis of some commonly used simple models, such as the WKB approximation with an empirical proximity potential and the EBD approach. By making an illustrative comparison of the different methods, it was concluded that the calculated values would roughly differ by less than one order of magnitude in the case of heavy reaction systems. This would be acceptable taking into account the simplicity of the capture model. On the other hand, the KEWPIE2 code has been presented in detail. Using this code, some theoretical calculations of ER cross-sections have been performed and a sensitivity analysis was carried out for both parameters and models for reaction systems without fusion hindrance. It should be emphasized that the KEWPIE2 code is much more complicated compared to the simple capture models, that is to say, it comprises a number of parameters or approximations. A detailed uncertainty analysis is thus highly needed. Moreover, compared to the capture and de-excitation steps, the formation one is much less known because of the remaining theoretical ambiguities. Hence, further efforts will be required to handle these tough issues related to the formation step, which is thought of as the key for synthesizing SHE.

Before doing a complete uncertainty analysis, it would be helpful to briefly review the present status of study on the synthesis of SHE as well as the experimental data which are available to compare with theoretical calculations. In this chapter, we first recall some of the basic experimental and theoretical concepts related to the production of SHE. Then, within a simple framework, the main theoretical issues that we are facing nowadays will be discussed. A strategy for solving these problems is outlined at the end of this chapter.

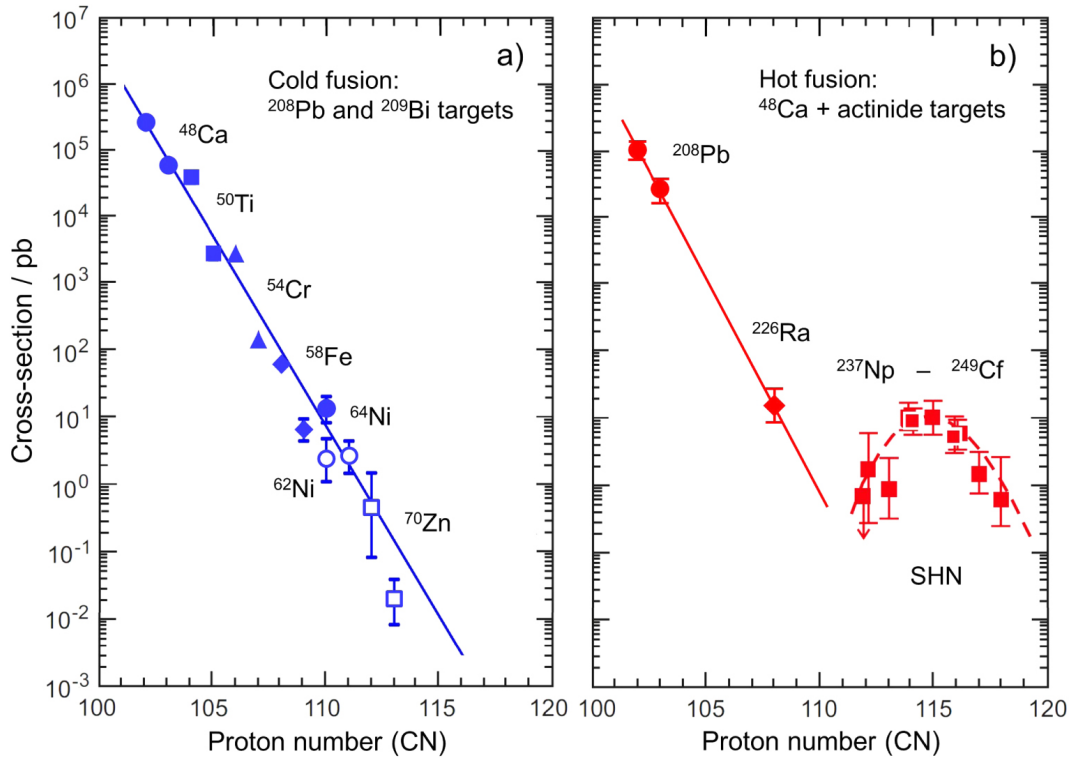

Figure VI.1 – Summary of experimental ER cross-sections for both cold- and hot-fusion reactions. Figure is taken from Ref. [189].

VI.1 Current status of experimental studies on SHE

As mentioned in the introduction chapter, two types of fusion reactions have been widely applied to the synthesis of new SHE over the past few decades. In this subsection, a brief review of some recent experimental achievements based upon these two approaches is presented. It should be noted that theoretical models presented in the previous chapters can be also applied to both cases.

VI.1.1 Cold-fusion reaction

Since the early 1970s, the cold fusion of ^{208}Pb and ^{209}Bi with medium-mass heavy-ion projectile beams (^{48}Ca, ^{50}Ti, ^{54}Cr, etc) have been largely used to synthesize the heaviest elements. Accordingly, the increase of the atomic and mass numbers of the reaction products is directly related to the increase in the mass and charge of the projectile. During a fusion process, the highly-stable magic target nucleus would give rise to a strong absorption of the incident energy in merging the two colliding nuclei into a heavier nucleus and thus compensate the energy necessary to overcome a relatively high Coulomb barrier. As a consequence, the excitation energy of the newly-formed CN would be expected to range from 10 to 20 MeV, which corresponds to a relatively low nuclear temperature. This is the main reason why this

kind of reaction is said to be "cold". Accordingly, during such a reaction, the newly-formed heavy nucleus would emit only one or two neutrons to reach the ground state. In practice, cold-fusion reactions with medium-mass projectiles were successfully applied to the synthesis of six new elements with $Z = 107-112$ at GSI [190]. Then, the group of RIKEN (Tokyo) repeated the same experiments for synthesizing the elements $110-112$ and observed decay events of element 113 [191, 192].

Nevertheless, it should be noted that, with increasing charge product of the projectile-target combination $Z_t Z_p$, the production cross-section dramatically falls because of the rapid increase of the Coulomb repulsion. Fig. VI.1 shows a summary of production cross-sections as a function of the atomic number of compound nuclei. It is clearly displayed that, from element 104 produced in the reaction ^{50}Ti+^{208}Pb($Z_p Z_t = 1804$) to element 112 produced in the reaction ^{70}Zn+^{208}Pb ($Z_p Z_t = 2460$), the maximum cross-section is even reduced by about four orders of magnitude. Another drawback of this approach is that the compound nuclei produced in cold-fusion reactions have a relatively low number of neutrons, which is generally close to the proton drip line. For instance, to produce element 112, the synthesized nucleus only possesses 165 neutrons, whereas the predicted "island of stability" might be located somewhere near the neutron-rich side, namely around $N = 184$ [15, 17]. Hence, to synthesize more neutron-rich SHE, the hot-fusion reaction should be considered. In such reactions, the actinide targets have been employed together with a medium-mass doubly magic projectile ^{48}Ca ($Z = 20$ and $N = 28$) [1].

VI.1.2 Hot-fusion reaction

As mentioned above, to approach the predicted "island of stability", one has to produce more neutron-rich isotopes of SHE. Actually, it is impossible to produce such exotic nuclei by means of cold-fusion reactions. Hence, one needs to find other ways using available targets that have the maximum neutron number in the nucleus. The hot-fusion reaction thus comes into play through the collision of ^{48}Ca with some actinide targets. The natural element of calcium contains about 97% of the isotope ^{40}Ca, but only 0.187% of the heaviest isotope ^{48}Ca (the maximum neutron number). Furthermore, the magic structure of ^{48}Ca also plays a crucial role in absorbing the incident energy. In practice, the resulting excitation energy will be a bit higher compared to cold-fusion reactions, say around $30-60$ MeV, which leads to the emission of more than two or three neutrons. To synthesize heavier nuclei, the hot-fusion reaction would be favored because the charge product in the entrance channel is generally less than 2000, which leads to a dramatic decrease of the Coulomb repulsion compared to cold-fusion reactions and thus the fusion probability or the production cross-section is expected to be relatively higher. As shown in Fig. VI.1, the experimental data on hot-fusion reactions reveal a different trend when the atomic number goes beyond around $Z \gtrsim 112$. The cross-sections rise again and seem to reach their maximum values of about several picobarns at element $Z \backsimeq 114$.

[1] There were also attempts of using other possible beams (Ar, S, Ne, Ti, Cr, etc) for hot fusion reactions. However, all of these have been proved to be unsuccessful so far.

Here, it should be borne in mind that the survival probability is lower due to the large number of neutrons that need to be emitted for cooling.

At the present time, the hot-fusion reaction appears to be the most efficient way for producing the heaviest elements. However, compared to cold-fusion reactions, the hot ones would require more sensitive experimental setups in order to separate the nuclei of interest from unwanted background during the reaction. Moreover, the identification of newly-produced elements is also a serious problem because their α-decay chains usually end in an unknown region. This is actually one of the most crucial challenges for experimentalists because the α-decay chain is the only way to identify heaviest elements.

Anyhow, by making use of the long-lived enriched isotopes of actinides (Pu, Am, Cm, and Cf) with the maximum neutron number, the elements ranging from $Z = 114$ to $Z = 118$ were successfully created at the FLNR laboratory (cf. Ref [193] and references therein) and confirmed in other independent experiments (cf., e.g., Refs [194, 195]).

VI.2 Theoretical issues related to the synthesis of SHE

So far, we have briefly reviewed the current status of experimental studies on the synthesis of SHE via two types of fusion reactions.

As previously introduced, based upon the Bohr independence hypothesis [106], the ER cross-section for a fusion-evaporation reaction leading to the formation of SHE can be expressed as

$$\sigma_{\rm ER}(E_{\rm cm}) = \sum_{J_C \geq 0}^{J_{\rm max}} \sigma_{\rm fus}(E_{\rm cm}, J_C) P_{\rm sur}(E_C^*, J_C). \tag{VI.1}$$

Recalling that the relationship between the incident energy in the center-of-mass frame $E_{\rm cm}$ and the total excitation energy of the compound nucleus E_C^* is simply given by $E_C^* = E_{\rm cm} + Q$. Note that Eq. (VI.1) takes into account all partial-wave contributions to the total cross-section, ending with an upper limit, say $J_{\rm max}$, which can be approximately determined once the partial-wave cross-section vanishes.

VI.2.1 A simplified model

In the case of SHE, the maximum spin $J_{\rm max}$ is mainly related to the survival probability $P_{\rm sur}(E_C^*, J_C)$ that usually corresponds to a narrow function of the spin J_C, which does not vanish only in the vicinity of $J_C \simeq 0$. Hence, one has $P_{\rm sur}(E_C^*, J_C) \simeq P_{\rm sur}(E_C^*)$, where $P_{\rm sur}(E_C^*)$ can be estimated by means of the Weisskopf-Ewing model, and the total ER cross-section can thus be approximated as

$$\sigma_{\rm ER}(E_{\rm cm}) \simeq \sigma_{\rm fus}(E_{\rm cm}) P_{\rm sur}(E_C^*). \tag{VI.2}$$

Moreover, for heavy fusing systems leading to the formation of SHE, the fusion probability should be rewritten as a product of the capture and formation probabilities. Accordingly, the

above approximate formula can be further transformed into

$$\sigma_{\rm ER}(E_{\rm cm}) \simeq \sigma_{\rm cap}(E_{\rm cm}) P_{\rm form}(E_{\rm cm}) P_{\rm sur}(E_C^*), \tag{VI.3}$$

where $P_{\rm form}(E_{\rm cm})$ stands for the formation probability due to the fusion hindrance. We should be aware that this simplified version of Eq. (VI.1), which is valid for both cold and hot fusions, has been widely employed to estimate ER cross-sections in many recent studies [3, 4, 48, 196].

For the sake of simplicity, as a first step, we mainly focus on the cold-fusion reaction with single-neutron evaporation. As mentioned above, owing to the basic character of cold fusions, the production cross-section is generally found to be higher compared to the hot ones for lighter super-heavy nuclei, so that more reliable experimental data are available in the literature. In this case, the ER cross-section for the $1n$-channel is simply given by

$$\sigma_{\rm ER}^{1n} \simeq \sigma_{\rm cap} P_{\rm form} P_{\rm sur}^{1n}. \tag{VI.4}$$

Note that the formation probability is sometimes denoted by $P_{\rm CN}$ as well [3, 4].

VI.2.2 Contradictory predictions on $P_{\rm form}$ and $\sigma_{\rm ER}$

Precise theoretical predictions of production cross-sections would be crucially important for conducting experiments on the synthesis of SHE in the sense that they can help save time and money! The first crucial question one might ask about production cross-sections is how exactly can we predict them with existing reaction theories? There are actually a number of theoretical calculations of the ER cross-sections for both hot- and cold-fusion reactions, which seem to agree remarkably well with the measured ER cross sections. This, of course, can be regarded as a significant theoretical achievement considering that the measured cross-sections usually span at least six orders of magnitude (cf. Fig. VI.1). Let us take cold-fusion reactions as an example, a typical set of theoretical calculations of the ER cross-sections in cold-fusion reactions are displayed in Fig. VI.2. The experimental measurements are remarkably well described by all the calculations within less than one order of magnitude. (As regards the prediction made by Veselskỳ, it was actually not correctly taken into account [199].) On the other side, however, if we take a closer look at the values of the formation probability, as shown in Fig. VI.3, it is strange that the values can differ by at least two orders of magnitude or even larger among the various models, even though all of them seem to reasonably converge to the measured data on the production cross-sections. Hence, there appears to be a serious contradiction between these two crucial quantities appearing in the same formula (cf. Eq. VI.4). The formation probability that cannot be measured is not quantitatively known so that the large uncertainty reaming in this quantity would not be a surprise. However, the capture and de-excitation steps are both relatively better known at a theoretical level. How come the better-known part can accommodate the large discrepancies of the calculated formation probabilities so as to reproduce the experimental data? How could this happen? To this extent, the predictive capability of the fusion model appears to be quite limited ...

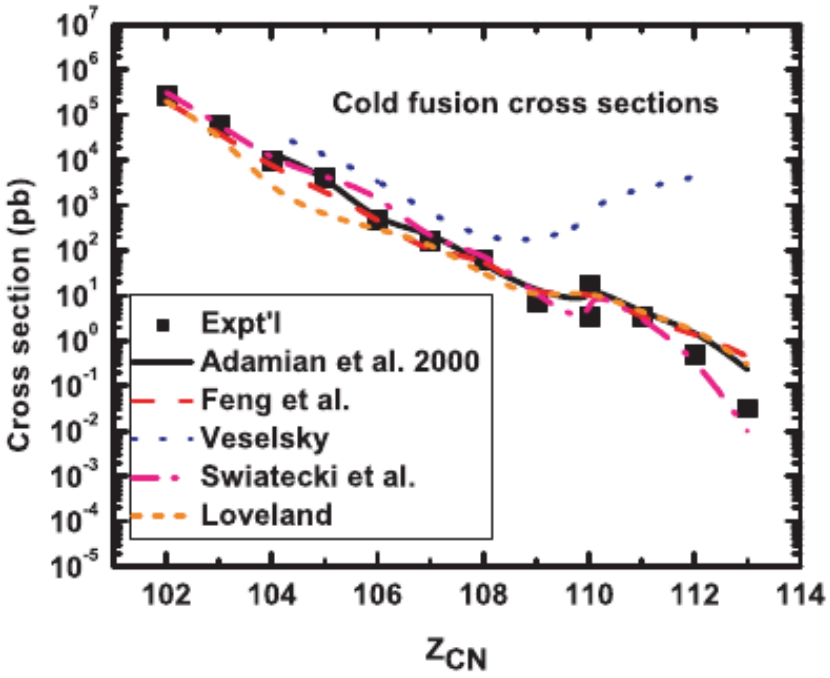

Figure VI.2 – Theoretical calculations of the ER cross-sections for cold-fusion reactions. The calculated results can be found in Refs. [3, 48, 86, 197, 198]. Figure is taken from Ref. [4].

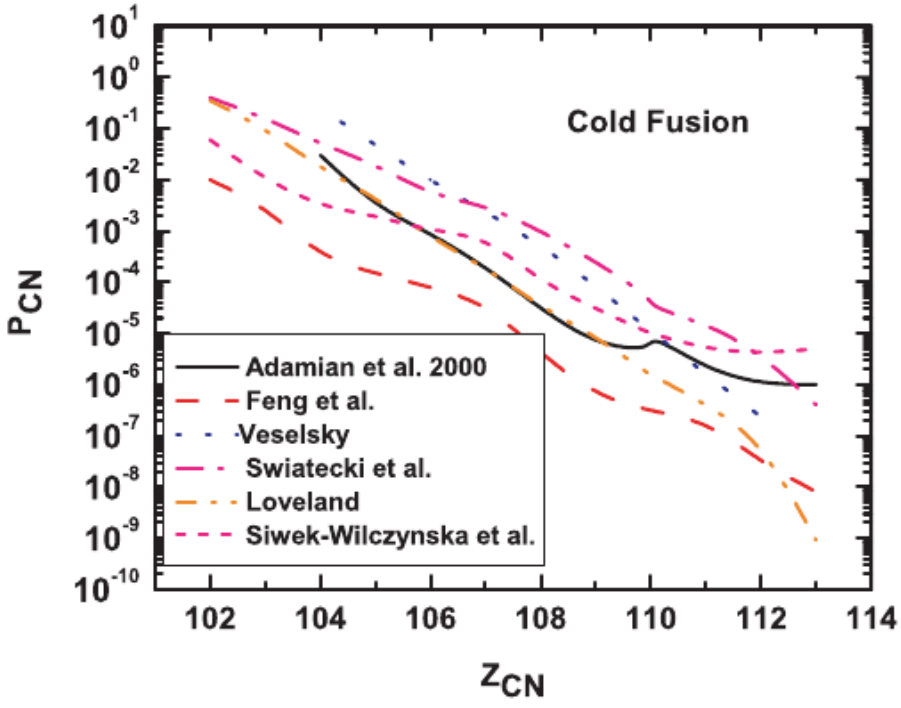

Figure VI.3 – Theoretical calculations of the formation probabilities for cold-fusion reactions. The calculated results can be found in Refs. [3, 48, 86, 196–198]. Figure is taken from Ref. [4].

To understand this contradiction, it is likely that the other two factors, namely the capture cross-section and the survival probability, have been somehow adjusted in order to give reasonable calculated results compared with the measured data. Therefore, it would be instructive to investigate the uncertainties in these two parts that are sandwiched with the formation probability (cf. Eq. VI.4). Regarding the capture cross-section, as previously mentioned, it corresponds to the sum of the quasi-fission, fusion-fission and ER cross-sections. It should be mentioned that, in the case of SHE, the ER cross-section is considered to be much smaller compared to the former two, so that the main contributions come from both the fission and quasi-fission processes. Thus, in practice, the capture cross-section can be relatively well measured without any ambiguity. On the theoretical side, it can be reproduced with a precision of less than about 50% or even poorer at sub-barrier energies, but apparently less than one order of magnitude in most cases. As regards the survival probability, it can be usually calculated by means of a computer code, such as KEWPIE2 [99, 100]. From previous studies, it has been well established that the calculation of this quantity would require a good understanding of uncertainty in the fission barrier. As will be demonstrated later, the uncertainty associated with the survival probability can be well determined and quantified with some advanced statistical methods. Anyhow, the formation probability is the most poorly known quantity in Eq. (VI.4), but the most crucial one for the production of SHE. This would be a two-fold issue. On the one hand, it is difficult to exactly measure this quantity because the identification of quasi-fission events is usually very difficult so that the measured data could not be reliable enough. On the other hand, large theoretical ambiguities still persist in different models. Therefore, it is unlikely to assess the fusion models directly from experimental measurements.

To establish a reliable and accurate reaction theory for guiding future experiments on the synthesis of SHE, it would be urgent to find new methods to constrain many existing fusion models. As a starting point, can we constrain the formation probability with the better-known parts as well as the available experimental data? It is actually related to an inverse problem, that is to say, deducing the information about the formation probability from the uncertainties in the better-known quantities. This strategy will be further outlined in the next subsection.

VI.2.3 Inverse problem with uncertainty analysis

The main issues that have been discussed above can be summarized as follows:

- All fusion-evaporation models reproduce well the experimental data, however, large discrepancies exist between the predictions of formation probabilities. Why does this happen and how to explain it?
- Can we constrain this quantity by examining the other two factors, namely the capture cross-section and the survival probability, which are relatively better known?

As regards the latter question, it can be regarded as an inverse problem. More concretely, what needs to be done consists in defining an empirical formation probability, denoted by $\overline{P}_{\mathrm{form}}$,

which will be extracted from the available measured data. It is simply defined as follows:

$$\overline{P}_{\text{form}} = \frac{\sigma^{1n}_{\text{exp}}}{\sigma_{\text{cap}} P^{1n}_{\text{sur}}}, \tag{VI.5}$$

where the numerator is the experimental production cross-section for the 1-n channel and the denominator the product of the capture cross-section and the survival probability, which are estimated with the help of the KEWPIE2 code at the corresponding experimental energy. Hence, the main idea of the proposed strategy is to quantify the uncertainties coming from each component of the right-hand side of Eq. (VI.5). More concretely, we attempt to see whether these uncertainties can constrain the empirical formation probability, that is to say, whether their amplitudes are smaller than the discrepancies between various models for estimating the formation probability.

Before entering into the main discussion on uncertainty analysis, it would be helpful to clarify some crucial concepts related to uncertainty.

What is uncertainty?

Uncertainty is commonly employed as an expression of confidence about what we know, and is therefore subjective to some degree. In this sense, people might reach different conclusions about how uncertain something is, on the basis of their own personal experiences and viewpoints, as well as the amount and quality of information available in hand.

It should be noted that uncertainty differs from ignorance because the latter involves a lack of awareness about our imperfect knowledge. It is also important to clarify the difference between error and uncertainty. For instance, a measurement result that differs from the "true value" (generally not known) is an error, and theoretically, adding or subtracting the error from the measurement result can derive the true value. To this extent, error would involve a specific departure from "reality". Uncertainty, on the other hand, corresponds to a range of values likely to be encountered during experimental measurements. The standard deviation is usually adopted as a measure of uncertainty together with the corresponding confidence interval. Ideally, the theoretical models would be perfectly accurate. Unfortunately, this is practically never the case. Put differently, we are always uncertain about errors in our model because of certain approximations. In addition, input parameters entering the model are seldom well known. However, one could specify some restrictions on uncertainty, which would allow us to explore its impact on the outcomes for the given input data. This is also the main target of doing uncertainty analysis.

How to analyze uncertainty?

The main steps for performing uncertainty analysis, as clearly illustrated in Fig. VI.4, can be summarized as follows:

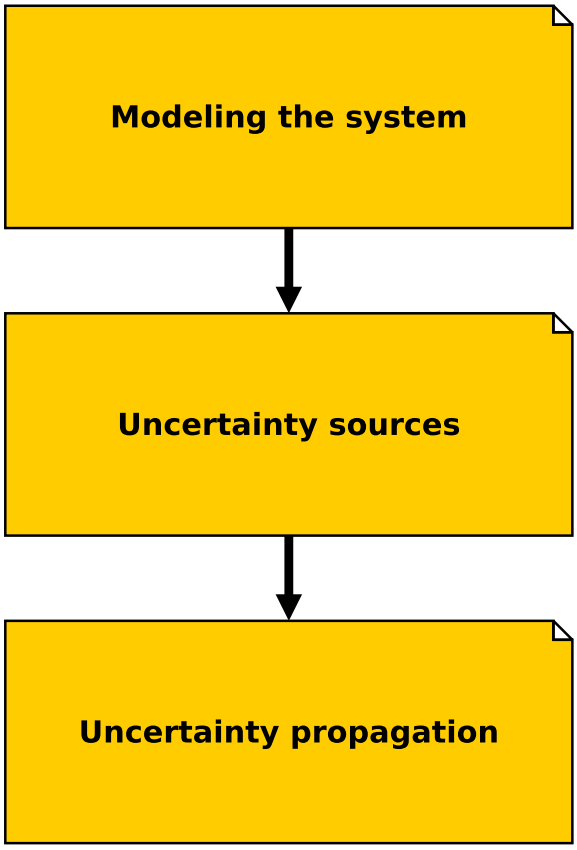

Figure VI.4 – Schematic representation of the procedure for doing uncertainty analysis.

1. Defining the model employed to survey the physical system under study. In the case of complex systems, a clear identification of the input and output of each sub-model should be required. This consists in gathering all the ingredients employed for describing the physical system to be analyzed.

2. Identifying and quantifying all the uncertainty sources related to the model, that is to say, identifying those input data that are not well determined and describing them in a probabilistic manner. In this sense, the input parameters become random variables and thus the final product of this step will be a vector of random variables.

3. Propagating uncertainties in the input data through the model, or in other words, characterizing the outcome of the model by taking into account random changes in the input parameters. To this end, some advanced statistical methods can be employed to complete this task, as will be presented in the following chapter.

This is actually the standard procedure for conducting uncertainty analysis, as recommended in the Guide to the Expression of Uncertainty in Measurement [5, 200, 201].

Besides the input parameters, how to determine the uncertainty associated with the model? This is a crucial problem in the sense that nuclear reaction models are much less accurate and are usually based upon many approximations. To solve this issue, we adopt the recommendation proposed in the Editorial of Physical Review A [6], which states that:

> ... The uncertainties can arise from two sources: (a) the degree to which the numerical results accurately represent the predictions of an underlying theoretical formalism, for example, convergence with the size of a basis set, or the step size in a numerical integration, and (b) physical effects not included in the calculation from the beginning, such as electron correlation and relativistic corrections. It is of course never possible to state precisely what the error is without in fact doing a larger calculation and obtaining the higher accuracy. However, the same is true for the uncertainties in experimental data. The aim is to estimate the uncertainty, not to state the exact amount of the error or provide a rigorous bound ...

More concretely, to quantify the uncertainty connected with the model, we simply attempt to explore the impact of changing theoretical models, such as the capture model and some correction factors, on the simulation outcomes. This could provide rough limits of the theoretical calculations.

VI.3 Summary and conclusions

In summary, we have provided a brief review of some delicate issues related to the production of SHE, mainly concerning how to access and constrain different fusion models. We have proposed a strategy that consists in examining the empirical formation probability by means of uncertainty quantification. For this purpose, we have introduced a general framework for performing such analysis.

In the next chapter, we will concretely apply these methods to studying the inverse problem so as to clarify the huge contradiction between the calculated formation probabilities and production cross-sections of SHE in cold-fusion reactions.

VII Uncertainty analysis in reaction modeling

> I think it is much more interesting to live with uncertainty than to live with answers that might be wrong.
>
> Richard Feynman

To assess the fusion models, we propose to extract the empirical formation probability from the available experimental data based upon cold-fusion reactions by taking into account the uncertainty in reaction modeling.

Over the last few decades, the importance of uncertainty analysis in modeling has been increasingly recognized, especially with the enormous development of computer simulation. It is mainly concerned with the characterization and quantification of uncertainty in numerical applications by means of running a number of calculations to investigate the impact of minor differences in input data on the corresponding outcomes. This kind of study would be essential in the sense that one often has very poor information about the input. For instance, as previously indicated, both the input parameters and the various theoretical models integrated into the KEWPIE2 code are usually not unambiguously determined, so that large uncertainties might remain in numerical modeling of the fusion-evaporation reaction.

In this chapter, we attempt to look more closely at the influence of both parameter and model uncertainties on the numerical results. The chapter is organized as follows. First, on the basis of the strategy proposed at the end of the last chapter, each step for doing uncertainty analysis is detailed throughout some illustrative examples. Then, a complete uncertainty analysis of the KEWPIE2 code (the de-excitation phase) is presented. After that, we shall apply the same framework to the investigation of the inverse problem, that is to say, quantifying the uncertainty connected with the survival and empirical formation probabilities so as to systematically assess the fusion models in a formal manner. Some crucial conclusions are drawn and the prospects are discussed in the end.

VII.1 The GUM framework

Before getting into details on uncertainty analysis, it would be meaningful to provide a brief introduction to the Guide to the expression of Uncertainty in Measurement [200, 201], commonly known as the GUM, which is a fundamental reference document on this subject and has been chosen to serve as the basic framework for the present study.

The GUM is the international standard adopted by many organizations (ISO, BIPM, IUPAP, etc). Together with the international system of units, it is regarded as the frame to express values taken by observables and establishes general rules for evaluating and expressing uncertainty in measurement, which are intended to be applicable to many fields. The uncertainty reflects the lack of exact knowledge of the value of a certain quantity. Despite the fact that a measurement is corrected for systematic effects, it is still only an estimate of the value of the quantity. There always remain uncertainties due to random effects and systematic effects. The uncertainty defined in the GUM corresponds to a parameter describing the dispersion of values that could be reasonably attributed to the outcome. In this sense, once a physical quantity is evaluated from the input data through a functional relationship or a model, uncertainties in the input data should propagate through the model and thus result in an uncertainty in the output quantity.

The methods recommended in the GUM have been widely employed for expressing and quantifying uncertainty. It provides a propagation formula based upon a first-order Taylor series approximation that has, however, a limited range of applications. Once these limitations are exceeded, the final results might become not valid anymore. Accordingly, in addition to the main document of GUM, a number of supplements have been proposed (or under preparation) to extend the uncertainty evaluation to the cases where the application of some basic formulas does not provide reliable results. The first supplement was published in 2008 [5] (GUMS1). It is mainly concerned with the propagation of the input distributions using the Monte-Carlo method, which should be employed when relative uncertainties are large or the relationship between input and output quantities is highly non-linear. Thus, the main concept of the GUMS1 consists in generalizing the propagation of uncertainty discussed in the GUM, such as the perturbation method based upon the Taylor series expansion, and thus provides a more general framework for uncertainty evaluation.

In brief, the GUMS1 proposes an easy-to-use numerical Monte-Carlo approach for propagating input distributions, which goes beyond the limitations inherent to the methods of the GUM. In general, the GUMS1 should be consistent with the GUM, knowing that the basic concepts and the terminology inspiring the guides are almost the same.

VII.2 Basic steps for uncertainty analysis

In this section, we shall concretely formulate the problem we are dealing with here, by linking with the KEWPIE2 model as well as the inverse problem for deducing the empirical

formation probability.

VII.2.1 Modeling the physical system

The main ingredient of a numerical simulation is establishing an abstract mathematical model for describing some basic features of the physical system under study.

In a general way, a model of a certain physical system can be abstracted as a set of multivariate real functions, namely

$$\begin{aligned} \boldsymbol{\mathcal{M}} &: \mathbb{R}^N \to \mathbb{R}^M \\ \boldsymbol{x} &\to \boldsymbol{y} = \boldsymbol{\mathcal{M}}(\boldsymbol{x}), \end{aligned} \tag{VII.1}$$

together with some constraints or restrictions so that the subsequent derivations would make sense. Here, the input parameters of the model can be represented by a N-dimensional vector $\boldsymbol{x} \in D \subset \mathbb{R}^N$, where D denotes the domain of the model function. The vector of M output quantities (or response variables) is thus a M-dimensional vector function. In rare cases, the model might be a simple closed-form function. But more generally, it would correspond to a black-box function, such as a computer program, which requires N input values and then yields some numerical results. It should be mentioned that the model itself can also be changed so that sometimes one has different model functions for the same issue.

In our case, KEWPIE2 is employed to model the fusion-evaporation reaction. As previously introduced, the main input parameters for the decay part are the reduced friction parameter β and the shell-damping energy E_d. It should be noted that the fission barrier has been considered to be model-dependent, instead of a free parameter. Besides input parameters, we have also incorporated several sub-models into the code (cf. the chapter on the KEWPIE2 code). Here, we are interested in the survival probability with respect to the $1n$-channel P_{sur}^{1n}. Accordingly, for a given excitation energy E_C^*, the model function $y = \mathscr{M}(\boldsymbol{x})$ can be written in the following form:

$$P_{\mathrm{sur}}^{1n} = P_{\mathrm{sur}}^{1n}(\beta, E_d), \tag{VII.2}$$

which is simply a scalar-valued model function because we have only one response variable.

In practice, the measured data points on the production cross-section are usually obtained by averaging over a certain range of excitation energy, due to the resolution of the detection set-up and the loss of beam energy in the target. When the calculation is confronted with experimental data, this dispersion effect would be crucially important in the case of SHE formed via cold-fusion reactions, as the survival probability is rather peaked (cf. Fig. VII.1). Therefore, to be close to experimental observables, it is common to take an average over a fixed energy width δE^*, as proposed in Ref. [48]. Thus, the average survival probability is defined as

$$\overline{P}_{\mathrm{sur}}^{1n} = \frac{1}{\delta E^*} \int_{E_C^* - \delta E^*/2}^{E_C^* + \delta E^*/2} P_{\mathrm{sur}}^{1n}(E^*, \beta, E_d) \mathrm{d}E^*, \tag{VII.3}$$

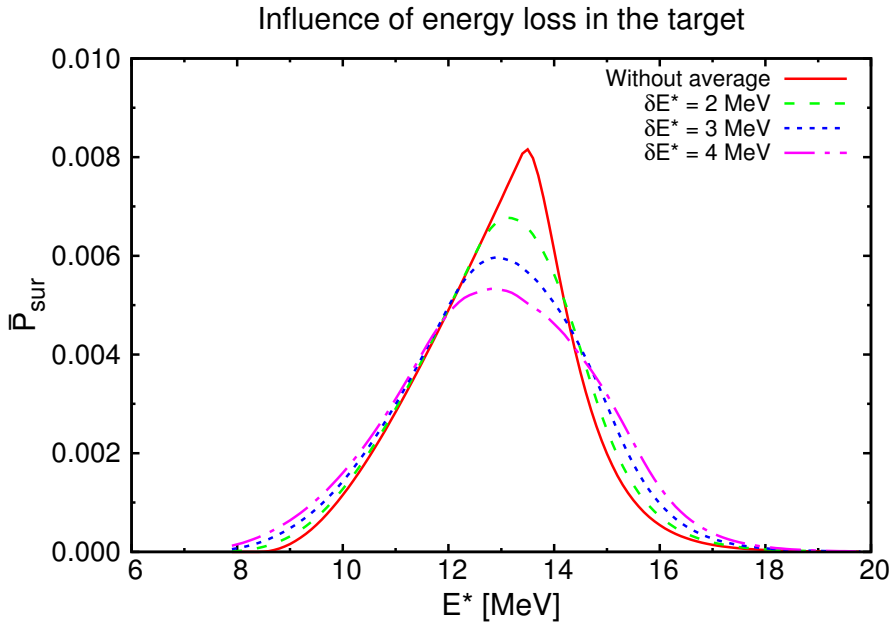

Figure VII.1 – Average of the survival probability for the $1n$-channel over different energy intervals to take into account the loss of beam energy in the target. The solid red curve indicates the calculated survival probability without taking average.

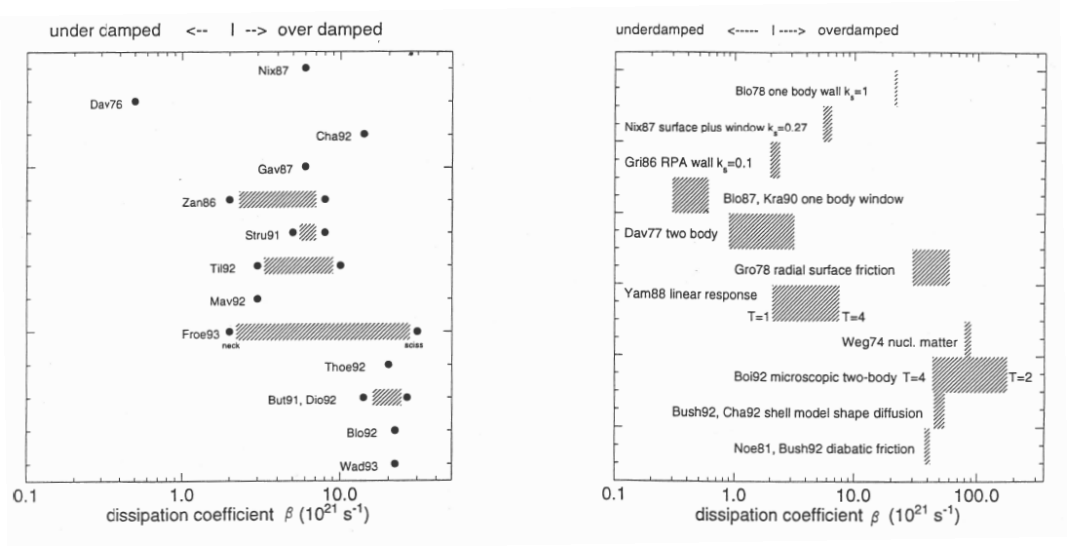

Figure VII.2 – Typical values of the reduced friction parameter that can be found in the literature. The frontier between the under-damped and over-damped regimes is 2.0 zs^{-1}. Figure is taken from Ref. [127].

which is also dependent on the energy loss δE^* in addition to the model parameters. To carry out the integral, we employ the Gauss-Legendre quadrature method (cf. Appendix A). Accordingly, the above equation is practically transformed into a sum of n terms, namely

$$\overline{P}_{\rm sur}^{1n} \simeq \frac{1}{2}\sum_{i=1}^{n} w_i P_{\rm sur}^{1n}(E_C^* + \delta E^* x_i/2, \beta, E_d). \tag{VII.4}$$

The number of abscissas has been chosen to be 12 with a precision of less than 1.0%.

As regards the empirical formation probability, the corresponding model function can be constructed in a similar manner. According to its definition, one readily obtains

$$\overline{P}_{\rm form} = \frac{\sigma_{\rm exp}^{1n}}{\sigma_{\rm cap}\overline{P}_{\rm sur}^{1n}} = \overline{P}_{\rm form}(\delta E^*, \beta, E_d, \sigma_{\rm exp}^{1n}), \tag{VII.5}$$

where the estimation of the capture cross-section is considered to be model-dependent (the WKB approximation or the EBD approach) and the measured data are assumed to be normally distributed. It should be noted that, sometimes, the uncertainty interval associated with the experimental data can also be asymmetric. In this case, the method presented in this chapter is still valid, provided the corresponding distribution is available.

VII.2.2 Identifying and quantifying uncertainty sources

The next step consists in identifying the uncertainty sources that might come up in various contexts and thus quantifying them using probabilistic methods. The common uncertainty sources are roughly summarized as follows [202]:

- Parameter uncertainty, which comes from the input parameters of the model but their exact values cannot be exactly inferred neither theoretically nor experimentally. In practice, one needs to construct some input probability distributions.
- Model uncertainty, which results from the lack of knowledge about the underlying true physics. Thus, it is dependent upon how accurately a model describes the true system in a realistic situation, knowing that models are only rough approximations of reality in most cases. As previously mentioned, to assess model uncertainty, we simply investigate the impact of changing models on the final outcomes.
- Experimental uncertainty, which are directly related to the precision and accuracy of measurements.
- Numerical uncertainty, which arises because of errors corresponding to the implementation of computational methods. We should be aware that most models are too complicated to be solved analytically, so that doing a certain numerical approximation would be necessary. This contribution can be negligible whenever possible.

It should be noted that the first two sources are essentially related to theoretical modeling. In the present case, the values of the input parameters are usually not well determined, that is

to say, we do not know their exact values. This has been well justified throughout the sensitivity analysis as previously introduced. Put differently, it is only likely to know their typical ranges, instead of exact values. Hence, representing the input parameters in a probabilistic manner would make sense. It should be recalled that, in the KEWPIE2 code, the typical ranges of values for the main parameters are summarized as follows:

- The reduced friction coefficient $\beta \sim 1.0 - 9.0$ zs^{-1};
- The damping energy $E_d \sim 13.0 - 25.0$ MeV.

The former one can be justified on the basis of Fig. VII.2, which illustrates typical values of β that can be found in the literature. Here, we mainly focus on the left panel, where the points or shaded bars indicate the values extracted from experimental data. It can be seen that the chosen range of β can cover most of these values. As regards the shell-damping energy, typical values can be found in some recent papers [152, 182], which justify the choice of the range of values for E_d. Accordingly, the default values of the above two parameters are taken to be 5.0 zs^{-1} and 19.0 MeV, namely the average values. It should be noted that the ranges of parameter values chosen here can cover most of the values found in the literature, although they appear to be a bit large. In view of this, smaller ranges, say reduced by 50%, would also be interesting to test in the following study.

Regarding the energy loss in the target δE^*, it is assumed to lie in the range of $2 - 4$ MeV [203]. Unlike the excitation energy, the uncertainty in the beam energy can be safely neglected because typically the relative uncertainty is only a few percents at most.

To determine the probability density function (PDF) associated with each parameter, one needs to take into account all available information. Here, it should be noted that, besides the normalization condition, only the lower and upper limits are available (not that exactly). Hence, according to the principle of maximum entropy theory [204, 205], a uniform probability distribution over the interval $[a, b]$ would be appropriate in such a circumstance [1]. The PDF for this uniform probability distribution will be marked as $U(a, b)$ for the following study. As regards the experimental data, they are considered to follow a Gaussian distribution, namely $N(\mu, \sigma^2)$ with the mean value μ and the variance σ^2. In addition to the parameters, it should be recalled that using different models can also have an impact on the final results. This influence needs to be taken into account during analysis.

The final product of this step is nothing else but a random vector of the input parameters in terms of their corresponding PDFs, namely $g_{\boldsymbol{X}}(\boldsymbol{x})$, which simply means that the parameter uncertainty can be modeled by a random vector, namely $\boldsymbol{X}$. These are actually common notations in probability theory, that is to say, the random variables are denoted by uppercase letters and the deterministic ones by lowercase letters. Thus, the model function $y = \mathscr{M}(\boldsymbol{x})$ is transformed into its probabilistic version, namely $Y = \mathscr{M}(\boldsymbol{X})$, where the output quantity y becomes a random variable Y. The probabilistic character of the random response variable

[1] A detailed list of PDFs under the various moment constraints can be found in Ref. [5].

Y is fully contained in its PDF, denoted by $f_Y(y)$, which is closely related to both the input random vector and the model function. It should be mentioned that the analytical output distribution is rarely available, except in some trivial cases. In practice, as will be shown later, the cumulative distribution function (CDF), represented by $F_Y(y)$, would be more pertinent. By definition, the PDF and the CDF are simply related by

$$F_Y(y) = \int_{-\infty}^{y} f_Y(t)\mathrm{d}t. \tag{VII.6}$$

As will shown later, calculations are generally not carried out in terms of PDFs or histograms, since the resolution of which depends on the choice of bin widths, hence only approximate. The histogram can, however, be useful as an aid to understanding the nature of the PDF, such as the extent of its asymmetry.

VII.2.3 Uncertainty propagation

Following the previous two steps, the stochastic model function has been built to approximately describe the physical phenomenon under consideration. This subsection further explains how to propagate input uncertainties through the model so as to quantify the output uncertainty.

Basically, the method of uncertainty propagation consists in evaluating uncertainties connected with the final outcomes, which are propagated from the input data. One of the main aims of uncertainty propagation is to evaluate lower-order moments of the outcome, namely the mean value and variance. In general, these quantities cannot be directly estimated, except in rare cases. Hence, some approximate methods have to be considered. In this subsection, two common approaches are presented.

Perturbation method

The commonly used perturbation method presented in the main text of the GUM is based upon the Taylor series expansion of the model function around the mean value of the input parameters. Supposing that one has a random input vector $\boldsymbol{X}$ and the Taylor series expansion of the model can be performed around its mean values $\mu_{\boldsymbol{X}} = \{\mu_{X_1}, \ldots, \mu_{X_N}\}$. With the help of the second-order Taylor series expansion of the model function, the expectation of the random model response $Y = \mathscr{M}(\boldsymbol{X})$ is given as

$$\mathrm{E}[Y] = \mathrm{E}[\mathscr{M}(\boldsymbol{X})] \simeq M(\mu_{\boldsymbol{X}}) + \sum_{i=1}^{N} \left.\frac{\partial \mathscr{M}}{\partial x_i}\right|_{\boldsymbol{x}=\mu_{\boldsymbol{X}}} \mathrm{E}[X_i - \mu_{X_i}]. \tag{VII.7}$$

Using the GUM notation for the covariance, namely $\mathrm{E}[(X_i - \mu_{X_i})(X_j - \mu_{X_j})] = u(X_i, X_j)$ and the usual property of the mean value, namely $\mathrm{E}[X_i - \mu_{X_i}] = 0$, the above formula can be further

simplified into

$$\mathrm{E}[Y] \simeq \mathscr{M}(\mu_{\boldsymbol{X}}) + \frac{1}{2}\sum_{i=1}^{N}\sum_{j=1}^{N}\left.\frac{\partial^2\mathscr{M}}{\partial x_i \partial x_j}\right|_{\boldsymbol{x}=\mu_{\boldsymbol{X}}} u(X_i, X_j). \tag{VII.8}$$

Here, $\mathscr{M}(\mu_{\boldsymbol{X}})$ is the first-order approximation of $\mathrm{E}(Y)$, which can be defined as the model response evaluated at the mean value of the input parameters. It should be emphasized that this result is exact if and only if the model $\mathscr{M}$ is an affine function of the input parameters. When neglecting higher-order terms, the above formula simply reduces to $\mathrm{E}[Y] \simeq \mathscr{M}(\mu_{\boldsymbol{X}})$.

With the help of Eq. (VII.7), the variance of the response can be computed as follows:

$$u^2(Y) = \mathrm{Var}(Y) = \mathrm{E}[(Y - \mathrm{E}[Y])^2] \simeq \mathrm{E}[(Y - \mathscr{M}(\mu_{\boldsymbol{X}}))^2]. \tag{VII.9}$$

Hence, by means of Eq. (VII.8) and performing a first-order Taylor series expansion, one obtains the following approximation expression for the variance:

$$u^2(Y) \simeq \sum_{i=1}^{N}\sum_{i=1}^{N}\left.\frac{\partial\mathscr{M}}{\partial x_i}\right|_{\boldsymbol{x}=\mu_{\boldsymbol{X}}}\left.\frac{\partial\mathscr{M}}{\partial x_j}\right|_{\boldsymbol{x}=\mu_{\boldsymbol{X}}} u^2(X_i, X_j). \tag{VII.10}$$

Once the uncertainty has been obtained, to report the final result, one usually needs the following concepts:

- **Expanded uncertainty**. In many practical applications, what is often required is a measure of uncertainty that defines a confidence interval about the final result within which the output value can be confidently assumed to lie. Additionally, the expanded uncertainty, which is obtained by multiplying $u(Y)$ by a coverage factor k, is commonly employed.
- **Coverage factor**. In general, the value of k is chosen on the basis of the desired level of confidence to be associated with the interval. For instance, when the normal distribution applies, one practically has $k = 2$ defines an interval having a level of confidence of approximately 95%. Thus, at a certain confidence level, it is believed that the output quantity is greater than or equal to $\mu_Y - ku(Y)$ and less than or equal to $\mu_Y + ku(Y)$, which is commonly written as $[\mu_Y - ku(Y), \mu_Y + ku(Y)]$.
- **Relative expanded uncertainty**. The relative expanded uncertainty is simply defined as $|ku(Y)/\mu_Y|$, provided that μ_Y is not equal to zero.

In most cases, the confidence interval is typically chosen to be 95%, knowing that this is nothing else but a common convention rather than other choices, such as 90% or 99%. Moreover, it should be kept in mind that the above discussions are only valid in the case of symmetric output distributions.

Monte-Carlo simulation

As proposed in GUMS1, the Monte-Carlo (MC) simulation is adopted in the case of complex systems for calculating the mean value μ_Y and the uncertainty or standard deviation $u(Y)$ associated with the model response. More concretely, supposing that one has a set of samples of the input random, namely $\{\boldsymbol{x}_1, \boldsymbol{x}_2, \ldots, \boldsymbol{x}_S\}$, the random model function is then evaluated for each of the S samples as follows:

$$y_r = \mathscr{M}(\boldsymbol{x}_r),\ r = 1, ..., S. \tag{VII.11}$$

Thus, the usual statistical estimators of these quantities are simply given by

$$\mu_Y = \frac{1}{S}\sum_{r}^{S} \mathscr{M}(\boldsymbol{x}_r), \tag{VII.12}$$

$$u^2(Y) = \frac{1}{S-1}\sum_{r}^{S} \left[\mathscr{M}(\boldsymbol{x}_r) - \mu_Y\right]^2. \tag{VII.13}$$

It is well known that the statistics calculated from a sample set are essentially random variables. In our case, it is practical to run a simple MC simulation, that is to say, in order to provide a set of realizations for an input random vector. As regards the sample size, it can be approximately determined by checking the stability and convergence of the calculated result. At a 95% confidence level, the value of S is determined to be 40000, which would give a numerical error of less than 1%. In the following study, the confidence level will be kept fixed at 95% as usual.

Rigorously, the MC simulation should also provide confidence intervals when reporting the final results. Unlike the perturbation method, this would not be easy because of the fact that output distribution of a non-linear model is usually asymmetric. To obtain the confidence interval, first, one needs the CDF of the output quantity, namely $F_Y(y)$. The estimated CDF, denoted by $\hat{F}_Y(y)$, can be obtained as follows:

- Sorting the values $\{y_r\}$ of the output quantity provided by the MC simulation into non-decreasing order. The sorted values are denoted by $\{y_{(r)}\}$.
- Assigning uniform cumulative probabilities $p_r = (r - 1/2)/S$ to the ordered values.

For more details on this approximation, the reader is referred to Ref. [5]. Finally, once the estimated CDF has been constructed, it is possible to determine the endpoints that define the required confidence interval. Let θ be any value between 0 and $1 - q$. The endpoints of a $100q$% confidence interval, represented by $I_q(Y)$ for the output quantity are $\hat{F}_Y^{-1}(\theta)$ and $\hat{F}_Y^{-1}(\theta + q)$, respectively, or put differently, the θ- and $(\theta + q)$-quantiles of $\hat{F}_Y(y)$ [2].

In the case of symmetric output distributions, the choice of $\theta = 0.025$ gives rise to a 95% confidence interval determined by the 0.025- and 0.975-quantiles. In this case, the probability for the value of Y to be smaller than the left-hand endpoint of the interval or larger than the

[2] It should be recalled that the θ'-quantile of F_Y is a number y' such that $F_Y(y') = \theta'$.

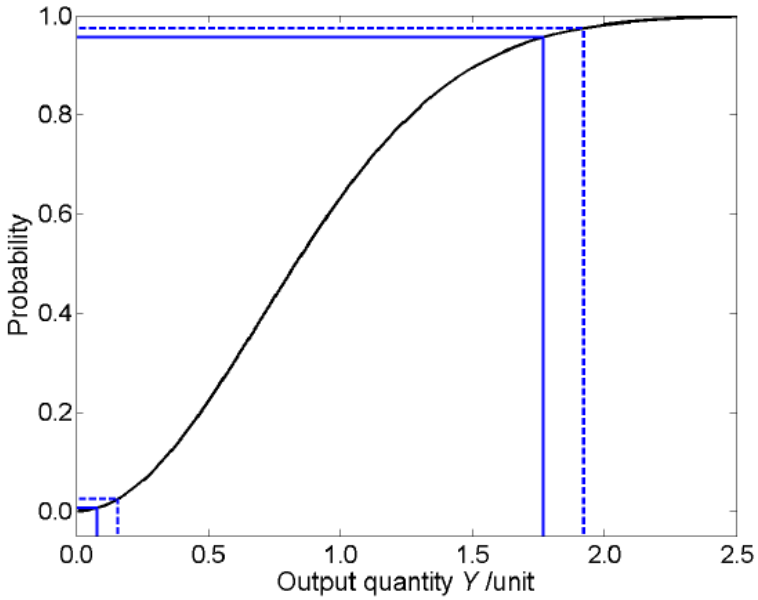

Figure VII.3 – Illustration of how to determine the shortest confidence interval for a given asymmetric distribution using its CDF. Dotted vertical lines represent the endpoints of the probabilistically symmetric 95% confidence interval and broken horizontal lines the corresponding probability points, namely 0.025 and 0.975. Solid lines mark the endpoints of the shortest 95% confidence interval and the corresponding probability points, which are 0.006 and 0.956 in this case. The lengths of the 95% coverage intervals in the two cases are 1.76 unit and 1.69 unit, respectively. Figure is taken from Ref. [5].

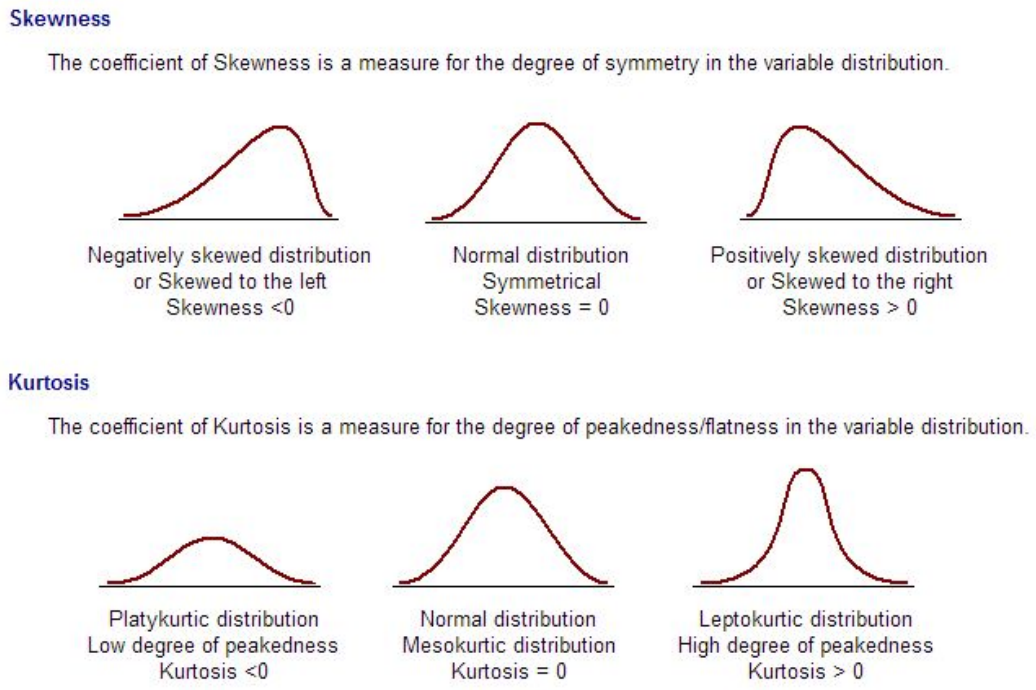

Figure VII.4 – Illustration of the asymmetric distribution characterized by the skewness and kurtosis parameters. Figure is taken from the website.

right-hand one is the same, that is to say, 0.025. The confidence interval is thus symmetric about the estimate of the output quantity, namely μ_Y.

What if the output distribution becomes asymmetric? A value of θ different from 0.025 would generally be pertinent. In this case, the shortest confidence interval should be adopted and can generally be obtained numerically from the estimated CDF by choosing a specified value of θ, say θ^*, such that the difference $\hat{F}_Y^{-1}(\theta^* + q) - \hat{F}_Y^{-1}(\theta^*)$ is a minimum. Fig. VII.3 shows an example of how to determine the shortest confidence interval for a given asymmetric distribution. For more details on the practical algorithm, the reader is referred to Ref. [5].

Shape of distributions

As can be seen from the above discussion, the confidence interval is mainly dependent on the shape of an output distribution.

It would be useful to remind the reader that, to formally estimate the shape of output distributions, one of the most commonly used statistical estimators is nothing else but the skewness parameter. According to the mathematical definition, for a given random variable Y, the skewness corresponds to the third standardized moment, which can be given as follows:

$$\mathrm{E}\left[\left(\frac{Y-\mu}{\sigma}\right)^3\right] = \frac{\mathrm{E}\left[(Y-\mu)^3\right]}{\mathrm{E}\left[(Y-\mu)^2\right]^{3/2}}, \tag{VII.14}$$

where μ is the mean value and σ the standard deviation. They can be readily estimated using Eqs. (VII.12) and (VII.13). Aside from skewness, another useful shape parameter is kurtosis. It simply corresponds to a higher-order moment, namely the forth standardized moment, which is defined as follows:

$$\mathrm{E}\left[\left(\frac{Y-\mu}{\sigma}\right)^4\right] - 3 = \frac{\mathrm{E}\left[(Y-\mu)^4\right]}{\mathrm{E}\left[(Y-\mu)^2\right]^2} - 3, \tag{VII.15}$$

As a reference example, the skewness and kurtosis of a normal distribution are both equal to zero, as illustrated in Fig. VII.4. In general, these two shape parameters define how data are distributed, but do not affect the location or scale of distributions. In the following study, they will be employed to characterize the shape of output distributions, which are usually not symmetric.

VII.2.4 Summary

Up to now, the formal procedure to perform uncertainty analysis of a certain numerical model has been detailed. This procedure is essentially based upon the suggestions given in GUMS1 which serves as the international standard.

As a result, two model functions have been constructed in our case, namely the average

survival probability and the empirical formation probability, which are defined as follows:

$$\overline{P}^{1n}_{\text{sur}} = \overline{P}^{1n}_{\text{sur}}(\delta E^*, \beta, E_d), \tag{VII.16}$$

and

$$\overline{P}_{\text{form}} = \overline{P}_{\text{form}}(\delta E^*, \beta, E_d, \sigma^{1n}_{\text{exp}}), \tag{VII.17}$$

respectively.

Regarding the PDFs for the model parameters, they are summarized as follows:

- σ^{1n}_{exp} is assumed to be normally distributed.
- $\delta E^* \sim U(2,4)$. Note that for each value of δE^*, the average of the survival probability has been taken (cf. Eq. (VII.3)).
- $\beta \sim U(1.0\times10^{21}, 9.0\times10^{21})$.
- $E_d \sim U(13.0, 25.0)$.

The above ranges of parameter values are considered to be the pessimistic case, which simply means that they appear to be somewhat large but can cover most of parameter values found in the literature. It would also be instructive to take a look into the effects of using smaller ranges of values on the final results. In this case (optimistic), the values of reduced friction parameter and the shell-damping energy are considered to lie within the following ranges:

- $\beta \sim U(3.0\times10^{21}, 7.0\times10^{21})$.
- $E_d \sim U(16.0, 22.0)$.

Put differently, the uncertainties in these two input parameters are reduced by 50%. It is expected that the uncertainty intervals will not be the same in pessimistic and optimistic cases.

In addition to the input parameters, the effects of changing models (model functions) on the calculated results should also be examined. Here, we mainly focus on the correction factors, namely the collective enhancement factor and the Kramers-Strutinsky factor, as well as the fission-barrier models, the level-density parameters and the capture models, which are considered to be the main physical ingredients included in the code.

It should be recalled that the default parameter values and models have been concretely presented in a previous chapter on the KEWPIE2 code. To briefly summarize, the EBD method for estimating capture cross-sections, the Tōke-Świątecki model for the level-density parameter, the Thomas-Fermi model for calculating fission barriers, the collective enhancement and the Kramers-Strutinsky factors have been included by default. The reader is referred to this chapter for more detailed information.

The MC approach will be employed to propagate input distributions through the model, as the uncertainty associated with each of the input parameters is considerably large. In the present work, the GSL scientific library [206] has been employed to generate uniform and

normal random numbers for input distributions, on the basis of the methods proposed in GUMS1. The perturbation method based upon the first-order Taylor series expansion would not be appropriate in such cases. However, as will be seen in a later chapter on the liquid-drop model, the perturbation method can be regarded as a good approximation for estimating the uncertainties connected with the fission barrier and neutron separation energy.

VII.3 Selection of experimental data

The experimental data employed in this chapter are mainly taken from Refs. [190, 207, 208]. As previously mentioned, to extract the formation probability, the experimental data are assumed to be normally distributed. Therefore, we only focus on the ones with symmetric uncertainty bars, even though there are more measured data in the literature. The selected reaction systems and the corresponding maximum production cross-sections are summarized in Tab. VII.1.

As a whole, it is clearly demonstrated that the maximal production cross-section drops considerably with increasing atomic number from $Z = 104$ to $Z = 108$, whereas the measurement uncertainty gradually rises due to increasing experimental difficulty.

VII.4 Uncertainty in $\overline{P}^{1n}_{\mathbf{sur}}$

In this section, we systematically analyze the theoretical uncertainty connected with the survival probability for the single-neutron evaporation. For this purpose, we start by showing an illustrative case, namely investigating the cold-fusion reaction leading to the production of the element Hs at its optimum energy, using the methods of uncertainty propagation. Then, a systematic study is carried out for all the cold-fusion reactions listed in Tab. VII.1.

VII.4.1 Influence of input distributions

Fig. VII.5 illustrates the estimated distribution of the survival probability by means of the KEWPIE2 code when the input parameters all vary within their pessimistic intervals. As

Table VII.1 – Experimental data for the $1n$-channel with the optimum energy and the corresponding maximal ER cross-section. The data are taken from Refs. [190, 207, 208].

Reaction	Z_C	A_C	E_{cm} [MeV]	$\max \sigma^{1n}_{\mathrm{exp}}$ [pb]
^{208}Pb(^{50}Ti,1n)^{257}Rf	104	258	185.02	$10\,419^{+1\,284}_{-1\,284}$
^{209}Bi(^{50}Ti,1n)^{258}Db	105	259	187.50	$2\,200^{+240}_{-240}$
^{208}Pb(^{54}Cr,1n)^{261}Sg	106	262	202.01	$2\,520^{+253}_{-253}$
^{209}Bi(^{54}Cr,1n)^{262}Bh	107	263	205.81	163^{+34}_{-34}
^{208}Pb(^{58}Fe,1n)^{265}Hs	108	266	219.27	69^{+12}_{-12}

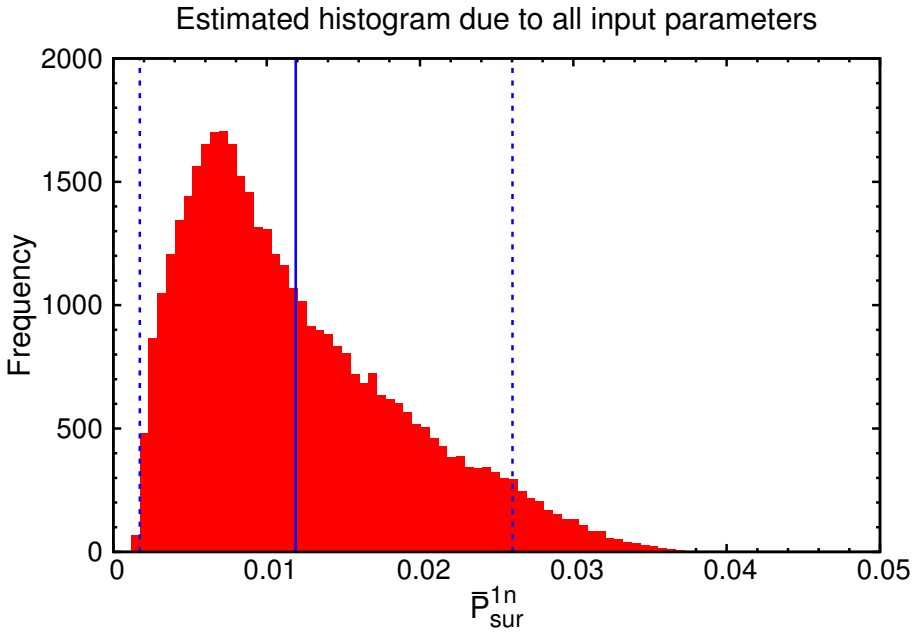

Figure VII.5 – Estimated distribution of the survival probability for the 1n-channel. The vertical solid line represents the mean value. The vertical dotted lines refer to the lower and upper bounds of the 95% confidence interval, respectively. The pessimistic case is considered here.

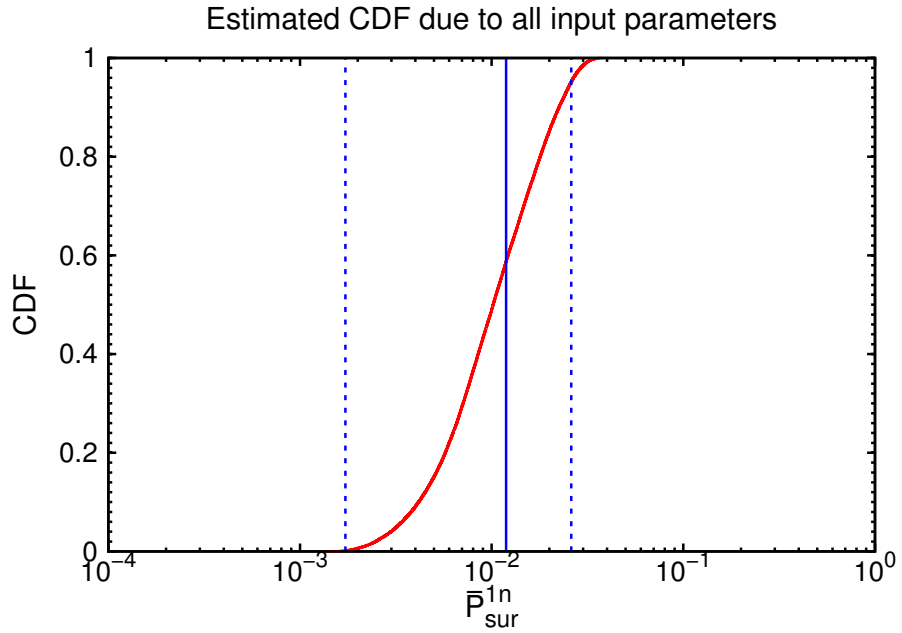

Figure VII.6 – Estimated CDF of the average survival probability for the 1n-channel. The vertical solid line represents the mean value. The vertical dotted lines refer to the lower and upper bounds of the 95% confidence interval, respectively. Note that the horizontal axis is in logarithmic scale.

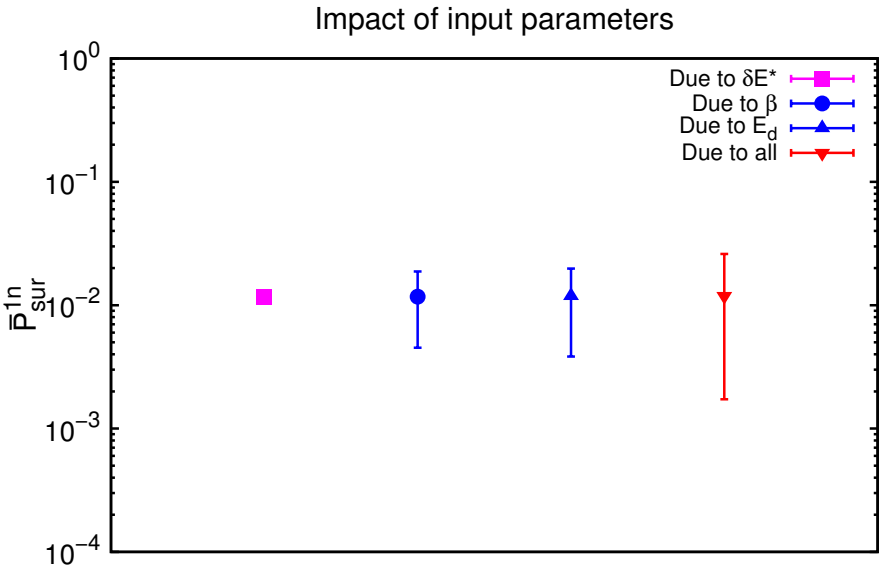

Figure VII.7 – Impact of input distributions on the uncertainties associated with the survival probability. Note that the pessimistic case is considered here.

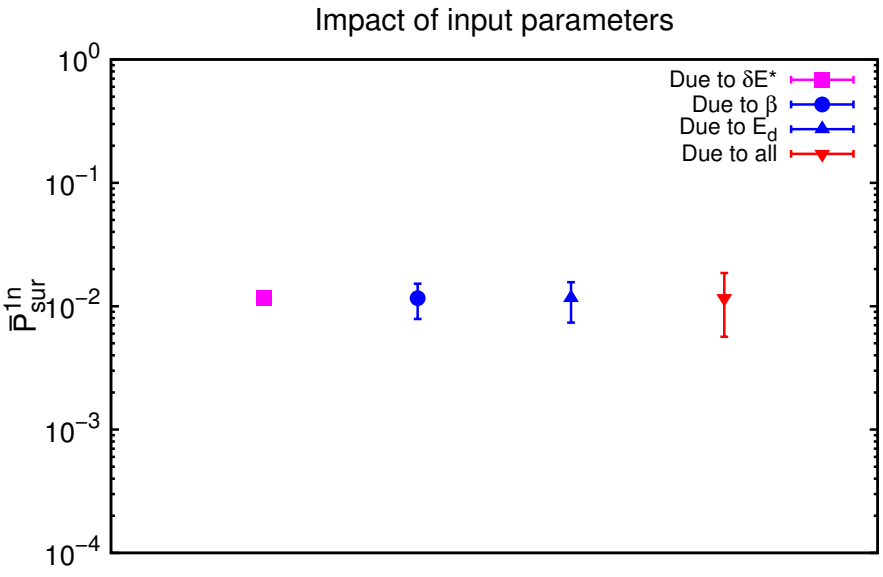

Figure VII.8 – Impact of input distributions on the uncertainties associated with the survival probability. Note that the pessimistic case is considered here.

previously mentioned, to obtain the confidence interval, it would be necessary to examine the shape of output distributions. Knowing that the skewness parameter is estimated to be 0.857, that is to say, the output distribution is skewed to the left or has a relatively long tail on the right hand side. Fig. VII.6 shows the corresponding CDF of the output quantity. Here, the lower and upper bounds of the 95% confidence interval can be estimated using the methods previously described.

The uncertainties connected with the average survival probability due to each of the input distributions are displayed in Fig. VII.7. Each point stands for the mean value of the output quantity, together with their 95% confidence intervals. The first one on the left is due to the effect of energy loss related to the target thickness. The upper bound is shown to be higher than the lower one by a factor of about 1.2, which means that the uncertainty associated with the energy loss appears to have a minor influence on the uncertainty related to the average survival probability. The following two points are due to the reduced friction parameter β and the shell-damping energy E_d, respectively. Their confidence intervals appear to have similar amplitudes. However, considering that the relative uncertainty of β is about 46%, which is much larger than that of E_d (about 18%), the uncertainty associated with the average survival probability is more sensitive to the damping energy. This is mainly because the shell-correction energy strongly influences the survival probability. In the case of super-heavy nuclei, the macroscopic fission barrier is known to gradually disappear, that is to say, only the shell-correction energy contributes to the total fission-barrier height. Hence, as a rough approximation, the effective fission barrier can be expressed as $|\Delta E_{\mathrm{sh}}| \exp(-E_C^*/E_d)$. Therefore, compared to the reduced friction parameter, a small change in the damping energy could lead to a large variation in the effective fission barrier and thus significantly affects the survival probability. Finally, when taking into account all the input distributions, the confidence interval spans slightly more than one order of magnitude, which is reasonably much larger compared to the individual ones.

In Fig. VII.8, we also investigate the influence of smaller input uncertainties on the final results. In the optimistic case, we have reduced the intervals for input parameter by 50%, but the mean values basically remain the same. Accordingly, the total uncertainty is decreased by about the same factor. This result unambiguously indicates that further constraints on the input parameters would have a crucial role to play in reducing the total uncertainty associated with the average survival probability.

VII.4.2 Influence of models

In this subsection, we would like to take a closer look at the impact of changing models on the final outcomes. Regarding the input distributions, all the input parameters have been taken into account to determine the 95% confidence interval under the pessimistic hypothesis of parameter intervals.

Fig. VII.9 shows how different correction factors affect the mean value and the confidence

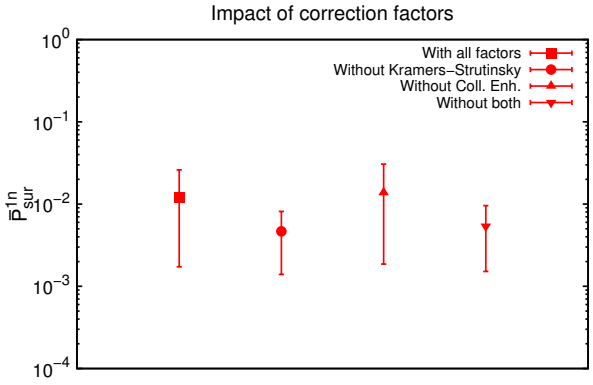

Figure VII.9 – Impact of correction factors on the survival probability. Note that the uncertainty interval is due to all parameters in the pessimistic case.

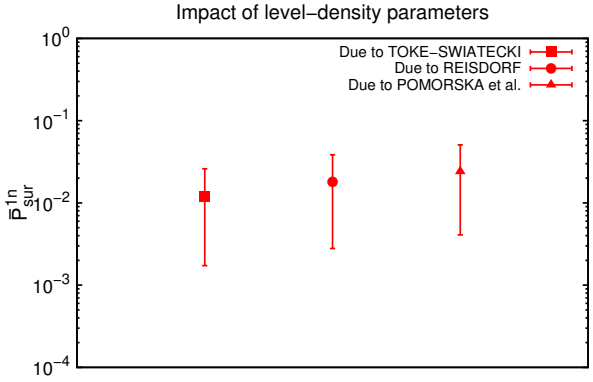

Figure VII.10 – Impact of level-density parameters on the survival probability. Note that the uncertainty interval is due to all parameters in the pessimistic case.

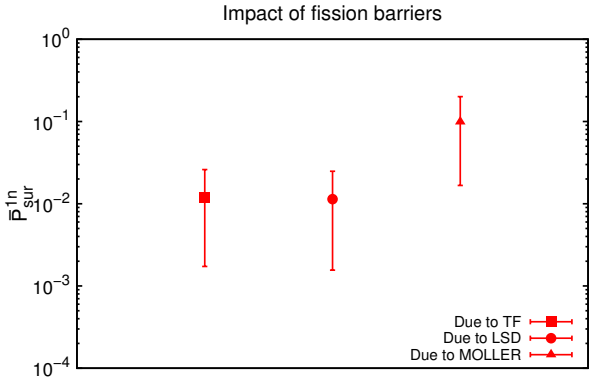

Figure VII.11 – Impact of fission barriers on the survival probability. Note that the uncertainty interval is due to all parameters in the pessimistic case.

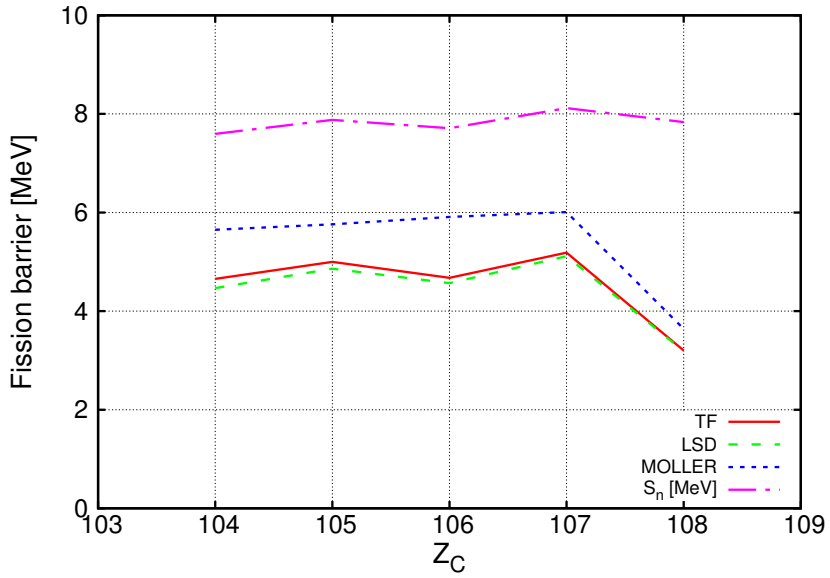

Figure VII.12 – Comparison of the calculated fission barriers of compound nuclei based upon the different models. In addition, the dash-dotted line indicates the neutron-separation energies for the same compound nuclei.

interval of the average survival probability. Without the Kramers-Strutinsky factor, the mean value slightly decreases by a factor of about 2, whereas it becomes slightly higher after taking out the collective enhancement factor. These results are therefore compatible with those obtained in the previous chapter on the KEWPIE2 code. As regards the amplitudes of their confidence intervals, it can be clearly seen that the interval becomes about twice narrower without considering the Kramers-Strutinsky factor, due to the fact that the reduced friction parameter has been jointly removed.

Fig. VII.10 displays the impact of different level-density parameters on the mean value and the confidence interval of the survival probability. It is clearly demonstrated that the mean value of the survival probability rises by a factor of around 2 at most, which appears to be the same amplitude as the previous case. Nevertheless, the amplitudes of their confidence intervals do not change so much because all the input parameters are considered in the model.

Fig. VII.11 displays how different fission-barrier models affect the mean value and the confidence interval of the average survival probability. Unlike the above two cases, the mean values can differ by almost one order of magnitude, which appears much more significant. To understand the reason behind this large influence, it would be meaningful to compare the estimated fission-barrier heights based upon the different models. As shown in Fig. VII.12, the fission barriers estimated on the basis of the Möller *et al.*'s model are generally higher than those based upon the TF or LSD models and thus result in a much lower survival probability. To this extent, the fission-barrier height is considered to be the most crucial factor for determining the average survival probability.

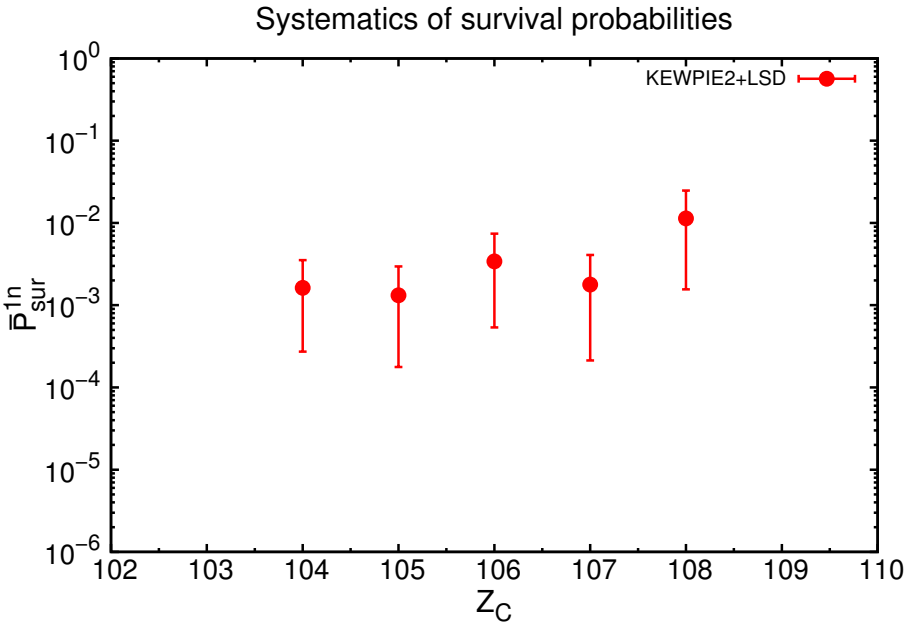

Figure VII.13 – Systematic comparison of the calculated mean values as well as the confidence intervals of the survival probability for the cold-fusion reactions leading to the synthesis of elements from $Z = 104$ to $Z = 108$ (cf. Tab. VII.1). The fission barriers are estimated using the LSD model. Note that the uncertainty interval is due to all parameters in the pessimistic case.

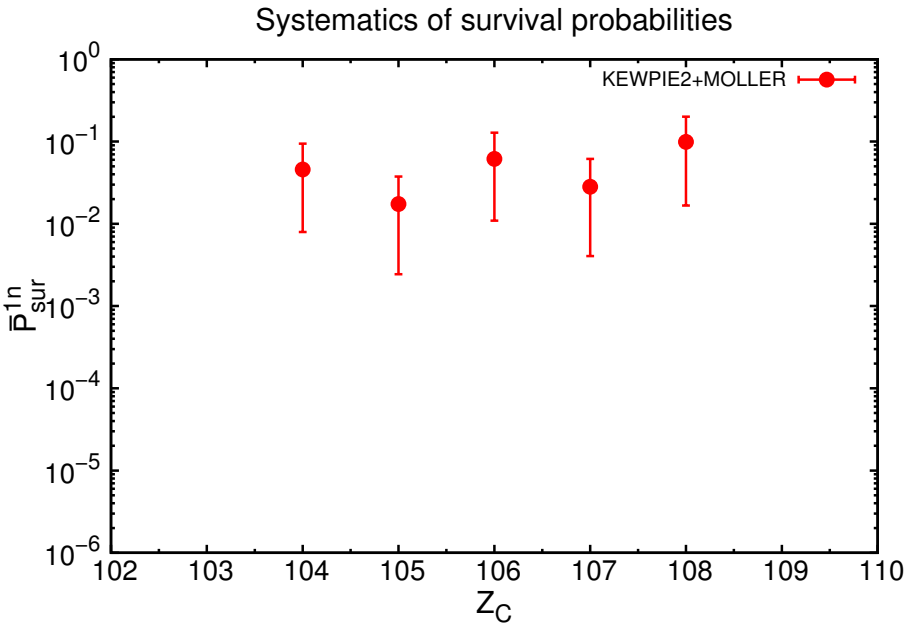

Figure VII.14 – Systematic comparison of the calculated mean values as well as the confidence intervals for the cold-fusion reactions leading to the synthesis of elements from $Z = 104$ to $Z = 108$ (cf. Tab. VII.1). The fission barriers are estimated using the Möller *et al.*'s model. Note that the uncertainty interval is due to all parameters in the pessimistic case..

VII.4.3 A systematic comparison and discussion

In this subsection, we attempt to make a systematic comparison of average survival probabilities with respect to the selected cold-fusion reactions.

The calculated results are systematically shown in Figs. VII.13 and VII.14. The mean values and the associated confidence intervals of the average survival probability for the cold-fusion reactions leading to the production of elements from $Z = 104$ to $Z = 108$ are estimated and carefully compared. The positions of mean values appear to be closely correlated with the neutron-separation energies and the corresponding fission barriers of the compound nuclei (cf. Fig. VII.12). Moreover, it is clearly demonstrated that, on average, the mean values based upon two extreme fission-barrier models could differ by one order of magnitude. In comparison, the amplitudes of confidence intervals are almost the same, around one order of magnitude on average, under the pessimistic assumption for the input parameters and at a 95% confidence level.

This study would be essential for understanding the contradictions between calculated formation probabilities and ER cross-sections, as discussed in the previous chapter. More concretely, it was clearly shown that the calculated formation probabilities can differ by around two orders of magnitude as a whole. The conclusion obtained here thus provides a possible explanation to this serious problem. Since the uncertainty associated with the average survival probability is almost the same as that of formation probabilities, it seems likely to adjust the former one in order to exactly reproduce the experimental data. Intuitively, this would be the main reason why all fusion models provide very different estimates of the formation probability, even though they systematically converge to the measured production cross-sections. In other words, some parameter values should be adjusted to reproduce similar results to the measured data. If the experimental data are not available, one can imagine that the predictive capability of a fusion model would be somewhat terrible.

In the next section, using the same method of uncertainty analysis, we shall concentrate on the inverse problem, namely, extracting the empirical formation probabilities from the available experimental data, so as to provide a systematic comparison of the results based upon different fusion models.

VII.5 Uncertainty associated with $\overline{P}_{\mathbf{form}}$

Like in the previous section, we would like to start by showing an illustrative example for the same cold-fusion reaction leading to the formation of element Hs at its optimum energy.

VII.5.1 Influence of input distributions

Fig. VII.15 illustrates the estimated distribution of the empirical formation probability obtained by means of the KEWPIE2 code together with available production cross-sections. It

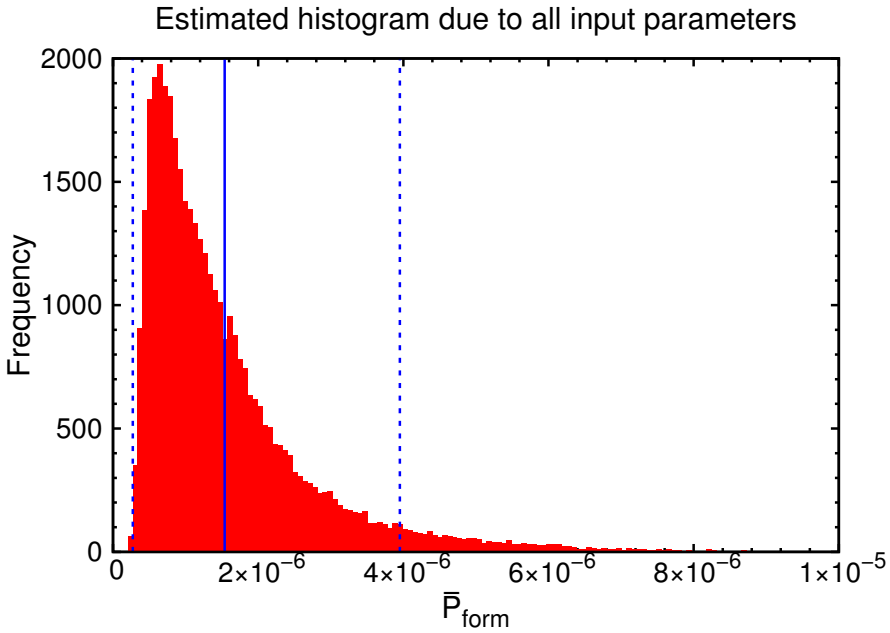

Figure VII.15 – Estimated distribution of the empirical formation probability. The solid vertical line represents the mean value. The vertical dotted lines refer to the lower and upper bounds of the 95% confidence interval, respectively. The pessimistic case is considered here.

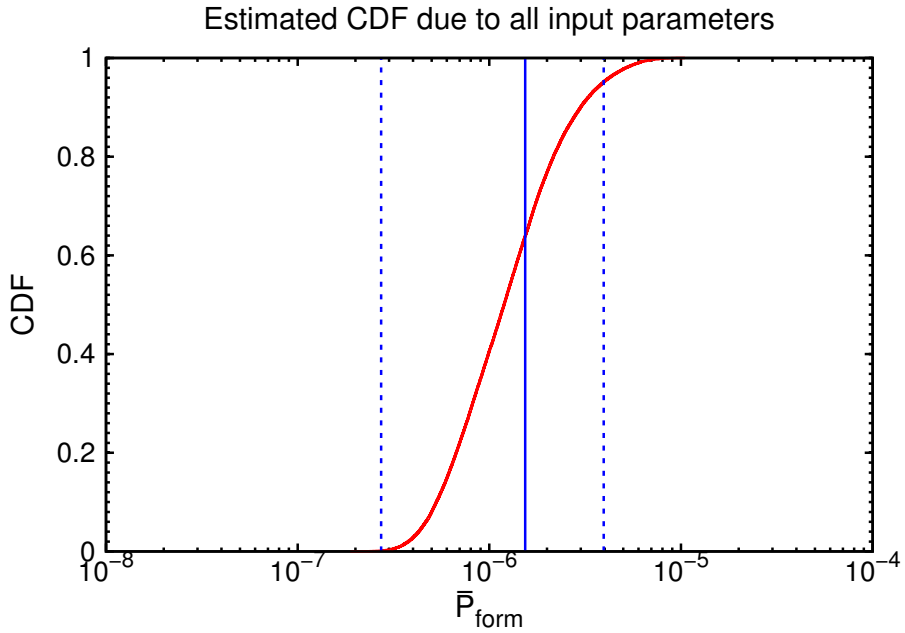

Figure VII.16 – Estimated CDF of the empirical formation probability. The solid vertical line represents the mean value. The vertical dotted lines refer to the lower and upper bounds of the 95% confidence interval, respectively. Note that the horizontal axis is in logarithmic scale.

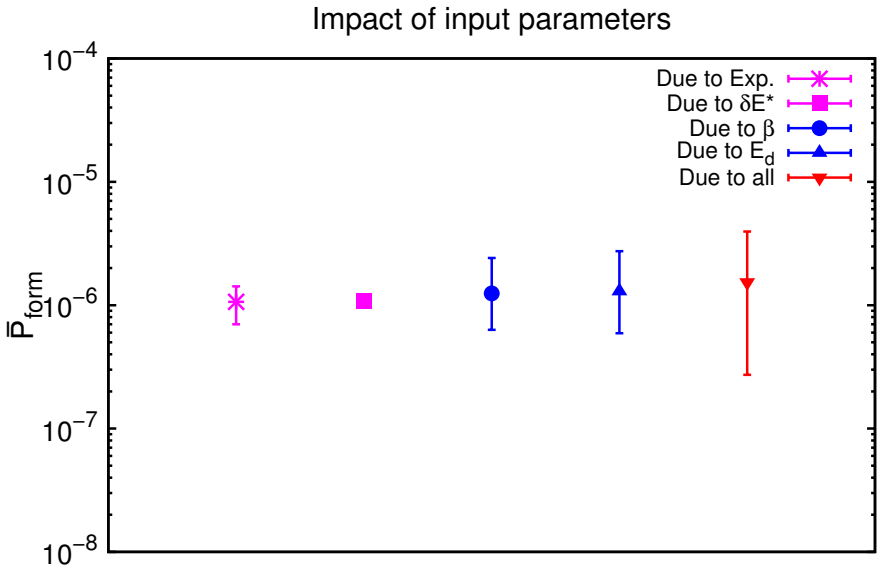

Figure VII.17 – Impact of input distributions on the uncertainties associated with the empirical formation probability. The pessimistic case is considered here.

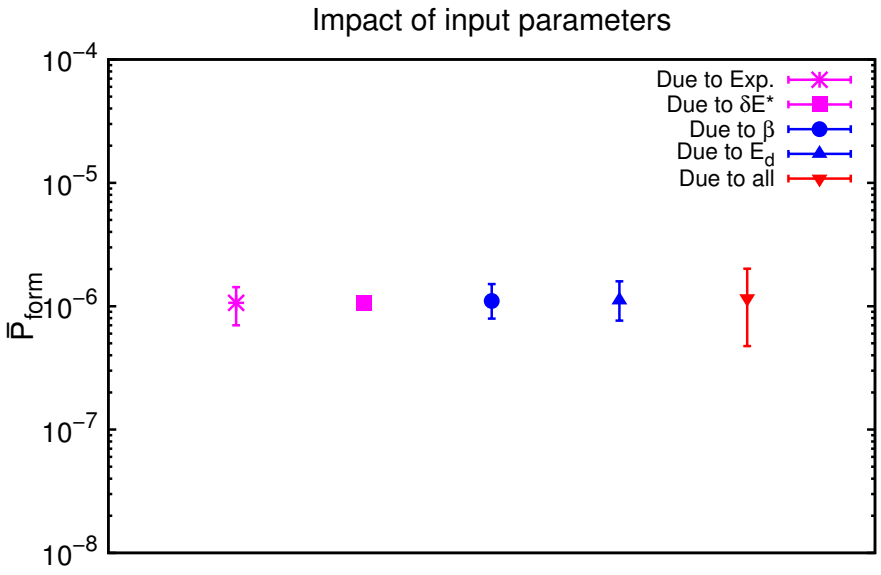

Figure VII.18 – Impact of input distributions on the uncertainties associated with the empirical formation probability. The optimistic case is considered here.

should be mentioned that all the input parameters have been included in calculations under the pessimistic hypothesis. In this case, the skewness parameter is estimated to be 2.087, so that the shape of distribution is highly skewed to the left, that is to say, has a long tail on the right hand side and thus results in a quite asymmetric confidence interval. The mean value is hence located on the right side of the peak value. In addition, Fig. VII.15 clearly displays the corresponding CDF. Their lower and upper bounds of the 95% confidence interval have been estimated using the same techniques.

The separate uncertainties associated with the empirical formation probability due to each of the input distributions are displayed in Fig. VII.17. Each point stands for the mean value of the output quantity, together with its 95% confidence interval. It should be noted that, owing to the experimental uncertainty, an additional input distribution is taken into consideration for extracting the empirical formation probability. This is represented by the first point on the left, together with its confidence interval, whose upper bound is higher than the lower one by a factor of less than 2. The following three points are connected with the energy loss in the target, reduced friction parameter β and shell-damping energy E_d, respectively. One can clearly notice that the theoretical contribution is always dominant. This is simply due to the fact that β and E_d are closely related to the fission process which is the ruling decay channel for SHE. It should also be recalled that the relative uncertainty of β is about 46%, which is much larger than that of E_d estimated to be about 18%, the uncertainty related to the empirical formation probability would be more sensitive to the shell-damping energy. Finally, when including all the input distributions, the confidence interval spans slightly more than one order of magnitude, which is much larger compared to the individual ones. This result is thus compatible with the previous case, namely the average survival probability. It is thus established that the experimental data appear to have only a minor influence on the final outcomes for this system due to the fact that experimental measurement in this case seems to be quite precise.

In the end, when reducing the intervals of parameter values by 50%, Fig. VII.18 clearly demonstrates that the total uncertainty is also decreased by almost the same factor. This result also indicates that further constraints on these two critical model parameters would be able to reduce the total uncertainty connected with the empirical formation probability so as to constrain the fusion models.

VII.5.2 Influence of models

In this subsection, we investigate the impact of changing models on deduced formation probabilities from the experimental data.

Fig. VII.19 shows how two capture models influence the mean value and confidence interval of the empirical formation probability. It should be recalled that two different approaches, namely the WKB approximation and the EBD method, have been considered in the present study. In general, the results based upon there two approaches seem to differ by a factor of

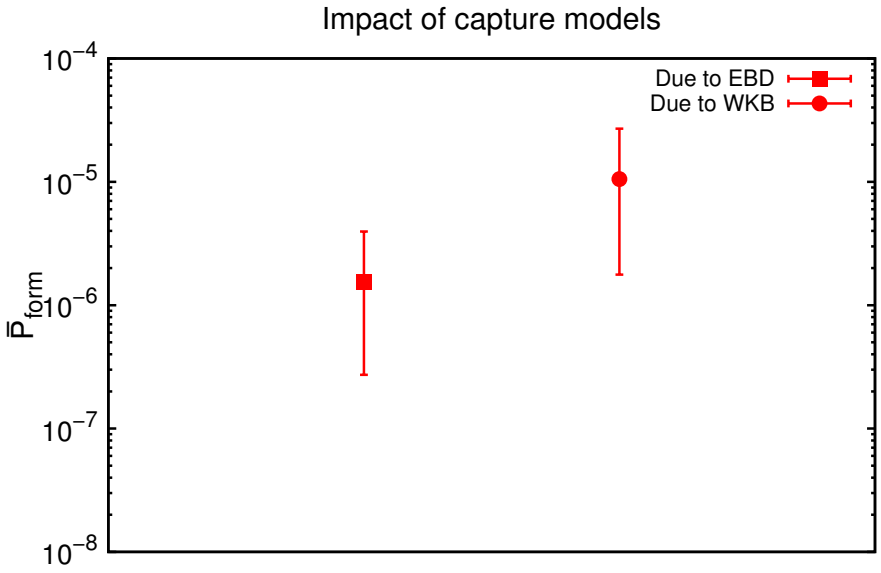

Figure VII.19 – Impact of capture models on the empirical formation probability. Note that the uncertainty interval is due to all parameters in the pessimistic case.

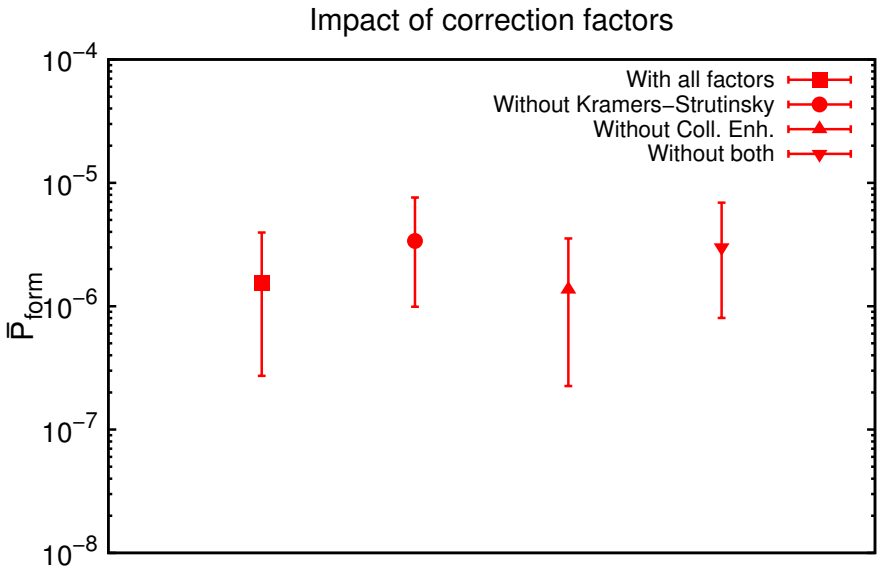

Figure VII.20 – Impact of correction factors on the empirical formation probability. Note that the uncertainty interval is due to all parameters in the pessimistic case.

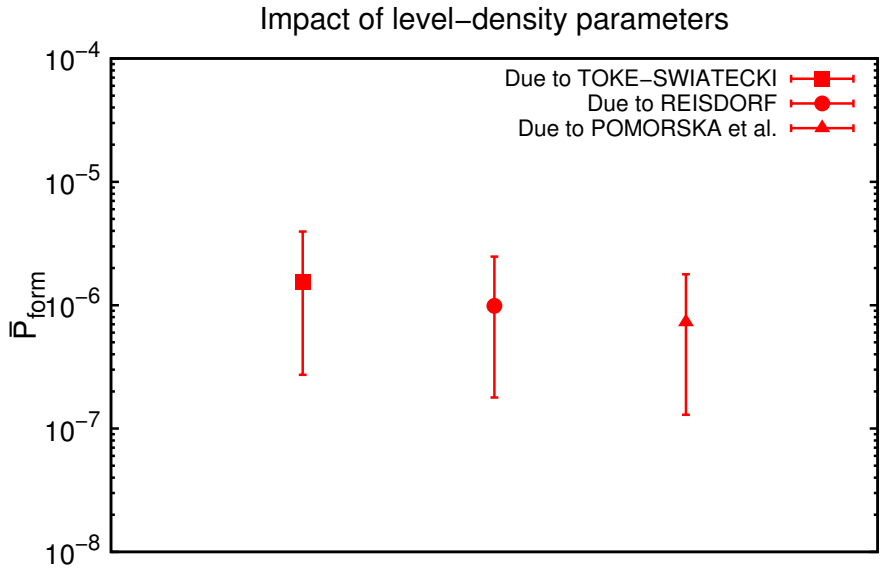

Figure VII.21 – Impact of level-density parameters on the empirical formation probability. Note that the uncertainty interval is due to all parameters in the pessimistic case.

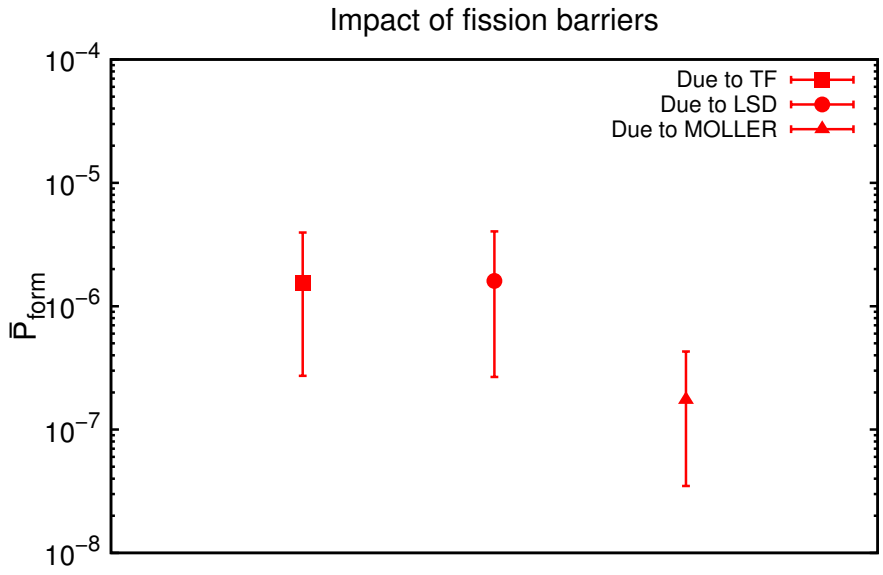

Figure VII.22 – Impact of fission barriers on the empirical formation probability. Note that the uncertainty interval is due to all parameters in the pessimistic case.

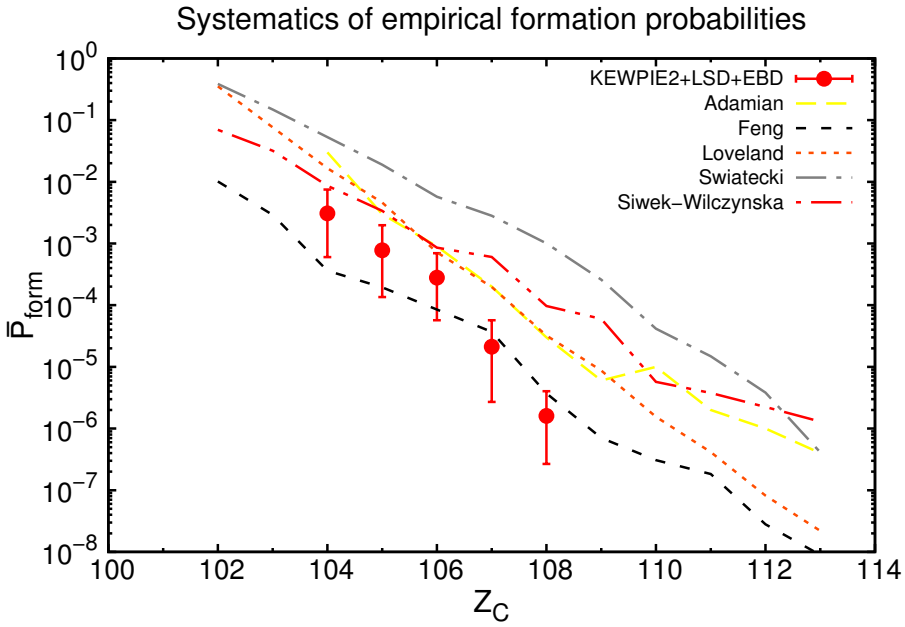

Figure VII.23 – Systematic comparison of the calculated mean values as well as the confidence intervals of the empirical formation probability for the cold-fusion reactions leading to the synthesis of the elements from $Z = 104$ to $Z = 108$ (cf. Tab. VII.1). The fission barriers are estimated using the LSD model. The theoretical data are adapted from Ref. [4].

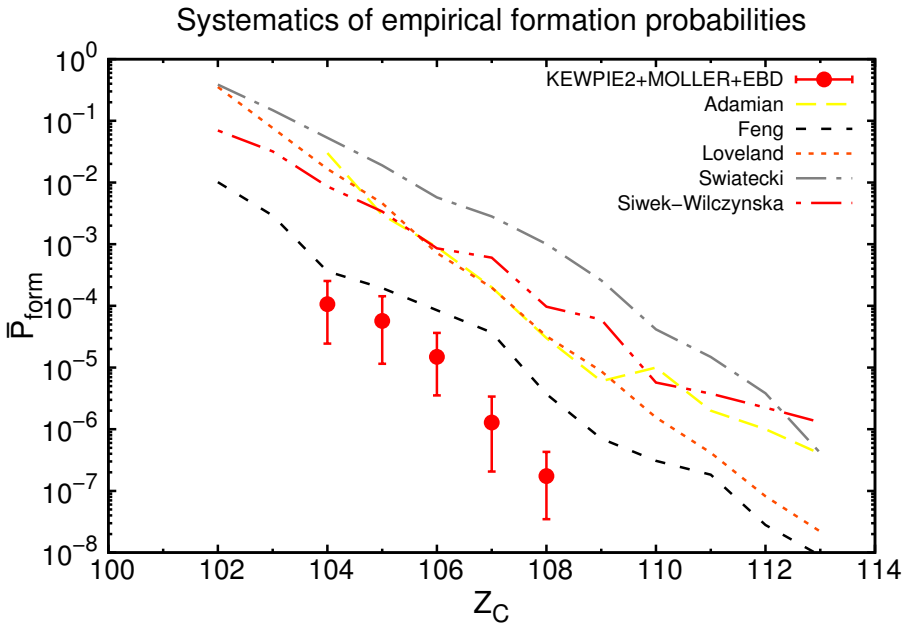

Figure VII.24 – Systematic comparison of the calculated mean values as well as the confidence intervals of the empirical formation probability for the cold-fusion reactions leading to the synthesis of the elements from $Z = 104$ to $Z = 108$ (cf. Tab. VII.1). The fission barriers are estimated using the Möller *et al.*'s model. The theoretical data are adapted from Ref. [4].

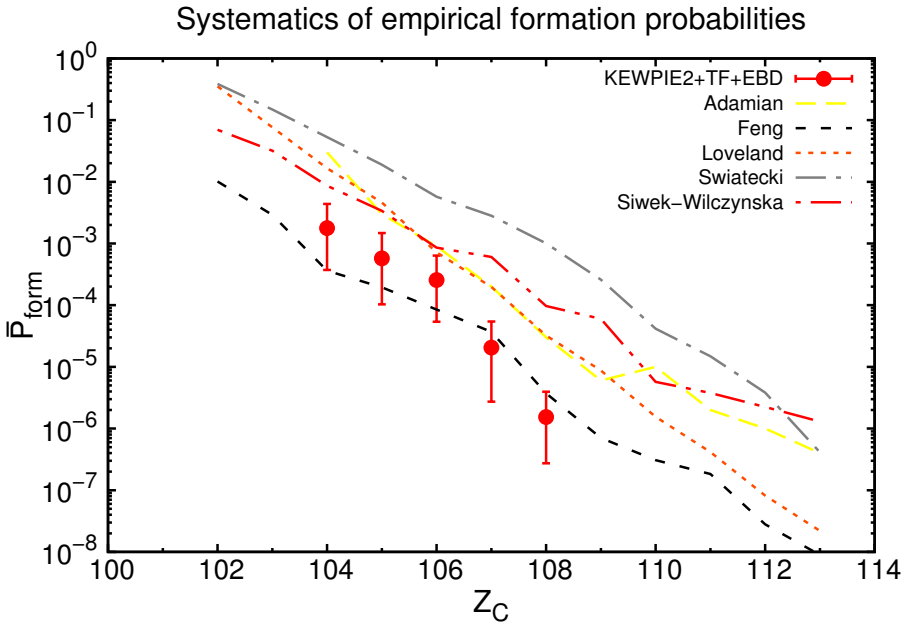

Figure VII.25 – Systematic comparison of the calculated mean values as well as the confidence intervals of the empirical formation probability for the cold-fusion reactions leading to the synthesis of the elements from $Z = 104$ to $Z = 108$ (cf. Tab. VII.1). The capture cross-section is estimated using the EBD approach. The theoretical data are adapted from Ref. [4].

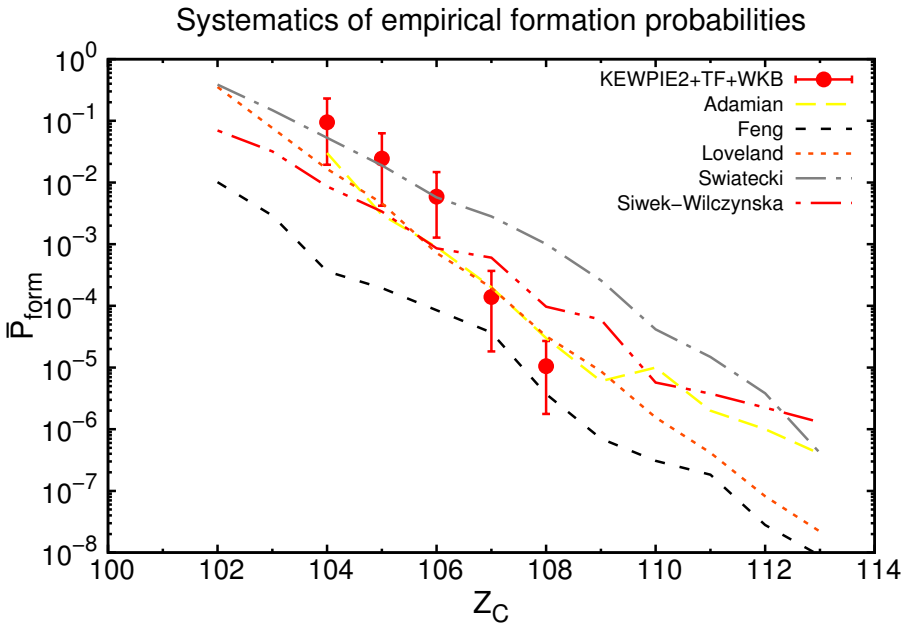

Figure VII.26 – Systematic comparison of the calculated mean values as well as the confidence intervals of the empirical formation probability for the cold-fusion reactions leading to the synthesis of the elements from $Z = 104$ to $Z = 108$ (cf. Tab. VII.1). The capture cross-section is estimated using the WKB approximation. The theoretical data are adapted from Ref. [4].

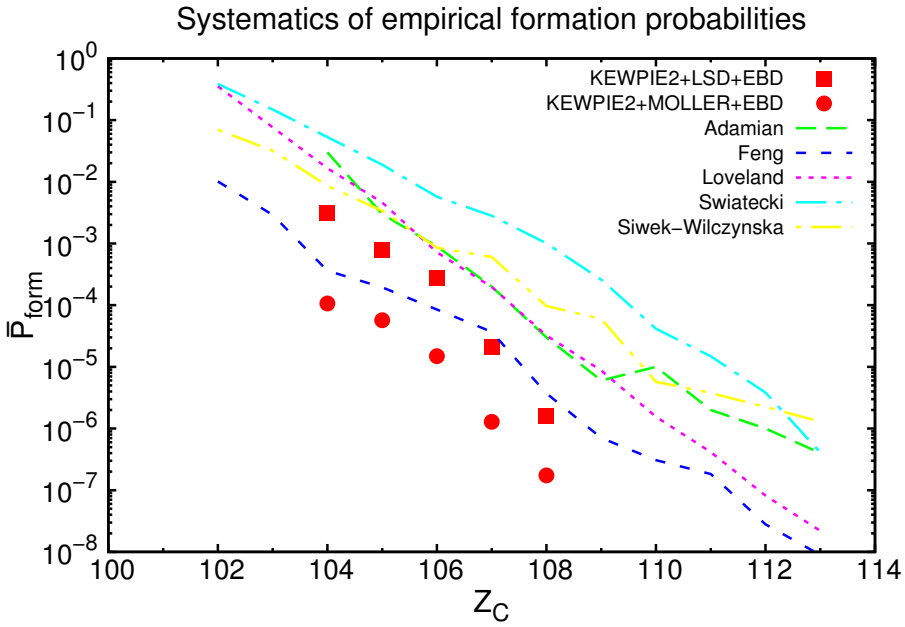

Figure VII.27 – Systematic comparison of the calculated mean values of the empirical formation probability for the cold-fusion reactions leading to the synthesis of the elements from $Z = 104$ to $Z = 108$ (cf. Tab. VII.1). The deduced formation probabilities are based upon two different fission-barrier models. The theoretical data are adapted from Ref. [4].

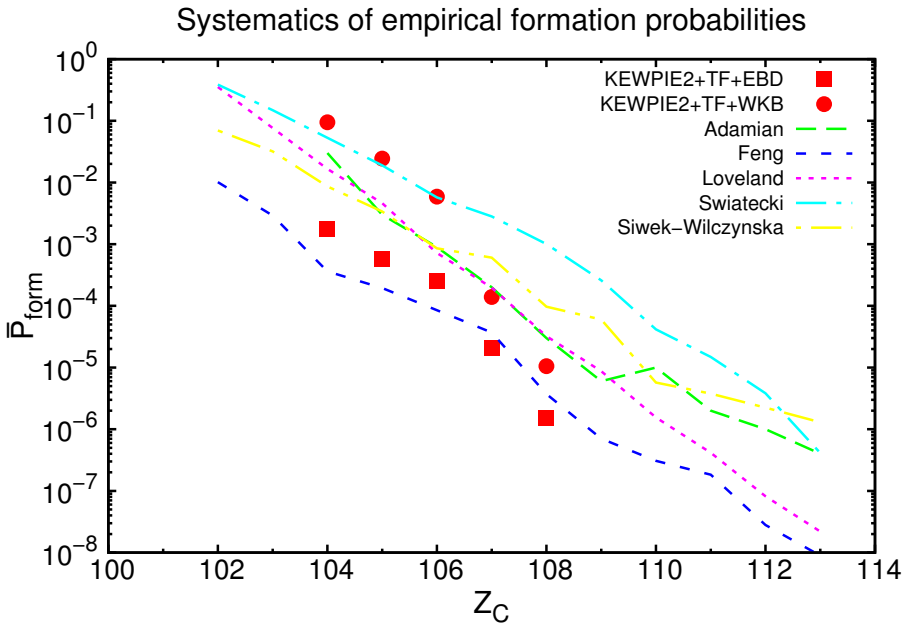

Figure VII.28 – Systematic comparison of the calculated mean values of the empirical formation probability for the cold-fusion reactions leading to the synthesis of the elements from $Z = 104$ to $Z = 108$ (cf. Tab. VII.1). The deduced formation probabilities are based upon two different capture models. The theoretical data are adapted from Ref. [4].

about 6, which is less than one order of magnitude. This is fully consistent with the estimate given in the chapter on heavy-ion fusion. However, special attention should always be drawn to the capture step because calculated cross-sections could differ by one order of magnitude, especially in the case of lighter colliding systems.

Fig. VII.20 illustrates how different correction factors affect the mean value and the confidence interval of the empirical formation probability. Without considering the Kramers-Strutinsky factor, it can be seen that the mean value slightly increases by a factor of 2, whereas it becomes a bit lower after removing the collective enhancement factor. These results are thus perfectly compatible with those obtained in the previous section. It should also be noted that the amplitudes do not remain the same due to the fact that reduced friction parameter is jointly removed along with the Kramers-Strutinsky factor.

Fig. VII.21 illustrates the impact of using different level-density parameters on the mean value of the empirical formation probability and the associated confidence interval. It is clearly demonstrated that the mean value of the empirical probability decreases by a factor of around 2 at most, which appears to be consistent with the conclusion drawn from the previous section. Moreover, the amplitudes of their confidence intervals seem to remain the same.

Fig. VII.22 demonstrates how the mean value and the confidence interval of the empirical formation probability evolve with different fission-barrier models. It is again observed that, the mean value can increase by almost one order of magnitude, which is more significant compared to the previous three cases.

VII.5.3 A systematic comparison and discussion

Finally, we perform a systematic comparison of deduced formation probabilities for the selected cold-fusion reactions.

In Figs. VII.23 and VII.24 are systematically compared the calculated mean values and the uncertainty intervals of the empirical formation probability for the cold-fusion reactions leading to the production of the elements ranging from $Z = 104$ to $Z = 108$. It is clearly shown that, as a whole, the mean values based upon two extreme fission-barrier models could differ by one order of magnitude. Meanwhile, the amplitudes of their corresponding uncertainty intervals can also reach about one order of magnitude overall. We thus reach the same conclusion as that drawn from the previous section. Similarly, Figs. VII.25 and VII.26 compare the deduced formation probabilities based upon two different capture models. It is thus demonstrated that the uncertainty connected with the lightest reaction system can even reach two orders of magnitude but gradually diminishes as the system becomes heavier. This is mainly due to the fact that, as the reaction becomes heavier, the incident energy is getting closer to the Coulomb barrier so that the uncertainty associated with the capture model due to the sub-barrier coupling effects should be gradually reduced. This is also fully compatible with the conclusion drawn from the chapter on heavy-ion fusion. To this extent, the uncertainty

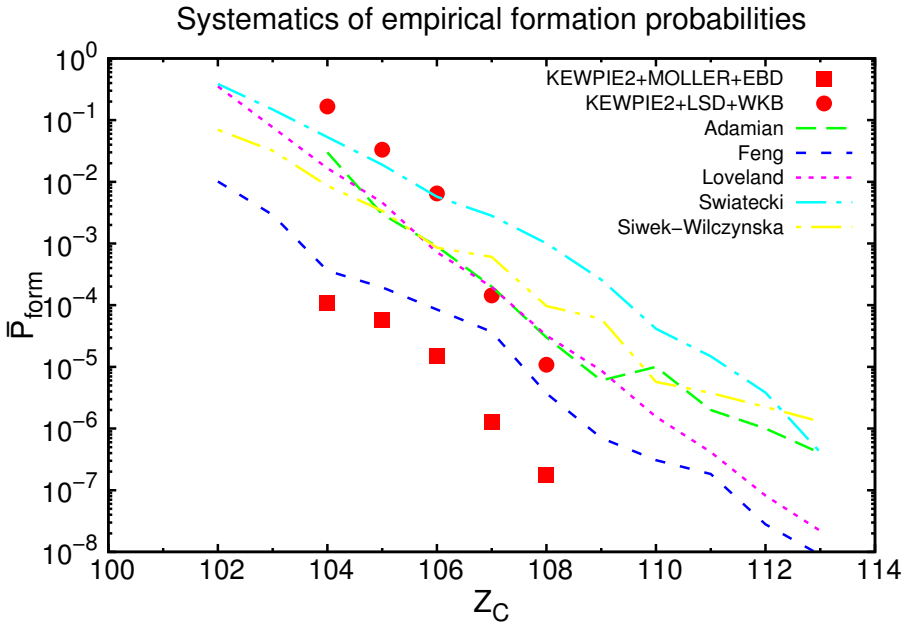

Figure VII.29 – Systematic comparison of the calculated mean values the empirical formation probability for the cold-fusion reactions leading to the synthesis of the elements from $Z = 104$ to $Z = 108$ (cf. Tab. VII.1). The extreme case is presented for both the capture model and the fission-barrier model.

existing in the estimated capture cross-section could also have a great impact on the final results, but fortunately it can be directly measured and thus constrained.

Two different cases for the deduced formation probabilities are shown in Figs. VII.27 and VII.28. The former displays mean values calculated with two different fission-barrier models and the latter shows those deduced from two different capture models. It is unambiguously demonstrated that the uncertainties due to the different capture models is gradually reduced, whereas the uncertainties due to the different fission-barrier models practically remain the same. It should be mentioned that the capture cross-section can be directly measured in experiments. Accordingly, one would expect the uncertainty associated with the capture model can be reasonably minimized. This indicates that the fission barrier would remain a crucial factor for constraining the fusion models.

It would also be interesting to look at the extreme case, namely, with two capture models and two extreme fission-barrier models. Fig. VII.29 shows the maximum difference between two sets of calculations based upon different capture and fission-barrier models. Regarding lighter systems, the amplitudes of their confidence intervals can reach three orders of magnitude, whereas it quickly decreases to around two orders of magnitude as the atomic number goes up.

Hence, after directly comparing the deduced formation probabilities, it seems unlikely

to assess the fusion models because of the fact that uncertainties in the capture and fission-barrier models, are both considerably large. The conclusions drawn from the uncertainty analysis presented in this chapter would be crucially important for understanding the contradiction between different fusion models. To improve the predictability and comprehend ambiguities concerning the formation step, it would be necessary to refine the accuracy of capture calculations and the fission-barrier models. Regarding the former, this can be done with the help of more accurate measurements as the capture cross-section can be directly measured, or using some more sophisticated capture models. As regards the latter, however, there are still large discrepancies between the various types of calculations and the fission-barrier height cannot be directly measured. How can we constrain the fission barrier by means of experimental data? It would be thus urgent to find new ways to constrain the fission barrier, which is essential for the synthesis of SHE.

VII.6 Summary and conclusions

In this chapter, we have introduced a complete framework for performing uncertainty analysis and for the first time applied it to the study related to the synthesis of SHE in cold-fusion reactions.

First, the uncertainty associated with the de-excitation step has been well investigated. It has been clearly revealed that, at a 95% confidence level, the uncertainty interval could reach one or two orders of magnitude, which appears comparable to that of the calculated formation probability based upon the different fusion models. It should be noted that this magnitude seems to be much larger than that estimated by Loveland in Ref. [209]. Thus, it would be likely for all fusion-evaporation models to well reproduce the measured production cross-sections, even though they provide contradictory predictions on the formation probability.

Second, on the basis of the same framework, we have closely looked at the uncertainty connected with the empirical formation probability as defined in the previous chapter. It has been rigorously shown that, at the same confidence level, the uncertainty might reach one or two orders of magnitude, which is also comparable to that in calculated formation probabilities based upon different fusion models. These results therefore provide a more direct evidence for the predictive limitations of the existing fusion models.

Is it possible to directly constrain the formation probability by means of experimental methods? It has been well established that, due to the quasi-fission process, the direct measurement of this crucial quantity would be quite challenging. To avoid this difficulty, here, we propose a possible experimental method with the aim of measuring the average magnitude of the formation probability under the same framework. As illustrated in Fig. VII.30, let us consider two different entrance channels, that is to say, one is hindered and the other is not. They both form the same compound state, which is subsequently de-excitated. By measuring the production cross-section at the same excitation energy, one might be able to directly extract some crucial information on the magnitude of the formation probability. More concretely,

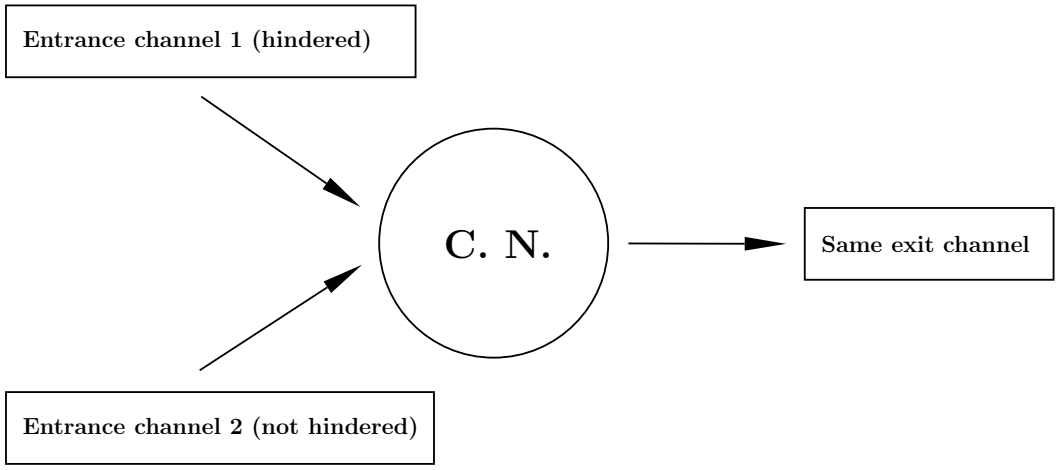

Figure VII.30 – Illustration of the proposed experimental method to directly constrain the formation probability (cf. text).

supposing that measured ER cross-sections are respectively denoted by $\sigma^1_{\rm ER}(E^*_C)$ and $\sigma^2_{\rm ER}(E^*_C)$, for the first entrance channel, one has $\sigma^1_{\rm ER}(E^*_C) = \sigma_{\rm cap}(E^1_{\rm cm})P_{\rm form}(E^1_{\rm cm})P_{\rm sur}(E^*_C)$, and for the second entrance channel, one has $\sigma^2_{\rm ER}(E^*_C) = \sigma_{\rm cap}(E^2_{\rm cm})P_{\rm sur}(E^*_C)$. After taking the ratio, one readily obtains

$$P_{\rm form}(E^1_{\rm cm}) = \frac{\sigma^1_{\rm ER}(E^*_C)\sigma_{\rm cap}(E^2_{\rm cm})}{\sigma^2_{\rm ER}(E^*_C)\sigma_{\rm cap}(E^1_{\rm cm})}. \tag{VII.18}$$

It should be noted that uncertainty associated with the ratio of $\sigma_{\rm cap}(E^2_{\rm cm})$ to $\sigma_{\rm cap}(E^1_{\rm cm})$ would be important at low energies. To overcome this issue, one might perform measurements at higher energies, for instance, above the Coulomb barrier, so as to reduce the uncertainty in the capture cross-section (less than a factor of 5 in general). In this case, it would be expected to precisely deduce the formation probability from experiments and thus to constrain the fusion models.

Another crucial problem is that, how to determine the fission-barrier height? It has been clearly demonstrated that the exact value of the fission-barrier height is crucially important for estimating the survival probability. Is there a formal way to estimate the uncertainty associated with the fission-barrier height? We shall consider this problem in the next chapter by using Bayesian inference.

VIII Bayesian inference on fission barrier

> Bayesian statistics is difficult in the sense that thinking is difficult.
>
> Don Berry

We have learned that fusion hindrance and fission barrier are considered to be the main factors limiting the predictive power of reaction models devoted to the study of the synthesis of SHE. It would be thus meaningful to find ways to constrain them separately. In this chapter, we shall only focus on fission barrier. Based upon the conclusions drawn from the previous chapter, it has been unambiguously established that fission barrier should have a crucial role to play in assessing the fusion models. Thus, one might ask whether it is likely to constrain this key parameter on the basis of some state-of-the-art theories?

Nuclear fission is known to be the ruling decay mode of SHE formed in heavy-ion collisions in the sense that experimental production cross-section is extremely sensitive to the fission-decay width. The fission-barrier height, which is considered to be one of the most fundamental characteristics of the synthesized nuclei, cannot be directly measured in experiments and generally, related theoretical predictions can differ by few MeV. In the case of SHE, the fission barrier is mainly due to the shell-correction energy, as the liquid-drop fission barrier practically vanishes. To this extent, the fission-barrier height is also a key parameter which can be employed to probe the structure of such very exotic nuclei.

To estimate the fission barrier and associated uncertainty from observed data, one would first need to reverse the fusion-evaporation model including uncertainties that result from both parameters and approximations of the model. We shall start by recapitulating some basic assumptions concerning parameter and model uncertainties. Then, a powerful tool called Bayesian inference will be introduced and applied to estimating the uncertainty related to the fission barrier.

VIII.1 Background and strategy

Determination of the "experimental" fission barrier is known to be model dependent. The heavy-ion fusion process aiming to synthesize SHE is known to be hindered with respect to what is expected from a simple extrapolation of fusion mechanisms for lighter colliding systems. It should be recalled that this hindrance phenomenon is mainly due to the strong Coulomb repulsion between colliding nuclei and is only qualitatively well understood. However, many experimental and theoretical ambiguities still persist and imply that the calculated results based upon the different fusion models can differ by orders of magnitude [3, 4]. Considering this context, we shall only focus on the synthesis of heavy nuclei for which the fusion process is assumed not to be hindered. Therefore, the fusion cross-section simply refers to the capture one, which shall be simulated using the KEWPIE2 code.

We shall consider a powerful statistical method, called Bayesian inference, to determine fission-barrier heights from the observed data. Previous analysis gave uncertainty in survival probabilities as a function of that in the fission barrier. Here, we are facing an inverse problem, that is to say, what information about the fission barrier can be extracted from measured data?

VIII.1.1 Uncertainties due to parameters

As previously mentioned, fission-barrier heights obtained by theoretical models could differ by $1-2$ MeV, depending on the model used. This could lead to a large variation of the calculated survival probability (e.g., up to one order of magnitude). In this sense, the associated uncertainty with the fission barrier can be essential the probability of synthesizing heavy or super-heavy nuclei in fusion-evaporation reactions.

The shell effect on the level-density parameter is usually taken into account by means of Ignyatuk's prescription which involves a energy damping parameter E_d that could range between 13.0 and 25.0 MeV. The reduced friction parameter β also has a very large uncertainty, usual values ranging from 1.0 to 9.0 zs^{-1}. Can we constrain these parameters from data?

In the present study, the fission barrier is of primary interest, whereas others are considered to be the so-called nuisance parameters, which are not of immediate interest but must be accounted for during statistical analysis. As will be shown later in this chapter, the joint distribution for the parameter of interest can be obtained by marginalizing over the nuisance parameters. However, this approach might not always be computationally efficient due to computation of multi-dimensional integrals which is usually time-consuming.

VIII.1.2 Uncertainties due to approximations

Various reaction codes do not only differ by the choice of the parameters but also by certain approximations. For instance, to estimate the fission-decay width, some people take into account Kramers-Strutinsky factors and others do not. Similarly, the collective enhancement

factor for the state density is sometimes not considered. In this sense, approximations of the theoretical model give rise to another contribution to the uncertainty in the outcome. So far, we have studied the impact of changing models on the calculated survival probability as well as the empirical formation probability. Here, the same investigation will be performed within the framework of Bayesian inference.

VIII.1.3 Frequentist vs. Bayesian statistics

Before entering into the main discussion, it would be helpful to provide a brief overview of these two completely different philosophies.

Much have been said about the difference between the frequentist and Bayesian statistics [210]. Perhaps, the deepest and most crucial conflict has to do with alternative interpretations of what a "probability" means. Let us now separately inspect these two alternative interpretations of probability.

Frequentist view

From a frequentist viewpoint, a probability can be interpreted in terms of the relative frequency of a particular repeatable event to occur. A consequence of this is that one would be able to discuss a repeatable event or experiment so as to apply frequentist techniques. Let us consider a repeatable experiment where the number of total possible outcomes is N and that of interesting events is n. Then, the frequentist probability of obtaining an interesting event is simply given by

$$P(I) = \lim_{N\to\infty} \frac{n}{N}, \tag{VIII.1}$$

which can be thus regarded as the long-run expected frequency of occurrence of the event. As a practical example, in the previous chapter, we have employed this definition to construct the cumulative probability distribution from the sampling events based upon the Monte-Carlo method.

It should be noted that, in most cases, it is not practical to calculate a frequentist probability as we clearly need to have an infinite set in order to produce an exact result. Nevertheless, this is practically never the case and it is only possible to compute an estimator of $P(I)$ to sufficient precision with a finite N. One of the most important advantages of this frequentist viewpoint is probably that the probability can be computed by following a defined set of logical steps, which would be an attractive feature of the prescription for many people.

Bayesian view

In contrast with the frequentist definition, the Bayesian view of probability is closely related to degree of belief. It is considered to be a measure of the plausibility of an event given incomplete knowledge based upon observation or experience. Thus, probability can be

regarded as plausibility contains all information on the values that might be affected to the quantities we are interested in.

A Bayesian approach to a problem usually starts with the formulation of a model that is assumed to be adequate for the description of a certain phenomenon. As a second step, a prior distribution over the unknown parameters of the model is proposed on the basis of our beliefs about the situation before seeing the data. After observing some data, we apply the Bayes rule (or the Bayes theorem) to obtain a posterior distribution for these unknowns, which takes account of both the prior information and the data. From this posterior distribution we can compute predictive distributions for future observations. In such a context, an experiment can be seen as a learning process.

The core of the Bayesian approach is thus the Bayes rule, which involves nothing more than the manipulation of conditional probabilities. Here, it should be recalled that the joint probability of two events, say A and B, can be commonly expressed as follows: $P(AB) = P(A \mid B)P(B) = P(B \mid A)P(A)$. In the inverse problem considered here, one of these "events" corresponds to the hypothesis (models or parameters), θ[1], and the other is data, D, and we would like to establish a bridge between them. According to the Bayes rule, which was rediscovered and first applied to physics by Laplace, this can be done via the following relationship:

$$P(\theta \mid D) = \frac{P(D \mid \theta)\,\pi(\theta)}{P(D)}, \tag{VIII.2}$$

where the term $P(D \mid \theta)$ is called the likelihood function and it assesses the probability of observed data interpreted by the model. Here, the term $\pi(\theta)$ is called the prior distribution, as it reflects our initial state of knowledge on the parameter before observing data. The specification of prior distribution is often the most subjective aspect of Bayesian probability theory and this is one of the reasons some statisticians held Bayesian inference in contempt. But nowadays there are clear rules to determine the prior based on maximum entropy approaches [205, 211, 212]. The term $P(D)$ is simply a normalization constant, which can be obtained by integrating over all possible values, namely

$$P(D) = \int P(D \mid \theta)\,\pi(\theta)\,\mathrm{d}\theta. \tag{VIII.3}$$

In writing the above formulas, only one parameter is taken into consideration. Mathematically, this can be readily extended to accommodate any number of parameters. Another way of looking at the Bayes rule is that it represents a learning process. More concretely, the transformation from the prior distribution, $\pi(\theta)$, to the posterior one, $P(\theta \mid D)$, formally reflects what we have learned about the validity of the hypothesis given data, or put differently, the plausibility of values that can be affected to θ. To this extent, parameters are unknown and can be described probabilistically, whereas data are considered to be fixed by a repeatable experiment.

[1] In the following study, we assume that the hypothesis corresponds to a set of model parameters.

The use of Bayes rule to determine what one can learn about the values of parameters from data is called parameter estimation. However, more strictly speaking, the Bayesian inference does not provide parameter estimates, but rather gives the full posterior PDF (cf. the left-hand side of Eq. (VIII.2)). Once the posterior PDF has been constructed, it would not be difficult to calculate some quantities of interest, such as the posterior mode (most probable value of the parameter) and the posterior mean value. To this extent, the basic idea of the Bayesian inference is somewhat simple [213]. However, it should be mentioned that huge numerical difficulties would sometimes hinder the development of this powerful approach.

VIII.2 Inverse problem in 1D

So far, we have briefly outlined the main idea of Bayesian inference. In a second step, we attempt to apply this approach to the determination of fission barrier. As previously mentioned, it is the most sensitive parameter in modeling the fusion-evaporation reaction. How accurately can it be constrained by experimental data?

To give a preliminary answer to this question, we have to solve the inverse problem so as to evaluate how experimental uncertainties affect the determination of the model parameters. In the previous chapter, we investigated the influence of parameter uncertainty on the calculated results. Conversely, here we would like to evaluate the influence of experimental uncertainty on the parameters. We shall then apply Bayesian inference to the inverse problem in combination with the KEWPIE2 code. For this purpose, as a first step, a set of simulated pseudo-data is generated from the KEWPIE2 code with the aim of testing this new approach. Then, based upon the KEWPIE2 code, Bayesian methods are systematically employed to determine the mean value of the fission barrier and its associated uncertainty.

VIII.2.1 Pseudo-data

For the sake of simplicity, we restrict our study to the cold fusion reaction (one-neutron-out evaporation) without hindrance. Since the reliable experimental data are not available in the literature, we decided to generate a set of pseudo-data points by means of the statistical part of the KEWPIE2 code. Here, we have assumed that the capture excitation function can be directly measured and so do the corresponding ER cross-section. Thus, the survival probability can be deduced from pseudo-data. This is also a good way to test the method and check if it gives back the true value of the parameter. In the remaining part of this chapter, the “experimental” data refer to the simulated pseudo-data, namely the survival probabilities based upon the KEWPIE2 code with default options.

The calculated survival probability can be dependent on both the fission barriers of mother and daughter nuclei. Fig. VIII.1 displays three calculations of the survival probability with different fission barriers in the daughter nucleus. It is clearly shown that the theoretical curve is mainly divided into two parts: the increasing part, which is dominated by the fission barrier

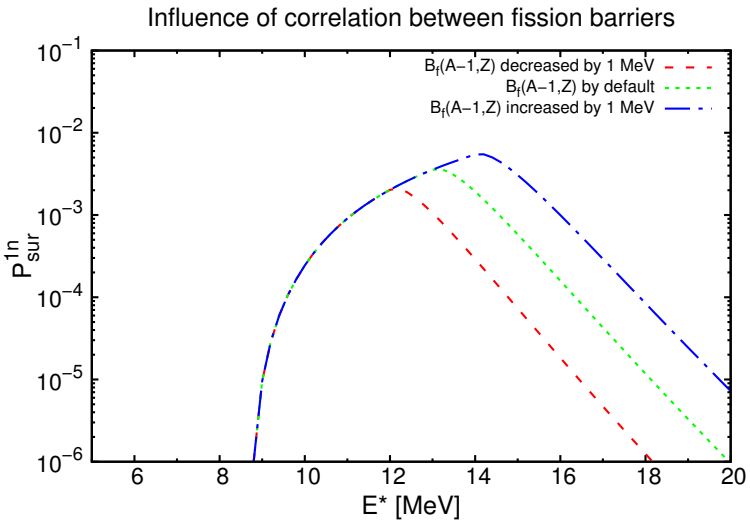

Figure VIII.1 – Influence of the correlation between fission barriers of mother and daughter nuclei (see text). The red dashed curve refers to the theoretical calculation with the default fission barrier of the daughter nucleus. The others correspond to the calculations with a fission barrier increased or decreased by 1.0 MeV.

of the mother nucleus, and the decreasing part, which is influenced by the fission barrier of the daughter nucleus. As we would like to constrain the fission barrier of the mother nucleus, we only consider the increasing part, which can be readily approximated by $\Gamma_n/(\Gamma_f+\Gamma_n)$ using the ratio of the neutron-evaporation and fission-decay widths. In our case, fission is assumed to be the dominant decay mode, that is to say, the fission-decay width should be much larger than the neutron-evaporation one.

Figs. VIII.2 and VIII.3 illustrate how to construct two types of the datasets for a fusion-evaporation reaction ^{208}Pb(^{40}Ar,1n)^{247}Fm. The first one corresponds to the set of pseudo-data directly extracted from the theoretical curve with an uncertainty of 60% and the second one refers to the same set but randomly ranged around the theoretical curve. In the following study, we shall apply Bayesian inference to these two specially designed datasets with the aim of inferring the fission barrier of the mother nucleus, whose true value is fixed at 4.30 MeV.

VIII.2.2 Bayesian inference with a single parameter

The pseudo-datasets have been constructed using the statistical part of the KEWPIE2 code. As a next step, we shall focus on the application of Bayesian inference so as to determine the fission barrier as well as the associated uncertainty. As mentioned above, the simulated pseudo-data refer to the extracted survival probabilities for the single-neutron evaporation, which are simply denoted by $P_{\rm sur}^{\rm exp}$.

If the fission barrier B_f is the only parameter, its probability density function can be simply

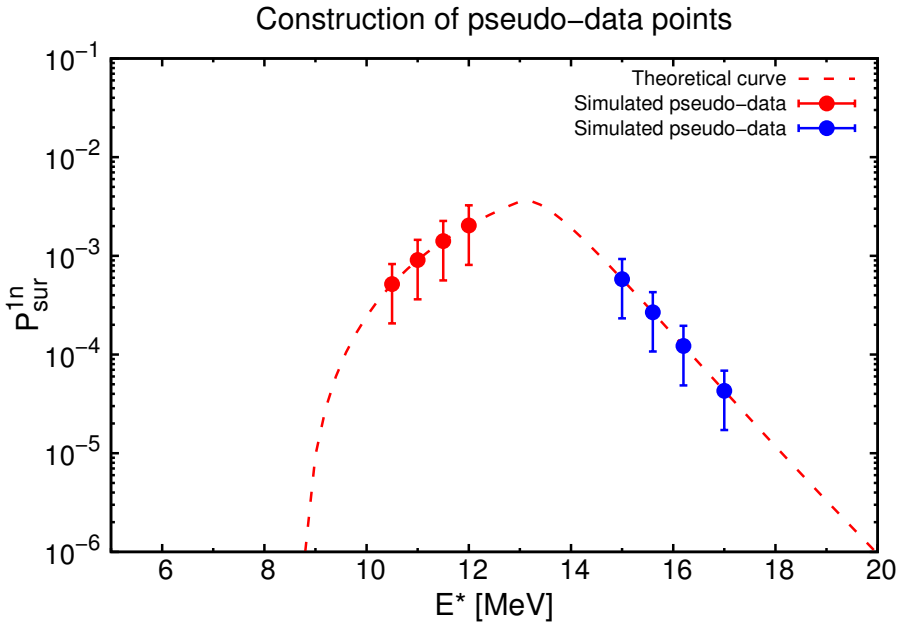

Figure VIII.2 – Construction of pseudo-data for the reaction ^{208}Pb(^{40}Ar,1n)^{247}Fm. Here, the uncertainty (standard deviation) is set equal to 60% of the mean value.

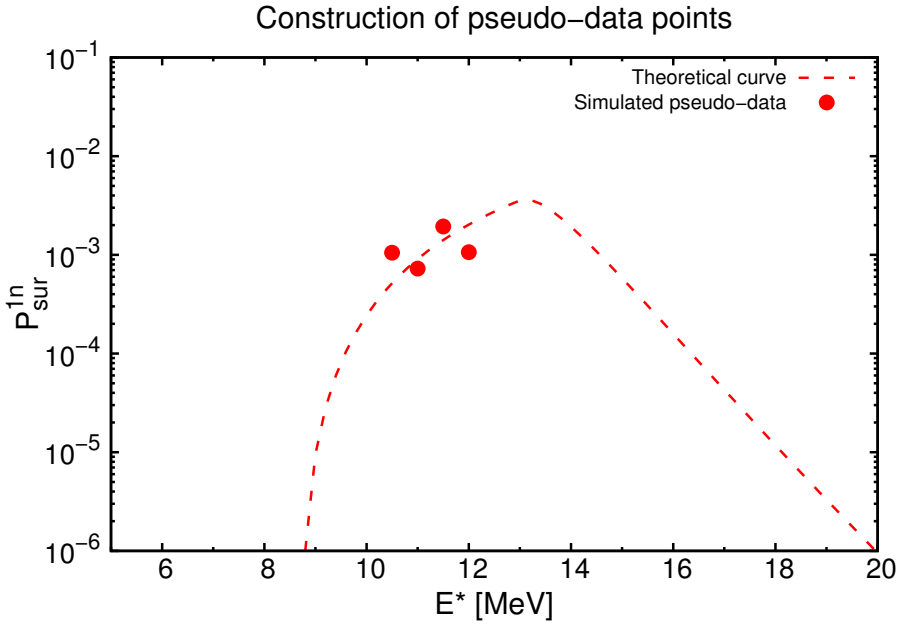

Figure VIII.3 – Construction of the pseudo-data for the reaction ^{208}Pb(^{40}Ar,1n)^{247}Fm. The data points are randomly arranged around the theoretical curve with a relative uncertainty of 60%.

given by Bayes rule, namely

$$P(B_f|P_{\rm sur}^{\rm exp}) = \frac{\pi(B_f) \times P(P_{\rm sur}^{\rm exp}|B_f)}{\int \pi(B_f) \times P(P_{\rm sur}^{\rm exp}|B_f) {\rm d}B_f}. \tag{VIII.4}$$

As will be shown later in this chapter, the above formula can be readily extended to accommodate other parameters, that is to say, the nuisance ones.

Here, we also assume that the experimental data are not correlated and follow a normal distribution, which is expressed as follows:

$$P(P_{\rm sur}^{\rm exp}|B_f) \propto \exp\left\{-\frac{\chi^2}{2}\right\}, \tag{VIII.5}$$

together with

$$\chi^2 = \sum_i \frac{\left(P_{\rm sur}^{\rm exp}(E_i^*) - P_{\rm sur}^{1n}(B_f, E_i^*)\right)^2}{u_i^2}, \tag{VIII.6}$$

where u_i stands for the uncertainty of pseudo-data and $P_{\rm sur}^{1n}(B_f, E_i^*)$ refers to the estimated survival probability based upon the KEWPIE2 code. It should be mentioned that energy loss in the target and thus the uncertainty connected with the excitation energy is considered to be negligible.

Since we have no idea about the value of B_f, it would be instructive to choose a non-informative prior distribution:

$$\pi\left(B_f\right) = \begin{cases} \text{constant}, & \text{for } B_f \geq 0, \\ 0, & \text{otherwhere.} \end{cases} \tag{VIII.7}$$

This choice is well justified on the basis of maximum entropy theory [205, 211], as mentioned in the previous chapter.

The posterior PDF, namely Eq. (VIII.4), would be able to give access to the mean value and variance of the fission barrier. More explicitly, one has the following formulas:

$$\left\langle B_f \right\rangle = \int_{B_f>0} B_f P(B_f|P_{\rm sur}^{\rm exp}) {\rm d}B_f, \tag{VIII.8}$$

$$u^2(B_f) = \int_{B_f>0} (B_f - \left\langle B_f \right\rangle)^2 P(B_f|P_{\rm sur}^{\rm exp}) {\rm d}B_f, \tag{VIII.9}$$

The above integrals can be estimated using the Gauss-Legendre quadrature method.

VIII.2.3 Influence of models

To look more closely at the effect of changing models on the final results, one can perform the same calculations without taking some correction factors. Here, as usual, we only

Table VIII.1 – Mean value of the fission barrier and the associated standard deviation. The true value of B_f = 4.30 MeV. "Random" refers to the case where pseudo-data points are normally distributed around the reference curve.

Number of data	Exp. uncertainty	$\langle B_f \rangle$ (MeV)	$u(B_f)$ (MeV)	$u(B_f)/\langle B_f \rangle$
2	20%	4.29	0.05	1.17%
2	40%	4.28	0.21	4.91%
2	60%	4.26	0.63	14.79%
4	60%	4.28	0.23	5.37%
6	60%	4.29	0.12	2.80%
6 (random)	60%	4.26	0.28	6.59%
6 (random)	40%	4.27	0.11	2.58%
6 (random)	20%	4.29	0.02	0.47%

Table VIII.2 – Influence of correction factors on the deduced fission barrier as well as the associated uncertainty. The relative uncertainty of pseudo-data is kept fixed at 60%. The Kramers-Strutinsky factor is removed.

Number of data	$\langle B_f \rangle$ (MeV)	$u(B_f)$ (MeV)	$u(B_f)$ (MeV)
2	4.51	0.62	13.75%
4	4.48	0.41	9.15%
6	4.47	0.25	5.59%

Table VIII.3 – Influence of correction factors on the deduced fission barrier as well as the associated uncertainty. The relative uncertainty of pseudo-data is kept fixed at 60%. The collective enhancement factor is removed.

Number of data	$\langle B_f \rangle$ (MeV)	$u(B_f)$ (MeV)	$u(B_f)$ (MeV)
2	4.13	0.54	13.08%
4	4.15	0.26	6.27%
6	4.16	0.17	4.09%

focus on the two correction factors, namely the Kramers-Strutinsky factor and the collective enhancement factor.

In our above calculations with the pseudo-datasets, the fission decay width has been corrected by both factors and the reduced friction parameter is set equal to 5.0 zs^{-1} and the damping energy to 19.0 MeV. As a comparison, we calculated the mean value of fission barrier and associated uncertainty without considering these two factors so as to investigate the influence coming from different models.

Table VIII.4 – Influence of nuisance parameters on the deduced fission barrier as well as the associated uncertainty. The relative uncertainty of pseudo-data is kept fixed at 60%.

Number of data	$\langle B_f \rangle$ (MeV)	$u(B_f)$ (MeV)	$u(B_f)$ (MeV)
2	4.20	0.82	19.52%
4	4.22	0.54	12.80%
6	4.23	0.33	7.80%

VIII.2.4 Results and discussion

The preliminary results are systematically given in the Tab. **??**. It can be clearly demonstrated that the relative uncertainty of the fission barrier is lower than that of the experimental data because the model is very sensitive to the fission barrier. As is well known, it is also very sensitive to the experimental precision and to the number of data points. The poorer the quality of the data, the larger the uncertainty associated with the deduced fission barrier. Conversely, the more the data points, the smaller the uncertainty in the estimated fission barrier. As regards the randomly distributed pseudo-data, the mean values doe not change so much, but the relative uncertainty increases by a factor of around 2.5. This might be due to the non-linearity of the KEWPIE2 model which could enlarge the resulting uncertainty. Actually, according to some preliminary tests, the resulting posterior distribution would not be symmetric, especially with very few data points. In this case, it would be more instructive to compute the 95% uncertainty interval instead of the standard deviation.

Regarding the effect of changing models, the results are listed Tabs. VIII.2 and VIII.3. It can be readily seen that the influence of the correction factors on the uncertainties are somewhat negligible. However, there appears to be a systematical shift with respect to the previous mean values. This is fully compatible with the results shown in a previous chapter on the KEWPIE2 code.

In brief, from the above results, it is unambiguously shown how to extract the fission barrier from experimental data with an accurate statistical treatment. The extracted fission barrier is well constrained although experimental uncertainties are generally large.

It should be recalled that other parameters, such as β or E_d, are also included in the KEWPIE2 code and could affect the final results. In our case, they are all considered to be the so-called nuisance parameters, whose impact on the outcomes will be investigated in the following section.

VIII.3 Influence of nuisance parameters

Obviously, the fission barrier is not the single parameter of the model. Other parameters with large uncertainties can also influence the final distribution of B_f. As a first test, we shall only consider two nuisance parameters here, namely the reduced friction coefficient β and

Table VIII.5 – Influence of experimental correlations on the deduced fission barrier as well as the associated uncertainty. The relative uncertainty of pseudo-data is kept fixed at 60%. Two pseudo-data points are considered.

Correlation coefficient	$\langle B_f \rangle$ (MeV)	$u(B_f)$ (MeV)	$u(B_f)/\langle B_f \rangle$
-0.2	4.29	0.38	8.86%
-0.1	4.27	0.50	11.71%
0.0	4.26	0.63	14.79%
0.1	4.20	0.71	16.90%
0.2	4.14	0.78	18.84%

Table VIII.6 – Influence of experimental correlations on the deduced fission barrier as well as the associated uncertainty. The relative uncertainty of pseudo-data is kept fixed at 60%. Four pseudo-data points are considered.

Correlation coefficient	$\langle B_f \rangle$ (MeV)	$u(B_f)$ (MeV)	$u(B_f)/\langle B_f \rangle$
-0.2	4.28	0.12	2.80%
-0.1	4.26	0.17	3.99%
0.0	4.25	0.23	5.37%
0.1	4.21	0.25	5.94%
0.2	4.16	0.28	6.73%

Table VIII.7 – Influence of experimental correlations on the deduced fission barrier as well as the associated uncertainty. The relative uncertainty of pseudo-data is kept fixed at 60%. Six pseudo-data points are considered.

Correlation coefficient	$\langle B_f \rangle$ (MeV)	$u(B_f)$ (MeV)	$u(B_f)/\langle B_f \rangle$
-0.2	4.29	0.07	1.63%
-0.1	4.29	0.09	2.10%
0.0	4.29	0.12	2.80%
0.1	4.27	0.15	3.51%
0.2	4.26	0.18	4.23%

the damping energy E_d.

In a similar manner, when taking into account the nuisance parameters, the Bayes rule can be generalized as follows:

$$P(B_f, \beta, E_d | P_{\text{sur}}^{\text{exp}}) = \frac{\pi(B_f, \beta, E_d) \times P(P_{\text{sur}_i}^{\text{exp}} | B_f, \beta, E_d)}{\int\int\int \pi(B_f, \beta, E_d) \times P(P_{\text{sur}_i}^{\text{exp}} | B_f, \beta, E_d) \mathrm{d}B_f \mathrm{d}\beta \mathrm{d}E_d}, \tag{VIII.10}$$

where $\pi(B_f, \beta, E_d)$ denotes the joint prior probability distribution for all parameters. In this sense, the whole problem has been converted into a multi-dimensional integration of the likelihood function over the joint prior probability distribution. For the sake of simplicity, it would be reasonable to rewrite the joint prior distribution as a product of individual densities

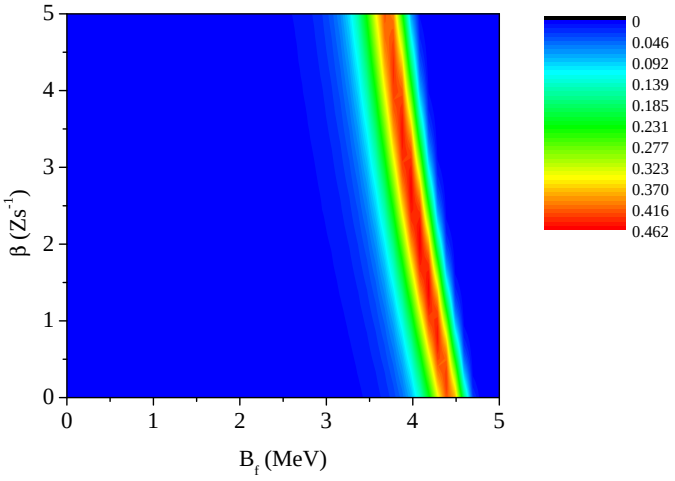

Figure VIII.4 – Illustration of the two-dimensional posterior probability distribution. Figure is taken from Ref. [214].

for B_f, β and E_d under the assumption that they are independent of each other. In the previous section, we showed a non-informative prior distribution for B_f (cf. Eq. (VIII.7)). Following the same reasoning, the prior distributions of β and $E_d$one might take similar forms, such as

$$\pi\left(\beta\right) = \begin{cases} \text{constant}, & \text{for } \beta \geq 0, \\ 0, & \text{otherwhere}, \end{cases} \tag{VIII.11}$$

and

$$\pi\left(E_d\right) = \begin{cases} \text{constant}, & \text{for } E_d \geq 0, \\ 0, & \text{otherwhere}. \end{cases} \tag{VIII.12}$$

Once the full posterior distribution has been worked out, it would be possible to get rid of the nuisance parameters using the following marginalization procedure:

$$P(B_f|P_{\text{sur}}^{\text{exp}}) = \frac{\int\int P(B_f,\beta,E_d|P_{\text{sur}}^{\text{exp}})\mathrm{d}\beta\mathrm{d}E_d}{\int\int\int P(B_f,\beta,E_d|P_{\text{sur}}^{\text{exp}})\mathrm{d}B_f\mathrm{d}\beta\mathrm{d}E_d}, \tag{VIII.13}$$

which can be employed to evaluate again the mean value of the fission barrier and its standard deviation. In practice, these integrals can be estimated using the quadrature technique, but calculations would become considerably time-consuming. This is known as one of the most challenging issues for Bayesian data analysis.

The calculated results are shown in Tab. VIII.4. The mean values seem not to differ so much compared to the previous results. Nevertheless, the relative uncertainties become significantly larger. To understand this, Fig. VIII.4 illustrates a simple example of the two-

dimensional posterior distribution based upon a toy model where only the reduce friction coefficient is taken into account as the nuisance parameter [214]. It is clearly demonstrated that β cannot be constrained by the studied observable, namely the survival probability. As shown in Fig. (VIII.4), B_f is dependent on the chosen value of β. After integrating all possible values of β, the uncertainty of B_f can be thus significantly enlarged.

This conclusion should be similar in the case where the other nuisance parameter, namely the shell-damping energy, is taken into account. It would be thus necessary to find new observables to better constrain the nuisance parameters. However, this is generally not so easy.

VIII.4 Correlation between experimental data

In the previous sections, we assumed that the experimental data were independent of each other. This should not be the case since they are usually determined with the same experimental set-up. However, none of the articles on SHE experiments has provided so far a covariance or a correlation coefficient. It would be worth giving further consideration to this issue when performing experimental measurements.

To take a look at the influence of experimental covariances on the final results, as a first step, we are going to consider only few data points with an uniform and arbitrary correlation coefficient ρ associated to all off-diagonal elements of the correlation matrix.

It should be recalled that the general form of χ^2 is given as follows:

$$\chi^2 = \left(P_{\text{sur}}^{\text{exp}} - P_{\text{sur}}(B_f, E^*)\right)^T \Sigma^{-1} \left(P_{\text{sur}}^{\text{exp}} - P_{\text{sur}}(B_f, E^*)\right), \tag{VIII.14}$$

where Σ denotes the covariance matrix of experimental data. In the simplest case where only two data points are available, Eq. (VIII.14) can be simplified into the following expression:

$$\begin{aligned} \chi^2 \quad = \quad & \frac{1}{1-\rho^2}\left[\frac{\left(P_{\text{suvr1}}^{\text{exp}} - P_{\text{suvr}}(B_f, E_1^*)\right)^2}{u_1^2} + \frac{\left(P_{\text{suvr2}}^{\text{exp}} - P_{\text{suvr}}(B_f, E_2^*)\right)^2}{u_2^2}\right. \\ & \left. - \frac{2\rho\left(P_{\text{suvr1}}^{\text{exp}} - P_{\text{suvr}}(B_f, E_1^*)\right)\left(P_{\text{suvr2}}^{\text{exp}} - P_{\text{suvr}}(B_f, E_2^*)\right)}{u_1 u_2}\right]. \end{aligned} \tag{VIII.15}$$

It should be mentioned that, in our case, the uncertainties are considered identical. The extension to more data points can be done in a similar manner but the expression becomes much more complicated. In this case, the matrix form of Eq. (VIII.14) would be more convenient.

Preliminary results are systematically given in Tabs VIII.5, VIII.6 and VIII.7. Note that the nuisance parameters are not taken into consideration. As a whole, it appears that the experimental correlation does not have a significant influence on the mean value of the fission barrier. However, the associated uncertainty gradually rises with increasing correlation coeffi-

cient. It can be readily observed that, the more data points we have, the smaller associated uncertainties we get and the stronger impact of experimental correlations on the relative uncertainties of fission barrier. This is compatible with the fact that, as the number of data points goes up, the influence of correlation matrix would become more effective and thus relative uncertainties rise more rapidly. It should be noted that the correlation coefficient could not be negative in general.

In practice, it would be difficult to estimate the experimental correlation. Further consideration will be thus required in a more realistic case.

VIII.5 Summary and conclusions

It has been well established that uncertainty should be taken into account in reaction modeling. How to compare or assess the prediction of model without uncertainties? How to evaluate the role of approximations? In this chapter, we addressed the problem in relatively simple situations.

Based upon the simulated pseudo-data, we have applied Bayesian inference to determining the fission barrier and its associated uncertainty. We have introduced preliminary results on the amplitude of uncertainty (standard deviation) associated with the fission barrier. We have learned that the so-called "experimental fission barriers" are actually dependent on both models and nuisance parameters. If the fission barrier is considered to be the single parameter, it has been well established that the uncertainty associated with this parameter would be smaller than experimental precision. In this sense, Bayesian inference is a very promising method, but the numerical implementation would be very difficult in some cases.

To estimate the production cross-section of heavy elements, fission barrier is known to be the parameter that has the largest influence on the calculated results. To constrain this parameter with experimental data, Bayesian inference has been demonstrated to be powerful. As a further step, the same code should be used to constrain parameters with other experimental observables. Bayesian approach can be regarded as a learning process which allows us to do that in a comprehensive manner. Unfortunately, uncertainties due to nuisance parameters can be very large and significantly affect the uncertainty connected with fission barrier. The calculations presented here are based upon the KEWPIE2 code and limited to cold-fusion reactions with evaporation of a single neutron is not hindered. Further application to hot-fusion reactions with evaporation of several neutrons would be more complicated. Moreover, some advanced techniques, such as the Markov-Chain Monte-Carlo method, should be considered with the purpose of directly sampling from the posterior distribution so as to estimate the 95% uncertainty interval.

IX Uncertainty analysis of the liquid-drop model

> With four parameters I can fit an elephant, and with five I can make him wiggle his trunk.
>
> Attributed to von Neumann by Enrico Fermi

Up to now, we have discussed the main issues related to the synthesis of SHE. Due to large uncertainties remaining in the formation process and fission barrier, the prediction of production cross-sections becomes quite difficult, but it is still essential for guiding future experiments. In the previous chapter, with the help of Bayesian inference, we have made our first attempts to constrain the fission barrier in the case where fusion hindrance is negligible. Nevertheless, this phenomenon becomes dominant for synthesis of SHE. One thus needs to work out how to constrain fusion hindrance and fission barrier simultaneously.

Actually, the description of both formation and de-excitation steps are not completely independent of each other in the sense that inner and fission barriers can be both estimated by means of the liquid-drop model. How do they correlate with each other? To give a first answer to this question, in this chapter, we aim at revisiting the liquid-drop model, especially the uncertainties in parameter values and their impact on the physical quantities, such as the neutron-separation energy and liquid-drop fission barrier. This can be done by means of the so-called linear regression theory, which is widely employed in natural and social sciences to describe possible relationships between model variables.

To apply the multiple linear regression theory, we first revisit an extended version of the liquid-drop mass formula as proposed in Ref. [215]. One of the main objectives of the first section is to show how the regression analysis works and to emphasize the importance of choosing pertinent statistics when fitting a nuclear mass model to experimental data. For this purpose, we perform a complete linear regression analysis with the most recent measured data [107, 108] and carefully examine some crucial statistical quantities. By comparing the

results with those already found in Ref. [215], this work also aims to establish a formal framework for performing nuclear mass fits. Afterwards, based upon the regression analysis results, we shall construct a simplified liquid-drop mass formula from which the particle-separation energies and fission barriers, as well as their covariances can be derived. The influence of correlations between these physical quantities on the survival probability is investigated with the help of a simplified single-neutron evaporation model.

To perform such calculations, a linear-regression code has been developed using Armadillo which refers to a linear algebra software library for the C++ programming language [216]. It aims to provide an efficient tool for doing matrix operations with a straightforward and easy way to use interface.

IX.1 Nuclear mass fit: role of statistics

IX.1.1 Background

The nuclear mass is considered to be one of the most fundamental properties of a atomic nucleus. It mostly refers to the total binding energy of the nucleus and provides crucial information on the nuclear force that binds nucleons together inside the nucleus. Since the Weizsäcker-Bethe empirical mass formula [8, 217], many mass formulas were proposed and great theoretical improvements have been achieved over the past decades. The main purpose of the study on mass formulas is not only to give more reliable mass values of known nuclei, but also to predict reliable masses of unknown ones. The latter would be also important for modeling fusion-evaporation reactions, as the particle-separation threshold is closely related to nuclear masses. In general, modern nuclear-mass models with shell-correction energies are able to reproduce all known experimental data with a precision of around 0.5 MeV or even less, which can be undoubtedly regarded as a remarkable theoretical achievement.

At the present time, one of the most important and challenging frontiers of nuclear physics is the study of new exotic nuclei far from the valley of stability, especially neutron-rich ones with weakly bound neutrons. However, even though the models mentioned above agree very well within the region of known masses, they can differ by up to tens of MeV in those unstable regions where nuclear masses are not precisely known. In this sense, the extrapolation of theoretical predictions to unknown nuclei is rather unreliable. In this context, since last few years, there has been increased interest in understanding the uncertainties and limitations of various types of nuclear mass models. For this reason, it would be necessary to analyze uncertainties related to the theoretical model. For instance, various versions of liquid-drop mass formulas have been proposed and surveyed in many recent studies (cf., e.g., Refs. [218, 219] and references therein). However, most of these studies are usually based upon some qualitative discussions.

In this section, we are mainly interested in employing correct statistics to evaluate a nuclear mass fit in a formal manner.

IX.1.2 Review of an extended liquid-drop mass formula

On the whole, the nuclear mass models can be roughly divided into three groups: macroscopic, microscopic and the hybrid macroscopic-microscopic. Here, we mainly concentrate on the last one, namely the macroscopic liquid-drop or droplet formula with some phenomenological microscopic terms such as the shell-correction and pairing energies.

As a starting point, we are going to revisit and apply the linear regression theory to an extended Weizsäcker-Bethe mass model that was proposed in Ref. [215], namely

$$\begin{aligned} B_n(A,Z) = & \left(a_v + a_{vt}\left(\frac{A-2Z}{A}\right)^2\right)A + \left(a_s + a_{st}\left(\frac{A-2Z}{A}\right)^2\right)A^{2/3} \\ & + a_C\frac{Z^2}{A^{1/3}} + a_{Cx}\frac{Z^{4/3}}{A^{1/3}} + a_R A^{1/3} + a_W\frac{|A-2Z|}{A} \\ & + a_p\frac{(-1)^{A-Z}+(-1)^Z}{\sqrt{A}} + \Delta E_{\rm sh}, \end{aligned} \tag{IX.1}$$

where the phenomenological shell-correction term is expressed as

$$\Delta E_{\rm sh} = a_m\frac{\nu_p\nu_n}{\nu_p+\nu_n} + b_m\left(\frac{\nu_p\nu_n}{\nu_p+\nu_n}\right)^2, \tag{IX.2}$$

with ν_p and ν_n representing the numbers of valence nucleons (deficient number between a given Z or N and the nearest magic numbers [1]) for protons and neutrons, respectively. It should be noted that this shell-correction term is not accurate but has the merit of depending on two adjustable parameters which can be fitted to experimental data. In addition, the same notations as used in Ref. [215] are adopted. It should be noted that the above formula is only valid for spherical ground states and has the advantage of containing only simple and linear terms.

For more details on Eq. (IX.1), the reader is referred to Ref. [215]. For the sake of clarity, we would like to recapitulate some essential points on the different terms entering Eq. (IX.1):

- The volume term, proportional to A, describes the saturation of the nucleon-nucleon interaction in infinite nuclear matter. This is the dominant attractive term, which is proportional to the volume or proportional to the number of nucleons confined within a nucleus.
- The volume symmetry term, proportional to $(A-2Z)^2/A$, is another effect that makes the total binding energy drop with the symmetry of the nucleus in terms of values of Z and $N = A-Z$. Put differently, any large asymmetry between protons and neutrons could reduce the binding energy and thus make the nucleus less stable. It should be noted that this term together with the volume term are usually expressed in a nonlinear form, namely $a_v\left(1-\kappa_v\left(\frac{A-2Z}{A}\right)^2\right)A$. In order to keep the linear expression, the product

[1] In this formula, the canonical values, namely 2, 8, 20, 28, 50, 82, 126 and 184, are employed for both protons and neutrons.

of a_v and $-\kappa_v$ is replaced by a single parameter a_{vt}.

- The surface term, proportional to $A^{2/3}$, lowers the binding energy. This is due to the fact that nucleons on the surface of a nucleus are not completely surrounded and thus interact with fewer neighbors than those in the interior. The total interaction energy is therefore reduced compared to bulk nuclear matter.
- The surface symmetry term, proportional to $(A-2Z)^2/A^{4/3}$, corresponds to a symmetry correction to the surface energy. The inclusion of this term is indispensable for the consistency of the semi-empirical mass formula [220, 221]. It should be mentioned that this term together with the surface term are usually combined into a non-linear form, namely $a_s\left(1-\kappa\left(\frac{A-2Z}{A}\right)^2\right)A^{2/3}$. Here the product of a_s and $-\kappa$ is simply denoted as a_{st} so as to maintain a linear form.
- The Coulomb term, proportional to $Z^2/A^{1/3}$, corresponds to the potential energy of a uniformly charged sphere. Hence, the total binding energy diminishes because of the electrostatic repulsion between protons.
- The Coulomb exchange term, proportional to $Z^{4/3}/A^{1/3}$, is a contribution to the classical Coulomb energy due to the quantum effect and can be estimated from the proton wave functions.
- The curvature term, proportional to $A^{1/3}$, is related to the integrated curvature and considered to be a necessary correction to the surface energy. However, it has been argued that the presence of this correction term might not be consistent with some theoretical calculations. Apparently, this inconsistency still remains an unsolved puzzle [162, 222, 223].
- The Wigner term, proportional to $|A-2Z|/A$, appears in the counting of identical pairs inside a nucleus and is mainly dependent on the isospin. It is experimentally known that the nuclei with an equal number of neutrons and protons are unusually tightly bound. An extra term, first recognized by Wigner on the basis of symmetry arguments [224], is thus specifically required to explain this effect. Several versions of this correction term can be found in the literature [218]. Here, it takes the simplest form which still lacks, however, a clear physical justification [225, 226].
- The pairing term, proportional to $[(-1)^{A-Z}+(-1)^Z]/\sqrt{A}$, reflects the effect of pairing between nucleons, which can usually be estimated using the microscopic theory.
- The shell correction term is essential for fitting to experimental masses. It is of great importance not only for improving the quality of the mass fit but also for the prediction of the "island of stability". In Eq. (IX.1), a pure phenomenological expression for the shell correction energy is employed instead of introducing the traditional Strutinsky procedure [227, 228]. However, further consideration on its validity would be needed [229].

The determination of the model parameters will be presented in the next subsection.

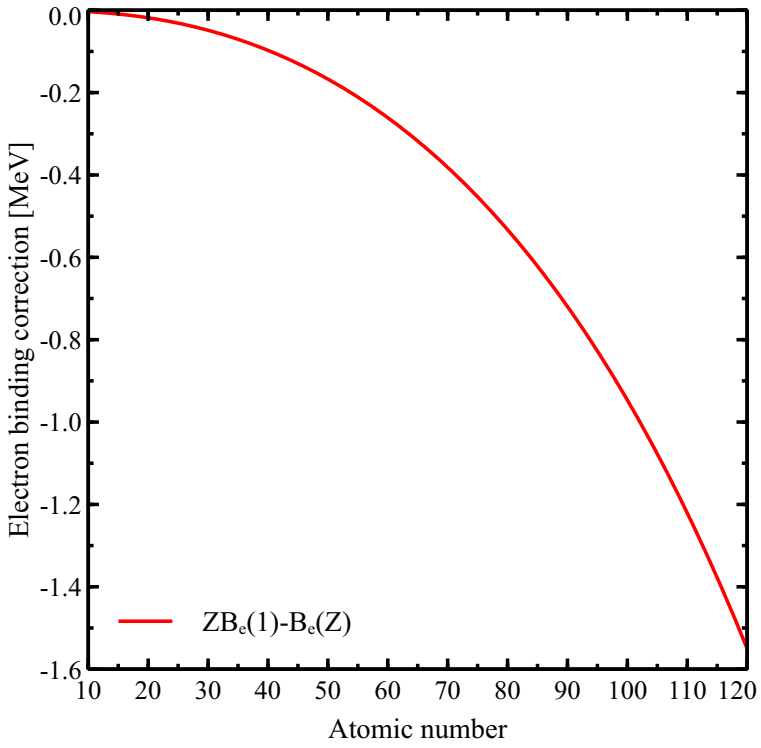

Figure IX.1 – Electron binding correction to the nuclear binding energy. See Eq. (IX.4).

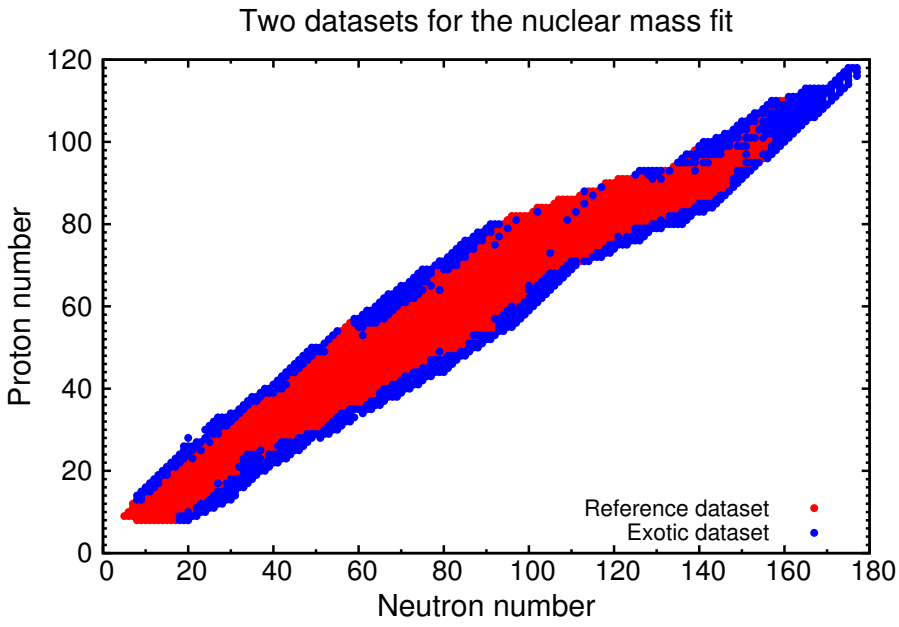

Figure IX.2 – Datasets of experimental masses considered for fitting the nuclear mass formula. The red and blue symbols represent the reference dataset and the exotic dataset, respectively (see text).

IX.1.3 Experimental data and some basic relationships

To obtain the best-fit parameter values, we have employed the most recent version of the Atomic Mass Evaluation (AME2012) which compiles a number of high-precision mass measurements [107, 108]. The tables presented in AME2012 provide atomic masses (or mass excesses) and various basic quantities. It should be noted that, as emphasized in Ref. [108], with very few exceptions, the experimental data always refer to measured atomic masses. This is the reason why we would prefer to use atomic masses or mass excesses rather other derived quantities presented in AME2012. Atomic masses can be measured by using different techniques, such as ion trap (Paul or Penning trap) and nuclear reaction. For more details about the atomic mass measurement, the reader is referred to Ref. [230].

The atomic mass excess is denoted by $\Delta(A,Z)$, which is related to the atomic mass by $\Delta(A,Z) = M_a(A,Z) - Am_u$ with the atomic mass unit $m_u = 931.494\,061$ MeV. The experimental atomic mass is linked to the binding energy described by Eq. (IX.1), one can simply employ the following definition for the nuclear mass: $M_n(A,Z) = M_a(A,Z) - Zm_e + B_e(Z)$, where m_e is the electron mass and $B_e(Z)$ the electron binding energy. The value of the former is equal to 0.510 998 928 MeV, whereas the precision of the later is still not clear. To evaluate B_e, a simple formula has been introduced in AME2012, namely

$$B_e(Z) = 14.438\,1 Z^{2.39} + 1.554\,68 \times 10^{-6} Z^{5.35}\ \text{eV} \tag{IX.3}$$

According to the definition of the nuclear binding energy, after performing some calculations and simplifications, one readily obtains

$$B_n(A,Z) = Z\Delta(1,1) + (A-Z)\Delta(1,0) - \Delta(A,Z) + ZB_e(1) - B_e(Z), \tag{IX.4}$$

where the last two terms, namely the electron binding correction, would only be significant for very heavy nuclei. (This correction can reach the order of 1.0 MeV, as shown in Fig. IX.1.) Accordingly, the experimental uncertainty associated with the nuclear binding energy can thus be estimated by means of the uncertainty propagation method, namely

$$\begin{aligned} u^2\left(B_n(A,Z)\right) &= Z^2 u^2\left(\Delta(1,1)\right) + (A-Z)^2 u^2\left(\Delta(1,0)\right) + u^2\left(\Delta(A,Z)\right) \\ &\simeq Z^2 u^2\left(\Delta(1,1)\right) + (A-Z)^2 u^2\left(\Delta(1,0)\right) + u^2\left(\Delta(A,Z)\right), \end{aligned} \tag{IX.5}$$

where the electron binding correction has been omitted. As indicated in AME2012, the experimental uncertainty is generally quite small ($\lesssim 150$ keV) compared to the theoretical one. Moreover, the covariance terms are not considered in the following fitting procedure. This is due to the fact that the experimental covariances provided in AME2012 are not complete, that is to say, the covariance between certain nuclei is still missing, so that it is currently impossible to construct a complete variance-covariance matrix for all the measured masses. This is certainly worth further consideration. Finally, by using Eq. (IX.4), the binding energies as well as their uncertainties are estimated in a more consistent manner compared to the ones

given the AME2012 table [2], which are only of educational interest as mentioned in Ref. [108] (e.g., Aston's curve of binding energy per nucleon, etc.).

In the following study, the reference dataset of nuclear masses taken into account in the fitting procedure refers to 2274 experimental data with $A \geq 16$, $Z \geq 8$ and experimental uncertainties less than 150 keV, as shown in Fig. IX.2. As discussed in Ref. [231], the lower limits for the neutron and proton numbers are chosen to ensure that the involved nuclei are large enough to be regarded as liquid drops and the restriction on the experimental uncertainties is caused by the precision of measurements. Moreover, the remaining 960 "exotic" nuclei whose masses are evaluated (marked by "#" in AME2012) or poorly known with uncertainties between 150 keV and 800 keV are also illustrated in Fig. IX.2. As shown in Ref. [219], these exotic nuclei will be employed to test the predictive capacity of the fitted mass formula.

IX.1.4 Least-squares fitting

In this subsection, we apply the linear regression theory to the nuclear mass fit. For the sake of simplicity, we only focus on the ordinary least squares (OLS), that is to say, each point is assigned equal weight (homoscedasticity) and model parameters are estimated using the OLS. This is commonly employed by almost all mass models.

To start the fitting procedure, let us first rewrite Eq. (IX.1) as

$$B_n(A_i, Z_i) = \sum_{j=1}^{p=11} X_{ij}\beta_j, \tag{IX.6}$$

or in a more compact form:

$$\mathbf{y} = \mathbf{X}\boldsymbol{\beta} + \mathbf{e}, \tag{IX.7}$$

where a Gaussian random vector with zero mean and constant variance σ_{th}^2 has been added so as to account for the theoretical uncertainty associated with the model. Here, $y_i = B(A_i, Z_i)$ denote theoretical binding energies that are fitted to measured values and the parameters in the mass formula are denoted by

$$\boldsymbol{\beta} = [a_v, a_{vt}, a_s, a_{st}, a_C, a_{Cx}, a_R, a_W, a_p, a_m, b_m]^{\mathrm{T}}, \tag{IX.8}$$

which can be estimated using the OLS. The elements of model matrix appearing in Eq. (IX.7)

[2] Actually, for certain nuclei, the uncertainties associated with the binding energies given in AME2012 are equal to zero.

for the i-th nucleus are given as follows:

$$\begin{aligned}
&X_{i1} = A_i,\ X_{i2} = A_i^{2/3},\ X_{i3} = \frac{Z_i^2}{A_i^{1/3}},\ X_{i4} = \frac{(A_i - 2Z_i)^2}{A_i}, X_{i5} = \frac{Z_i^{4/3}}{A_i^{1/3}},\\
&X_{i6} = \frac{|A_i - 2Z_i|}{A_i},\ X_{i7} = \frac{(A_i - 2Z_i)^2}{A_i^{4/3}},\ X_{i8} = \frac{(-1)^{A_i - Z_i} + (-1)^{Z_i}}{\sqrt{A_i}},\ X_{i9} = A_i^{1/3}, \qquad \text{(IX.9)}\\
&X_{i10} = \frac{\nu_p^i \nu_n^i}{\nu_p^i + \nu_n^i},\ X_{i11} = X_{i10}^2.
\end{aligned}$$

Once the model matrix has been constructed, the best-fit parameter values can be readily obtained with the help of the OLS. More concretely, the Gauss–Markov theorem states that the best linear unbiased estimator (BLUE) of the model parameters is given by the OLS estimator. In practice, the formulas for BLUE is given as follows:

$$\hat{\boldsymbol{\beta}} = (\mathbf{X}^{\mathrm{T}}\mathbf{X})^{-1}\mathbf{X}^{\mathrm{T}}\mathbf{y}^{\mathrm{exp}}, \qquad \text{(IX.10)}$$

where $\mathbf{y}^{\mathrm{exp}}$ represents a experimental dataset. Accordingly, the corresponding variance-covariance matrix is given by

$$\mathrm{Var}[\hat{\boldsymbol{\beta}}] = \hat{\sigma}_{\mathrm{th}}^2 (\mathbf{X}^{\mathrm{T}}\mathbf{X})^{-1}. \qquad \text{(IX.11)}$$

These formulas can be readily proved and found in any mathematical textbook, such as in Ref. [232]. As will be shown in the next subsection, by inspecting the ratio of the OLS estimator to the corresponding standard deviation, one can test the significance of each model parameter appearing the mass formula.

It should be borne in mind that the theoretical uncertainty connected with the model is always unknown. In general, it can be estimated as follows:

$$\hat{\sigma}_{\mathrm{th}}^2 = D_{\mathrm{rms}}^2 = \frac{1}{M-p}\sum_{i=1}^{M}\left(y_i^{\mathrm{exp}} - \hat{y}_i\right)^2, \qquad \text{(IX.12)}$$

where $\hat{y}_i$ denote the estimated values and the number of data points M is equal to 2274 for the reference dataset. In the literature, the standard deviation is also commonly denoted by D_{rms}, which would reflect to some extent the quality of the nuclear mass fit.

In the end, it would be important to say a few more words about the variance $\hat{\sigma}_{\mathrm{th}}^2$. As discussed in Ref. [233], as a whole, the total model uncertainty can be decomposed into the statistical and systematical ones. The former is usually quantifiable for many models. The commonly employed tool to estimate statistical uncertainties is nothing else but the regression analysis. In this case, if the model is perfectly accurate, the regression theory tells us that the residuals (differences between the observed and estimated values) are expected to be symmetrically distributed around zero.

Regarding the systematic uncertainty, it is mainly due to imperfection of the model, such

as wrong assumptions and missing physics due to our lack of knowledge. Since in most cases it is impossible to have an exact model, the related systematic uncertainty can be extremely difficult to estimate. This is especially the case when doing extrapolations to unknown nuclei, no perfect strategy exists to assess, mostly, huge systematic uncertainties.

As will be shown in the next subsection, in the case of the mass fit, one of the efficient means of exploring systematic uncertainties consists in examining the general trend of residuals, which would tell us whether adding more data makes sense. One would expect that, if the dataset is sufficiently diverse and large, the resulting statistical uncertainties might become small (centered around zero with a small variance). In this sense, by investigating the non-statistical behavior of residuals, one might be able to identify the missing parts leading to systematic uncertainties.

IX.1.5 Regression analysis

The methods of regression analysis are systematically discussed in this subsection. Here, the main purpose is to illustrate a general framework for the nuclear mass fit. To this end, we recall some crucial statistics that are commonly adopted in regression analysis.

Significance test for model parameters

A nuclear mass model is usually composed of several phenomenological parameters. It is thus interesting to know whether some inappropriate parameters can be dropped from the model when fitting to experimental data. To this end, the null hypothesis should be needed. In the linear regression model, the t-test is commonly employed to check the significance of each parameters. (Another similar method is the so-called F-test.)

Adding a significant variable would make the model more effective and thus avoid the over-fitting problem (too many parameters), whereas adding an unimportant one might make the model much worse. The hypothesis statements to test the significance of a particular parameter, β_i, are formulated as follows [234]:

$$H_0 : \hat{\beta}_i = 0, \tag{IX.13}$$

$$H_1 : \hat{\beta}_i \neq 0. \tag{IX.14}$$

The statistic for this test is based upon the t-distribution (according to Cochran's Theorem), namely

$$t_0 = \frac{\hat{\beta}_i}{u(\hat{\beta}_i)} \sim t(\nu), \tag{IX.15}$$

where ν denotes the number of degrees of freedom and the standard deviation in BLUE is obtained using the previous results. Hence, one would fail to reject the null hypothesis if the test statistic lies in the acceptance region: $-t^{\nu}_{\alpha/2} < t_0 < t^{\nu}_{\alpha/2}$. This test measures the contribution

of a variable while the remaining variables are included in the model. Alternatively, one can also employ the p-value, namely $[1 - P(T < |t_0|)] \times 2$ (two-tailed). The p-value for each term tests the null hypothesis that the parameter is equal to zero (no effect). A low p-value (less than 5%) indicates that you can reject the null hypothesis. In other words, a model parameter that has a low p-value is likely to be a meaningful addition to the model because changes in this parameter are related to those in the outcome. Conversely, a larger p-value would suggest that changes in the parameter are not related with those in the response of the model, or put differently, the corresponding parameter value would not significantly differ from zero. However, it should be borne in mind that the t-test is nothing else but a sort of auxiliary tool to investigate the significance of a theoretical model. The physical meaning of each parameter should also be carefully inspected.

Analysis of variance: partitioning of the sum of squares

To investigate the quality of the fit, one of the most crucial indicators is the so-called coefficient of determination, denoted by R^2. The coefficient of determination usually regarded as a measure of the amount of variability in the data considered in the regression model.

The total variability of the data is measured by the total sum of squares, denoted by TSS. The amount of this variability coming from the model is the explained sum of squares, denoted by ESS. Before giving the definition of R^2, we first summarize the following statistics:

- $\text{TSS} = \sum_i (y_i^{\text{exp}} - \overline{y})^2$, the total sum of squares of differences between data and simple mean, proportional to the sample variance.
- $\text{ESS} = \sum_i (\hat{y}_i - \overline{y})^2$, the sum of squares of differences between predicted values and sample mean.
- $\text{RSS} = \sum_i \hat{e}_i^2 = \sum_i (y_i^{\text{exp}} - \hat{y}_i)^2$, the residual sum of squares.

Here, the sample mean is simply given by $\overline{y} = \sum y_i^{\text{exp}} / M$. The coefficient of determination is the ratio of the explained sum of squares to the total sum of squares, namely $R^2 = \text{ESS/TSS} = 1 - \text{RSS/TSS}$. In doing this, we have employed the so-called ANOVA relationship: TSS = RSS + ESS (cf., e.g., Ref. [235]).

The coefficient of determination indicates the amount of total variability explained by the regression model. The value of R^2 increases as more terms are added to the model, even if the new term does not contribute significantly to the model. Therefore, an increase in the value of R^2 cannot be regarded as a sign to conclude that the new model is better than the old one. Another statistic commonly used is the adjusted coefficient of determination, noted R^2_{adj}, which is defined as follows:

$$R^2_{\text{adj}} = 1 - \frac{\text{RSS}/(M-p)}{\text{TSS}/(M-1)}, \tag{IX.16}$$

where M represents the size of the dataset. It can be seen that when the number of model parameters p is largely smaller than that of data points, the R^2_{adj} simply tends to R^2, as in our

case.

Analysis of residuals

Investigating the statistical trend of residuals would be essential for determining systematical uncertainties. If the model is perfect, the residual distribution is expected to be normal or nearly-normal, with a mean value close to zero. The systematic uncertainty, however, can break the normality because of some missing ingredients in modeling.

In statistics, the normality test is often employed to determine whether residuals can be modeled by a normal distribution. This is typically essential in the sense that many statistics involved in regression analysis require that a residual distribution must be normal or nearly-normal. In general, there are both graphical and statistical methods of evaluating normality. The former usually includes the histogram and normality plot and the latter involves thoroughly examining two shape parameters, namely skewness and kurtosis (cf. the chapter on uncertainty analysis), or performing a statistical hypothesis testing by calculating the p-value, which can be formulated by

$$H_0: \text{ The population is normally distributed,} \tag{IX.17}$$

$$H_1: \text{ The population is not normally distributed.} \tag{IX.18}$$

In the present study, the Shapiro-Wilk test [236] is adopted and employed to test whether the residual distribution is normal. It is known that this is a powerful test that is able to detect most departures from normality when the sample size $\lesssim 5000$. Regarding the significance level, if the p-value is larger than 5%, then the residuals pass the normality test. Conversely, it might be indicated that the residuals do not follow the normal distribution. In this case, however, by the law of large numbers and the central limit theorem, BLUE can still be approximately normally distributed around the true parameter values, which implies the estimated parameters and their confidence interval estimates remain robust. Hence, in a large sample, the use of a linear regression technique introduced above, even if the dependent variable violates the "normality assumption" on the random error vector, remains valid. In contrast with BLUE, if the residual distribution is significantly non-normal, the confidence interval of predictions might be too wide or too narrow, or in other words, the predictive power of the linear regression model becomes limited.

IX.1.6 Results and discussion

In this subsection, we attempt to apply the linear regression theory to the fit of the extended liquid-drop mass formula so as to illustrate the use of this powerful mathematical tool.

The principal results of linear regression are listed in Tab. IX.1. The last column reports the p-values for parameter estimates (cf. Eq. (IX.15)).

Table IX.1 – Best-fit values of the model parameters obtained with the OLS. The t-scores and p-values are also listed in the last two columns. Note that the significance level has been set equal to 5% for t-test. The standard deviation (SD) represents the uncertainty of the estimate.

	Estimate [MeV]	SD [MeV]	Relative SD [%]	t-score	p-value
a_v	16.597	0.068	0.410	244.150	0.000
a_{vt}	-33.229	0.327	0.984	-101.580	0.000
a_s	-26.421	0.466	1.763	-56.711	0.000
a_{st}	64.872	1.748	2.695	37.109	0.000
a_C	-0.767	0.003	0.405	-246.980	0.000
a_{Cx}	1.796	0.070	3.903	25.620	0.000
a_R	14.762	0.802	5.435	18.400	0.000
a_W	-63.441	2.879	4.539	-22.033	0.000
a_p	10.787	0.473	4.381	22.826	0.000
a_m	-1.990	0.043	2.172	-46.032	0.000
b_m	0.155	0.005	3.069	32.581	0.000
				D_{rms} [MeV]	1.603 51
				R^2	0.999 988
				R^2_{adj}	0.999 988

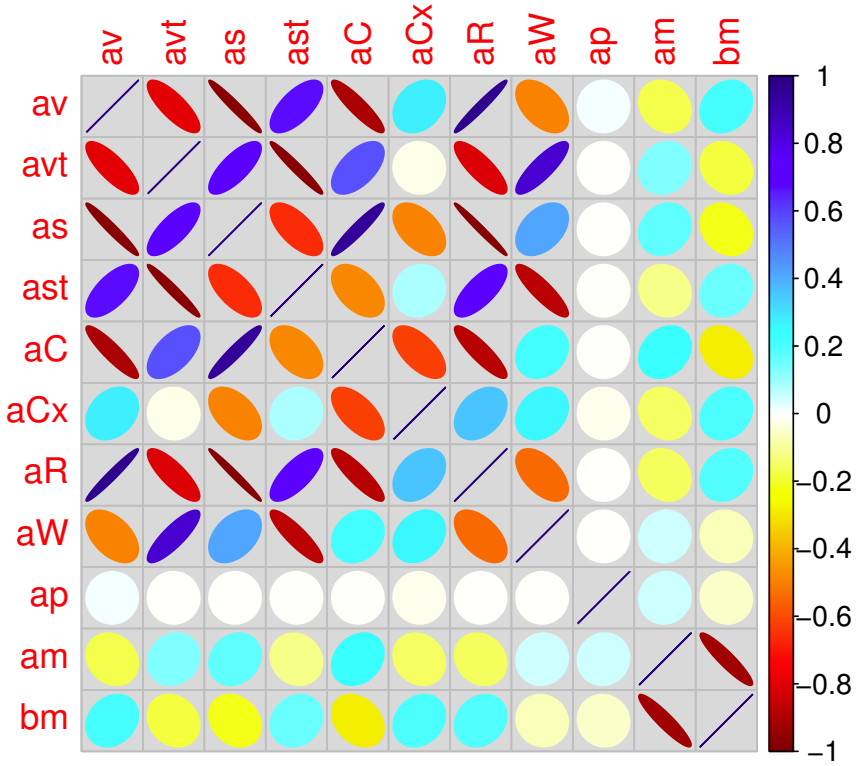

Figure IX.3 – Illustration of the correlations between the model parameters (in colored shapes). This can be obtained by means of Eq. (IX.11).

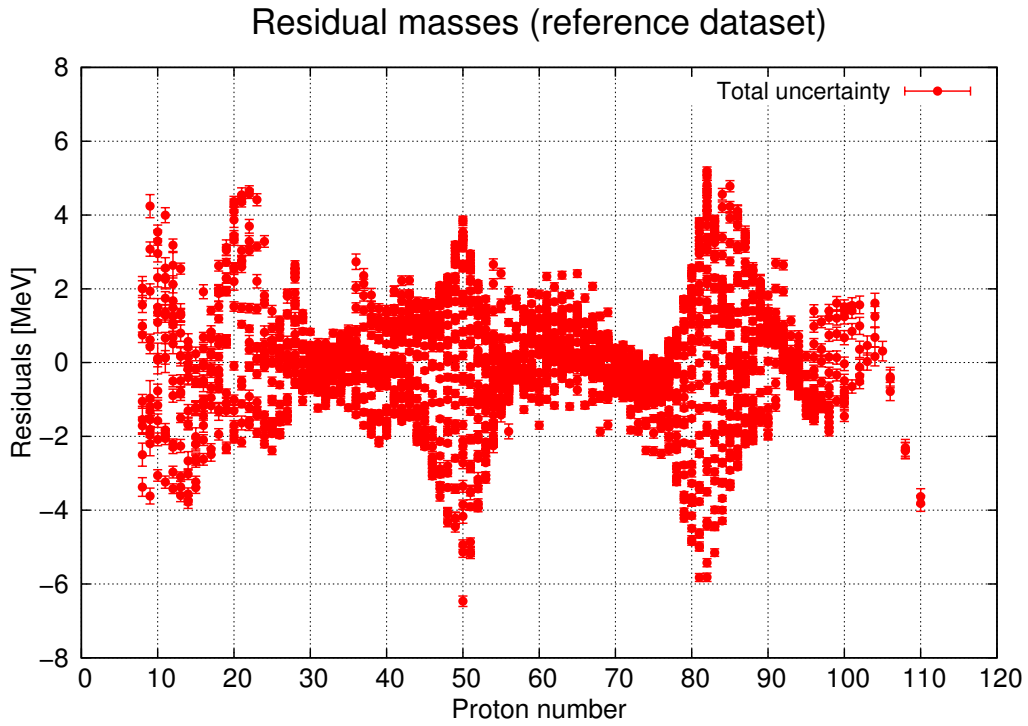

Figure IX.4 – Differences between the theoretical and experimental (residual masses). The total uncertainty refers to the sum of the theoretical and experimental ones.

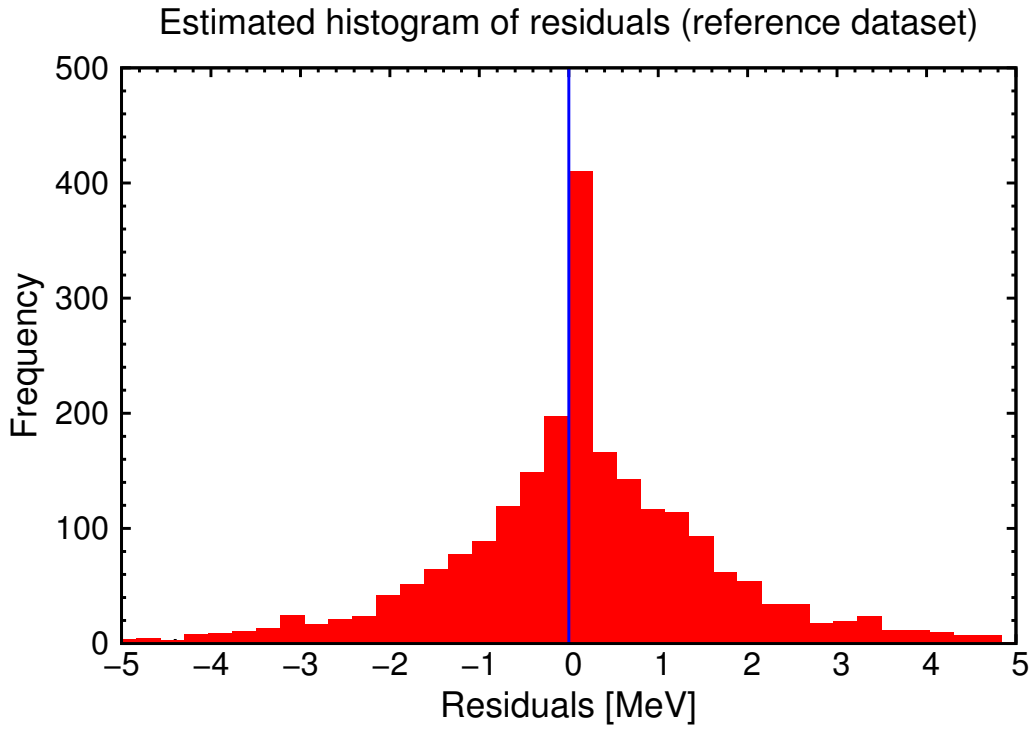

Figure IX.5 – Distribution of residuals. The skewness and kurtosis parameters are estimated to be −0.1055 and 0.9857, respectively. The vertical line denotes the mean value.

As previously discussed, a small p-value provides evidence against the null hypothesis so that one can reject it when the p-value is sufficiently small or less than a certain significance level. Actually, it is conventional in statistics to reject the null hypothesis at the 5% level. Hence, when the p-value is less than 5%, the event that has occurred is said to be statistically significant at the 5% level. It should be mentioned that this choice is simply a conventional cut-off value adopted by most communities. Values close to 5% provide moderate evidence against the null hypothesis, while values less than 1% provide considerable evidence against the null hypothesis. Let us get back to Tab. IX.1, one can readily note that the p-value corresponding to each term is practically equal to zero. This means that the null hypothesis can be rejected. In other words, each term would be significant for the mass fit and hence cannot be dropped. This result is thus fully consistent with many of the previous studies.

The goodness of fit can be measured by the root-mean-square D_{rms}, which is estimated to be around 1.6 MeV or the coefficient of determination R^2 that is equal to 0.999 988. The former indicates the estimate of the unknown random error of the model and the latter tells us that almost all experimental data can be well explained by the fitted nuclear mass model. In spite of this advantage, it should always be kept in mind that R^2 has several limitations, for instance, it cannot determine whether the parameter estimates and predictions are biased and it does not indicate whether a regression model is adequate. For instance, one might have a low R^2 value for a correct model, or even a high value for a model that does not fit the data well. In this sense, the value of R^2 would only be a necessary condition for testing the goodness of the fit.

Furthermore, on the basis of Fig. IX.3, one can make some conclusions about the relationships between model parameters. First, the correlations of pairing (a_p) and shell corrections (a_m, b_m) with other terms appear to be quite weak. Especially, the pairing term is considerably stable and independent of any other terms. The fact that the pairing and shell corrections are practically uncorrelated with the other macroscopic terms is a well known result and would allow us to replace these by some specific ones, as will be shown in the next section. The curvature term appears to strongly correlate with the volume term and anti-correlate with both the surface and Coulomb terms. A possible geometric interpretation was recently proposed in Ref. [231]. Regarding the Wigner term, it should be mentioned that there exist other possible expressions which can be found in Refs [15, 162, 237, 238]. Adding this term to the nuclear mass formula is able to improve to some extent the description of the nuclei with $N \sim Z$. However, most of these analytical expressions lack a clear physical justification [225, 226]. In addition to the Wigner term, the shell correction term seems not so reliable.

In the end, Fig. IX.4 shows the differences between the measured and estimated values, namely residual masses. It can be seen that the distribution of residuals appears to be symmetrically distributed around zero. Here, the total uncertainty refers to the sum of the statistical and experimental uncertainties. To look at this more closely, it would be meaningful to investigate the estimated residual distribution that is displayed in Fig. IX.5. The skewness and kurtosis parameters are estimated to be -0.1055 and 0.9857, respectively. It should be

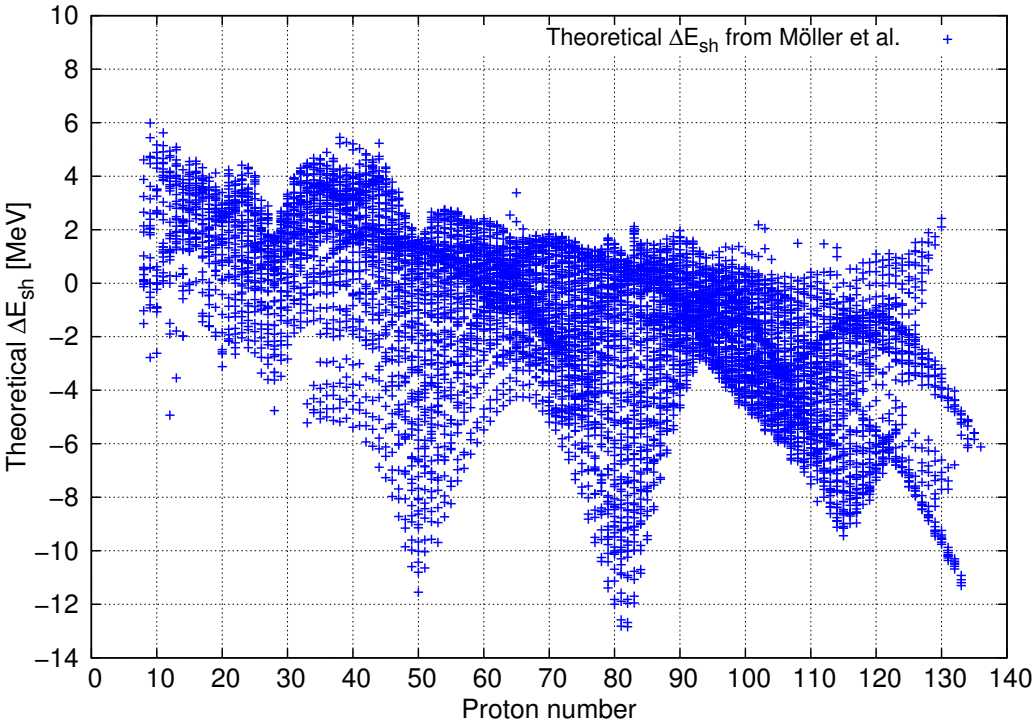

Figure IX.6 – Illustration of theoretical shell-correction energies employed in the nuclear mass fit. The experimental data are taken from Ref. [15].

mentioned that the skewness and kurtosis of a normal distribution are both equal to zero. In our case, the skewness parameter is quite close to zero, which means that the distribution is slightly skewed to the left and nearly symmetric around its mean value ($\simeq 0$). As regards the kurtosis parameter, the value is close to unity, which indicates that the distribution is more peaked compared to the normal one. This is well demonstrated as is shown in Fig. IX.5. As a last step, the Shapiro-Wilk test tells us that the p-value practically vanishes, that is to say, the distribution of residuals significantly differ from the normal one. This result might indicate that some systematic uncertainties might be present in the nuclear mass model (cf. Eq. (IX.1)), for instance, the ground-state deformation is not taken into account in the formula and the shell-correction energy appears rather crude. Due to systematic uncertainties, the extrapolation might not be fully reliable.

IX.1.7 Summary

So far, by means of regression analysis of an extended liquid-drop mass formula, we have attempted to establish a formal framework for doing nuclear mass fits. The results obtained in this section are fully compatible with those found by many of previous studies. The advantage of the present approach is to provide a rigorous mathematical tool which would be helpful to investigate the correlations between different quantities depending on the the liquid-drop

mass formula.

This approach will be employed in the remaining part of this chapter. It should be always kept in mind that the statistical methods can only be regarded as auxiliary tools when dealing with physical problems.

IX.2 A simplified liquid-drop mass formula

First, based upon the previous discussions, we attempt to establish a simplified but hopefully more accurate mass formula in the following manner:

- The pairing term will be replaced by a more complete expression as employed in Ref. [238]. By doing so, the root-mean-square can be slightly improved, as will be shown later.
- The theoretical shell correction shall be replaced by a more realistic model based upon the Strutinsky shell-correction method, namely Möller *et al.*'s table [15]. Fig. IX.6 shows the predicted shell-correction energies which are employed to correct the measured nuclear masses.
- The curvature term shall not be considered, since some ambiguities still remain. It has been replaced by a Coulomb diffuseness term, denoted as $a_{Cd}Z^2/A$, which accounts for the correction to the Coulomb energy due to the diffuseness of the nuclear surface.
- The Coulomb exchange term will not be considered. According to the t-test results, it would not be significant when including the Coulomb diffuseness term. Hence, we keep only one correction term related to the Coulomb energy, namely the diffuseness term. This choice can slightly reduce the root-mean-square.
- The Wigner term is kept, even though there are still some ambiguities on its form, as previously explained. Anyhow, its influence on the final fit result does not seem so large, but fairly important for light nuclei with $Z \lesssim 30$.

By means of all these modifications, Eq. (IX.1) has been transformed into a slightly simplified mass formula with nine terms (eight free parameters). In the following study, we thus adopt this modified version of the mass formula, namely

$$\begin{aligned} B_n(A,Z) = &\left(a_v + a_{vt}\left(\frac{A-2Z}{A}\right)^2\right)A + \left(a_s + a_{st}\left(\frac{A-2Z}{A}\right)^2\right)A^{2/3} \\ &+ a_C\frac{Z^2}{A^{1/3}} + a_{Cd}\frac{Z^2}{A} + a_W\frac{|A-2Z|}{A} + a_p\frac{\delta_{np}(A,Z)}{A^{1/3}} - \Delta E_{\mathrm{sh}}^{\mathrm{MN}}, \end{aligned} \tag{IX.19}$$

where the shell-correction energy $\Delta E_{\mathrm{sh}}^{\mathrm{MN}}$ denotes the one taken from the Möller and Nix mass table [15] and the pairing function $\delta_{np}(A,Z)$ is taken from Ref. [238].

When the nuclear deformation comes into play, one can simply extend the above formula by adding the deformation-dependent terms to the surface term and the Coulomb term. Thus,

Table IX.2 – Best-fit values of the model parameters obtained with the OLS. The t-scores and p-values are also listed in the last two columns. Note that the significance level has been set equal to 5% for t-test. The standard deviation (SD) represents the uncertainty of the estimate.

	Estimate [MeV]	SD [MeV]	Relative SD [%]	t-score	p-value
a_v	15.453	0.007	0.046	2190.600	0.000
a_{vt}	-28.224	0.080	0.285	-351.000	0.000
a_s	-17.430	0.037	0.212	-472.230	0.000
a_{st}	35.258	0.514	1.459	68.544	0.000
a_C	-0.703	0.001	0.088	-1131.800	0.000
a_{Cd}	0.895	0.029	3.277	30.514	0.000
a_W	-24.995	1.041	4.163	-24.018	0.000
a_p	6.394	0.111	1.732	57.741	0.000
				$D_{\rm rms}$ [MeV]	0.687 73
				R^2	0.999 998
				$R^2_{\rm adj}$	0.999 998

Eq. IX.19 becomes

$$B_n(A,Z,\mathrm{def}) = \left(a_v A + a_{vt}\left(\frac{A-2Z}{A}\right)^2\right)A + \left(a_s + a_{st}\left(\frac{A-2Z}{A}\right)^2\right)A^{2/3}\mathfrak{B}_s(\mathrm{def}) + a_C\frac{Z^2}{A^{1/3}}\mathfrak{B}_C(\mathrm{def}) + a_{Cd}\frac{Z^2}{A} + a_W\frac{|A-2Z|}{A} + a_p\frac{\delta_{np}(A,Z)}{A^{1/3}} - \Delta E^{\rm MN}_{\rm sh}, \tag{IX.20}$$

where $\mathfrak{B}_s(\mathrm{def})$ and $\mathfrak{B}_C(\mathrm{def})$ are the relative surface and Coulomb energies, respectively. They are all dependent on the nuclear shape, and to a first approximation, dominated by the quadrupole deformation parameter α_2. (For spherical ground states these terms are simply equal to one.) As will be shown later in this section, Eq. (IX.20) can be used to estimate the liquid-drop fission barrier [173]. It should be noted that Eq. IX.20 is somewhat similar to the formula proposed in Ref. [162].

It should be mentioned that, for the moment, we do not know how to evaluate neither uncertainties associated with shell-correction energies nor their covariances. This would surely be worth further consideration as the uncertainty could be quite large. It would have a crucial impact on the relevant quantities, especially on the total fission-barrier height.

IX.2.1 Linear regression analysis

To determine the best-fit values of the parameters appearing in Eq. (IX.19), as fully discussed in the previous section, one can similarly perform a linear regression analysis. The best-fit estimates of the model parameter are thus obtained on the basis of the OLS (cf. Tab. IX.2). It can be immediately seen that the root-mean-square is remarkably decreased to about 0.68773 MeV, which is mainly due to the fact that the shell-correction energy has been considerably improved by using a more realistic model. As regards the significance test for

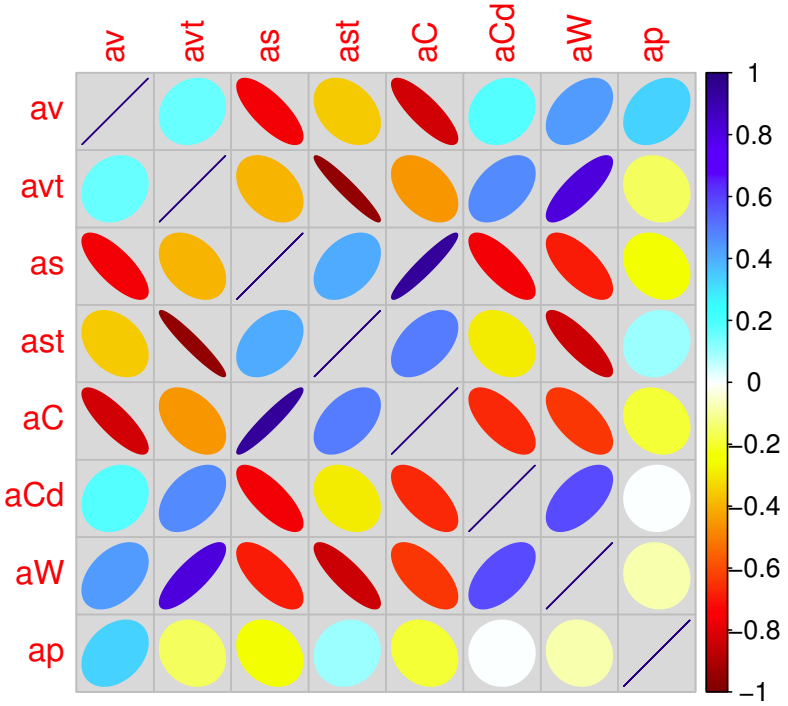

Figure IX.7 – Illustration of the correlations between the model parameters (in colored shapes).

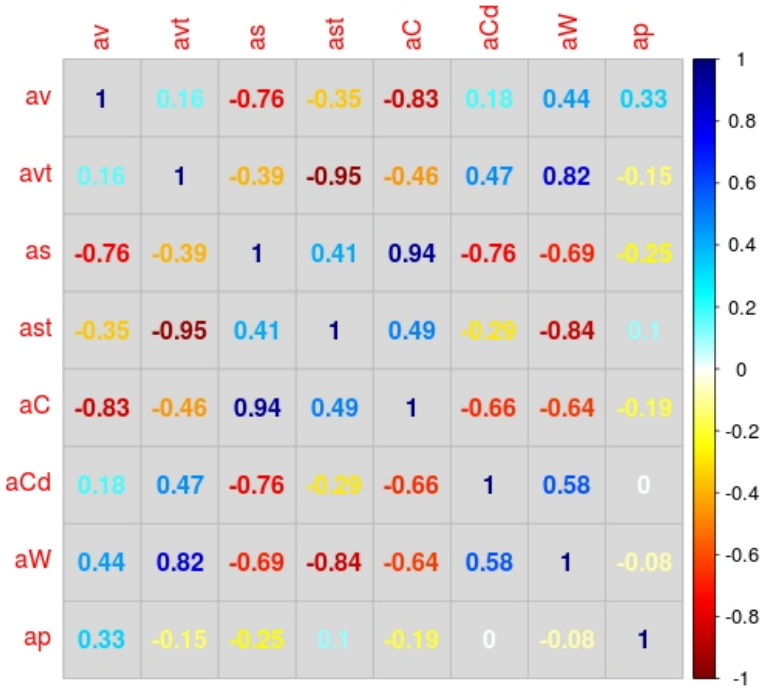

Figure IX.8 – Illustration of the correlations between the model parameters (in colored shapes).

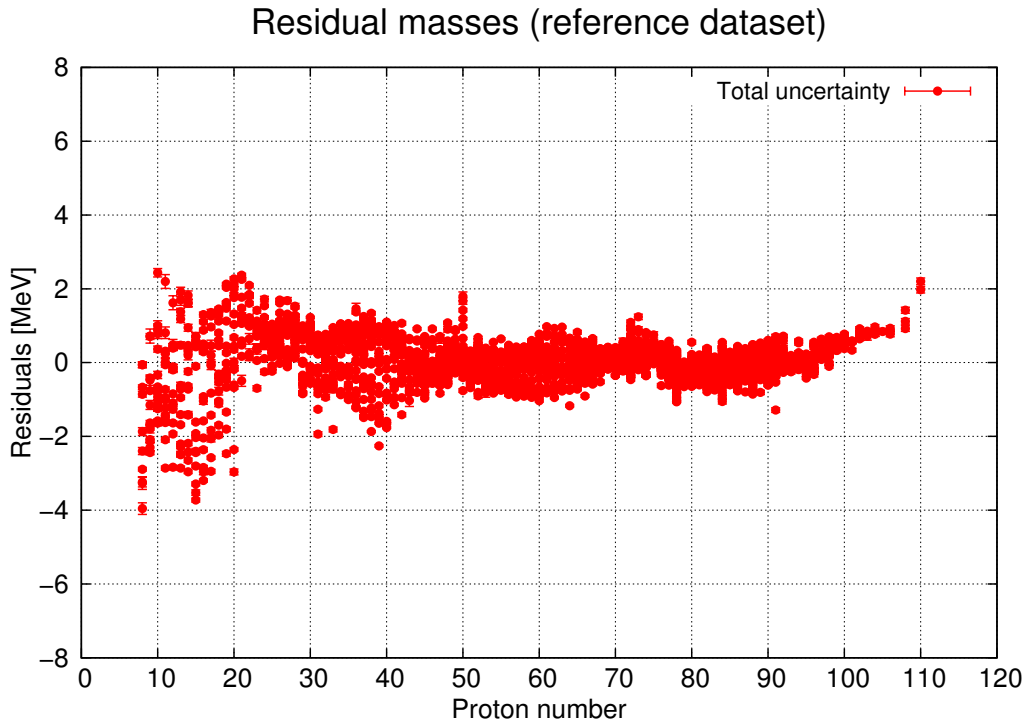

Figure IX.9 – Differences between the theoretical and experimental masses (residuals). The total uncertainty refers to the sum of the theoretical and experimental ones.

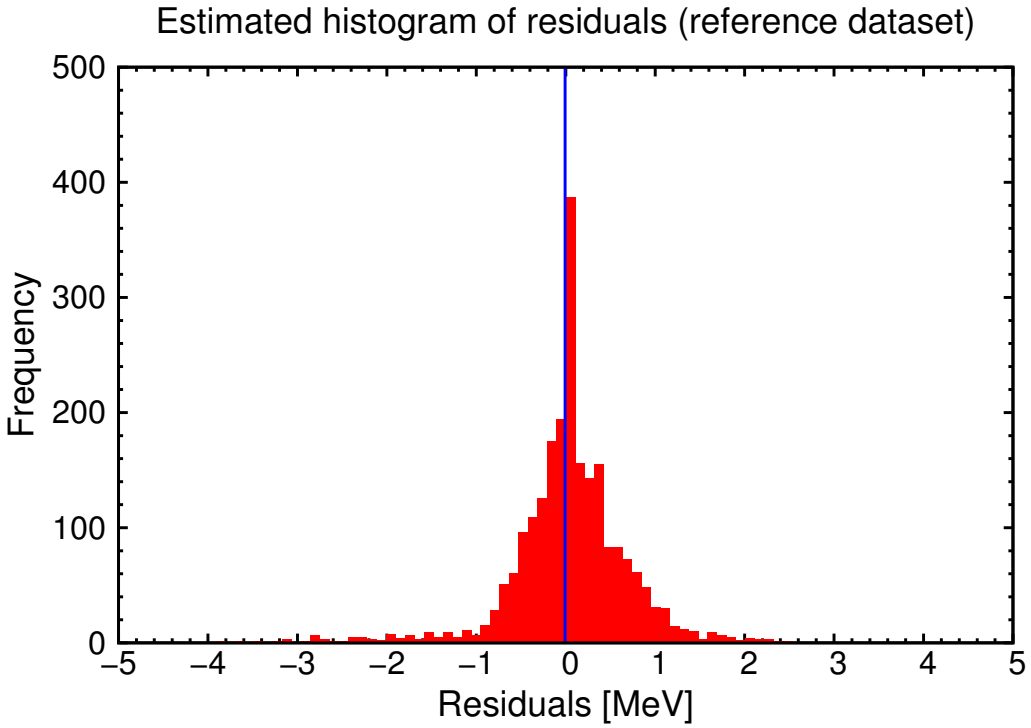

Figure IX.10 – Distribution of residuals. The skewness and kurtosis parameters are estimated to be −0.8176 and 3.1513, respectively. The vertical line denotes the mean value.

model parameters, it is clearly seen that the p-value corresponding to each term is well below the significance level. This means that the terms included in the model would be all significant to the mass fit. In Fig. IX.7, the correlation coefficients between the model parameters in the modified liquid-drop mass formula are illustrated. The correlation of the pairing term with other ones is still quite weak. However, it should be noted that the correlation between the surface term and the Coulomb term is considerably strong. This could have a crucial impact on the liquid-drop fission barrier.

Fig. IX.9 displays the residual masses obtained based upon the reference dataset. It is clearly seen that the distribution of residuals seems to be symmetrically distributed around zero. However, for light nuclei, it is observed that the differences between the calculated and experimental masses become somewhat large. This can be interpreted by the fact that the liquid-drop model does not work so well in the light mass region.

The corresponding residual distribution is displayed in Fig. IX.10, with the estimated skewness and kurtosis parameters equal to -0.8176 and 3.1513, respectively. It should be recalled that the skewness and kurtosis of a normal distribution are both equal to zero. Here, the negative skewness parameter value means that the distribution is moderately skewed to the left and nearly symmetric around its mean value ($\simeq 0$). As regards the kurtosis parameter, its value directly indicates that the distribution of residual masses appears to be much more peaked compared to the normal one. Similarly, the Shapiro-Wilk test confirms that the distribution of residuals significantly differ from the normal one, as the p-value practically vanishes. This probably means that the normality of the residual distribution is destroyed because of some systematic uncertainties, as shown in the light and super-heavy mass regions, which would make the theoretical predictions less reliable.

In the following part of this section, we shall extrapolate the fitted mass formula to the "exotic" observables so as to take a closer look at its predictive capacity.

IX.2.2 Extrapolation to exotic masses

As a first example, the exotic dataset of 960 poorly-known masses (cf. the first section of this chapter) is employed to inspect the predictive power of the fitted the mass formula.

Fig. IX.11 shows the exotic masses obtained based upon the reference dataset. It is immediately seen that the distribution of residuals is not statistically distributed. Especially in the super-heavy mass region, theoretical predictions appear to largely overestimate the exotic masses. It should be noted that the large discrepancy within the super-heavy mass region might also be due to the unreliable data presented in AME2012 (marked by "#").

The corresponding residual distribution is displayed in Fig. IX.10, with a root-mean-square of around 1.28 MeV, which is about twice that with respect to the best-known dataset. The estimated skewness and kurtosis parameters are calculated to be 1.1805 and 2.0803, respectively. The former indicates that the distribution is highly skewed to the right while it seems to

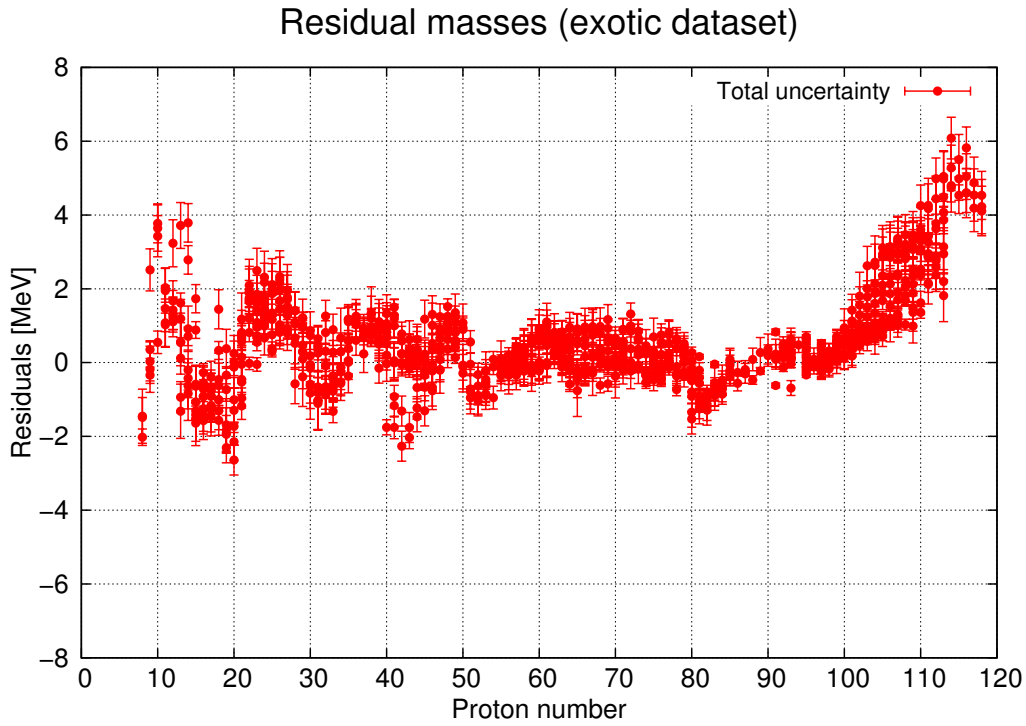

Figure IX.11 – Differences between the theoretical and experimental masses (residuals). The total uncertainty refers to the sum of the theoretical and experimental ones.

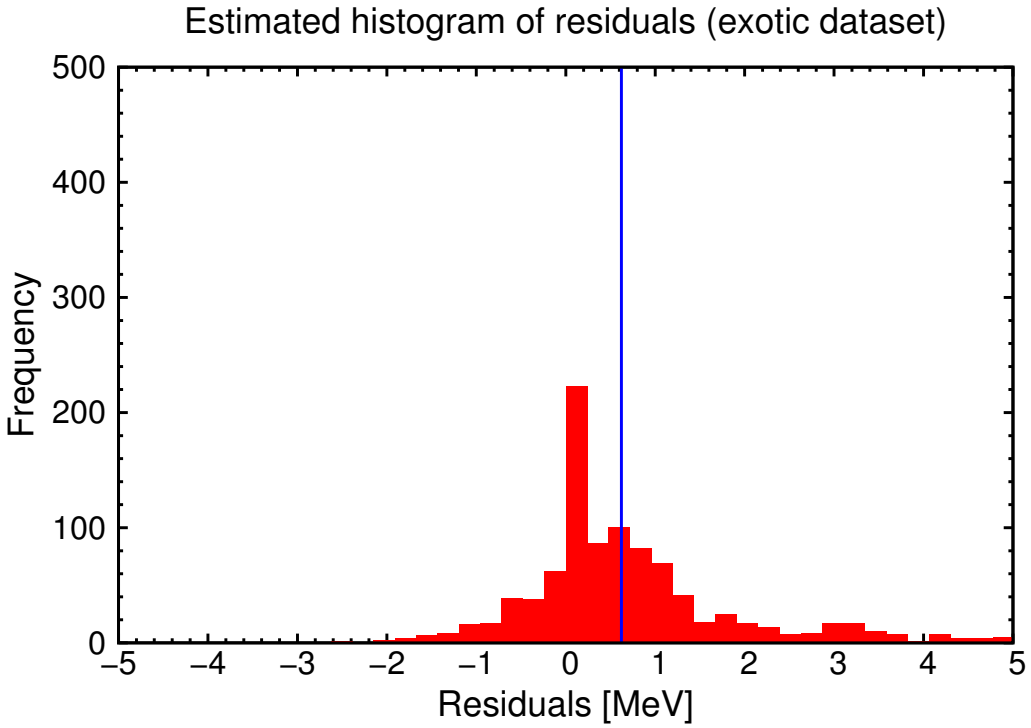

Figure IX.12 – Distribution of residuals. The skewness and kurtosis parameters are estimated to be 1.1805 and 2.0803, respectively. The vertical line denotes the mean value

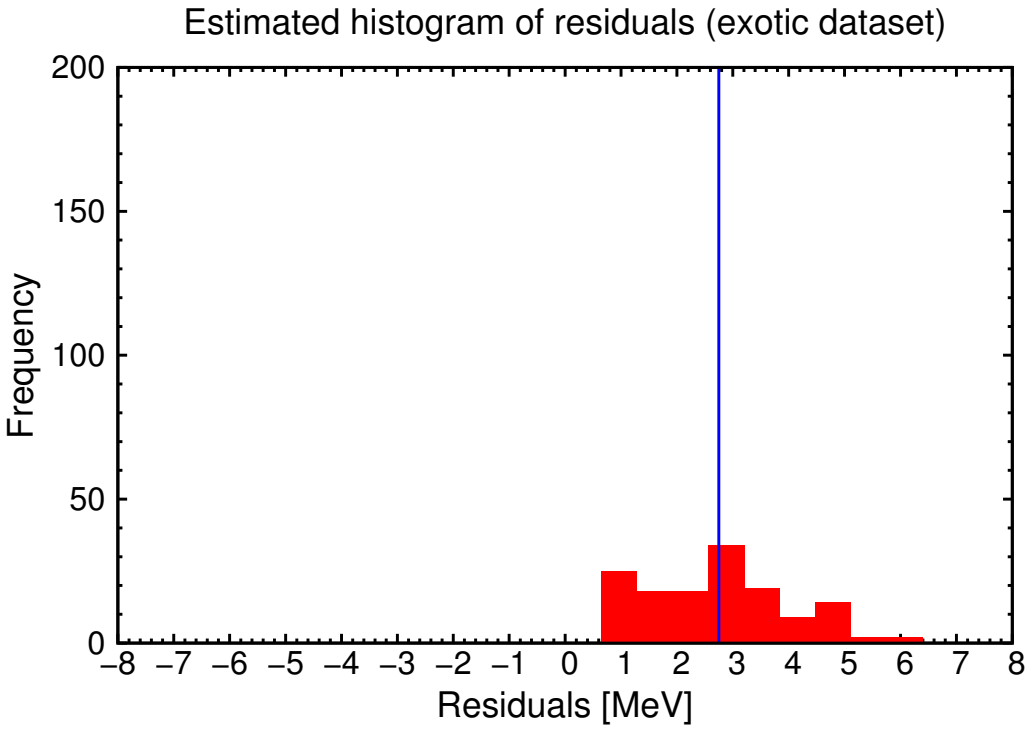

Figure IX.13 – Same as Fig. IX.12 but for the super-heavy mass region ($Z \geqslant 104$).

be symmetric around its mean value ($\simeq 0.6226$). This can be more readily demonstrated in Fig. IX.13, where a significant deviation has been observed in the super-heavy mass region. As regards the kurtosis parameter, its value directly shows that the residual distribution of fitted masses appears more peaked compared to the normal one. In addition, the Shapiro-Wilk test confirms that the distribution of residuals significantly differs from the normal one, as the p-value practically vanishes. The non-normality of the residual distribution and the systematic shift of its mean value might be caused by the unreliability of the empirical mass values as well as the theoretical limitations remaining in the mass formula, such as the predicted shell-correction energies for super-heavy nuclei.

IX.2.3 Prediction of neutron-separation energies

As a second example, we would like to examine the theoretical predictions of the fitted mass formula on the neutron-separation energy, which is particularly crucial for the evaporation of neutrons from the excited nucleus. The theoretical neutron-separation energy is simply defined as

$$S_n^{\text{th}}(A,Z) = B_n(A,Z) - B_n(A-1,Z), \tag{IX.21}$$

where the binding energies are calculated using the fitted mass formula (cf. Eq. (IX.19)). Here, the residual is simply defined as $S_n^{\text{th}} - S_n^{\text{exp}}$.

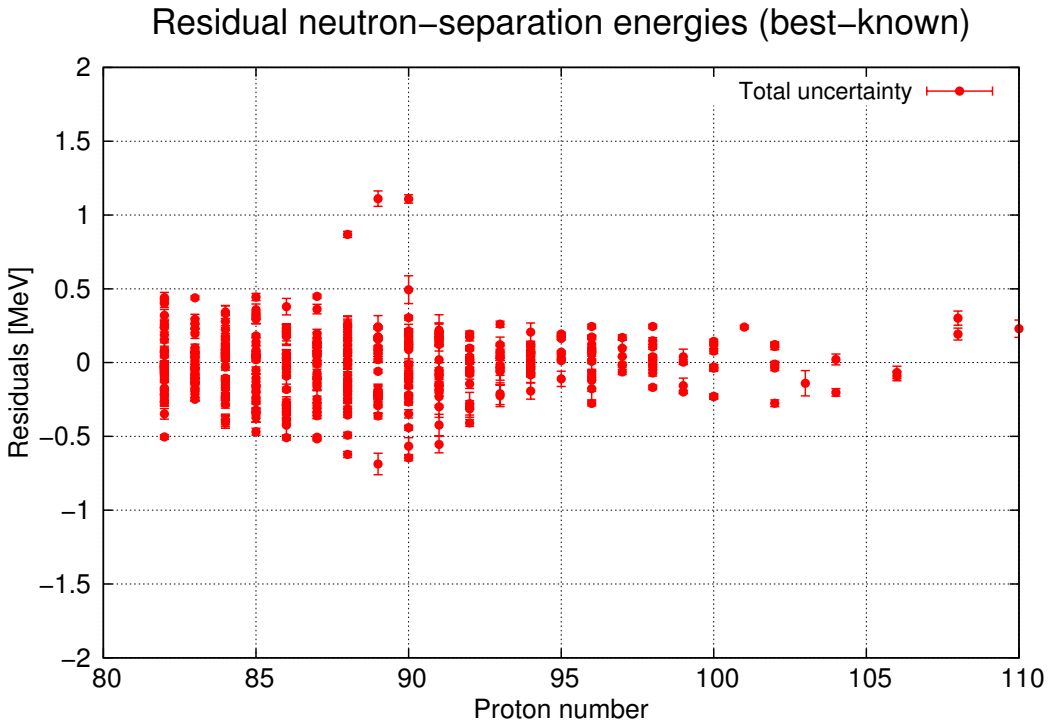

Figure IX.14 – Differences between the theoretical and experimental neutron-separation energies (residuals). The total uncertainty refers to the sum of the theoretical and experimental ones.

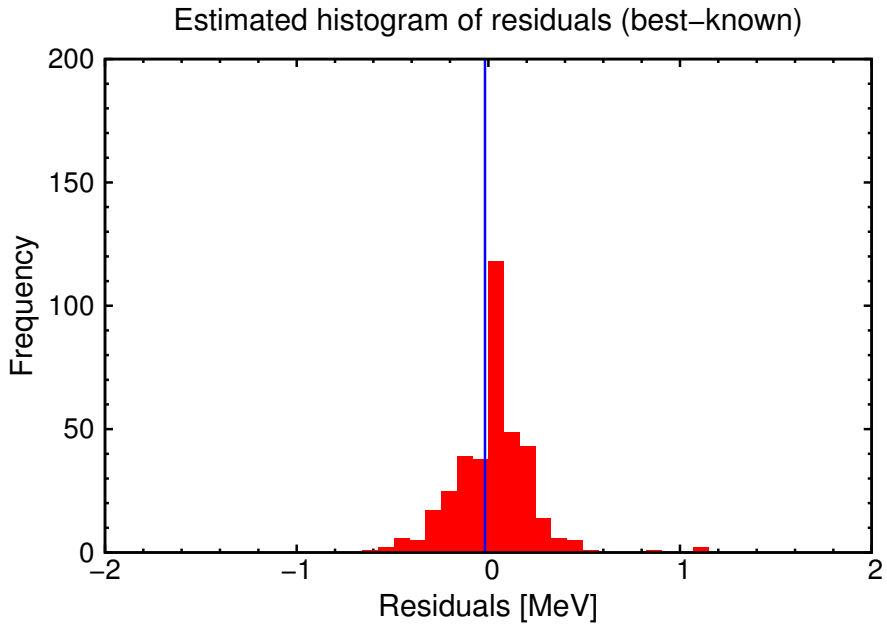

Figure IX.15 – Distribution of residuals. The skewness and kurtosis parameters are estimated to be 0.4555 and 2.8847, respectively. The vertical line denotes the mean value.

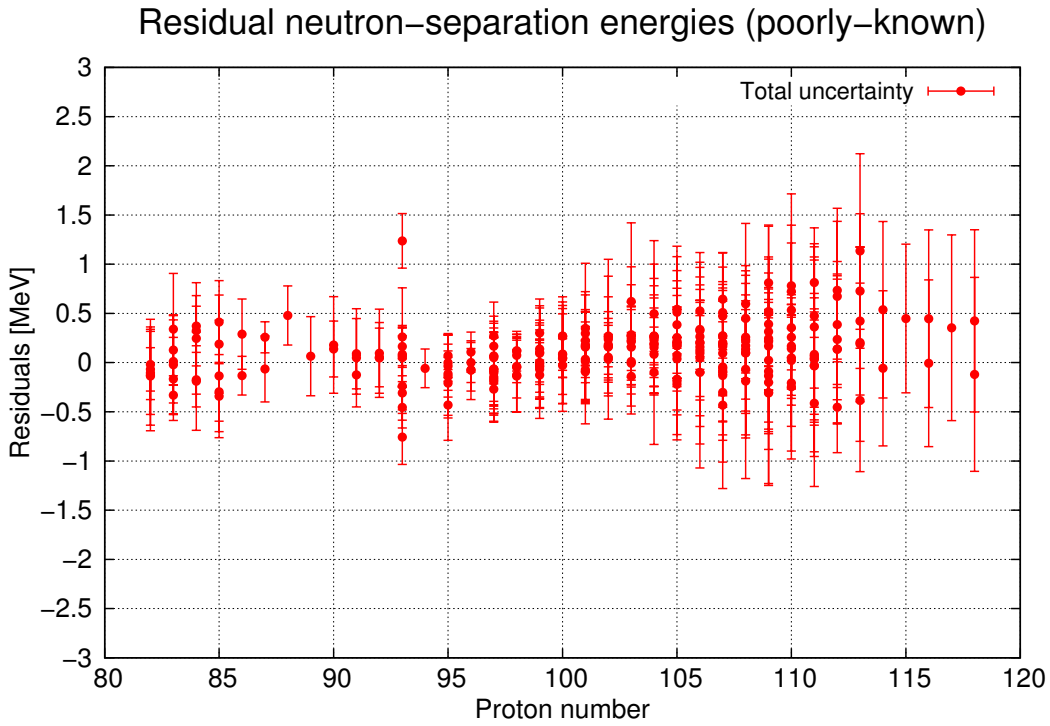

Figure IX.16 – Differences between the theoretical and experimental neutron-separation energies (residuals). The total uncertainty refers to the sum of the theoretical and experimental ones.

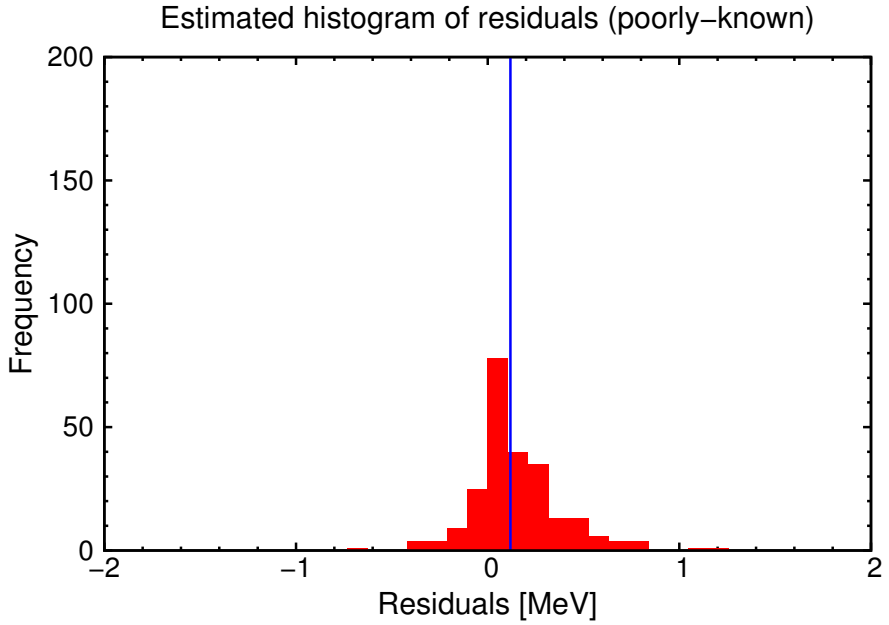

Figure IX.17 – Distribution of residuals. The skewness and kurtosis parameters are estimated to be 0.5656 and 1.7545, respectively. The vertical line denotes the mean value.

Two datasets are considered for heavy nuclei ($Z \geqslant 82$). The first one corresponds to the best-known dataset containing 372 well-measured neutron-separation energies with experimental uncertainties less than 150 keV. The second one is the poorly-known dataset that refers to 238 less-known neutron-separation energies with experimental uncertainties greater or equal than 150 keV or the evaluated ones (marked by "#" in AME2012).

To test the predictability of the mass formula, it would also be meaningful to calculate the following statistic:

$$\frac{1}{M}\sum_{i}^{M}\frac{(S_{ni}^{\rm exp}-S_{ni}^{\rm th})^2}{u^2(S_{ni}^{\rm exp})+u^2(S_{ni}^{\rm th})}. \tag{IX.22}$$

The above definition is somewhat similar to the reduced χ^2 function as employed in Refs. [15, 233]. If it is very close to one, the predictive power of the mass formula would be good enough.

In the case of the best-known dataset, the residuals of neutron-separation energies and the corresponding distribution are shown in Figs. IX.14 and IX.15. The root-mean-square is estimated to be about 0.23 MeV, which is of the same order of magnitude as that for nuclear masses and thus means that the calculated neutron-separation energies would be accurate enough for most of the nuclei near the valley of nuclear stability. As can be seen in Fig. IX.14, almost all of the residuals are comprised within 1.0 MeV, except for two nuclei relatively farther away from the valley of stability ($Z = 90, N = 221$ and $Z = 89, N = 220$) whose residuals can reach more than 1.0 MeV. This is not so surprising because in our case the nuclear binding energies can only be estimated rather well in the mass region of stable nuclei. The statistic of Eq. (IX.22) is estimated to be 104.054 which means that the predictive power of the fitted mass formula might be quite limited as the uncertainty associated with the shell-correction energy is not considered here. Moreover, Fig. IX.15 clearly demonstrates the non-normality of the residual distribution.

As regards the poorly-known dataset, the residual neutron-separation energies and the corresponding distribution are displayed in Figs. IX.16 and IX.17. It is readily observed that the total uncertainty connected with each data point becomes larger, especially in the super-heavy mass region. This is mainly due to the theoretical and experimental uncertainties which are much more important (with standard deviations up to 1.0 MeV) compared to the best-known dataset. The statistic of Eq. (IX.22) is calculated to be 0.544 which is mainly due to the large experimental uncertainty. However, the root-mean-square is estimated to be about 0.28 MeV, which is almost the same as that for the best-known dataset.

IX.3 Correlation between physical quantities

As is well known, the competition between neutron evaporation and fission process is essential for the synthesis of SHE by means of fusion-evaporation reactions. These two decay modes are respectively dominated by the neutron-separation energy S_n and fission barrier B_f, which can be estimated on the basis of the same liquid-drop mass formula. In this sense, they

should be correlated with each other.

In this section, we are going to inspect correlations between the neutron-separation energies and fission barriers estimated with the simplified liquid-drop mass formula (cf. Eq. (IX.19)). For this purpose, it might be helpful to recall the following relationships concerning the variance-covariance matrix elements for linear models:

$$\begin{aligned} u(ax_i + bx_j, cx_k + dx_l) &= ac\,u(x_i,x_k) + ad\,u(x_i,x_l) + bc\,u(x_j,x_k) + bd\,u(x_j,x_l), \\ u^2\left(\sum_i a_i x_i\right) &= \sum_i a_i^2 u^2(x_i) + 2\sum_{i<j} a_i a_j u(x_i,x_j), \text{ with } u(x_i,x_j) = u(x_j,x_i). \end{aligned} \tag{IX.23}$$

IX.3.1 Correlation between neutron-separation energies

First, we attempt to investigate correlations between the theoretical neutron-separation energies of heavy and super-heavy nuclei. The fitted liquid-drop mass formula is employed to calculate the neutron-separation energy. Uncertainties and correlations can be estimated with the help of the variance-covariance matrix for model parameters. It can be readily estimated as follows:

$$\mathrm{Var}[S_n] = (\mathbf{X}_A - \mathbf{X}_{A-1})\hat{\boldsymbol{\beta}}(\mathbf{X}_A - \mathbf{X}_{A-1})^{\mathrm{T}}, \tag{IX.24}$$

where $\mathbf{X}_A$ and $\mathbf{X}_{A-1}$ represent the model matrices of the mother and daughter nuclei, respectively.

The calculated neutron-separation energies for heavy and super-heavy nuclei are shown in Tabs. IX.3 and IX.4. The relative uncertainties are found to be quite small, less than 1%. The correlations are displayed in Figs. IX.18, IX.19, IX.20 and IX.21. It can be readily demonstrated that, for a given isotope chain, the correlation coefficient is periodically changed between positive and negative values. This is mainly due to the pairing term present in the mass formula, as the mass numbers of isotopes have different parities. This odd-even effect also appears in the calculated neutron-separation energies, as shown in the second columns of Tabs. IX.3 and IX.4.

IX.3.2 Correlation between fission barriers

In general, the liquid-drop fission barrier can be approximated as follows [173]:

$$B_f^{\mathrm{LDM}} = -A^{2/3}\left(a_s + a_{st}\left(\frac{A-2Z}{A}\right)^2\right)F(x), \tag{IX.25}$$

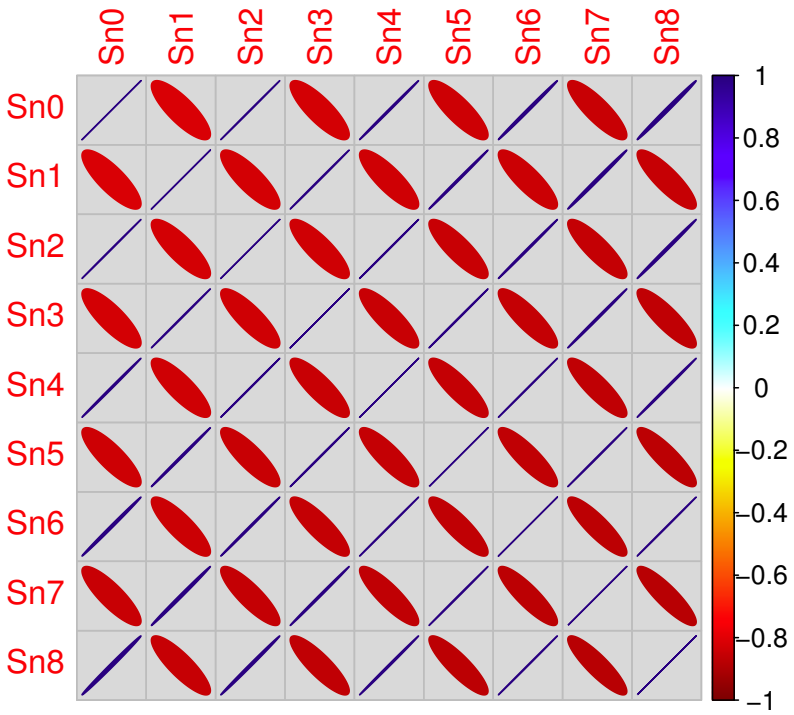

Figure IX.18 – Correlations between the calculated neutron-separation energies for the isotopes of fermium from $A_0 = 257$ to $A_8 = 249$ (in colored shapes).

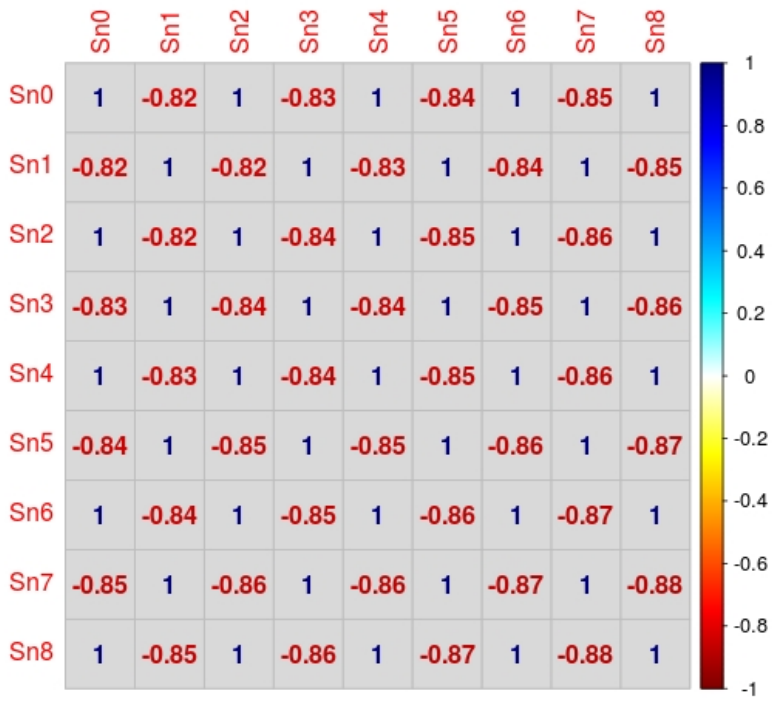

Figure IX.19 – Correlations between the calculated neutron-separation energies for the isotopes of fermium from $A_0 = 257$ to $A_8 = 249$ (in colored numbers).

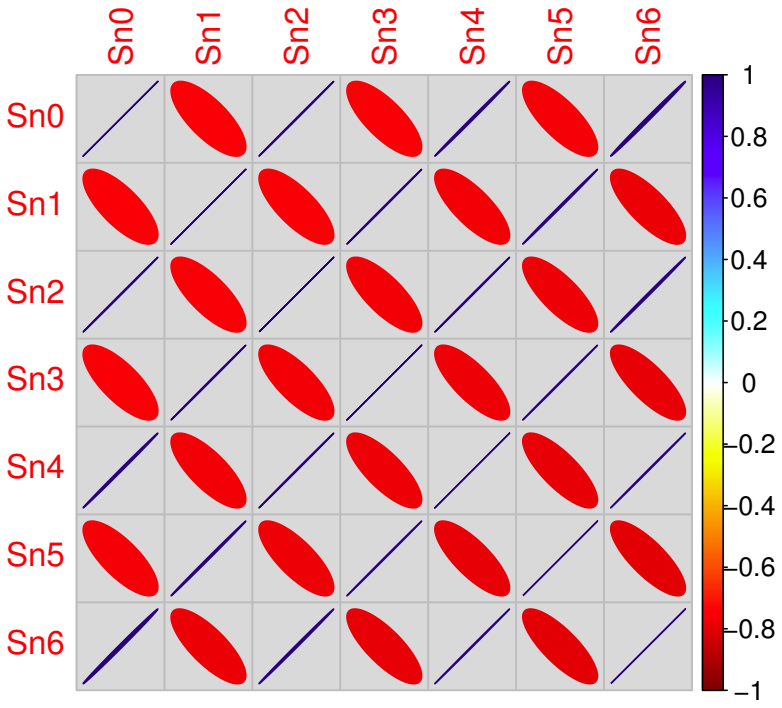

Figure IX.20 – The correlation coefficients between the calculated neutron-separation energies for the isotopes of livermorium from $A_0 = 296$ to $A_6 = 290$ (in colored shapes).

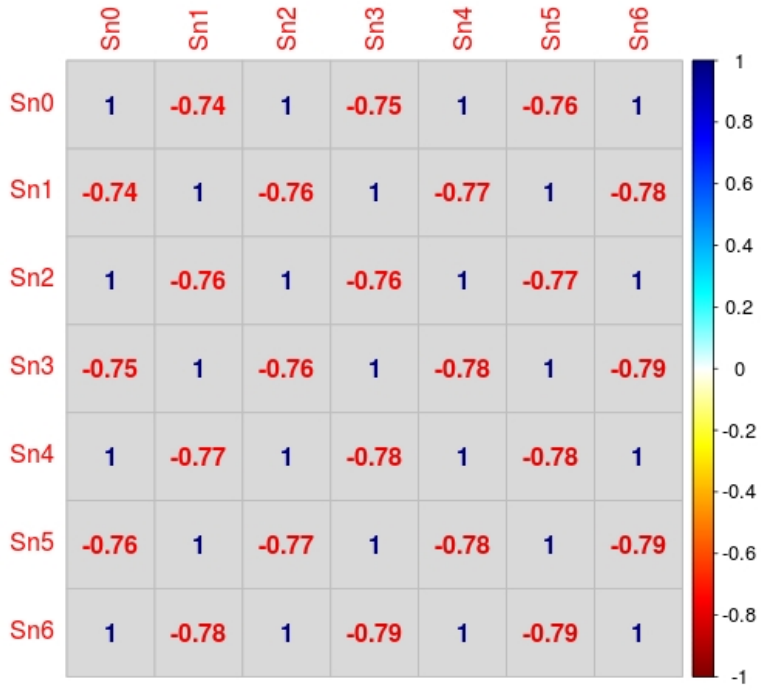

Figure IX.21 – The correlation coefficients between the calculated neutron-separation energies for the isotopes of livermorium from $A_0 = 296$ to $A_6 = 290$ (in colored numbers).

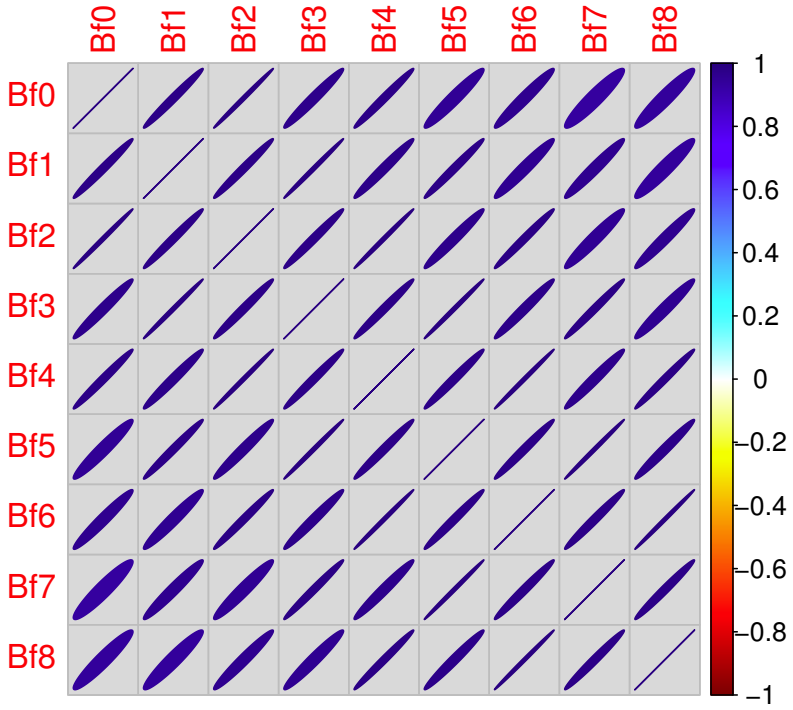

Figure IX.22 – Correlations between the calculated fission barriers for the isotopes of fermium from $A_0 = 257$ to $A_8 = 249$ (in colored shapes).

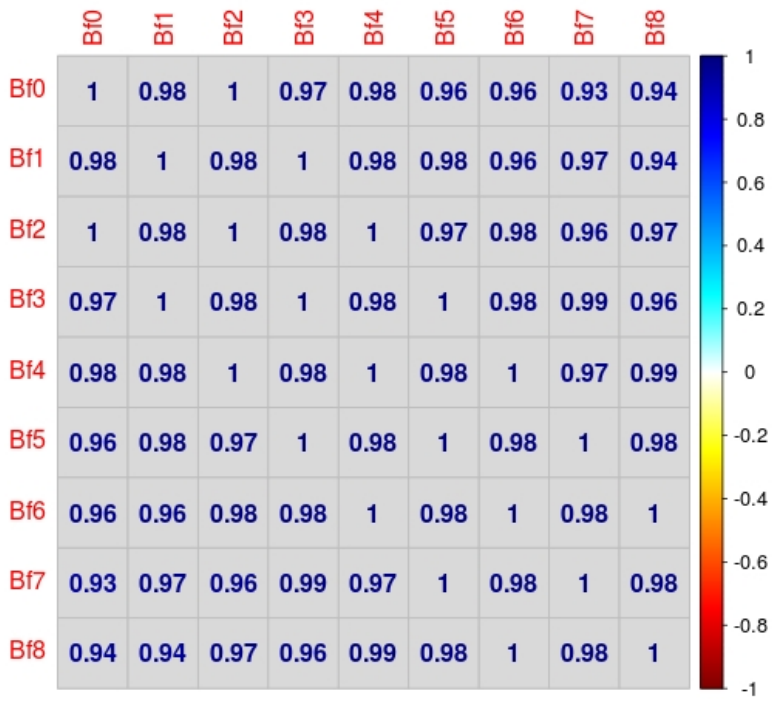

Figure IX.23 – Correlations between the calculated fission barriers for the isotopes of fermium from $A_0 = 257$ to $A_8 = 249$ (in colored numbers).

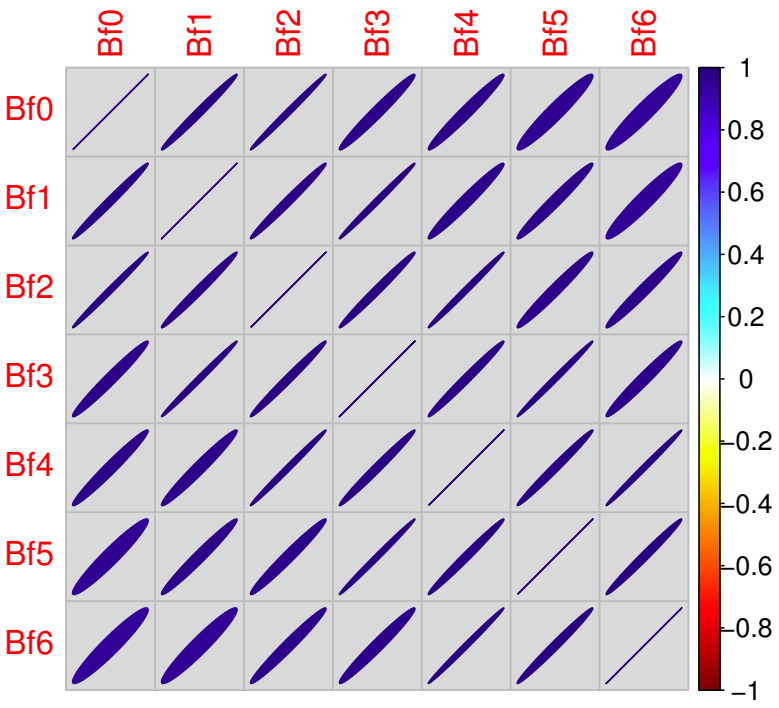

Figure IX.24 – The correlation coefficients between the calculated fission barriers for the isotopes of livermorium from $A_0 = 296$ to $A_6 = 290$ (in colored shapes).

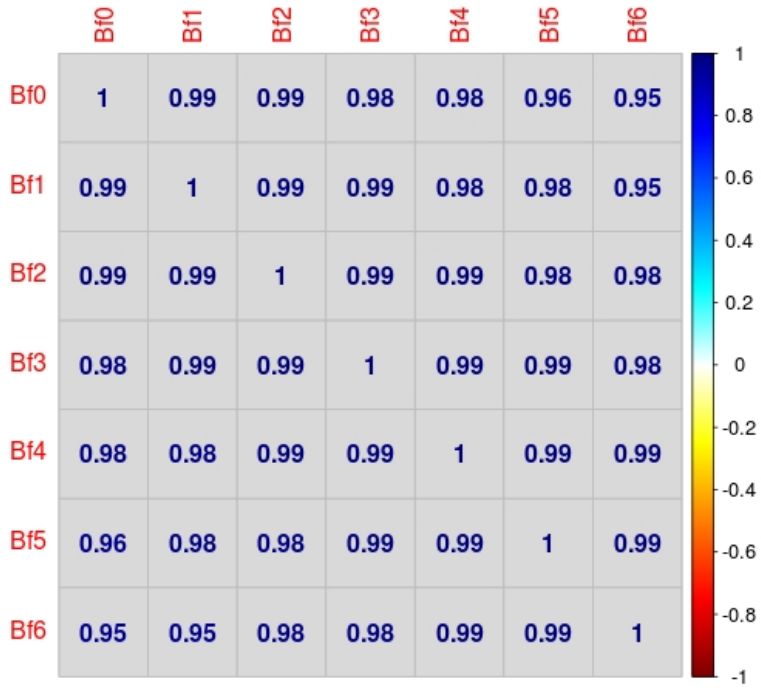

Figure IX.25 – The correlation coefficients between the calculated fission barriers for the isotopes of livermorium from $A_0 = 296$ to $A_6 = 290$ (in colored numbers).

Table IX.3 – Calculated neutron-separation energies for the isotopes of fermium from $A_0 = 257$ to $A_8 = 249$ as well as their standard deviations.

Isotopes of fermium	S_n [MeV]	$u(S_n)$ [MeV]	$u(S_n)/S_n$ [%]
A0	5.1237	0.0146	0.28
A1	6.1539	0.0140	0.23
A2	5.1402	0.0146	0.28
A3	6.6594	0.0141	0.21
A4	5.3115	0.0147	0.28
A5	7.1702	0.0143	0.20
A6	6.3080	0.0147	0.23
A7	7.5964	0.0144	0.19
A8	6.4196	0.0148	0.23

Table IX.4 – Calculated neutron-separation energies for the isotopes of livermorium from $A_0 = 296$ to $A_6 = 290$ as well as their standard deviations.

Isotopes of livermorium	S_n [MeV]	$u(S_n)$ [MeV]	$u(S_n)/S_n$ [%]
A0	6.5800	0.0137	0.21
A1	5.8535	0.0143	0.24
A2	7.2763	0.0138	0.19
A3	6.0979	0.0143	0.23
A4	7.6466	0.0139	0.18
A5	6.2463	0.0143	0.23
A6	7.6210	0.0140	0.18

Table IX.5 – Calculated fission-barrier heights for the isotopes of fermium from $A_0 = 257$ to $A_8 = 249$ as well as their standard deviations.

Isotopes of fermium	B_f [MeV]	$u(B_f)$ [MeV]	$u(B_f)/B_f$ [%]
A0	4.2361	0.0779	1.84
A1	4.1765	0.0763	1.83
A2	4.7761	0.0763	1.60
A3	4.9249	0.0751	1.52
A4	5.2630	0.0754	1.43
A5	5.4704	0.0746	1.36
A6	5.5471	0.0750	1.35
A7	4.9931	0.0745	1.49
A8	4.8986	0.0750	1.53

where the prefactor corresponds to the total surface energy of a sphere (positive) and $F(x)$ denotes a function of fissility parameter x that is defined as follows:

$$x = \frac{E_C^0}{2E_s^0} = \frac{Z^2}{A} \frac{a_C}{2\left[a_s + a_{st}\left(\frac{A-2Z}{A}\right)^2\right]}, \tag{IX.26}$$

Table IX.6 – Calculated fission-barrier heights for the isotopes of livermorium from $A = 296$ to $A = 290$ as well as their standard deviations.

Isotopes of livermorium	B_f [MeV]	$u(B_f)$ [MeV]	$u(B_f)/B_f$ [%]
A0	8.5787	0.0917	1.07
A1	8.9784	0.0921	1.03
A2	8.6981	0.0908	1.04
A3	8.6177	0.0917	1.06
A4	8.2973	0.0911	1.10
A5	8.0668	0.0924	1.15
A6	7.8062	0.0924	1.18

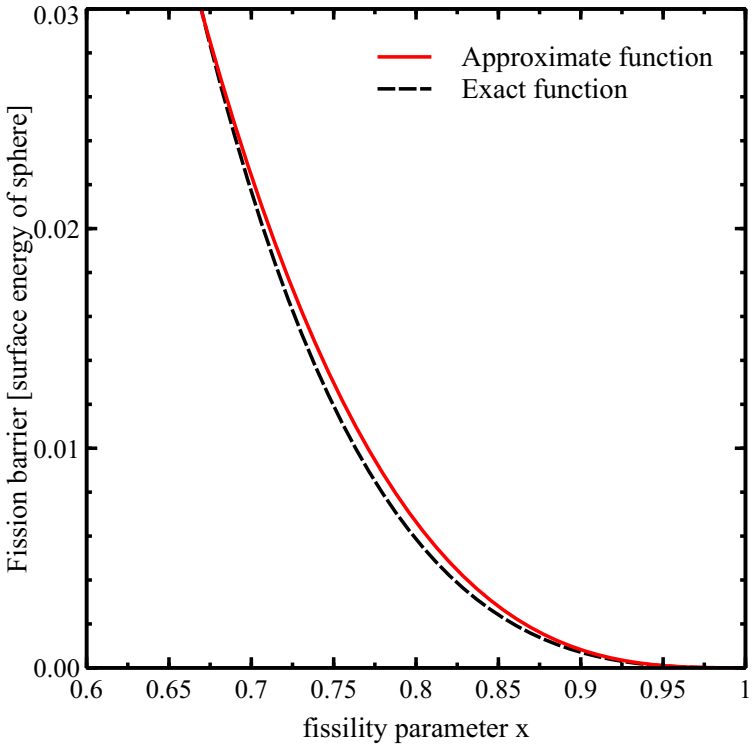

Figure IX.26 – Comparison between two parameterizations for the liquid-drop fission barrier.

where E_s^0 and E_C^0 represent the surface and Coulomb energies of a sphere. Eq. (IX.25) can be actually demonstrated on the basis of the total deformation energy, which is defined as the potential energy (or binding energy B_n with minus sign) for a deformed nucleus subtracts the value for a spherical shape, that is to say, $U_{\text{def}}(\alpha_2) \simeq B_n(A,Z,\alpha_2 = 0) - B_n(A,Z,\alpha_2)$, which can be approximately calculated with the help of Eq. (IX.20) (without shell-correction term) and

the following relationships:

$$\mathfrak{B}_s(\alpha_2) = 1 + \frac{2}{5}\alpha_2^2 - \frac{4}{105}\alpha_2^3 - \frac{66}{175}\alpha_2^4, \tag{IX.27}$$

$$\mathfrak{B}_C(\alpha_2) = 1 - \frac{1}{5}\alpha_2^2 - \frac{4}{105}\alpha_2^3 + \frac{51}{245}\alpha_2^4. \tag{IX.28}$$

In doing this, we have assumed that the nuclear deformation is governed by the quadrupole component which is a good approximation for heavy nuclei. The location of the saddle point is conventionally determined by solving the following conditional equation:

$$\frac{\mathrm{d}U_{\mathrm{def}}(\alpha_2)}{\mathrm{d}\alpha_2} = 0. \tag{IX.29}$$

The solution of the above equation gives the location of the saddle point, from which the liquid-drop fission barrier can be estimated in an approximate manner. It should be mentioned that this demonstration is generally valid provided that the mass formula contains only two deformation-dependent terms, namely the surface term and Coulomb term [173, 239].

Regarding the closed-form expression for the function $F(x)$, two possible choices are given and discussed in Ref. [173]. The first one is given by

$$F(x) = 0.83(1-x)^3, \tag{IX.30}$$

and the second one is

$$\begin{aligned} F(x) = {} & 0.7295(1-x)^3 \\ & - 0.3302(1-x)^4 + 0.6387(1-x)^5 \\ & + 7.8727(1-x)^6 - 12.0061(1-x)^7, \end{aligned} \tag{IX.31}$$

which would be sightly more accurate than the first one. Here, it is assumed that the fissility parameter is greater than 0.7, which is always true for heavy and super-heavy nuclei. The discrepancy between these two analytical expressions appears not significant, as shown in Fig. IX.26. For the sake of simplicity, in the present study, the first one is employed to estimate the liquid-drop fission barrier, which thus becomes a function of three model parameters, namely a_s, a_{st} and a_C.

When the shell-correction energy is taken into account, the total fission barrier can usually be approximated by the following formula:

$$B_f = B_f^{\mathrm{LDM}}(\hat{\boldsymbol{\beta}}) - \Delta E_{\mathrm{sh}}^{\mathrm{MN}}, \tag{IX.32}$$

where $\Delta E_{\mathrm{sh}}^{\mathrm{MN}}$ denotes the theoretical shell-correction energy taken from Ref. [15]. It should be noted that, since the liquid-drop fission barrier is dependent on the parameter vector $\hat{\boldsymbol{\beta}}$ so that it can be represented by $B_f^{\mathrm{LDM}}(\hat{\boldsymbol{\beta}})$. To compute the variance-covariance matrix of the estimated fission barrier, since uncertainties in the model parameters are much smaller than

their best-fit estimates (~ 1% or even less), one can safely employ the local expansion-based method, namely making a first-order Taylor series approximation, to propagate uncertainties coming from the model parameters (cf. the chapter on uncertainty analysis). Thus, the corresponding variance-covariance matrix is simply given as follows:

$$\mathrm{Var}[B_f] = \left(\frac{\mathrm{d}B_f^{\mathrm{LDM}}(\hat{\boldsymbol{\beta}})}{\mathrm{d}\hat{\boldsymbol{\beta}}} \right) \mathrm{Var}[\hat{\boldsymbol{\beta}}] \left(\frac{\mathrm{d}B_f^{\mathrm{LDM}}(\hat{\boldsymbol{\beta}})}{\mathrm{d}\hat{\boldsymbol{\beta}}} \right)^{\mathrm{T}}, \tag{IX.33}$$

where $\mathrm{d}B_f^{\mathrm{LDM}}(\hat{\boldsymbol{\beta}})/\mathrm{d}\hat{\boldsymbol{\beta}}$ refers to the Jacobian matrix that can be explicitly calculated. To this end, one only needs to calculate the partial derivatives of the liquid-drop fission barrier with respect to a_s, a_{st} and a_C. (The partial derivatives with respect to the other parameters are simply equal to zero.) They are given as follows:

$$\frac{\partial B_f^{\mathrm{LDM}}}{\partial a_s} = K \left[\left(1 - \frac{a_C X}{a_{st} I^2 + a_s} \right)^3 + \frac{3 a_C X \left(1 - \frac{a_C X}{a_{st} I^2 + a_s} \right)^2}{a_{st} I^2 + a_s} \right], \tag{IX.34}$$

$$\frac{\partial B_f^{\mathrm{LDM}}}{\partial a_{st}} = I^2 \frac{\partial B_f^{\mathrm{LDM}}}{\partial a_s}, \tag{IX.35}$$

$$\frac{\partial B_f^{\mathrm{LDM}}}{\partial a_C} = -3KX \left(1 - \frac{a_C X}{a_{st} I^2 + a_s} \right)^2, \tag{IX.36}$$

where $K = -0.83 A^{2/3}$, $X = Z^2/(2A)$ and the neutron-proton asymmetry $I = (A - 2Z)/A$.

Figs. IX.22, IX.23, IX.24 and IX.25 illustrate the correlations between the calculated fission barriers for the same isotope chains. As expected, strong correlations have been found due to the correlation between the surface term and the Coulomb term (cf. Fig. IX.7). The estimated fission-barrier heights as well as their uncertainties are reported in Tabs. IX.5 and IX.6. It is clearly shown that the relative uncertainties are estimated to be around 1%, which is on average about ten times greater than those of neutron-separation energies.

IX.3.3 Correlation between B_f and S_n

Finally, we are trying to compute the variance-covariance matrix for both neutron separation energies and fission barriers. This can be similarly done by employing the first-order Taylor series approximation. After making some simplifications, we arrive at

$$\mathrm{Cov}[B_f, S_n] = \left(\frac{\mathrm{d}B_f^{\mathrm{LDM}}(\hat{\boldsymbol{\beta}})}{\mathrm{d}\hat{\boldsymbol{\beta}}} \right) \mathrm{Var}[\hat{\boldsymbol{\beta}}] \left(\mathbf{X}_A - \mathbf{X}_{A-1} \right)^{\mathrm{T}}, \tag{IX.37}$$

where $\mathrm{d}B_f^{\mathrm{LDM}}(\hat{\boldsymbol{\beta}})/\mathrm{d}\hat{\boldsymbol{\beta}}$ refers to the Jacobian matrix and $\mathbf{X}_A$ and $\mathbf{X}_{A-1}$ represent the model matrices of the mother and daughter nuclei, respectively.

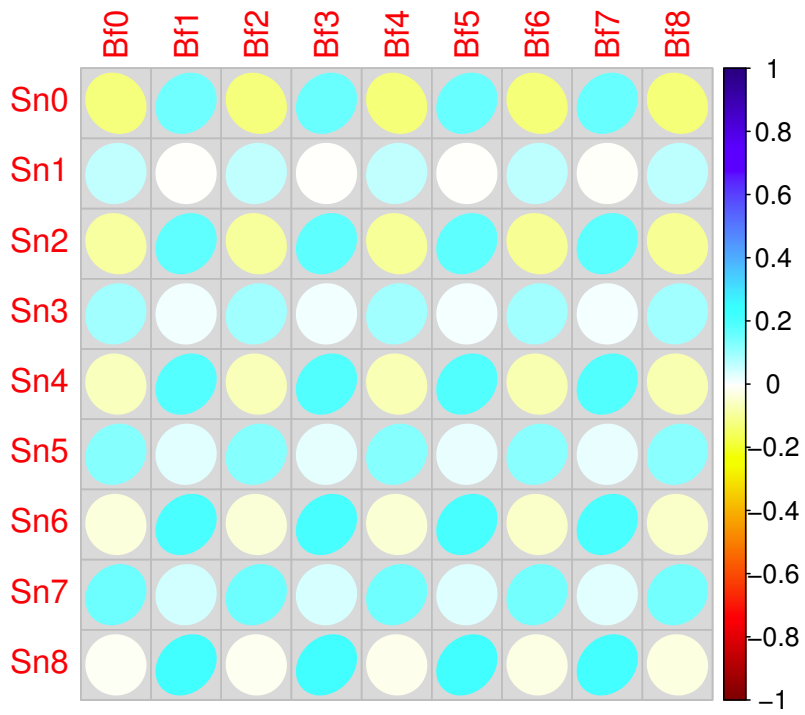

Figure IX.27 – Correlations between the calculated neutron-separation energies (columns) and fission barriers (rows) for the isotopes of fermium from $A_0 = 257$ to $A_8 = 249$ (in colored shapes).

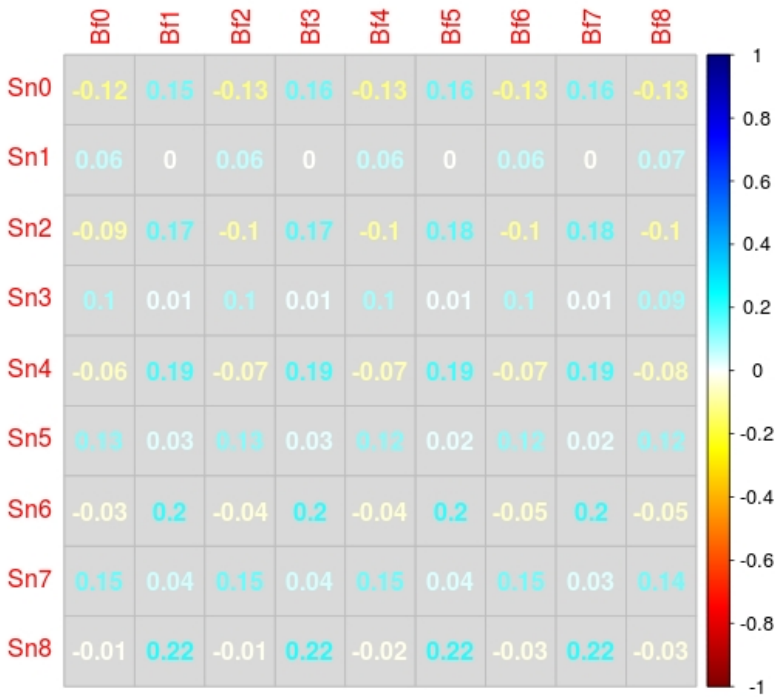

Figure IX.28 – Correlations between the calculated neutron-separation energies (columns) and fission barriers (rows) for the isotopes of fermium from $A_0 = 257$ to $A_8 = 249$ (in colored numbers).

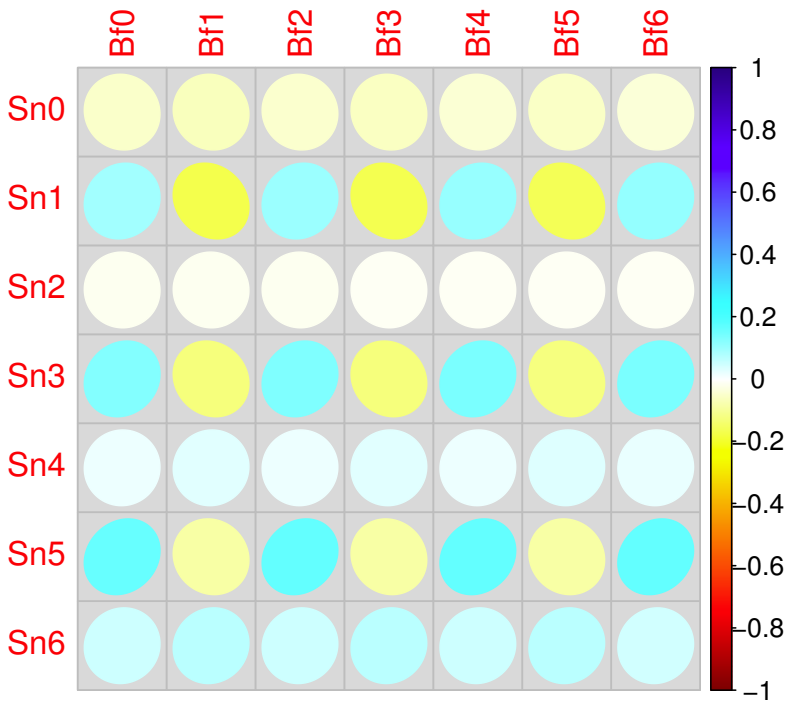

Figure IX.29 – The correlation coefficients between the calculated neutron-separation energies (columns) and fission barriers (rows) for the isotopes of livermorium from $A_0 = 296$ to $A_6 = 290$ (in colored shapes).

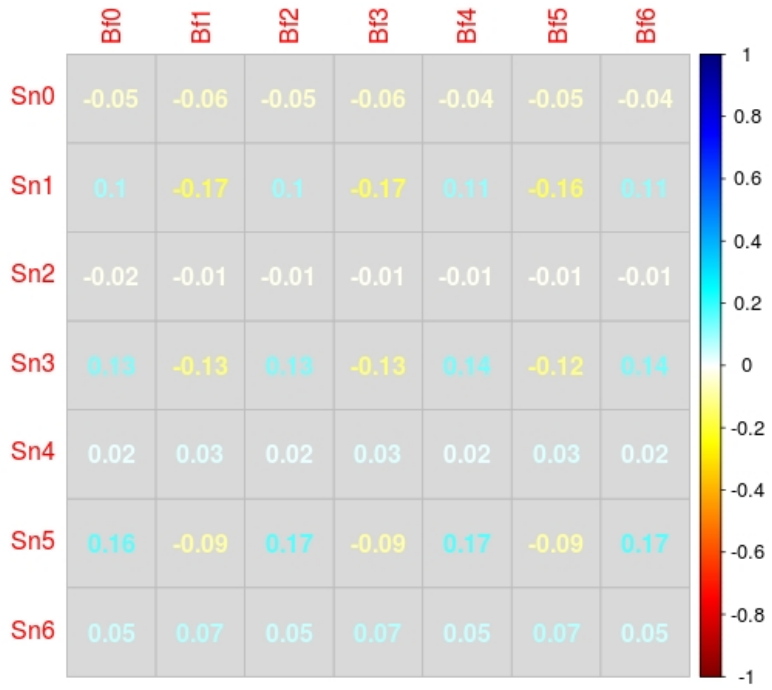

Figure IX.30 – The correlation coefficients between the calculated neutron-separation energies (columns) and fission barriers (rows) for the isotopes of livermorium from $A_0 = 296$ to $A_6 = 290$ (in colored numbers).

Figs. IX.27, IX.28, IX.29 and IX.30 tell us how the calculated neutron-separation energies and fission barriers for the same isotope chains are correlated between each other. Nevertheless, no significant correlation has been observed.

IX.4 Influence on the survival probability

IX.4.1 Analytical modeling

To investigate the impact of correlations between neutron-separation energies and fission barriers on the survival probability, we employ a simplified single-neutron evaporation model (cf. Appendix C).

Within this framework, the survival probability for the $1n$-channel is simply given as follows:

$$P_{\mathrm{sur}}^{1n} = \frac{\Gamma_n^A}{\Gamma_f^A + \Gamma_n^A} R_{1n}, \tag{IX.38}$$

where the superscript A represents the excited mother nucleus and R_{1n} is the probability of realization of $1n$-channel reads [240]

$$R_{1n} = \left(1 + \frac{\epsilon_1^{\max} - E_{\mathrm{th}}^{A-1}}{T_A}\right) \exp\left(-\frac{\epsilon_1^{\max} - E_{\mathrm{th}}^{A-1}}{T_A}\right), \tag{IX.39}$$

provided that the maximum kinetic energy of the neutron $\epsilon_1^{\max} = E_A^* - S_n^A$ is greater than E_{th}^{A-1}. For $\epsilon_1^{\max} - E_{\mathrm{th}}^{A-1} < 0$, one simply has $R_{1n} = 1$. The threshold E_{th}^{A-1} is defined as $\min(B_f^{A-1}, S_n^{A-1})$, where B_f^{A-1} and S_n^{A-1} denote the fission barrier and the neutron-separation energy of the daughter nucleus, respectively. It should be noted that, in the case of very heavy and superheavy nuclei, the fission is usually the dominant decay mode, which means that E_{th}^{A-1} is always taken to be B_f^{A-1}. Regarding the ratio Γ_n/Γ_f, it can be estimated using the well-known approximate formula proposed by Vandenbosch and Huizenga [241], namely,

$$\frac{\Gamma_n}{\Gamma_f} = \frac{4A^{2/3} a_f (E_A^* - S_n^A)}{k_0 a_n \left[2\sqrt{a_f (E_A^* - B_f^A)} - 1\right]} \exp\left[2\sqrt{a_n (E_A^* - S_n^A)} - 2\sqrt{a_f (E_A^* - B_f^A)}\right], \tag{IX.40}$$

where k_0 and $a_n = a_f$ are estimated to be 9.8 MeV and $A/10$ MeV^{-1}, respectively. It should be noted that the above formula is based upon a simple Fermi-gas model without taking into account any correction (dissipation, shell damping, etc).

It is readily seen that the survival probability (cf. Eq. (IX.38)) is dependent on both the neutron-separation energies and the fission barriers of the mother and daughter nuclei. They can be well estimated with the help of a liquid-drop model. It should be noted that the main input quantities appearing in Eq. (IX.38) are correlated with each other as unambiguously demonstrated in the previous sections of this chapter. To further estimate how the uncertainty and correlation affect the survival probability, we are going to employ the same Monte-Carlo

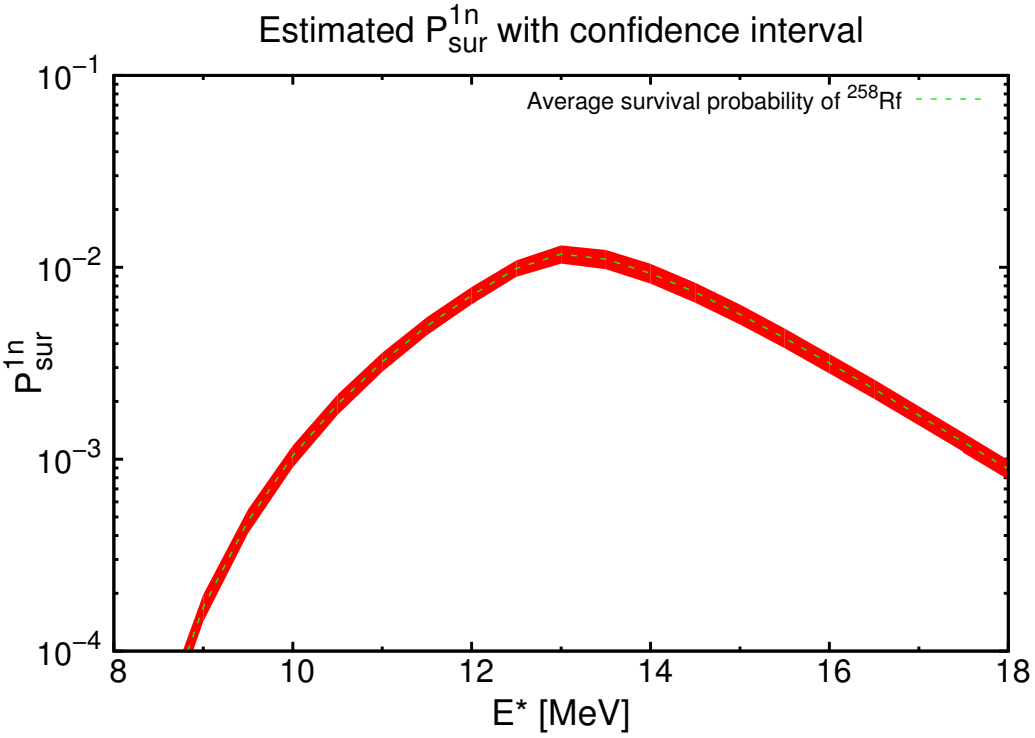

Figure IX.31 – Estimated survival probability for ^{266}Rf as a function of excitation energy. The shaded area indicates the 95% confidence interval.

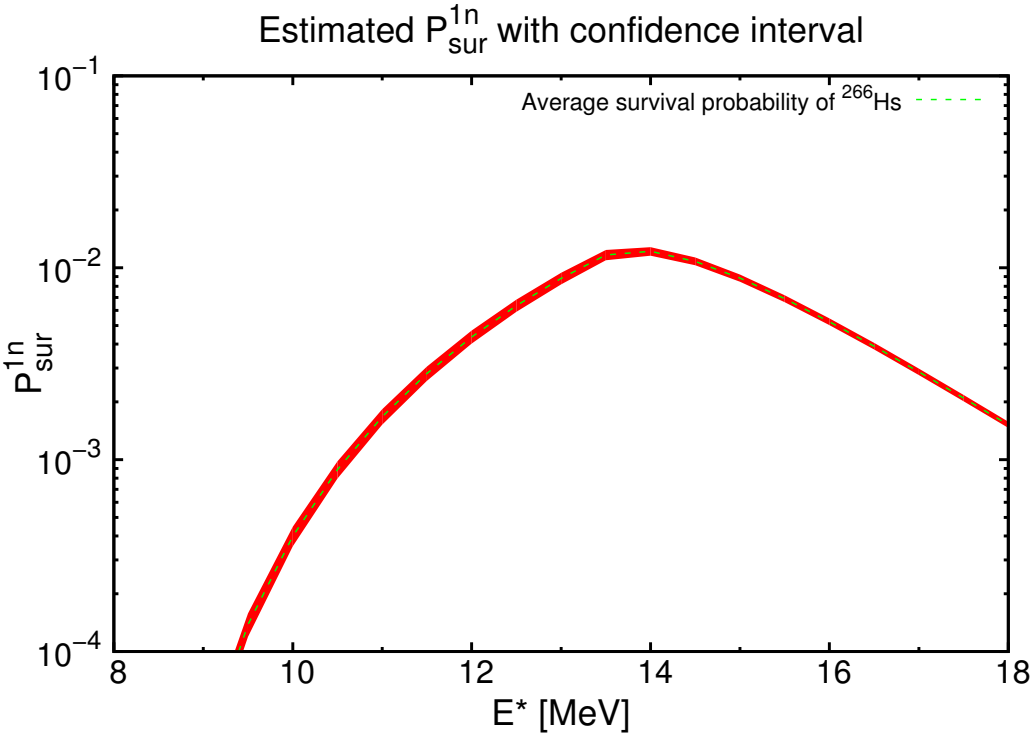

Figure IX.32 – Estimated survival probability for ^{258}Hs as a function of excitation energy. The shaded area indicates the 95% confidence interval.

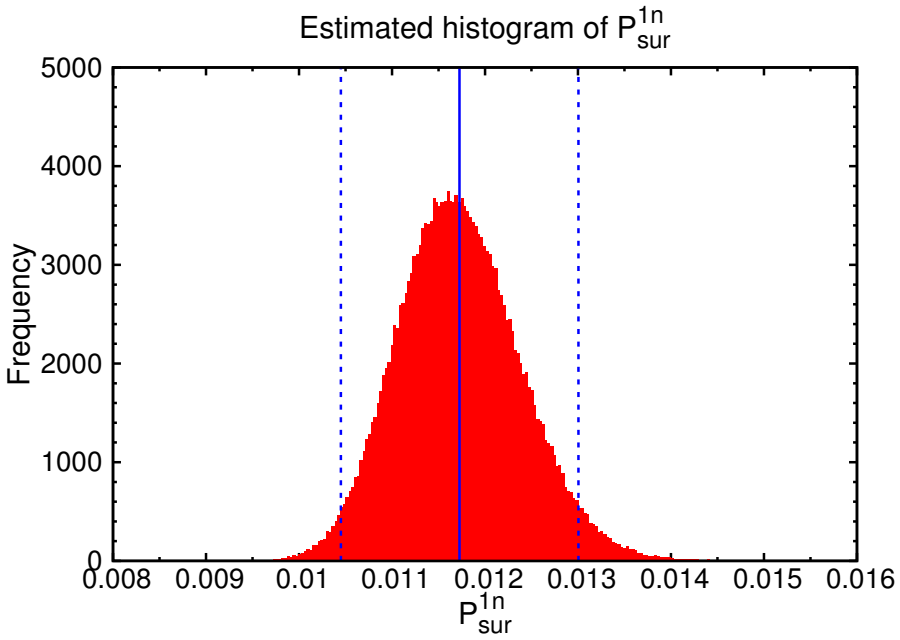

Figure IX.33 – Estimated distribution of the survival probability for ^{258}Rf. The solid vertical line represents the mean value. The dotted vertical lines refer to the lower and upper limits of the confidence interval, respectively. The skewness and kurtosis parameters are estimated to be 0.2425 and 0.1290, respectively.

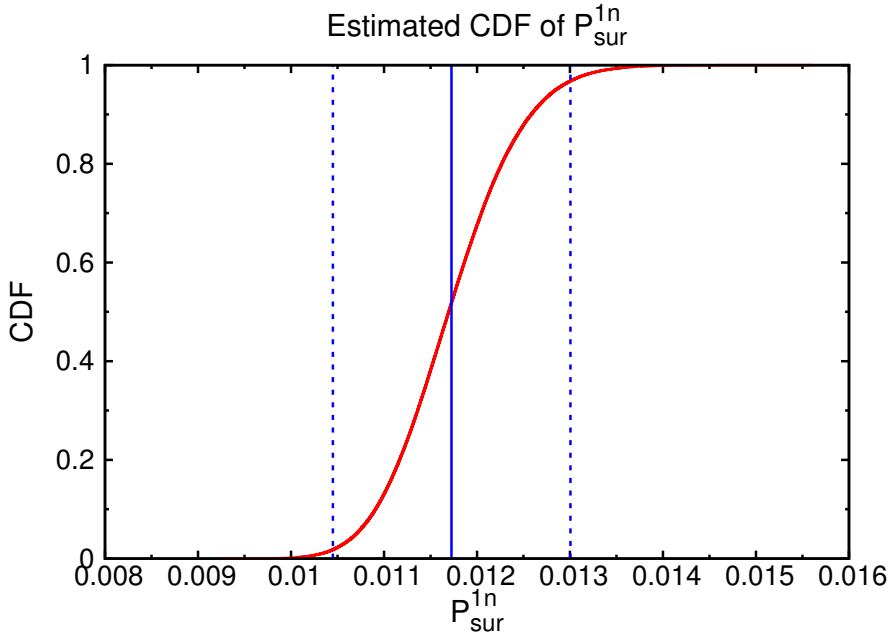

Figure IX.34 – Estimated CDF of the survival probability for ^{258}Rf. The solid vertical line represents the mean value. The dotted vertical lines refer to the lower and upper limits of the confidence interval, respectively. Note that the horizontal axis is in logarithmic scale.

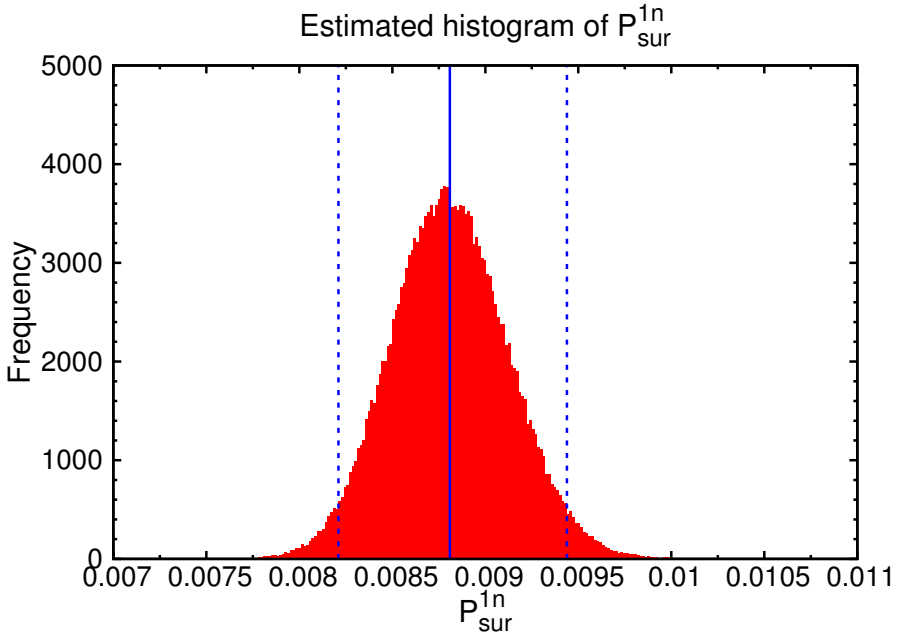

Figure IX.35 – Estimated distribution of the survival probability for ^{266}Hs. The solid vertical line represents the mean value. The dotted vertical lines refer to the lower and upper limits of the confidence interval, respectively. The skewness and kurtosis parameters are estimated to be 0.0984 and 0.0069, respectively.

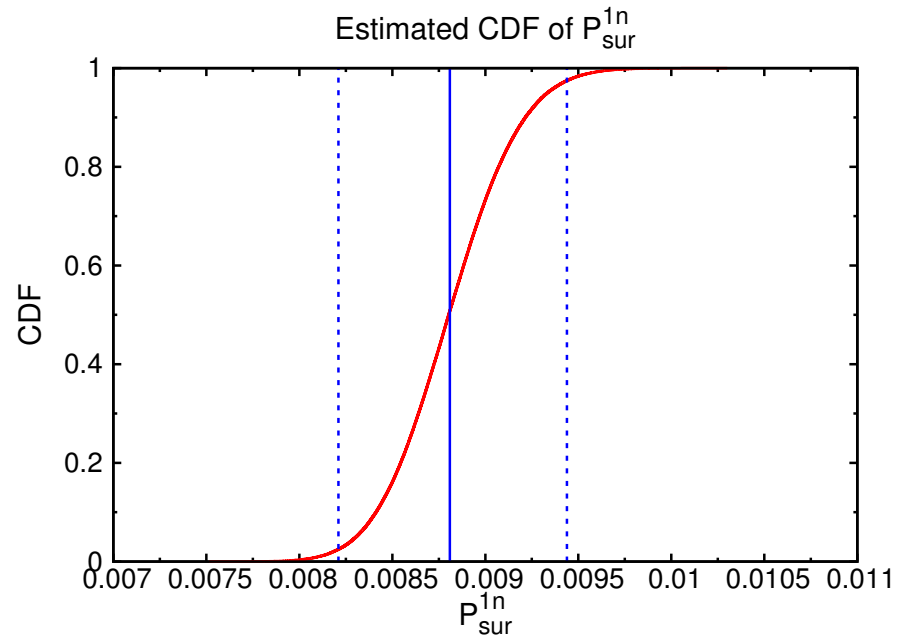

Figure IX.36 – Estimated CDF of the survival probability for ^{266}Hs. The solid vertical line represents the mean value. The dotted vertical lines refer to the lower and upper limits of the confidence interval, respectively. Note that the horizontal axis is in logarithmic scale.

approach based on the GUMS1 to propagate the input distributions through the model. For this aim to be achieved, one needs to know the input distributions of neutron-separation energies and fission barriers. It should be mentioned that the calculated neutron-separation energy and fission barrier are both connected with the terms in mass formula, or in other words, the input distributions are essentially dependent on the model parameters of the liquid-drop mass formula. This allows to simplify the calculation of variances and covariances related to the relevant quantities.

In brief, the input distributions are simply given by the parameter vector $\hat{\boldsymbol{\beta}}$, which is assumed to follow a multivariate Gaussian distribution with the variance-covariance matrix $\mathrm{Var}[\hat{\boldsymbol{\beta}}]$. In this case, the model function for a given excitation energy E^* is simply written as $P_{\mathrm{sur}}^{1n}(\hat{\boldsymbol{\beta}})$.

IX.4.2 Results and discussion

One the basis of the toy model described above, the decays of two super-heavy nuclei, namely ^{266}Rf and ^{258}Hs, have been systematically investigated using the method of uncertainty analysis based on the GUMS1.

The calculated survival probabilities as a function of excitation energy are illustrated in Figs. IX.31 and IX.32. It is clearly shown that the 95% confidence intervals seem to be quite narrow because of small input uncertainties.

Now, let us zoom in a chosen area corresponding to an excitation energy of 13 MeV. Figs. IX.33 and IX.35 illustrate the distributions of survival probabilities estimated by means of the toy model. Here, the excitation energy is kept fixed at 13.0 MeV. Both of them appear to be normally distributed around their mean values. This can be clearly demonstrated by examining the corresponding skewness and kurtosis parameters, which seem to be very close to zero. It should be recalled that the skewness and kurtosis for a normal distribution are equal to zero.

To determine their confidence intervals, one can employed the same approach as proposed in GUMS1. Figs. IX.34 and IX.36 display the estimated CDFs at the same excitation energy. It is readily seen that the lower and upper limits of the confidence interval are perfectly symmetric compared to the mean value. This also indicates that the distribution of the survival probability can be well approximated by a normal distribution, which is essentially based upon the fact that, in our case, the input random vector has very small standard deviations ($\lesssim 5\%$). Accordingly, the confidence intervals are estimated to be $[1.05\times10^{-2}, 1.31\times10^{-2}]$ and $[8.56\times10^{-3}, 9.07\times10^{-3}]$ for ^{266}Rf and ^{258}Hs, respectively. It would be also interesting to look into the impact of neglecting all the covariances between S_n^A, B_f^A and B_f^{A-1} on the final results. In doing so, the confidence intervals become $[4.01\times10^{-3}, 6.84\times10^{-3}]$ and $[5.76\times10^{-3}, 1.03\times10^{-2}]$ for ^{266}Rf and ^{258}Hs, respectively. Compared to the previous case where all correlations are taken into account, they are decreased by a factor of about 1.1 and

increased by a factor of about 8.9, respectively. The latter appears to be rather significant. Thus, according to this preliminary study, it is unambiguously demonstrated that the correlation between physical quantities might be able to change the 95% confidence interval or the uncertainty associated with the survival probability.

IX.5 Summary and conclusions

In this chapter, we have carefully examined the nuclear mass formula on the basis of the linear regression theory.

We first revisited an extended version of the liquid-drop mass formula and attempted to establish a general framework based upon the linear regression theory for performing nuclear mass fits. By analyzing different crucial statistics, such as the significance test for model parameters and analysis of residuals, the validity of this kind of approach has been verified. Then, with the help of a modified mass formula, we have closely examined the limitations of the liquid-drop model on the theoretical predictions. We have also studied for the first time the correlations between the estimated neutron-separation energies and fission barriers. It has been confirmed that some strong correlations exist between these physical quantities which are crucial for studying the synthesis of SHE. Finally, their influence on the survival probability was carefully inspected by means of a toy model for single-neutron evaporation. It is rigorously shown that, at a 95% confidence level, the resulting uncertainty can be quite small. However, after removing all the covariances between neutron-separation energies and fission barriers, the resulting uncertainty significantly rises. It should be kept in mind that uncertainties related to the nuisance parameters and models are not taken into account here.

Moreover, it should be emphasized that, for all the calculations presented in this chapter, the uncertainty of shell corrections has not been considered, whereas it could be remarkably large, especially in the super-heavy mass region. To put it differently, the uncertainty related to the outcome, namely the survival probability might become significantly larger than those presented here. Further consideration will be hence needed within a more general framework including the correlation between theoretical shell-correction energies.

X Conclusions and perspectives

To summarize the present work, we have made our first attempts to apply uncertainty analysis methods to the study of fusion-evaporation reactions leading to the formation of SHE. As mentioned at the beginning of the thesis, the nuclear reaction theory for heavy systems, which is essential for the synthesis of SHE, has not been well established yet. Although we have reached a general agreement on the reaction mechanism, large discrepancies between quantitative predictions based upon different fusion models still persist because of the so-called fusion hindrance phenomenon. The central question that we have posed here is that, how to assess the fusion models so as to establish an accurate reaction theory for guiding future experiments? To find answers, the existing state-of-the-art theories need to be reviewed and considered under the framework of uncertainty analysis.

It should be recalled that, from a conventional viewpoint, the fusion process can be divided into two consecutive stages, namely the capture phase corresponding to the passage over the Coulomb barrier and the formation phase corresponding to overcoming the inner barrier (only existing in heavy systems). Regarding the former, experimental data are generally available in the literature, whereas this is not the case for the latter due to the quasi-fission process which is extremely difficult to measure and survey. Some canonical heavy-ion reaction models commonly used to estimate capture cross-sections were briefly recalled in the first part of Chapter 4. Illustrative examples were shown and theoretical results were carefully confronted with the available data mainly at sub- or near-barrier energy regions. This qualitative study allowed us to roughly evaluate the uncertainty associated with capture models, which could reach one order of magnitude in the case of heavy colliding systems. In view of the simplicity of the capture models, the predictive power is rather limited and hence it would be necessary to further quantify the associated uncertainty that is essential for the study of cold-fusion reactions. For this purpose, an overview of all the capture models available on the market would be helpful and a systematic comparison with the measured data needs to be conducted.

As a second step, to better understand the formation phase, which is a key to the production of SHE, we presented a recent work on the mechanism of the fusion hindrance within a simple framework based upon a coupled two-dimensional Langevin equation. It has been

established that the coupling between the neck and radial degrees of freedom has a crucial role to play in describing the formation step during the fusion process. It should be noted that the present model is still somewhat crude and the follow-up work is currently underway with the purpose of clarifying the influence of other collective variables, such as the asymmetry parameter, on the fusion probability. Other crucial questions, like how to exactly estimate the inner barrier height and what is the strength of dissipation, would also need to be further investigated. Besides theoretical ambiguities, since experimental data on the fusion probability are not available or reliable, the main challenge is to find ways to assess the theoretical description of this step.

Compared to the fusion phase, the de-excitation of SHE is relatively better understood. However, some of the physical ingredients are not well known and more free parameters get involved. In Chapter 5, we gave a complete description of the main physical ingredients for modeling the de-excitation phase. In this context, we presented in detail a newly-developed cascade code called KEWPIE2 [99, 100], which comprises various reaction models that are commonly employed to estimate the survival probability of excited nuclei. On the basis of KEWPIE2, some typical calculations were illustrated and compared with the available data (without fusion hindrance). Since input uncertainties remain quite large, it would be necessary to look more closely into their influence on the outcomes. To this extent, although the de-excitation phase is well described, some of the key ingredients or parameters, such as the fission barrier, cannot be precisely determined.

We then came up with a promising strategy to assess the fusion models with the help of uncertainty quantification of the de-excitation phase as well as the empirical formation probability. Some advanced uncertainty analysis methods, which are mainly based upon the Monte-Carlo sampling, were presented in detail and successfully applied to a systematic investigation of the survival probability as well as the empirical fusion probabilities for cold-fusion reactions (single-neutron evaporation). By inspecting the estimated uncertainties due to both parameters and models, it was unambiguously shown that the fission barrier has a significant influence on the output. More concretely, the impact was shown to be of the same order of magnitude as the one coming from the fusion phase. Accordingly, the most important issue we are facing is that, how to simultaneously take into account both the fission barrier and formation process? Is it possible to do it separately? If not, how can we improve the accuracy of the fusion models? All these questions should be addressed in order to assess the fusion models.

How to rigorously determine the uncertainty associated with the fission barrier? Based upon the conclusions drawn from uncertainty analysis, we proposed to consider Bayesian inference which aims at studying an inverse problem, that is to say, how to extract useful information on fission barrier from experimental data? Some interesting results were shown and discussed under the assumption that competition only takes place between single-neutron evaporation and nuclear fission. Since experimental data are not available at the present time, we restricted ourselves to the invented pseudo-data and tried to apply Bayesian inference to

reaction systems without fusion hindrance. It has been clearly demonstrated that the extracted uncertainty in the fission barrier appears be quite sensitive to the number and precision of data points. The influence of nuisance parameters on the extracted uncertainty of fission barrier was also investigated. Due to large uncertainties remaining in nuisance parameters, it would not be possible to decrease the uncertainty related to fission barrier. Furthermore, the correlation between pseudo-data was also shown to have a significant impact on the final results. Knowing that this type of calculation is usually quite time-consuming, further efforts will be required with the purpose of constructing a more general framework based upon some advanced techniques for completely sampling the posterior probability distribution of the fission barrier, such as Markov-chain Monte-Carlo method, in order to improve the computational efficiency.

To incorporate the fusion phase (inner barrier) and the fission barrier into the same framework, it is already known that they can be both described using the liquid-drop model. To this extent, they should be correlated with each other. To understand this issue, as a very first step, it would be instructive to revisit the liquid-drop mass formula with the help of regression theory in order to determine uncertainties in the model parameters as well as the correlation between calculated neutron-separation energies and fission barriers. According to the obtained results, it has been clearly revealed that the correlation existing between these quantities could be considerably strong in some cases. Moreover, the influence of their covariances on the survival probability was concretely investigated by means of uncertainty analysis with a simplified single-neutron evaporation model. It has been demonstrated that the 95% confidence interval for the outcome can be quite narrow, that is to say, the uncertainty related to the calculated survival probability could be quite small, whereas the impact of correlations would be important. It should be also noted that uncertainties associated with shell corrections have not been taken into account, but they could be remarkably large, especially in the super-heavy mass region. Finally, it should be mentioned that this approach could also be extended to the study related to the formation process, as the estimation of the inner barrier is essentially based upon the liquid-drop model and thus might be similar to the calculation of the fission-barrier height. Further consideration will be needed to account for the correlation between shell corrections and fusion barriers. Hence, uncertainty analysis would have a crucial role to play and needs to be further developed and adapted to the reaction theory devoted to studying the synthesis of SHE. In this sense, the present thesis has opened new paths and there is still much work to do in the future.

As a general prospect, we would also need to have more experimental data with the aim of better constraining the fusion models. In this sense, what are the pertinent observables that can be employed? Is it possible to design such experiments with the next-generation facility? The present thesis will not go till the end, but the strategy proposed here can be hopefully further exploited for comprehending the reaction mechanism with new available experimental data.

A Gauss-Legendre quadrature

The numerical integration is quite time-consuming especially in the fusion and cascade calculations. One should somehow avoid the traditional discretization methods, such as the rectangle and trapezoidal rules, because they would imply a large number of iterations. The Gauss-Legendre quadrature rule has been employed to evaluate the integral involved in the WKB approach and Bayesian inference. Recalling that, to calculate $\int_a^b f(x)\mathrm{d}x$, one has the following quadrature formula:

$$\int_a^b f(x)\mathrm{d}x \simeq \frac{b-a}{2}\sum_{i=1}^{n} w_i f\left(\frac{b-a}{2}x_i + \frac{b+a}{2}\right), \tag{A.1}$$

where x_i refers to the i^{th} root of the Legendre polynomial $P_n(x)$ and the weight w_i is given by $2/\{\left(1-x_i^2\right)\left[P_n^{'}(x_i)\right]^2\}$. In the KEWPIE2 code, the default value of n has been chosen to be 32 for the WKB approximation, which can be modified according to the precision requirement. The exact values of weights and roots can be found in Ref. [242].

B Derivation of the state-density formula

A modified state-density formula was proposed in Ref. [170], which has been included in the KEWPIE2 code. The advantage of introducing this formula is that the state density does not diverge anymore when the excitation energy tends to zero. Here, we try to reproduce the derivation of this formula and stress that special attention should be paid to the numerical implementation of this formula. For the sake of consistency, I shall use the same notations as those in Ref. [170].

B.1 Modified Laplace transform method

Starting with the standard form of the grand canonical partition function for a non-interacting Fermi gas (one type of particle):

$$Z(\alpha,\beta)=\prod_i\left[1+\exp(-\beta\varepsilon_i+\alpha)\right]=\prod_i\left\{1+\exp\left[-\beta(\varepsilon_i-\mu)\right]\right\}, \tag{B.1}$$

where $\mu=\alpha/\beta$ is the chemical potential (Fermi level) and $\beta=1/T$ the thermodynamic temperature. The Lagrange multipliers α and β are given by:

$$A=\frac{\partial}{\partial\alpha}\ln Z(\alpha,\beta)\quad\text{and}\quad E=-\frac{\partial}{\partial\beta}\ln Z(\alpha,\beta), \tag{B.2}$$

where A and E correspond to the average number of particles and internal energy, respectively. To evaluate the grand canonical partition function, Ref. [180] gives

$$\ln Z(\alpha,\beta)=\int_0^{\alpha/\beta}2g(\varepsilon)(\alpha-\beta\varepsilon)\mathrm{d}\varepsilon+\frac{\pi^2}{3\beta}g(\alpha/\beta), \tag{B.3}$$

where $g(\varepsilon)$ refers to the single-particle level density and the spin degeneracy has been considered. On the other hand, we have two constraints on the ground state:

$$A_0=\int_0^{\varepsilon_F}2g(\varepsilon)\mathrm{d}\varepsilon\quad\text{and}\quad E_g(A_0)=\int_0^{\varepsilon_F}2g(\varepsilon)\varepsilon\mathrm{d}\varepsilon, \tag{B.4}$$

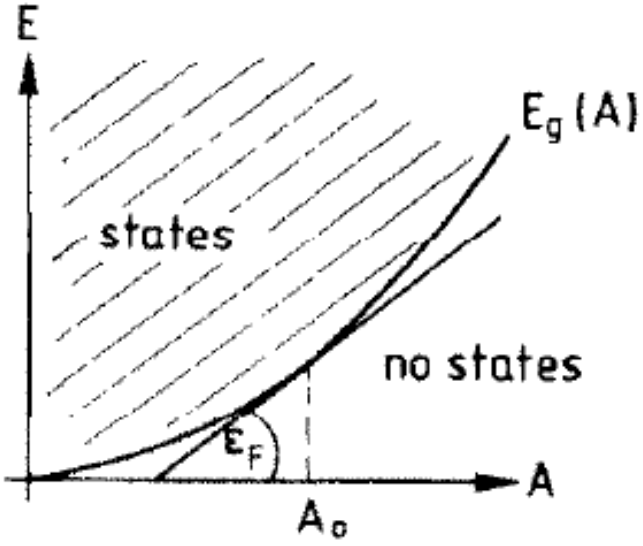

Figure B.1 – Illustration of the modified Laplace transform method. Figure is taken from Ref. [170].

where A_0 is a given mean particle number. By means of the above relations, the partition function can be analytically calculated as follows:

$$\begin{aligned}\ln Z(\alpha,\beta) &= \int_0^{\varepsilon_F} 2g(\varepsilon)(\alpha-\beta\varepsilon)\mathrm{d}\varepsilon + \int_{\varepsilon_F}^{\alpha/\beta} 2g(\varepsilon)(\alpha-\beta\varepsilon)\mathrm{d}\varepsilon + \frac{\pi^2}{3\beta}g(\alpha/\beta) \\ &= \alpha A_0 - \beta E_g(A_0) + \beta g_0(\mu-\varepsilon_F)^2 + \frac{\pi^2 g_0}{3\beta},\end{aligned} \tag{B.5}$$

where g_0 denotes $g(\varepsilon_F)$. The single-particle state density has been assumed constant above the Fermi level (Equidistant-level approximation) and equals to its value at the Fermi energy ε_F.

In Ref. [170], a modified Laplace transformation method was proposed. We shall then illustrate this idea and derive an analytical expression for the state density formula. We consider first the general form of the partition function:

$$Z(\alpha,\beta) = \int_0^\infty \mathrm{d}A \int_0^\infty \mathrm{d}E\, \omega(E,A)\exp(-\beta E + \alpha A), \tag{B.6}$$

from which the state density $\omega(E,A)$ can be obtained by means of an inverse Laplace transformation:

$$\omega(E,A) = \frac{1}{(2\pi i)^2}\int_{\delta_1-i\infty}^{\delta_1+i\infty}\mathrm{d}\alpha \int_{\delta_2-i\infty}^{\delta_2+i\infty}\mathrm{d}\beta\, Z(\alpha,\beta)\exp(\beta E - \alpha A). \tag{B.7}$$

Then, we define the excitation energy that is related to the internal energy by $E^* = E - E_g(A)$. As discussed in Ref. [170], the ground-state energy $E_g(A)$ should be regarded as the lower boundary in Eq. (B.6) (cf. Fig. B.1). Thus, Eq. (B.6) becomes:

$$\begin{aligned} Z(\alpha,\beta) &= \int_0^\infty \mathrm{d}A \int_{E_g(A_0)}^\infty \mathrm{d}E\omega(E,A)\exp(-\beta E + \alpha A) \\ &\simeq \exp\left(-\beta E_g(A_0) + \beta\varepsilon_F A_0\right) \int_0^\infty \mathrm{d}A \int_0^\infty \mathrm{d}E^*\omega(E,A)\exp(-\beta E^* + (\alpha - \beta\varepsilon_F)A), \end{aligned} \tag{B.8}$$

where, by expanding $E_g(A)$ around A_0, we have employed the following relationship:

$$E_g(A) \simeq E_g(A_0) + \frac{\mathrm{d}E_g(A_0)}{\mathrm{d}A}(A - A_0) = E_g(A_0) + \varepsilon_F(A - A_0), \tag{B.9}$$

Put differently, the contribution of the ground state should be removed from the state density,

$$\Omega(E^*, A) = \omega(E, A) - \delta\left(E - E_g\right)\delta\left(A - A_0\right). \tag{B.10}$$

Therefore, one can naturally define a modified partition function by

$$\tilde{Z}(\alpha,\beta) = \int_0^\infty \mathrm{d}A \int_0^\infty \mathrm{d}E^*\Omega(E^*, A)\exp(-\beta E^* + \alpha A), \tag{B.11}$$

which is related to the original one (cf. Eq. (B.8)) by:

$$\tilde{Z}(\alpha,\beta) = Z(\alpha + \beta\varepsilon_F, \beta)\exp(\beta E_g(A_0) - \beta\varepsilon_F A_0) - \exp(\alpha A_0). \tag{B.12}$$

According to Eq. (B.5), an explicit expression for the modified partition function can thus be obtained:

$$\begin{aligned} \tilde{Z}(\alpha,\beta) &= \exp(\alpha A_0 + g_0\beta\mu^2 + \pi^2 g_0/3\beta) - \exp(\alpha A_0) \\ &= \exp(\alpha A_0)\left[\exp\left(g_0\beta\mu^2 + \frac{\pi^2 g_0}{3\beta}\right) - 1\right] \\ &= \exp(\alpha A_0)\left\{\exp\left[\frac{1}{\beta}(g_0\alpha^2 + a)\right] - 1\right\}, \end{aligned} \tag{B.13}$$

where $a = \pi^2 g_0/3$ is the so-called level-density parameter. Furthermore, by virtue of the new partition function (cf. Eq. (B.11)), one can readily obtain the corresponding state density via

$$\Omega(E^*, A) = \frac{1}{(2\pi i)^2}\int_{\delta_1 - i\infty}^{\delta_1 + i\infty} \mathrm{d}\alpha \int_{\delta_2 - i\infty}^{\delta_2 + i\infty} \mathrm{d}\beta\tilde{Z}(\alpha,\beta)\exp(\beta E^* - \alpha A). \tag{B.14}$$

By applying the saddle-point approximation to the above integral, we finally obtain an analytical expression for the new state density:

$$\Omega(E^*, A) \simeq \frac{1}{2\pi\sqrt{D_0}}\exp\left(\ln\tilde{Z}(\alpha_0,\beta_0) + \beta_0 E^* - \alpha_0 A\right), \tag{B.15}$$

where the saddle-point position (α_0, β_0) is given by:

$$A = \frac{\partial}{\partial \alpha} \ln \tilde{Z}(\alpha_0, \beta_0) \quad \text{and} \quad E^* = -\frac{\partial}{\partial \beta} \ln \tilde{Z}(\alpha_0, \beta_0) \tag{B.16}$$

and the determinant D_0 is defined as follows:

$$D_0 = \det \begin{vmatrix} \dfrac{\partial^2 \ln \tilde{Z}_0}{\partial \alpha^2} & \dfrac{\partial^2 \ln \tilde{Z}_0}{\partial \alpha \partial \beta} \\ \dfrac{\partial^2 \ln \tilde{Z}_0}{\partial \alpha \partial \beta} & \dfrac{\partial^2 \ln \tilde{Z}_0}{\partial \beta^2} \end{vmatrix} \tag{B.17}$$

where $\tilde{Z}_0$ denotes $\tilde{Z}(\alpha_0, \beta_0)$.

In order to determine the Lagrange multipliers at the saddle point, α_0 and β_0, one needs to employ Eq. (B.16). Moreover, due to the fact that $E_g(A)$ has been approximated in the vicinity of A_0, which implies that A should be of the order of A_0 and thus one can set $A = A_0$. Hence, the following calculations can be readily carried out with Eq. (B.13):

$$A_0 = \frac{1}{\tilde{Z}_0} \frac{\partial \tilde{Z}_0}{\partial \alpha} = \frac{\left(A_0 + \dfrac{2 g_0 \alpha_0}{\beta_0}\right) \exp\left[\alpha_0 A_0 + \dfrac{1}{\beta}\left(g_0 \alpha_0^2 + a\right)\right] - A_0 \exp\left(\alpha_0 A_0\right)}{\tilde{Z}_0}. \tag{B.18}$$

Obviously, one has $\alpha_0 = 0$.

In the same manner, β_0 can be determined as follows

$$E^* = -\frac{1}{\tilde{Z}_0} \frac{\partial \tilde{Z}_0}{\partial \beta} = -\frac{1}{\tilde{Z}_0} \left[-\frac{a}{\beta_0^2} \exp\left(\frac{a}{\beta_0}\right)\right] = \frac{a}{\beta_0^2} \frac{\tilde{Z}_0 + 1}{\tilde{Z}_0} = \frac{a}{\beta_0^2} \frac{1}{1 - \exp(-a/\beta_0)}, \tag{B.19}$$

where we have used the relation $\tilde{Z}_0 = \exp(a/\beta_0) - 1$. Therefore, we obtain an implicit relation between β_0 and E^*:

$$\left(\frac{a}{\beta_0}\right)^2 = \left(a E^*\right)\left[1 - \exp\left(-\frac{a}{\beta_0}\right)\right]. \tag{B.20}$$

Finally, from a straightforward calculation, the determinant (B.17) is given by:

$$D_0 = \det \begin{vmatrix} \dfrac{6 \beta_0 E^*}{\pi^2} & 0 \\ 0 & 0\left(\dfrac{2}{\beta_0} + \dfrac{a}{\beta_0^2} - E^*\right) \end{vmatrix} = \frac{6 \beta_0 E^*}{\pi^2} \left(\frac{2}{\beta_0} + \frac{a}{\beta_0^2} - E^*\right) E^*, \tag{B.21}$$

and the state density of a Fermi gas with A_0 particles reads:

$$\Omega(E^*, A_0) = \Omega_{A_0}(E^*) = \frac{\exp(\beta_0 E^* + a/\beta_0)}{\sqrt{48} E^*} \frac{1 - \exp(-a/\beta_0)}{\left[1 - \frac{1}{2} E^* \beta_0 \exp(-a/\beta_0)\right]^{1/2}}. \tag{B.22}$$

Together with Eq. (B.20), we obtain the same state-density formula as derived in Ref. [170].

The above calculations can be readily generalized to take into account additional quantum numbers. For example, we consider the consequences of the fact that the Fermi gas is composed of two kinds of particles, such as neutrons and protons. The partition function must be modified as follows [180]:

$$\begin{aligned}\ln Z(\alpha_n,\alpha_p,\beta) = &\int_0^{\alpha_n/\beta} 2g_n(\varepsilon)(\alpha_n-\beta\varepsilon)\mathrm{d}\varepsilon + \int_0^{\alpha_p/\beta} 2g_p(\varepsilon)(\alpha_p-\beta\varepsilon)\mathrm{d}\varepsilon \\ &+ \frac{\pi^2}{3\beta}g_n(\alpha_n/\beta) + \frac{\pi^2}{3\beta}g_p(\alpha_p/\beta),\end{aligned} \tag{B.23}$$

where α_n and α_p are the Lagrange multipliers corresponding to two kinds of particles (neutrons and protons). Proceeding in a similar manner, i.e. subtracting the ground-state contribution in the state density before using the saddle-point approximation, and beware that the determinant is now given by

$$D_0 = \det\begin{vmatrix} \dfrac{\partial^2\tilde{Z}_0}{\partial\alpha_n^2} & \dfrac{\partial^2\tilde{Z}_0}{\partial\alpha_n\partial\alpha_p} & \dfrac{\partial^2\tilde{Z}_0}{\partial\alpha_n\partial\beta} \\ \dfrac{\partial^2\tilde{Z}_0}{\partial\alpha_p\partial\alpha_n} & \dfrac{\partial^2\tilde{Z}_0}{\partial\alpha_p^2} & \dfrac{\partial^2\tilde{Z}_0}{\partial\alpha_p\partial\beta} \\ \dfrac{\partial^2\tilde{Z}_0}{\partial\beta\partial\alpha_n} & \dfrac{\partial^2\tilde{Z}_0}{\partial\beta\partial\alpha_p} & \dfrac{\partial^2\tilde{Z}_0}{\partial\beta^2} \end{vmatrix}, \tag{B.24}$$

we finally obtain the state-density formula for two kinds of particles [170]:

$$\Omega(E^*,N_0,Z_0) = \Omega_{N_0,Z_0}(E^*) = \frac{\sqrt{\pi}}{12}\frac{\exp(\beta_0 E^* + a/\beta_0)}{\sqrt{\beta_0 E^{*3}}}\left(\frac{g_0^2}{4g_n g_p}\right)^{1/2}\frac{1-\exp(-a/\beta_0)}{\left[1-\frac{1}{2}E^*\beta_0\exp(-a/\beta_0)\right]^{1/2}}, \tag{B.25}$$

In fact, the other quantum numbers, such as the angular momentum and parity, can also be included in the state density formula. For more details, the reader is referred to Ref. [171].

B.2 Angular-momentum dependence

According to Ref. [243, 244], the angular-momentum dependence can be derived as follows:

$$\rho_{A_0,J}(E^*) = \rho_{A_0,M=J}(E^*) - \rho_{A_0,M=J+1}(E^*) = \frac{\rho_{A_0}(E^*)}{\sqrt{2\pi\langle M^2\rangle}}\frac{2J+1}{2\langle M^2\rangle}\exp\left[-\frac{(J+1/2)^2}{2\langle M^2\rangle}\right], \tag{B.26}$$

where we employed the state density with the given projection of J on a fixed axis, which is given by

$$\rho_{A_0,M}(E^*) = \rho_{A_0}(E^*)P(M) = \frac{\rho_{A_0}(E^*)}{\sqrt{2\pi\langle M^2\rangle}}\exp\left[-\frac{M^2}{2\langle M^2\rangle}\right], \tag{B.27}$$

where $P(M)$ denotes the probability of having a projection M, which is described by a Gaussian. This is due to the fact that the total angular momentum is obtained by a statistical coupling to many one-particle momenta (central limit theorem). Naturally, we could set $\langle M \rangle = 0$, which implies that the variance of the distribution (spin cut-off parameter) σ_M^2 equals $\langle M^2 \rangle$.

As previously mentioned, one should be careful with two concepts, observed level density and state density (or level density in the non-degenerate case). The former refers to the number of energy levels per MeV regardless of their nuclear spin degeneracy, whereas the latter takes into account the $2J+1$ degeneracy for the given total angular momentum. Another crucial quantity called total level density $\rho_{A_0}^{\mathrm{tot}}(E^*)$, which is usually fitted to experimental data, can be readily obtained by dividing the state density by the mean number of states per energy level. In practice, one can perform an integration over all possible values of the angular momentum:

$$\begin{aligned}\rho_{A_0}^{\mathrm{tot}}(E^*) &= \int_0^{+\infty} \rho_{A_0,J}\mathrm{d}J = \int_0^{+\infty} \frac{\rho_{A_0}(E^*)}{\sqrt{2\pi\langle M^2\rangle}} \frac{2J+1}{2\langle M^2\rangle} \exp\left[-\frac{(J+1/2)^2}{2\langle M^2\rangle}\right] \mathrm{d}J \\ &\backsimeq \frac{\rho_{A_0}(E^*)}{\sqrt{2\pi\sigma_M^2}},\end{aligned} \tag{B.28}$$

where the spin cut-off parameter σ_M^2 reads [180]

$$\sigma_M^2 = \frac{\vartheta_{\mathrm{rig}}}{\hbar^2\beta_0} \quad \text{with } \vartheta_{\mathrm{rig}} = \frac{2}{5} A_0 m_N R_N^2, \tag{B.29}$$

where ϑ_{rig} denotes the rigid-body inertia moment of a sphere. m_N and R_N are the nucleon mass and the radius of the spherical nucleus, respectively. Hence, the total level density is related to the state density by Eq.(B.28).

Experimentally, the observed level density can be measured by means of different methods [245], such as neutron (or charged-particle) resonances and counting of low-lying excited states. For example, from the observed level spacing D_{obs} in neutron resonances, one can derive $\rho^{\mathrm{tot}}(E^*)$ as follows:

$$\frac{1}{\rho^{\mathrm{tot}}(E^*)} = \frac{D_{\mathrm{obs}}(E^*)}{4\sigma_M^2} \sum_{J^\pi} (2J^\pi + 1) \exp\left[-\frac{(J^\pi + 1/2)^2}{2\sigma_M^2}\right]. \tag{B.30}$$

Here J^π denotes the sum extends over all possible combinations of nuclear spin and parity (J and π) of nuclear levels. As pointed out in Ref. [176], the above relation is a direct consequence of Eq. (B.28) and beware that the total level density $\rho^{\mathrm{tot}}(E^*)$ is related to the state density by

$$\rho(E^*) = \rho^{\mathrm{tot}}(E^*)\sqrt{2\pi\sigma_M^2}. \tag{B.31}$$

C Analytical neutron-evaporation model

C.1 A toy model for single-neutron evaporation

When a nucleus ${}^{A}_{Z}X$ is produced, it is usually energetically excited and hence needs to lose a certain mount of energy for surviving. To simplify the problem, we only consider two different decay channels, namely fission and neutron evaporation. Here, we restrict ourselves to the $1n$-channel. The branching ratio for this decay mode is thus given by

$$\frac{\Gamma_n^A}{\Gamma_f^A+\Gamma_n^A}=\frac{\Gamma_n^A/\Gamma_f^A}{1+\Gamma_n^A/\Gamma_f^A}, \tag{C.1}$$

where Γ_n^A is the neutron-evaporation width and Γ_f^A fission-decay width. In the case of the formation of super-heavy nuclei, the dominant decay mode is nuclear fission because their fission-barrier heights are much smaller compared to the thresholds for neutron emissions. According to the transition-state theory, the ratio Γ_n^A/Γ_f^A reads

$$\frac{\Gamma_n^A}{\Gamma_f^A}=\frac{N_n^A}{N_f^A}, \tag{C.2}$$

where N_f^A denotes the number of levels (or decay channels) accessible in the energy slot between the fission-saddle point and the total energy and N_n^A the number of levels accessible between the top of neutron-emission barrier and the total energy. They can be precisely evaluated by using the method introduced in Ref. [246]. Once the ratio of decay widths have been obtained, the survival probability for the excited nucleus to evaporate only one neutron is simply given by

$$P_{\rm sur}^{1n}=\frac{\Gamma_n^A}{\Gamma_f^A+\Gamma_n^A}R_{1n}, \tag{C.3}$$

where R_{1n} is the probability of realization of $1n$-channel. As argued in Ref. [48], the reason we introduce such a realization probability is that, after evaporating one neutron, the excitation energy of the residual nucleus should be less than the threshold $E_{\rm th}^{A-1}$ for second chance fission

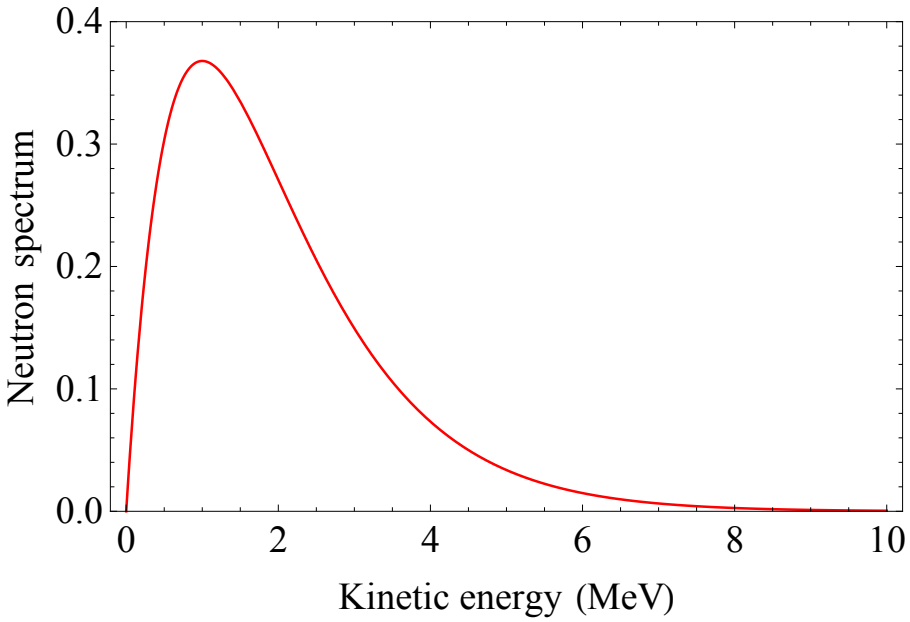

Figure C.1 – An example of the neutron spectrum. Here the nuclear temperature has been taken to be 1 MeV.

or neutron emission. Thus, one needs to compare two potential barriers in the daughter nucleus, namely the fission-barrier height B_f^{A-1} and the neutron separation energy S_n^{A-1}, and then select the lower one for the threshold, that is to say, $E_{\text{th}}^{A-1} = \min(B_f^{A-1}, S_n^{A-1})$. To calculate the realization probability, for the sake of simplicity, one can assume that the kinetic energy of the first emitted neutron ϵ_1 obeys a Maxwell-like distribution $D_1(\epsilon_1, T_A)$, which is proportional to the following expression [240]: $\epsilon_1 \exp(-\epsilon_1/T_A)$ (cf. Fig. C.1), where T_A denotes the temperature of the excited nucleus and the proportionality constant can be determined on the basis of the normalization condition, namely

$$\int_0^{\epsilon_1^{\max}} D_1(\epsilon_1, T_A)\mathrm{d}\epsilon_1 = 1, \tag{C.4}$$

where $\epsilon_1^{\max} = E_A^* - S_n^A$ corresponds to the maximum kinetic energy of the neutron and T_A the temperature of the excited nucleus ($T \lesssim 0.5$ MeV). For $\epsilon_1^{\max} \gg T_A$, the proportionality constant N can be calculated as follows:

$$N = \frac{1}{\int_0^{\epsilon_1^{\max}} \epsilon_1 \exp(-\epsilon_1/T_A)\mathrm{d}\epsilon_1} \simeq \frac{1}{\int_0^{+\infty} \epsilon_1 \exp(-\epsilon_1/T_A)\mathrm{d}\epsilon_1} = \frac{1}{T_A^2}. \tag{C.5}$$

Thus, the energy spectrum of the evaporated neutron reads

$$D_1(\epsilon_1, T_A) \simeq \frac{1}{T_A^2}\epsilon_1 \exp(-\epsilon_1/T_A). \tag{C.6}$$

Finally, the expression for the realization probability is given as follows:

$$\begin{aligned} R_{1n} &= \frac{1}{T_A^2}\int_{\epsilon_1^{\max}-E_{\rm th}^{A-1}}^{\epsilon_1^{\max}} \epsilon_1 \exp(-\epsilon_1/T_A)\mathrm{d}\epsilon_1, \\ &\simeq \frac{1}{T_A^2}\int_{\epsilon_1^{\max}-E_{\rm th}^{A-1}}^{+\infty} \epsilon_1 \exp(-\epsilon_1/T_A)\mathrm{d}\epsilon_1, \\ &= \left(1+\frac{\epsilon_1^{\max}-E_{\rm th}^{A-1}}{T_A}\right)\exp\left(-\frac{\epsilon_1^{\max}-E_{\rm th}^{A-1}}{T_A}\right), \end{aligned} \tag{C.7}$$

under the condition that $\epsilon_1^{\max}-E_{\rm th}^{A-1}\geq 0$. For $\epsilon_1^{\max}-E_{\rm th}^{A-1}<0$, we simply have $R_{1n}=1$. It should be kept in mind that the threshold energy $E_{\rm th}^{A-1}=\min(B_f^{A-1},S_n^{A-1})$.

C.2 Approximate expression for the ratio of decay widths

Regarding the ratio Γ_n/Γ_f, it can be estimated using the classical formalism proposed by Vandenbosch and Huizenga [241, 246], that is to say,

$$\frac{\Gamma_n}{\Gamma_f} = \frac{4A^{2/3}a_f(E^*-S_n)}{k_0 a_n\left[2\sqrt{a_f(E^*-B_f)}-1\right]}\exp\left[2\sqrt{a_n(E^*-S_n)}-2\sqrt{a_f(E^*-B_f)}\right], \tag{C.8}$$

where k_0 and $a_n=a_f$ are estimated to be 9.8 MeV and $A/10$ MeV^{-1}. For the sake of simplicity, we have assumed that the constant level-density parameter appropriate to the saddle point, a_f, is equal to that appropriate to the ground state, a_n. Here, it should be noted that Eq. (C.8) has been derived within the framework of the simple Fermi-gas model, where the shell correction is not taken into consideration. In Refs. [136, 247, 248], some more accurate expressions for the ratio of the decay widths were presented in both cases (with and without shell corrections).

Bibliography

[1] A. H. Becquerel, CR Acad. Sci. Paris **122**, 501 (1896).

[2] N. Bohr and J. A. Wheeler, Phys. Rev. **56**, 426 (1939).

[3] W. Loveland, Phys. Rev. C **76**, 014612 (2007).

[4] R. S. Naik, W. Loveland, P. H. Sprunger, A. M. Vinodkumar, D. Peterson, C. L. Jiang, S. Zhu, X. Tang, E. F. Moore, and P. Chowdhury, Phys. Rev. C **76**, 054604 (2007).

[5] BIPM, IEC, IFCC, ILAC, ISO, and IUPAC, "Evaluation of Measurement Data-Supplement 1 to the 'Guide to the Expression of Uncertainty in Measurement'-Propagation of distributions using a Monte Carlo method", Joint Committee for Guides in Metrology, JCGM **101** (2008).

[6] Editors, Phys. Rev. A **83**, 040001 (2011).

[7] G. Gamow, Proceedings of the Royal Society of London A: Mathematical, Physical and Engineering Sciences **126**, 632 (1930).

[8] C. Weizsäcker, Z. Phys. **96**, 431 (1935).

[9] O. Hahn and F. Strassmann, Naturwissenschaften **27**, 11 (1939).

[10] O. Hahn and F. Strassmann, Naturwissenschaften **27**, 89 (1939).

[11] L. Meitner and O. R. Frisch, Nature **143**, 239 (1939).

[12] M. G. Mayer, Phys. Rev. **78**, 16 (1950).

[13] M. G. Mayer, Phys. Rev. **78**, 22 (1950).

[14] O. Haxel, J. H. D. Jensen, and H. E. Suess, Phys. Rev. **75**, 1766 (1949).

[15] P. Möller, J. Nix, W. Myers, and W. Swiatecki, At. Data. Nucl. Data Tables **59**, 185 (1995).

[16] K. Rutz, M. Bender, T. Bürvenich, T. Schilling, P.-G. Reinhard, J. A. Maruhn, and W. Greiner, Phys. Rev. C **56**, 238 (1997).

[17] M. Bender, W. Nazarewicz, and P.-G. Reinhard, Phys. Lett. B **515**, 42 (2001).

[18] V. Zagrebaev and W. Greiner, Nucl. Phys. A , (2015).

[19] S. Gales, Journal of Physics: Conference Series **267**, 012009 (2011).

[20] R. Ferrer, B. Bastin, D. Boilley, P. Creemers, P. Delahaye, E. Liénard, X. Fléchard, S. Franchoo, L. Ghys, M. Huyse, Y. Kudryavtsev, N. Lecesne, H. Lü, F. Lutton, E. Mogilevskiy, D. Pauwels, J. Piot, D. Radulov, L. Rens, H. Savajols, J. Thomas, E. Traykov, C. V. Beveren, P. V. den Bergh, and P. V. Duppen, Nucl. Instrum. Methods Phys. Res., Sect. B **317, Part B**, 570 (2013).

[21] J. Péter, C. Ngô, F. Plasil, B. Tamain, M. Berlanger, and F. Hanappe, Nucl. Phys. A **279**, 110 (1977).

[22] C. Lebrun, F. Hanappe, J. LeColley, F. Lefebvres, C. Ngô, J. Péter, and B. Tamain, Nucl. Phys. A **321**, 207 (1979).

[23] B. Borderie, M. Berlanger, D. Gardès, F. Hanappe, L. Nowicki, J. Péter, B. Tamain, S. Agarwal, J. Girard, C. Grégoire, J. Matuszek, and C. Ngô, Zeitschrift für Physik A Atoms and Nuclei **299**, 263 (1981).

[24] W. J. Swiatecki, Phys. Scr. **24**, 113 (1981).

[25] B. B. Back, H. G. Clerc, R. R. Betts, B. G. Glagola, and B. D. Wilkins, Phys. Rev. Lett. **46**, 1068 (1981).

[26] J. Tōke, R. Bock, G. Dai, A. Gobbi, S. Gralla, K. Hildenbrand, J. Kuzminski, W. Müller, A. Olmi, H. Stelzer, B. Back, and S. Bjørnholm, Nucl. Phys. A **440**, 327 (1985).

[27] W. Q. Shen, J. Albinski, A. Gobbi, S. Gralla, K. D. Hildenbrand, N. Herrmann, J. Kuzminski, W. F. J. Müller, H. Stelzer, J. Tke, B. B. Back, S. Bjrnholm, and S. P. Srensen, Phys. Rev. C **36**, 115 (1987).

[28] K. H. Schmidt and W. Morawek, Rep. Prog. Phys. **54**, 949 (1991).

[29] A. Quint, W. Reisdorf, K.-H. Schmidt, P. Armbruster, F. Heßberger, S. Hofmann, J. Keller, G. Münzenberg, H. Stelzer, H.-G. Clerc, W. Morawek, and C.-C. Sahm, Z. Phys. A **346**, 119 (1993).

[30] http://nucalf.physics.fsu.edu/ riley/gamma/gamma2-5.html .

[31] R. Bass, Phys. Rev. Lett. **39**, 265 (1977).

[32] A. Chbihi, L. Manduci, J. Moisan, E. Bonnet, J. D. Frankland, R. Roy, and G. Verde, Journal of Physics: Conference Series **420**, 012099 (2013).

[33] M. Dasgupta, D. J. Hinde, A. Diaz-Torres, B. Bouriquet, C. I. Low, G. J. Milburn, and J. O. Newton, Phys. Rev. Lett. **99**, 192701 (2007).

[34] K. Nishio, H. Ikezoe, Y. Nagame, M. Asai, K. Tsukada, S. Mitsuoka, K. Tsuruta, K. Satou, C. J. Lin, and T. Ohsawa, Phys. Rev. Lett. **93**, 162701 (2004).

[35] K. Nishio, S. Mitsuoka, I. Nishinaka, H. Makii, Y. Wakabayashi, H. Ikezoe, K. Hirose, T. Ohtsuki, Y. Aritomo, and S. Hofmann, Phys. Rev. C **86**, 034608 (2012).

[36] C. R. Morton, A. C. Berriman, M. Dasgupta, D. J. Hinde, J. O. Newton, K. Hagino, and I. J. Thompson, Phys. Rev. C **60**, 044608 (1999).

[37] K. Hagino and N. Takigawa, Prog. Theor. Phys. **128**, 1001 (2012).

[38] V. Zagrebaev and V. Samarin, Phys. At. Nucl. **67**, 1462 (2004).

[39] K. Hagino, N. Rowley, and A. Kruppa, Comput. Phys. Commun. **123**, 143 (1999).

[40] R. Broglia and A. Winther, *Heavy Ion Reactions: Elastic and inelastic reactions*, Frontiers in Physics (Benjamin/Cummings Publishing Company, Advanced Book Program, 1981).

[41] M. Dasgupta, A. Navin, Y. Agarwal, C. Baba, H. Jain, M. Jhingan, and A. Roy, Nucl. Phys. A **539**, 351 (1992).

[42] M. Dasgupta, D. Hinde, J. Newton, and K. Hagino, Progress of Theoretical Physics Supplement **154**, 209 (2004).

[43] R. Broglia, C. Dasso, S. Landowne, and G. Pollarolo, Phys. Lett. B **133**, 34 (1983).

[44] C. Dasso, S. Landowne, and A. Winther, Nucl. Phys. A **405**, 381 (1983).

[45] N. Rowley, G. Satchler, and P. Stelson, Phys. Lett. B **254**, 25 (1991).

[46] P. Stelson, Phys. Lett. B **205**, 190 (1988).

[47] K. Siwek-Wilczyńska and J. Wilczyński, Phys. Rev. C **69**, 024611 (2004).

[48] W. J. Świątecki, K. Siwek-Wilczyńska, and J. Wilczyński, Phys. Rev. C **71**, 014602 (2005).

[49] T. Cap, K. Siwek-Wilczyńska, and J. Wilczyński, Phys. Rev. C **83**, 054602 (2011).

[50] E. C. Kemble, Phys. Rev. **48**, 549 (1935).

[51] J. Blocki, J. Randrup, W. Swiatecki, and C. Tsang, Ann. Phys. **105**, 427 (1977).

[52] W. D. Myers and W. J. Świątecki, Phys. Rev. C **62**, 044610 (2000).

[53] W. Reisdorf, Z. Phys. A **300**, 227 (1981).

[54] W. Reisdorf, F. Hessberger, K. Hildenbrand, S. Hofmann, G. Münzenbergnznenberg, K.-H. Schmidt, J. Schneider, W. Schneider, K. Sümmerer, G. Wirth, J. Kratz, and K. Schlitt, Nucl. Phys. A **438**, 212 (1985).

[55] C. Y. Wong, Phys. Rev. Lett. **31**, 766 (1973).

[56] N. Rowley and K. Hagino, Phys. Rev. C **91**, 044617 (2015).

[57] B. Reiner, *Nuclear reactions with heavy ions* (Springer-Verlag New York, 1980).

[58] http://www.nndc.bnl.gov/nudat2/ .

[59] J. R. Leigh, M. Dasgupta, D. J. Hinde, J. C. Mein, C. R. Morton, R. C. Lemmon, J. P. Lestone, J. O. Newton, H. Timmers, J. X. Wei, and N. Rowley, Phys. Rev. C **52**, 3151 (1995).

[60] T. Murakami, C.-C. Sahm, R. Vandenbosch, D. D. Leach, A. Ray, and M. J. Murphy, Phys. Rev. C **34**, 1353 (1986).

[61] E. Vulgaris, L. Grodzins, S. G. Steadman, and R. Ledoux, Phys. Rev. C **33**, 2017 (1986).

[62] B. B. Back, R. R. Betts, J. E. Gindler, B. D. Wilkins, S. Saini, M. B. Tsang, C. K. Gelbke, W. G. Lynch, M. A. McMahan, and P. A. Baisden, Phys. Rev. C **32**, 195 (1985).

[63] B. B. Back, Phys. Rev. C **31**, 2104 (1985).

[64] A. Gavron, P. Eskola, A. J. Sierk, J. Boissevain, H. C. Britt, K. Eskola, M. M. Fowler, H. Ohm, J. B. Wilhelmy, S. Wald, and R. L. Ferguson, Phys. Rev. Lett. **52**, 589 (1984).

[65] T. Sikkeland, Phys. Rev. **135**, B669 (1964).

[66] V. E. Viola and T. Sikkeland, Phys. Rev. **128**, 767 (1962).

[67] E. Prokhorova, A. Bogachev, M. Itkis, I. Itkis, G. Knyazheva, N. Kondratiev, E. Kozulin, L. Krupa, Y. Oganessian, I. Pokrovsky, V. Pashkevich, and A. Rusanov, Nucl. Phys. A **802**, 45 (2008).

[68] D. Morrissey, W. Loveland, R. Otto, and G. Seaborg, Phys. Lett. B **74**, 35 (1978).

[69] A. J. Pacheco, J. O. Fernández Niello, D. E. DiGregorio, M. di Tada, J. E. Testoni, Y. Chan, E. Chávez, S. Gazes, E. Plagnol, and R. G. Stokstad, Phys. Rev. C **45**, 2861 (1992).

[70] H. Esbensen, W. Jian-Qun, and G. Bertsch, Nucl. Phys. A **411**, 275 (1983).

[71] R. Spear, At. Data. Nucl. Data Tables **42**, 55 (1989).

[72] D. McDaniels, J. Lisantti, I. Bergqvist, L. Swenson, X. Chen, D. Horen, F. Bertrand, E. Gross, C. Glover, R. Sayer, B. Burks, O. Häusser, and K. Hicks, Nucl. Phys. A **467**, 557 (1987).

[73] P. Armbruster, C. R. Phys. **4**, 571 (2003).

[74] Y. Jiang, *Study of dynamical effects of the nucleus-nucleus potential using the quantum molecular dynamics model*, Master's thesis, Guangxi Normal University (2011).

[75] W. Swiatecki, Nucl. Phys. A **376**, 275 (1982).

[76] C. Shen, G. Kosenko, and Y. Abe, Phys. Rev. C **66**, 061602 (2002).

[77] Y. Aritomo, T. Wada, M. Ohta, and Y. Abe, Phys. Rev. C **55**, R1011 (1997).

[78] Y. Abe, D. Boilley, B. G. Giraud, and T. Wada, Phys. Rev. E **61**, 1125 (2000).

[79] R. Kubo, Rep. Prog. Phys. **29**, 255 (1966).

[80] J. Maruhn and W. Greiner, Z. Phys. **251**, 431 (1972).

[81] K. Sato, A. Iwamoto, K. Harada, S. Yamaji, and S. Yoshida, Z. Phys. A **288**, 383 (1978).

[82] N. Antonenko, E. Cherepanov, A. Nasirov, V. Permjakov, and V. Volkov, Phys. Lett. B **319**, 425 (1993).

[83] N. V. Antonenko, E. A. Cherepanov, A. K. Nasirov, V. P. Permjakov, and V. V. Volkov, Phys. Rev. C **51**, 2635 (1995).

[84] G. Adamian, N. Antonenko, W. Scheid, and V. Volkov, Nucl. Phys. A **627**, 361 (1997).

[85] G. Adamian, N. Antonenko, W. Scheid, and V. Volkov, Nucl. Phys. A **633**, 409 (1998).

[86] G. Adamian, N. Antonenko, and W. Scheid, Nucl. Phys. A **678**, 24 (2000).

[87] D. Boilley, Y. Abe, and J.-D. Bao, Eur. Phys. J. A **18**, 627 (2003).

[88] S. Chandrasekhar, Rev. Mod. Phys. **15**, 1 (1943).

[89] D. Boilley, H. Lü, C. Shen, Y. Abe, and B. G. Giraud, Phys. Rev. C **84**, 054608 (2011).

[90] Y.-J. Liang, M. Zhu, Z.-H. Liu, and W.-Z. Wang, Eur. Phys. J. A **48**, 133 (2012).

[91] Z. Min, F. Jun-Li, Q. Zhen, L. Zu-Hua, and W. Wen-Zhong, Chinese Physics Letters **30**, 082401 (2013).

[92] Y.-J. Liang, M. Zhu, Z.-H. Liu, and W.-Z. Wang, Phys. Rev. C **89**, 034627 (2014).

[93] C. Shen, Y. Abe, D. Boilley, G. Kosenko, and E. Zhao, Int. J. Mod. Phys. E **17**, 66 (2008).

[94] H. J. Krappe, J. R. Nix, and A. J. Sierk, Phys. Rev. C **20**, 992 (1979).

[95] S. Shlomo and J. B. Natowitz, Phys. Rev. C **44**, 2878 (1991).

[96] P. Fröbrich, Phys. Rep. **116**, 337 (1984).

[97] G. Kosenko, C. Shen, and Y. Abe, Journal of Nuclear and Radiochemical Sciences **3**, 19 (2002).

[98] J. Pouthas, B. Borderie, R. Dayras, E. Plagnol, M. Rivet, F. Saint-Laurent, J. Steckmeyer, G. Auger, C. Bacri, S. Barbey, A. Barbier, A. Benkirane, J. Benlliure, B. Berthier, E. Bougamont, P. Bourgault, P. Box, R. Bzyl, B. Cahan, Y. Cassagnou, D. Charlet, J. Charvet, A. Chbihi, T. Clerc, N. Copinet, D. Cussol, M. Engrand, J. Gautier, Y. Huguet, O. Jouniaux, J. Laville, P. L. Botlan, A. Leconte, R. Legrain, P. Lelong, M. L. Guay, L. Martina,

C. Mazur, P. Mosrin, L. Olivier, J. Passerieux, S. Pierre, B. Piquet, E. Plaige, E. Pollacco, B. Raine, A. Richard, J. Ropert, C. Spitaels, L. Stab, D. Sznajderman, L. Tassan-got, J. Tillier, M. Tripon, P. Vallerand, C. Volant, P. Volkov, J. Wieleczko, and G. Wittwer, Nucl. Instrum. Methods Phys. Res., Sect. A **357**, 418 (1995).

[99] A. Marchix, *Etude de l'influence de l'énergie de correction de couches sur les réactions nucléaires menant à la région des noyaux superlourds*, Thesis, Université de Caen (2007).

[100] H. Lü, A. Marchix, Y. Abe, and D. Boilley, paper submitted to Comput. Phys. Commun. (2015).

[101] O. Tarasov and D. Bazin, Nuclear Instruments and Methods in Physics Research Section B: Beam Interactions with Materials and Atoms **204**, 174 (2003), 14th International Conference on Electromagnetic Isotope Separators and Techniques Related to their Applications.

[102] B. Bouriquet, Y. Abe, and D. Boilley, Comput. Phys. Commun. **159**, 1 (2004).

[103] C. Wang, J. Zhang, Z. Z. Ren, and C. W. Shen, Phys. Rev. C **82**, 054605 (2010).

[104] J. Zhang, C. Wang, and Z. Ren, Nucl. Phys. A **909**, 36 (2013).

[105] G. Henning, T. L. Khoo, A. Lopez-Martens, D. Seweryniak, M. Alcorta, M. Asai, B. B. Back, P. F. Bertone, D. Boilley, M. P. Carpenter, C. J. Chiara, P. Chowdhury, B. Gall, P. T. Greenlees, G. Gürdal, K. Hauschild, A. Heinz, C. R. Hoffman, R. V. F. Janssens, A. V. Karpov, B. P. Kay, F. G. Kondev, S. Lakshmi, T. Lauritsen, C. J. Lister, E. A. McCutchan, C. Nair, J. Piot, D. Potterveld, P. Reiter, A. M. Rogers, N. Rowley, and S. Zhu, Phys. Rev. Lett. **113**, 262505 (2014).

[106] N. Bohr, Nature **137**, 334 (1936).

[107] G. Audi, M. Wang, A. Wapstra, F. Kondev, M. MacCormick, X. Xu, and B. Pfeiffer, Chin. Phys. C **36**, 1287 (2012).

[108] M. Wang, G. Audi, A. Wapstra, F. Kondev, M. MacCormick, X. Xu, and B. Pfeiffer, Chin. Phys. C **36**, 1603 (2012).

[109] V. Weisskopf, Phys. Rev. **52**, 295 (1937).

[110] V. F. Weisskopf and D. H. Ewing, Phys. Rev. **57**, 472 (1940).

[111] W. Hauser and H. Feshbach, Phys. Rev. **87**, 366 (1952).

[112] A. Gavron, Phys. Rev. C **21**, 230 (1980).

[113] R. Charity, M. McMahan, G. Wozniak, R. McDonald, L. Moretto, D. Sarantites, L. Sobotka, G. Guarino, A. Pantaleo, L. Fiore, A. Gobbi, and K. Hildenbrand, Nucl. Phys. A **483**, 371 (1988).

[114] R. J. Charity, Phys. Rev. C **82**, 014610 (2010).

[115] F. Pühlhofer, Nucl. Phys. A **280**, 267 (1977).

[116] T. Thomas, Nucl. Phys. **53**, 558 (1964).

[117] T. Thomas, Nucl. Phys. **53**, 577 (1964).

[118] A. Cole, N. Longequeue, J. Menet, J. Lucas, R. Ost, and J. Viano, Nucl. Phys. A **341**, 284 (1980).

[119] P. Young, E. D. Arthur, and M. Chadwick, "Comprehensive nuclear model calculations: Introduction to the theory and use of the gnash code," Tech. Rep. (Los Alamos National Lab., NM (United States), 1992).

[120] M. Herman, R. Capote, B. Carlson, P. Obložinský, M. Sin, A. Trkov, H. Wienke, and V. Zerkin, Nucl. Data Sheets **108**, 2655 (2007), special Issue on Evaluations of Neutron Cross Sections.

[121] A. Koning, S. Hilaire, and M. Duijvestijn, in *Proceedings of the International Conference on nuclear data for science and technology* (2007) pp. 211–214.

[122] H. Kramers, Physica **7**, 284 (1940).

[123] P. Grangé and H. A. Weidenmüller, Phys. Lett. B **96**, 26 (1980).

[124] P. Grangé, L. Jun-Qing, and H. A. Weidenmüller, Phys. Rev. C **27**, 2063 (1983).

[125] H. A. Weidenmüller and Z. Jing-Shang, Phys. Rev. C **29**, 879 (1984).

[126] Y. Abe, C. Grégoire, and H. Delagrange, Le Journal de Physique Colloques **47**, C4 (1986).

[127] Y. Abe, S. Ayik, P.-G. Reinhard, and E. Suraud, Phys. Rep. **275**, 49 (1996).

[128] A. Junghans, M. de Jong, H.-G. Clerc, A. Ignatyuk, G. Kudyaev, and K.-H. Schmidt, Nucl. Phys. A **629**, 635 (1998).

[129] V. Plujko, Nucl. Phys. A **649**, 209 (1999).

[130] V. Plujko, Acta Phys. Pol. B **31**, 435 (2000).

[131] J. Blocki, Y. Boneh, J. R. Nix, J. Randrup, M. Robel, A. J. Sierk, and W. J. Swiatecki, Ann. Phys. **113**, 330 (1978).

[132] I. Dutt and R. K. Puri, Phys. Rev. C **81**, 044615 (2010).

[133] H. Bateman, in *Proc. Cambridge Philos. Soc*, Vol. 15 (1910) pp. 423–427.

[134] S. Hassani and P. Grangé, Phys. Lett. B **137**, 281 (1984).

[135] P. Grangé, S. Hassani, H. A. Weidenmüller, A. Gavron, J. R. Nix, and A. J. Sierk, Phys. Rev. C **34**, 209 (1986).

[136] H. Delagrange, C. Grégoire, F. Scheuter, and Y. Abe, Z. Phys. A **323**, 437 (1986).

[137] I. Dostrovsky, Z. Fraenkel, and G. Friedlander, Phys. Rev. **116**, 683 (1959).

[138] M. A. McMahan and J. M. Alexander, Phys. Rev. C **21**, 1261 (1980).

[139] F. D. Becchetti and G. W. Greenlees, Phys. Rev. **182**, 1190 (1969).

[140] D. Wilmore and P. Hodgson, Nucl. Phys. **55**, 673 (1964).

[141] R. Varner, W. Thompson, T. McAbee, E. Ludwig, and T. Clegg, Phys. Rep. **201**, 57 (1991).

[142] A. Koning and J. Delaroche, Nucl. Phys. A **713**, 231 (2003).

[143] M. Nolte, H. Machner, and J. Bojowald, Phys. Rev. C **36**, 1312 (1987).

[144] V. Avrigeanu, P. E. Hodgson, and M. Avrigeanu, Phys. Rev. C **49**, 2136 (1994).

[145] J. M. Alexander, M. T. Magda, and S. Landowne, Phys. Rev. C **42**, 1092 (1990).

[146] G. Rawitscher, Nucl. Phys. **85**, 337 (1966).

[147] P. Reiter, T. L. Khoo, T. Lauritsen, C. J. Lister, D. Seweryniak, A. A. Sonzogni, I. Ahmad, N. Amzal, P. Bhattacharyya, P. A. Butler, M. P. Carpenter, A. J. Chewter, J. A. Cizewski, C. N. Davids, K. Y. Ding, N. Fotiades, J. P. Greene, P. T. Greenlees, A. Heinz, W. F. Henning, R.-D. Herzberg, R. V. F. Janssens, G. D. Jones, F. G. Kondev, W. Korten, M. Leino, S. Siem, J. Uusitalo, K. Vetter, and I. Wiedenhöver, Phys. Rev. Lett. **84**, 3542 (2000).

[148] V. F. Weisskopf, Phys. Rev. **83**, 1073 (1951).

[149] D. M. Brink, *unpublished*, Ph.D. thesis, Oxford University (1955).

[150] P. Axel, Phys. Rev. **126**, 671 (1962).

[151] J. Kopecky, M. Uhl, and R. E. Chrien, Phys. Rev. C **47**, 312 (1993).

[152] R. Capote, M. Herman, P. Obložinský, P. Young, S. Goriely, T. Belgya, A. Ignatyuk, A. Koning, S. Hilaire, V. Plujko, M. Avrigeanu, O. Bersillon, M. Chadwick, T. Fukahori, Z. Ge, Y. Han, S. Kailas, J. Kopecky, V. Maslov, G. Reffo, M. Sin, E. Soukhovitskii, and P. Talou, Nucl. Data Sheets **110**, 3107 (2009), special Issue on Nuclear Reaction Data.

[153] P. Ring, L. Robledo, J. Egido, and M. Faber, Nucl. Phys. A **419**, 261 (1984).

[154] J. L. Egido and H. A. Weidenmüller, Phys. Rev. C **39**, 2398 (1989).

[155] J. L. Egido and P. Ring, J. Phys. G **19**, 1 (1993).

[156] V. Plujko, O. Gorbachenko, and E. Kulich, Int. J. Mod. Phys. E **18**, 996 (2009).

[157] V. Plujko, R. Capote, and O. Gorbachenko, At. Data. Nucl. Data Tables **97**, 567 (2011).

[158] B. L. Berman and S. C. Fultz, Rev. Mod. Phys. **47**, 713 (1975).

[159] S. Raman, O. Shahal, and G. G. Slaughter, Phys. Rev. C **23**, 2794 (1981).

[160] D. L. Hill and J. A. Wheeler, Phys. Rev. **89**, 1102 (1953).

[161] V. Strutinsky, Phys. Lett. B **47**, 121 (1973).

[162] W. Myers and W. Swiatecki, Nucl. Phys. A **601**, 141 (1996).

[163] A. Dobrowolski, K. Pomorski, and J. Bartel, Phys. Rev. C **75**, 024613 (2007).

[164] N. Wang, Z. Liang, M. Liu, and X. Wu, Phys. Rev. C **82**, 044304 (2010).

[165] M. Liu, N. Wang, Y. Deng, and X. Wu, Phys. Rev. C **84**, 014333 (2011).

[166] N. Chamel, S. Goriely, and J. Pearson, Nucl. Phys. A **812**, 72 (2008).

[167] S. Goriely, N. Chamel, and J. M. Pearson, Phys. Rev. Lett. **102**, 152503 (2009).

[168] W. D. Myers and W. J. Świątecki, Phys. Rev. C **60**, 014606 (1999).

[169] F. A. Ivanyuk and K. Pomorski, Phys. Rev. C **79**, 054327 (2009).

[170] M. Grossjean and H. Feldmeier, Nucl. Phys. A **444**, 113 (1985).

[171] A. Gilbert and A. G. W. Cameron, Can. J. Phys. **43**, 1446 (1965).

[172] J. Tōke and W. Światecki, Nucl. Phys. A **372**, 141 (1981).

[173] R. W. Hasse and W. D. Myers, *Geometrical relationships of macroscopic nuclear physics* (Springer-Verlag Heidelberg, 1988).

[174] M. Dahlinger, D. Vermeulen, and K.-H. Schmidt, Nucl. Phys. A **376**, 94 (1982).

[175] B. d. z. Nerlo-Pomorska, K. Pomorski, and J. Bartel, Phys. Rev. C **74**, 034327 (2006).

[176] A. Iljinov, M. Mebel, N. Bianchi, E. D. Sanctis, C. Guaraldo, V. Lucherini, V. Muccifora, E. Polli, A. Reolon, and P. Rossi, Nucl. Phys. A **543**, 517 (1992).

[177] A. Bohr and B. R. Mottelson, *Nuclear structure, vol. II* (Benjamin, New York, 1975).

[178] A. V. Ignatyuk, G. Smirenkin, and A. Tishin, Yad. Fiz., v. 21, no. 3, pp. 485-490 **21** (1975).

[179] V. I. Zagrebaev, Y. Aritomo, M. G. Itkis, Y. T. Oganessian, and M. Ohta, Phys. Rev. C **65**, 014607 (2001).

[180] A. Bohr and B. R. Mottelson, *Nuclear structure, vol. I* (W. A. Benjmain, Inc., 1969).

[181] D. Hilscher and H. Rossner, Ann. Phys. Fr. **17**, 471 (1992).

[182] P. C. Rout, D. R. Chakrabarty, V. M. Datar, S. Kumar, E. T. Mirgule, A. Mitra, V. Nanal, S. P. Behera, and V. Singh, Phys. Rev. Lett. **110**, 062501 (2013).

[183] P. Möller, A. J. Sierk, T. Ichikawa, A. Iwamoto, R. Bengtsson, H. Uhrenholt, and S. Åberg, Phys. Rev. C **79**, 064304 (2009).

[184] R. Sagaidak, Proceedings of the VI International School-Seminar on Heavy Ion Physics, 22-27 September 1997, Dubna, Russia (1998).

[185] R. Yanez, W. Loveland, L. Yao, J. S. Barrett, S. Zhu, B. B. Back, T. L. Khoo, M. Alcorta, and M. Albers, Phys. Rev. Lett. **112**, 152702 (2014).

[186] Y. T. Oganessian, V. K. Utyonkov, Y. V. Lobanov, F. S. Abdullin, A. N. Polyakov, I. V. Shirokovsky, Y. S. Tsyganov, A. N. Mezentsev, S. Iliev, V. G. Subbotin, A. M. Sukhov, K. Subotic, O. V. Ivanov, A. N. Voinov, V. I. Zagrebaev, K. J. Moody, J. F. Wild, N. J. Stoyer, M. A. Stoyer, and R. W. Lougheed, Phys. Rev. C **64**, 054606 (2001).

[187] H. Gäggeler, D. Jost, A. Türler, P. Armbruster, W. Brüchle, H. Folger, F. Heßberger, S. Hofmann, G. Münzenberg, V. Ninov, W. Reisdorf, M. Schädel, K. Sümmerer, J. Kratz, U. Scherer, and M. Leino, Nucl. Phys. A **502**, 561 (1989).

[188] G. Henning, *Stability of Transfermium Elements at High Spin : Measuring the Fission Barrier of* ^{254}*No*, Thesis, Université Paris Sud - Paris XI (2012).

[189] S. Hofmann, J. Phys. G: Nucl. Part. Phys. **42**, 114001 (2015).

[190] S. Hofmann and G. Münzenberg, Rev. Mod. Phys. **72**, 733 (2000).

[191] K. Morita, K. Morimoto, D. Kaji, T. Akiyama, S. Goto, H. Haba, E. Ideguchi, R. Kanungo, K. Katori, H. Koura, H. Kudo, T. Ohnishi, A. Ozawa, T. Suda, K. Sueki, H. Xu, T. Yamaguchi, A. Yoneda, A. Yoshida, and Y. Zhao, J. Phys. Soc. Jpn. **73**, 2593 (2004), http://dx.doi.org/10.1143/JPSJ.73.2593 .

[192] K. Morita, K. Morimoto, D. Kaji, H. Haba, K. Ozeki, Y. Kudou, T. Sumita, Y. Wakabayashi, A. Yoneda, K. Tanaka, S. Yamaki, R. Sakai, T. Akiyama, S. ichi Goto, H. Hasebe, M. Huang, T. Huang, E. Ideguchi, Y. Kasamatsu, K. Katori, Y. Kariya, H. Kikunaga, H. Koura, H. Kudo, A. Mashiko, K. Mayama, S. Mitsuoka, T. Moriya, M. Murakami, H. Murayama, S. Namai, A. Ozawa, N. Sato, K. Sueki, M. Takeyama, F. Tokanai, T. Yamaguchi, and A. Yoshida, J. Phys. Soc. Jpn. **81**, 103201 (2012), http://dx.doi.org/10.1143/JPSJ.81.103201 .

[193] Y. T. Oganessian, F. S. Abdullin, C. Alexander, J. Binder, R. A. Boll, S. N. Dmitriev, J. Ezold, K. Felker, J. M. Gostic, R. K. Grzywacz, J. H. Hamilton, R. A. Henderson, M. G. Itkis, K. Miernik, D. Miller, K. J. Moody, A. N. Polyakov, A. V. Ramayya, J. B. Roberto, M. A. Ryabinin, K. P. Rykaczewski, R. N. Sagaidak, D. A. Shaughnessy, I. V. Shirokovsky, M. V. Shumeiko, M. A. Stoyer, N. J. Stoyer, V. G. Subbotin, A. M. Sukhov, Y. S. Tsyganov, V. K. Utyonkov, A. A. Voinov, and G. K. Vostokin, Phys. Rev. Lett. **109**, 162501 (2012).

[194] D. Rudolph, U. Forsberg, P. Golubev, L. G. Sarmiento, A. Yakushev, L.-L. Andersson, A. Di Nitto, C. E. Düllmann, J. M. Gates, K. E. Gregorich, C. J. Gross, F. P. Heßberger, R.-D. Herzberg, J. Khuyagbaatar, J. V. Kratz, K. Rykaczewski, M. Schädel, S. Åberg, D. Ackermann, M. Block, H. Brand, B. G. Carlsson, D. Cox, X. Derkx, K. Eberhardt, J. Even, C. Fahlander, J. Gerl, E. Jäger, B. Kindler, J. Krier, I. Kojouharov, N. Kurz, B. Lommel, A. Mistry, C. Mokry, H. Nitsche, J. P. Omtvedt, P. Papadakis, I. Ragnarsson, J. Runke, H. Schaffner, B. Schausten, P. Thörle-Pospiech, T. Torres, T. Traut, N. Trautmann, A. Türler, A. Ward, D. E. Ward, and N. Wiehl, Phys. Rev. Lett. **111**, 112502 (2013).

[195] J. Khuyagbaatar, A. Yakushev, C. E. Düllmann, D. Ackermann, L.-L. Andersson, M. Asai, M. Block, R. A. Boll, H. Brand, D. M. Cox, M. Dasgupta, X. Derkx, A. Di Nitto, K. Eberhardt, J. Even, M. Evers, C. Fahlander, U. Forsberg, J. M. Gates, N. Gharibyan, P. Golubev, K. E. Gregorich, J. H. Hamilton, W. Hartmann, R.-D. Herzberg, F. P. Heßberger, D. J. Hinde, J. Hoffmann, R. Hollinger, A. Hübner, E. Jäger, B. Kindler, J. V. Kratz, J. Krier, N. Kurz, M. Laatiaoui, S. Lahiri, R. Lang, B. Lommel, M. Maiti, K. Miernik, S. Minami, A. Mistry, C. Mokry, H. Nitsche, J. P. Omtvedt, G. K. Pang, P. Papadakis, D. Renisch, J. Roberto, D. Rudolph, J. Runke, K. P. Rykaczewski, L. G. Sarmiento, M. Schädel, B. Schausten, A. Semchenkov, D. A. Shaughnessy, P. Steinegger, J. Steiner, E. E. Tereshatov, P. Thörle-Pospiech, K. Tinschert, T. Torres De Heidenreich, N. Trautmann, A. Türler, J. Uusitalo, D. E. Ward, M. Wegrzecki, N. Wiehl, S. M. Van Cleve, and V. Yakusheva, Phys. Rev. Lett. **112**, 172501 (2014).

[196] K. Siwek-Wilczyńska, I. Skwira-Chalot, and J. Wilczyński, International Journal of Modern Physics E **16**, 483 (2007).

[197] M. Veselskỳ, acta physica slovaca **49**, 101 (1999).

[198] Z.-Q. Feng, G.-M. Jin, J.-Q. Li, and W. Scheid, Phys. Rev. C **76**, 044606 (2007).

[199] M. Veselskỳ, Private communication (2015).

[200] BIPM, IEC, IFCC, ILAC, ISO, and IUPAC, Guide to the expression of uncertainty in measurement (GUM), ISO, Geneva (1995).

[201] BIPM, IEC, IFCC, ILAC, ISO, and IUPAC, GUM 1995 with minor corrections. Evaluation of measurement data—Guide to the expression of uncertainty in measurement (2008).

[202] M. C. Kennedy and A. O'Hagan, J. R. Stat. Soc. Series B Stat. Methodol. **63**, 425 (2001).

[203] C. Stodel, private communications (2015).

[204] C. Shannon, Bell System Technical Journal **27**, 379 (1948).

[205] E. T. Jaynes, Phys. Rev. **106**, 620 (1957).

[206] B. Gough, *GNU scientific library reference manual* (Network Theory Ltd., 2009).

[207] G. Münzenberg, S. Hofmann, F. Heßberger, W. Reisdorf, K. Schmidt, J. Schneider, P. Armbruster, C. Sahm, and B. Thuma, Z. Phys. A **300**, 107 (1981).

[208] S. Hofmann, F. Heßberger, D. Ackermann, S. Antalic, P. Cagarda, B. Kindler, P. Kuusiniemi, M. Leino, B. Lommel, O. Malyshev, R. Mann, G. Münzenberg, A. Popeko, S. Śaro, B. Streicher, and A. Yeremin, Nucl. Phys. A **734**, 93 (2004), proceedings of the Eighth International Conference On Nucleus-Nucleus Collisions.

[209] W. Loveland, arXiv preprint arXiv:1301.1759 (2013).

[210] E. T. Jaynes, *Probability theory: the logic of science* (Cambridge university press, 2003).

[211] E. T. Jaynes, Phys. Rev. **108**, 171 (1957).

[212] J. Shore and R. Johnson, IEEE Transactions on Information Theory **26**, 26 (1980).

[213] D. S. Sivia, *Data analysis: a Bayesian tutorial* (Oxford university press, 1996).

[214] H. Lü and D. Boilley, EPJ Web of Conferences **62**, 03002 (2013).

[215] M. W. Kirson, Nucl. Phys. A **798**, 29 (2008).

[216] C. Sanderson, Armadillo: An open source C++ linear algebra library for fast prototyping and computationally intensive experiments (2010).

[217] H. A. Bethe and R. F. Bacher, Rev. Mod. Phys. **8**, 82 (1936).

[218] G. Royer, Nucl. Phys. A **807**, 105 (2008).

[219] G. Royer and A. Subercaze, Nucl. Phys. A **917**, 1 (2013).

[220] P. Danielewicz, Nucl. Phys. A **727**, 233 (2003).

[221] P. Danielewicz and J. Lee, Nucl. Phys. A **818**, 36 (2009).

[222] W. Stocker, J. Bartel, J. Nix, and A. Sierk, Nucl. Phys. A **489**, 252 (1988).

[223] M. Durand, P. Schuck, and X. Viñas, Z. Phys. A **346**, 87 (1993).

[224] E. Wigner, Phys. Rev. **51**, 947 (1937).

[225] P. Van Isacker, O. Juillet, and B. Gjelsten, Found. Phys. **27**, 1047 (1997).

[226] D. D. Warner, M. A. Bentley, and P. Van Isacker, Nat. Phys. **2**, 311 (2006).

[227] V. Strutinsky, Nucl. Phys. A **95**, 420 (1967).

[228] V. Strutinsky, Nuclear Physics A **122**, 1 (1968).

[229] P. Van Isacker, in *XXX Mazurian Lakes Conference Nuclear Physics and The Fundamental Processes*, Vol. 39 (Piaski, Poland, 2007) pp. 421–431.

[230] D. Lunney, J. M. Pearson, and C. Thibault, Rev. Mod. Phys. **75**, 1021 (2003).

[231] L. G. Moretto, P. T. Lake, L. Phair, and J. B. Elliott, Phys. Rev. C **86**, 021303 (2012).

[232] A. Tarantola, *Inverse problem theory and methods for model parameter estimation* (siam, 2005).

[233] J. Dobaczewski, W. Nazarewicz, and P.-G. Reinhard, J. Phys. G: Nucl. Part. Phys. **41**, 074001 (2014).

[234] G. J. Kerns, *Introduction to probability and statistics using R* (2010).

[235] N. R. Draper and H. Smith, *Applied regression analysis* (John Wiley & Sons, 2014).

[236] S. S. Shapiro and M. B. Wilk, Biometrika **52**, 591 (1965).

[237] K. Pomorski and J. Dudek, Phys. Rev. C **67**, 044316 (2003).

[238] N. Wang, M. Liu, and X. Wu, Phys. Rev. C **81**, 044322 (2010).

[239] W. J. Świątecki, Phys. Rev. **101**, 97 (1956).

[240] J. Blatt and V. Weisskopf, *Theoretical nuclear physics* (Springer-Verlag New York Inc., 1979).

[241] R. Vandenbosch and J. Huizenga, *Nuclear fission* (Academic Press, 1973).

[242] M. Abramowitz and I. A. Stegun, *Handbook of mathematical functions: with formulas, graphs, and mathematical tables*, 55 (Courier Dover Publications, 1972).

[243] H. A. Bethe, Phys. Rev. **50**, 332 (1936).

[244] H. A. Bethe, Rev. Mod. Phys. **9**, 69 (1937).

[245] J. R. Huizenga and L. G. Moretto, Annu. Rev. Nucl. Sci. **22**, 427 (1972).

[246] W. J. Świątecki, K. Siwek-Wilczyńska, and J. Wilczyński, Phys. Rev. C **78**, 054604 (2008).

[247] D. Wilgenbus, Rapport de stage, GANIL, Université d'Orsay (1998).

[248] H. Lü, Rapport de stage, GANIL, Université de Caen (2012).

Résumé :

L'existence d'éléments super-lourds (SHE) a été prédite par le modèle en couches. Cependant, la description théorique de la réaction nucléaire pour les systèmes lourds, essentielle pour la synthèse de SHE, n'a pas encore été bien établie. Bien qu'il y ait un accord général sur le mécanisme de réaction, de grands écarts entre les prévisions quantitatives persistent toujours en raison de la présence du phénomène de la fusion entravée. Le premier objectif de cette thèse est d'étudier différents modèles liés à la description complète de la réaction de fusion-évaporation. Puis, une analyse d'incertitude, en combinaison avec un code de cascade appelé KEWPIE2, est effectuée. En inspectant les incertitudes dues aux paramètres et modèles, il est clairement montré que la barrière de fission a le rôle le plus crucial pour contraindre les modèles de fusion à partir des données expérimentales. Comment faire pour déterminer l'incertitude associée à la barrière de fission? Puisque nous ne disposons pas d'assez de données fiables, nous avons cherché à appliquer l'inférence Bayésienne. À l'aide de KEWPIE2 et des pseudo-données inventées (sans fusion entravée), des résultats préliminaires nous indiquent que l'incertitude de la barrière de fission est sensible à la fois au nombre et à la précision de données ainsi qu'aux paramètres de nuisance. En outre, il est connu que le processus de fusion et la barrière de fission peuvent être décrits dans le même cadre du modèle de la goutte liquide. Ainsi, ils doivent être corrélées entre eux. En revisitant une simple formule de masse avec la théorie de la régression linéaire, les incertitudes sur les paramètres du modèle ainsi que la corrélation entre l'énergie de séparation du dernier neutron et la barrière de fission sont étudiés. L'impact de leurs covariances sur la probabilité de survie est concrètement analysée. Une étude plus complète sera nécessaire pour tenir compte de la corrélation avec les corrections de couches.

Mots-clés : Eléments super-lourds; Analyse d'incertitude; Collisions nucléaires; Inférence Bayésienne; Modèle de la goutte liquide; Théorie de la régression linéaire

---

Synthesis of Super-Heavy Elements: Role of Uncertainty Analysis in Theoretical Modeling

Abstract:

The existence of super-heavy elements (SHE) has been predicted by the nuclear shell model. However, the nuclear reaction theory for heavy systems, which is essential for the synthesis of SHE, has not been well established yet. Although we have reached a general agreement on the reaction mechanism, large discrepancies between quantitative predictions still persist because of the presence of the fusion hindrance phenomenon. The first aim of this Ph.D. work is to investigate different models associated with the complete description of the heavy-ion fusion-evaporation reaction. Then, a complete uncertainty analysis, in combination with a newly-developed cascade code called KEWPIE2, is performed. By inspecting uncertainties due to parameters and models, it is clearly revealed that the fission barrier has the most crucial role to play in constraining the fusion models. How to determine the uncertainty associated with the fission barrier? Since we do not have enough reliable data, we propose to consider Bayesian inference by reversing the usual mode of thinking. Based upon the KEWPIE2 code with simulated pseudo-data (without fusion hindrance), preliminary results tell us that the estimated uncertainty in the fission barrier appears to be quite sensitive to the number and precision of data points as well as the nuisance parameters. Furthermore, it is known that the fusion process and the fission barrier can be both described within the framework of the liquid-drop model. Thus, they should be correlated with each other. With the help of a simple liquid-drop mass formula and the regression theory, uncertainties in the model parameters as well as the correlation between the neutron-separation energy and fission barrier are inspected. The influence of their covariances on the survival probability is concretely investigated. Further consideration will be required to account for the correlation with the shell corrections.

Keywords: Super-heavy elements; Uncertainty analysis; Nuclear collisions; Bayesian inference; Liquid-drop model; Linear regression